Department of Geological Sciences, University of Cape Town

Denudation rates and geomorphic evolution of the Cape Mountains, determined by the analysis of *in situ*-produced cosmogenic ^{10}Be

by

Taryn E. Scharf

Dissertation presented in February 2012 for the degree of Master of Science in Geology

Supervisors:

Prof. Maarten J. de Wit
African Earth Observatory Network; Nelson Mandela Metropolitan University

Dr. Alexandru T. Codilean
Deutches GeoForschungsZentrum

Abstract

Southern Africa is host to a unique mountain system, the Cape Mountains, which includes the coastal Cape Fold Belt (CFB) and an inland Escarpment. Apatite fission track analysis has shown that this mountain system is an erosion feature, exhumed from beneath 2-7 km of overburden by large-scale denudation processes affecting the subcontinent during Gondwana break-up (ca. 140 – 65 Ma).

Despite its antiquity and location on a passive continental margin, the ruggedness of the present-day topography of the Cape Mountains compares to that of the world's active orogens. The coastal Cape Mountains are traversed by deeply-incised, meandering rivers that cut canyons through the most resistant quartzite ridges of these mountains, perpendicular to their structural grain inherited from the CFB. The evolution of this landscape is poorly understood, because little quantitative data exists on the denudation history of the Cape Mountains. This study presents the first *in situ*-produced cosmogenic ^{10}Be inventories determined for quartz from catchment sediments and bedrock surfaces within the coastal Cape Mountains, with which to quantify denudation rates, exposure ages and the recent geomorphic evolution of these Cape Mountains.

River sediments sampled from catchments within the Langeberg and Swartberg Ranges of the Western Cape, as well as bedrock from the Tradouw River traversing the Langeberg Range, were analysed. In addition, charcoal from alluvial material was collected for radiocarbon dating.

Catchment-averaged denudation rates reported from these mountains range between 2.1 ± 0.3 and 6.9 ± 1.9 $m \cdot Myr^{-1}$. These are amongst the lowest reported rates globally, despite the rugged terrain of the mountain system. The spatial consistency between the low denudation rates suggests a landscape approaching geomorphic steady-state. This finding is best attributed to lithological control on denudation rates in a tectonically quiescent environment, and a relatively dry climate. Bedrock samples collected from the flanking interfluves, and from the bedrock channel along the Tradouw River, indicate that slow down wearing of exposed bedrock surfaces contributes to most of the sediment production in the

sampled catchments. Results contrast with previous studies that propose the steep canyons are Miocene or younger in age, and lend support to those studies that suggest these canyons are older, cut perhaps in the late-Mesozoic to mid-Cenozoic. The results of this study are consistent with apatite fission track analysis and other cosmogenic nuclide analyses carried out elsewhere across southern Africa, and which all suggest the landscape of the subcontinent has experienced relatively long-term stability. No evidence was found to support theories which attribute much of the present-day topography of the Cape Mountains to epeirogenic uplift in the Pliocene (ca. 3-5 Ma).

Relationships between denudation rate and roughness (e.g. the hillslope, relief, and catchment steepness) determined for the sampled catchments suggest caution in using topography as a proxy for denudation rate in comparative studies, and suggest that linear hillslope-denudation rate models may also be applicable to rugged terrains that are located in relatively quiescent tectonic environments.

Acknowledgements

I would like to express my sincere gratitude towards a great number of people who have assisted me throughout this study:

Prof. Maarten de Wit (AEON, NMMU) is thanked for his continued encouragement and guidance throughout this project; for his valuable critique of the dissertation; and for the instrumental role he played in providing the funding for this project through the German - South African research collaboration, Inkaba yeAfrika. Without the assistance of Prof. de Wit this project would surely not have come about.

Dr. Alexandru Codilean (GFZ-Potsdam) is thanked for his continued positive attitude, endless patience, and tireless assistance in many aspects of this work. The many hours spent assisting and teaching me in the field, laboratory and lecture rooms went beyond what could be asked of him, and have provided an inspiration at times of low morale. Dr. Codilean has also provided valuable guidance in the scripting of this dissertation.

Dr. Samuel Niedermann (GFZ-Potsdam) is thanked for his assistance and knowledgeable guidance during fieldwork, and for providing me with the opportunity to learn through hands-on experience in the Nobel Gas Laboratory at the GFZ-Potsdam. Dr. Niedermann has furthermore contributed a number of field photographs to this final dissertation, for which I am grateful.

Thanks are owed to my colleagues during my time spend at the Section 3.4, Earth Surface Geochemistry, GFZ-Potsdam, who gave patiently of their time and input when asked. Further thanks are owed to Friedhelm von Blanckenburg, Head of Section 3.4, for hosting me in his section for the duration of my stay in Germany.

Special recognition is due to the many scientists from various institutes who have crossed my path over the past two years and provided input on this work. Most notable are Dr. Michael Attol (University of Edinburgh), Prof. Roderick Brown (University of Glasgow), Dr. Jean Dixon (GFZ), Prof. Dr. Friedhelm von Blanckenburg (GFZ), Dr. John Jansen (University of Wollongong), Dr. Eric Kirby

(Pennsylvania State University), and Dr. Angela Landgraf (University of Potsdam),

Andre and Annamarie Nel, owners of Hoekraal farm near Zuurbrak, opened their home to me for the duration of my field work. A heart-felt thank you is owed to Mr and Mrs Nel for their kindness, generosity, and warm-hearted hospitality which were of invaluable assistance in the field.

Henry and Hester Barry, owners of Lismore farm near Zuurbrak, are thanked for allowing me full access to their land and for their continued enthusiasm for my work. Special thanks are owed to Henry for assisting me when I ran into difficulties in the field.

Connor Scheckle gave generously of his time to assist me in the field and has been a part of this project every day since its inception. Many thanks are owed to Connor for his tireless support.

Dr. Patrick Goldstone is thanked for his language expertise in technical aspects of the final dissertation.

A deep and heartfelt thank-you is owed to my parents: my father, Heinrich Scharf, whose infectious enthusiasm for natural science has been an inspiration at the most needed times; and my mother, Marlene Scharf, whose personal strength has taught me that no task is too long or too hard for one to persevere. Collectively, their passion for knowledge and excellence has taught me to strive to deliver my best at all times.

A final thank-you is owed to my many friends across two world hemispheres that have been a source of encouragement throughout this project

Table of Contents

List of Figures

List of Tables

Glossary

Frequently used acronyms and terms as defined in text

AMS	Accelerator mass spectrometer
ICP-OES	Inductively coupled plasma optical emission spectroscopy
TCN	Terrestrial cosmogenic nuclide, synonymous with '*in situ*-produced cosmogenic nuclide'.
AFTA	Apatite fission track analysis
CDF	Chemical depletion fraction. The proportion of the chemical weathering rate to overall denudation rate.
k_{sn}	Normalised channel steepness index. Channel steepness index, as defined in Flint's Law, normalised for drainage area.
Kd	Equilibrium distribution coefficient in chromatography. This parameter describes an ion's affinity for a resin in a particular aqueous medium.
z*	Attenuation path length. This parameter describes the distance (z*) into a material at which the penetrating cosmic ray flux will have been attenuated to 33% of its original flux strength.
Averaging timescale	The averaging timescale is the time period for which a given geochronometry or thermochronometry technique returns an averaged denudation rate. In cosmogenic nuclide analysis, the averaging timescale refers to the time period required to

	remove a depth of one absorption path length from the denuding material, at the given denudation rate.
Denudation	The sum of physical erosion and chemical weathering.
Terrace	The term 'terrace' as used in this study refers to a previous position that a river channel once held and which has since been abandoned due to river incision.
^{10}Be	Unless otherwise stated, ^{10}Be refers to the *in situ*-produced cosmogenic radioisotope ^{10}Be.
Geomorphic steady state	All points within a landscape denudation at a similar rate, thus maintaining the form of the landscape as it denudes.
Detachment limited	A detachment limited river channel is one in which the river sediment carrying capacity exceeds the sediment load supplied to the river.
Transport limited	A transport limited river channel is one in which the sediment load supplied to the river exceeds the sediment carrying capacity of the river.

Chapter 1

Introduction

1.1 Aim of study

This study aims to assess the nature of the recent geomorphic evolution of the coastal Cape Mountains, by quantifying denudation rates and surface exposure ages of various landscape elements within these mountains. To achieve this aim, analysis of quartz-hosted *in situ*-produced cosmogenic ^{10}Be is carried out in conjunction with radiocarbon dating and river channel steepness assessments.

1.2 The Cape Mountains

The Cape Fold Belt (CFB) of southern Africa encompasses a series of coast-parallel ranges that dominate the southern and western coastal hinterland of South Africa. At the time of its formation ca. 250 Ma, a larger regional orogenic system was uplifted across southern Gondwana in a four-phase deformational event, which affected not only South Africa, but Antarctica, Argentina, Australia and the Falkland Islands as well (Newton et al., 2006; Du Toit, 1937; Milani and de Wit, 2008). The E-W oriented ranges of the southern CFB and northwest to north trending ranges of the western CFB form a series of gentle arcs, concave towards their adjacent shorelines, that converge near the Cape Peninsula in a region of complex folding and faulting termed the 'Cape syntaxis' (Figure 1.1, Figure 1.2).

The mountains and their intermontane basins form a series of anticlines and synclines juxtaposed through thrust faulting and are themselves characterised by intense micro- and mesoscale folds and thrusts. Deformation of the Cape Orogeny was born largely by the Cape and Karoo Supergroups. The present-day ranges and their adjacent basins comprise largely low-grade metasedimentary rocks; resistant quartzites and metasandstones form the major component of the high ground,

while valleys are comprised of incompetent shales and schists. Basement rock was also affected by the orogeny and can be found outcropping in the exposed cores of eroded anticlines within the mountain belt (Figure 1.3) (Newton et al., 2006). These basement rock inliers include outcrops of the Klipheuwel, Kansa, Cango Caves, Gamtoos, Kaaimans and Malmesbury Groups.

Today it is believed that the CFB is an exhumed mountain belt which originally lay buried beneath 2-7 km of material (Tinker, 2005; Tinker and de Wit, 2004). This overburden is speculated to have belonged to the upper Karoo Supergroup and possibly an unknown formation of younger or equivalent age, whose removal begun in the early to mid-Cretaceous. Further evidence for this extensive excavation are perched synclines within the fold belt, and landscape inversion as evidenced by the presence of boulder-capped mesas ('table lands') at the foot of these mountains (Twidale and van Zyl, 1981). This realisation has led to the recognition of two geomorphological entities associated with this mountain belt, namely the Cape Fold Belt formed between 278 Ma – 230 Ma and its present-day erosional remnant whose rapid excavation was related to the end-Mesozoic break-up of Gondwana and the consequent rapid denudation that characterised the margins of southern Africa at that time (Brown et al., 1998; Cockburn et al., 2000; Brown et al., 2002; Tinker et al., 2008a; Tinker et al., 2008b; Kounov et al., 2009; Flowers and Schoene, 2010). This present-day remnant of the Cape Fold Belt forms part of what is referred to as the 'Cape Mountains', a term which also includes the Great Escarpment (Figure 1.1 and Figure 1.2).

The remnant Cape Fold Belt (CFB) and Great Escarpment (or simply Escarpment) have long been viewed as two geomorphologically distinct features and indeed, their origins are different. In contrast to the Permo-Triassic Cape Fold Belt, the Escarpment arose at the time of continental rifting and has been attributed to parallel retreat of uplifted rift margins (e.g. Moore, 1999; King, 1962; King, 1951; King, 1953; Partridge and Maud, 1987; Moore and Blenkinsop, 2006) or alternatively, to the excavation of a pre-existing drainage divide (e.g. van der Beek et al., 2002; Gilchrist et al., 1994; Cockburn et al., 2000; Brown et al., 2002). Despite their distinctly different origins, the present-day remnants of the Cape Fold Belt and Escarpment are geomorphic features of similar age and origin, owing much of their present-day topography to denudational processes that have operated on the landscape of southern Africa since the time of continental rifting.

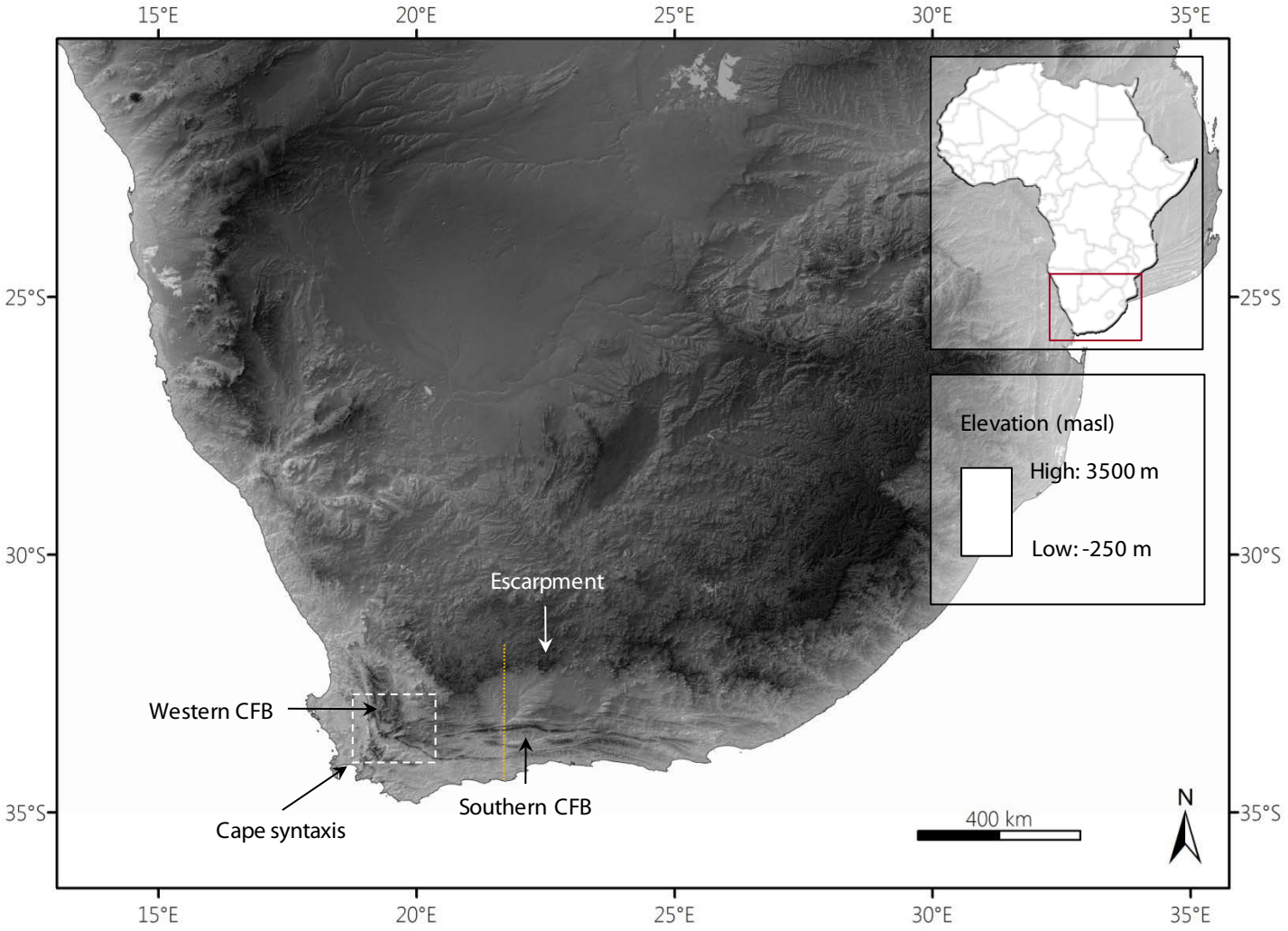

Figure 1.1: The term 'Cape Mountains' refers to the mountainous terrains of southern Africa that were sculpted into their present form following the extensional tectonic regime of the end-Mesozoic rifting of Gondwana. These include the coastal remnants of the Cape Fold Belt and the Escarpment mountains located further inland.

Main image: A digital elevation model of southern Africa showing the arcuate limbs of the western and southern remnant Cape Fold Belt (CFB), the area of the Cape syntaxis outlined with a white stippled box, and the Escarpment. The stippled yellow line shows the line of cross-section in Figure 1.2. This figure was constructed using SRTM 90 m resolution digital elevation model, sourced from the AEON database. Top insert: The location of the main image within the African continent (red box).

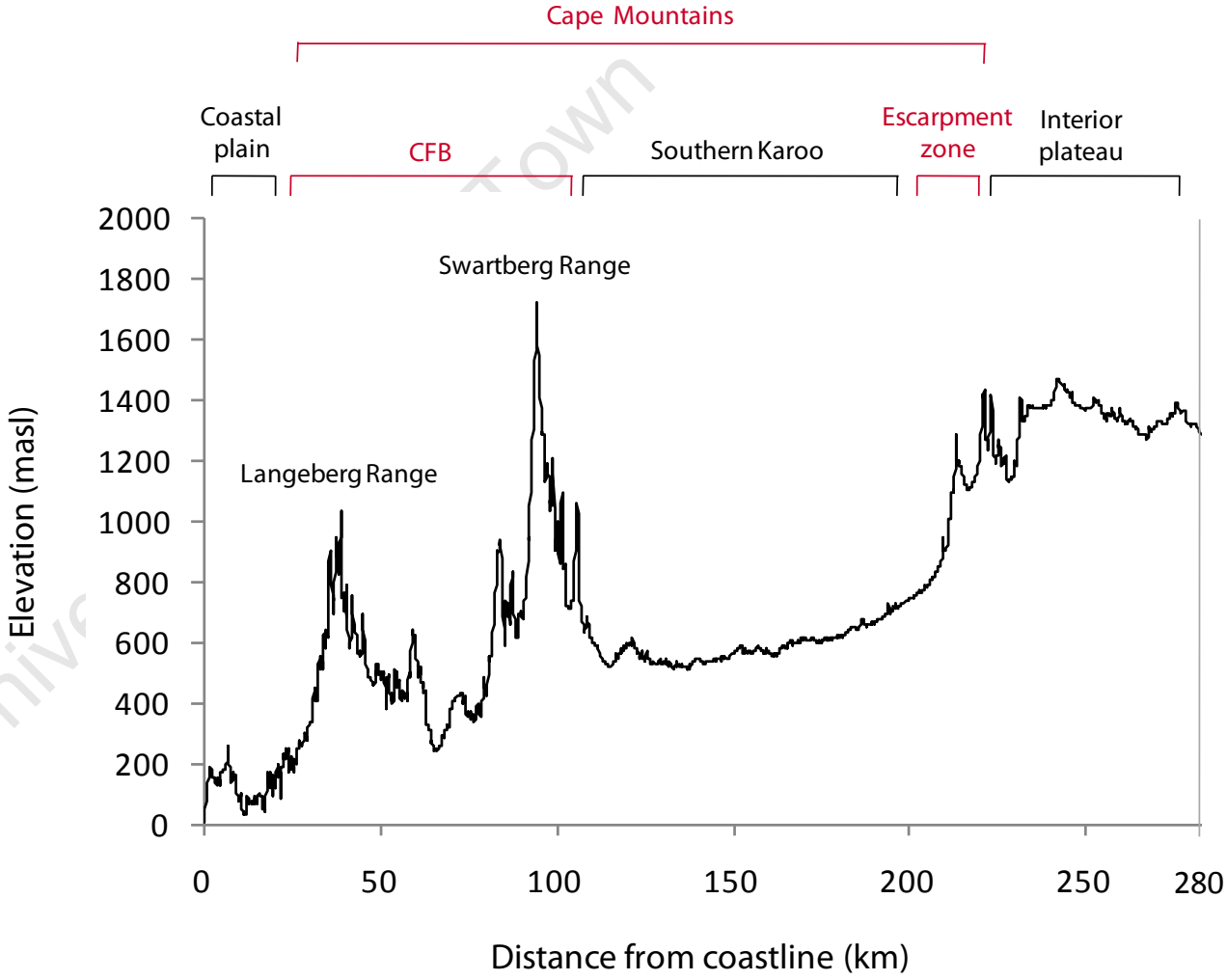

Figure 1.2: Cross-section showing three main morphological zones of southern Africa: the coastal plain, Escarpment zone and interior plateau. Note that the south and south-west coastal plains contain the localised exhumed geomorphic region of the Cape Fold Belt (Langeberg and Swartberg Ranges visible in this cross-section). This mountain belt divides the coastal plain into two regions, namely the coastal plain south of the fold belt and the Karoo plains north of the fold belt (cf. Figure 1.1). This figure was compiled using the SRTM 90 m resolution digital elevation model, sourced from the AEON database.

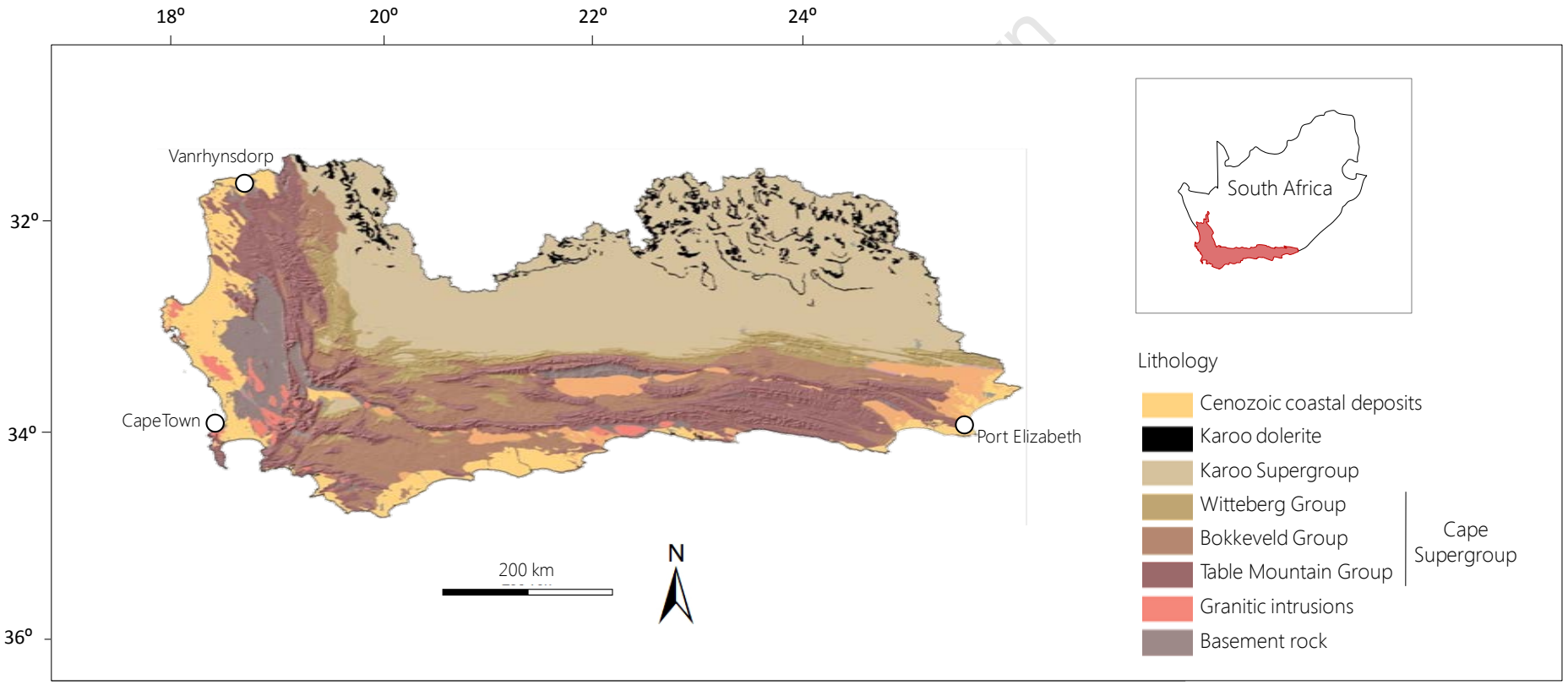

Figure 1.3: Geological map for the extent of the present-day remnants of the Cape Fold Belt (i.e. coastal Cape Mountains) with topography selectively superimposed in the region of the remnant Cape Fold Belt. Note that the ranges are comprised largely of the quartzitic Table Mountain and Witteberg Group rocks (cf. Table 1.1), while intermontane basins and the coastal plain lie on shales of the Bokkeveld Group and Karoo Supergroup. The SRTM 90 m resolution digital elevation model and lithological data were sourced from the AEON database.

Table 1.1: Simplified stratigraphic column for the Cape Supergroup, according to Thamm and Johnson (2006). Formations names and descriptions apply to outcrops west of 21° E. The high peaks of the Cape Fold Belt mountains are largely comprised of Table Mountain Group Rocks (cf. Figure 1.3). Note that both quartzite and sandstone are listed as sandstone.

CAPE SUPERGROUP			
GROUP	**SUBGROUP**	**FORMATION**	**LITHOLOGY**
Witteberg	Lake Menz	Waaipoort	Mudrock, sandstone
		Floriskraal	Shale, Sandstone
		Kweekvlei	Shale
	-	Witpoort	Sandstone
	Weltevrede	Swartruggens	Shale, siltstone, sandstone
		Blinkberg	Sandstone, siltstone
		Wagen Drift	Shale, stilstone, sandstone
Bokkeveld	Bidouw	Karoopoort	Mudrock, stiltstone, sandstone
		Osberg	Sandstone, siltstone
		Klipbokkop	Mudrock, siltstone, sandstone
		Wuppertal	Sandstone, siltstone
		Waboomberg	Mudrock, siltstone, sandstone
	Ceres	Boplaas	Sandstone
		Tra-Tra	Mudrock, siltstone
		Hex River	Sandstone
		Voorstehoek	Mudrock, siltstone
		Gamka	Sandstone
		Gydo	Mudrock, siltstone
Table Mountain	Nardouw	Rietvlei	Sandstone
		Skurweberg	Sandstone
		Goudini	Sandstone
		Cedarberg	Shale, siltstone
		Pakhuis	Diamictite, sandstone
		Peninsula	Sandstone
		Graafwater	Sandstone, siltstone, shale
		Piekenierskloof	Sandstone, conglomerate

The term 'Cape Mountains' therefore extends to those mountainous terrains of southern Africa which owe much of their present-day topography to large-scale denudation that accompanied the Mesozoic rifting of Gondwana. This mountain system is an erosion feature. To facilitate the discussion of these geographically separate regions of the Cape Mountains, the terms 'coastal Cape Mountains' and 'Escarpment' will be used to refer to the present-day erosion remnants of the Cape Fold Belt and Great Escarpment, respectively.

The geomorphology of the Cape Mountains and in particular, the coastal Cape Mountains, appears incongruent with its present-day geologic setting. Its rugged terrain is like that of present-day active orogens, despite its antiquity and location on a passive continental margin. Within the coastal Cape Mountains, the occurrence of winding and occasionally meandering canyons incised 1-2 km into the quartzites of the mountains and drained by undersized rivers, is common place (Figure 1.4). In southern Africa, this trellis drainage pattern is unique to the coastal Cape Mountains (Stankiewicz et al., 2005; Stankiewicz et al., 2008) and its peculiarity has provided the stimulus for a number of investigations into the nature and timing of its development (e.g. van Zyl, 1982; Rogers, 1903; Taljaard, 1948; Taljaard, 1949; Davis, 1906a and 1906b; Lenz, 1953; Twidale and van Zyl, 1981).

Bedrock benches within the mountains (Figure 1.5) and subhorizontal platforms along the mountain flanks (Figure 1.6) lend a 'stepped' appearance to the landscape. This stepped appearance is perpetuated in the flood plains by 'table lands', apparently preserved intact by their resistant cappings of fluvial pebbles and boulders, often cemented with silcrete or ferricrete, while the surrounding land has been lowered to a few hundred meters below (Figure 1.7). These surfaces and their deposits have played a key role in past attempts to unravel the geomorphic history of the region through their use as datum surfaces of loosely constrained age in a landscape where very little is known of the relative timing of events. Fluvial deposits similar to those capping the table lands can be found in the present-day streams and depositional terraces that flank them. These tablelands have been interpreted as a series of abandoned river terraces cut by trunk streams (Lenz, 1953) or flights of pediments cut by tributary streams and subsequently dissected (Twidale and van Zyle, 1981).

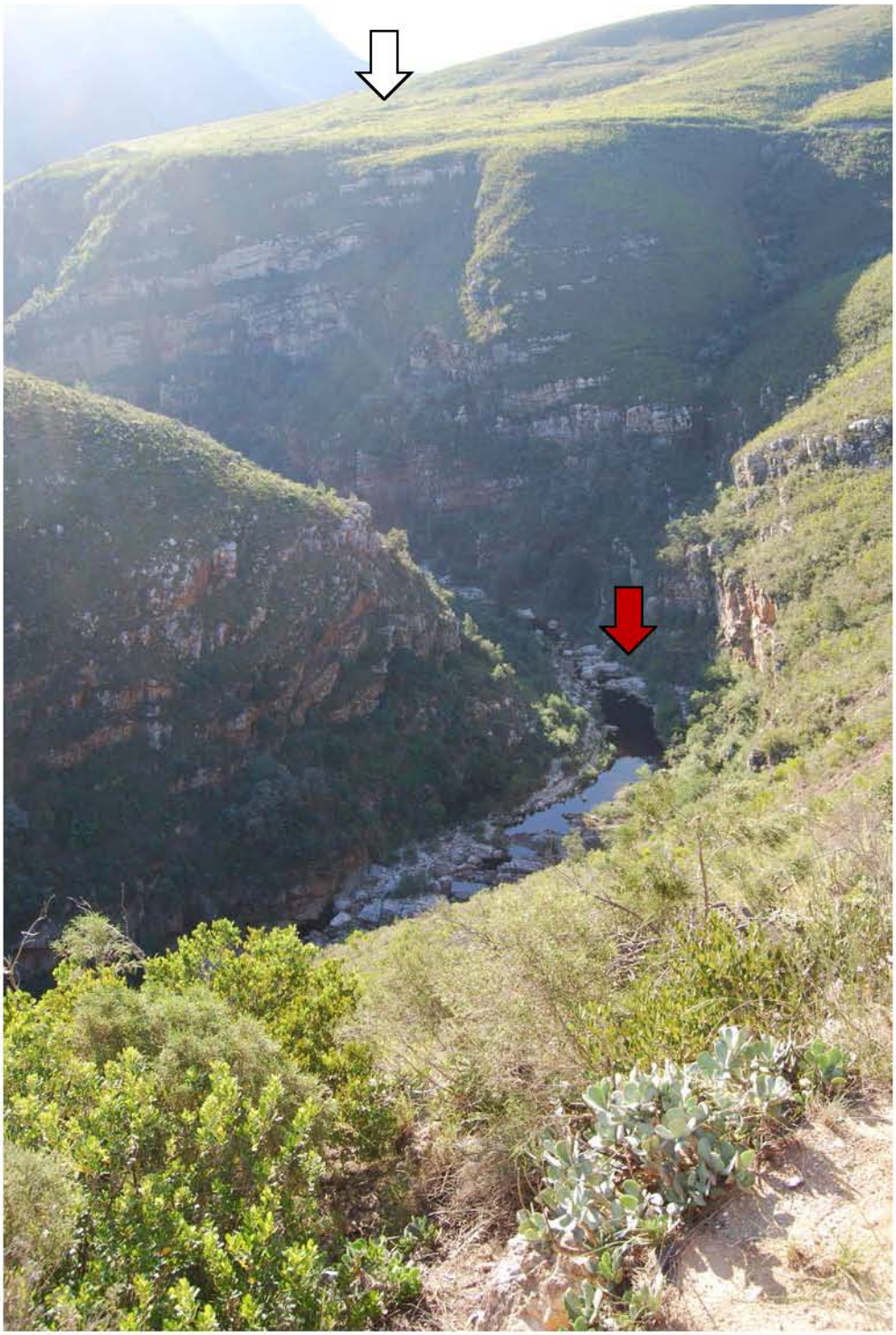

Figure 1.4: Tradouw River (red arrow) meanders its way through the Langeberg Range of the coastal Cape Mountains. The small present-day Tradouw River lies at the bottom of a gorge, cut hundreds of meters into the massive quartzites of the Table Mountain Group. A sub-horizontal platform is clearly visible above the river (white arrow). The height difference between the red and white arrows is over 100 m. View is towards the north. This photo is courtesy of Dr. Samuel Niedermann (GFZ-Potsdam).

Figure 1.5: Bedrock benches (white arrows) line the channel of Tradouw River which cuts through the Langeberg Range of the coastal Cape Mountains. Behind the bedrock benches, the characteristically steep hillslopes of the coastal Cape Mountains are lit with the afternoon sun. The view is towards the north. This photo is courtesy of Dr Samuel Niedermann (GFZ-Potsdam).

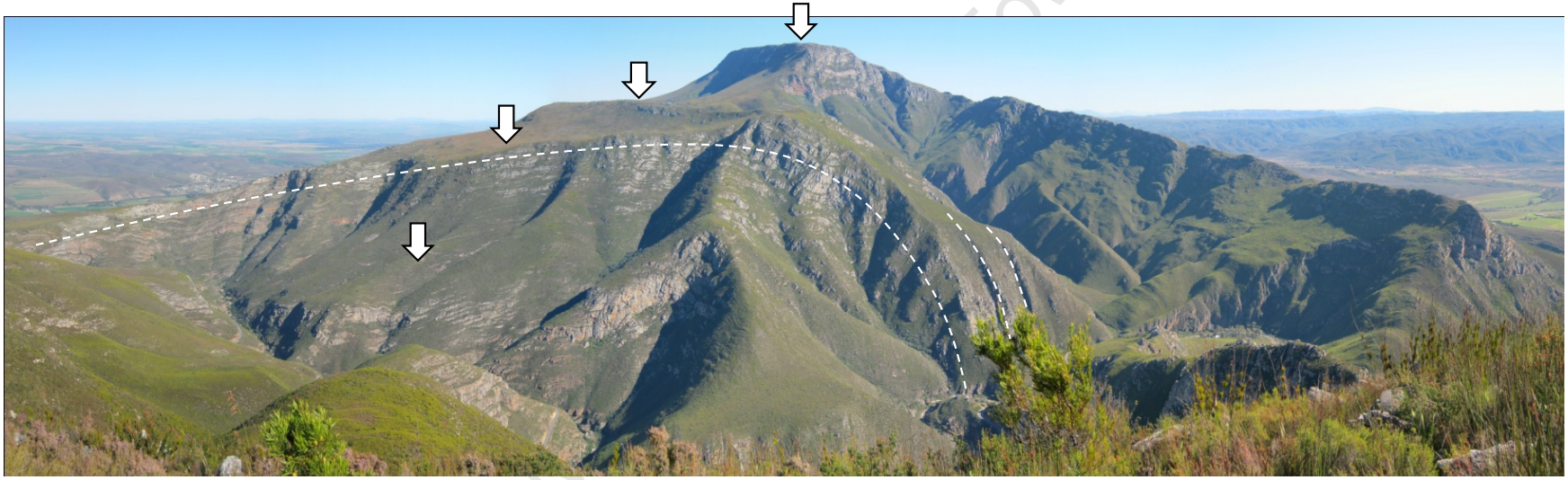

Figure 1.6: A west-facing view of the apex of the Langeberg Range, within the coastal Cape Mountains. Subhorizontal platforms within the Langeberg Range give the landscape a "stepped" appearance (white arrows). The structure of the Langeberg Range, like many in the southern coastal Cape Mountains, is a north-verging anticline (bedding indicated by white stippled lines). Note the steep slopes characteristic of the ranges that comprise the coastal Cape Mountains.

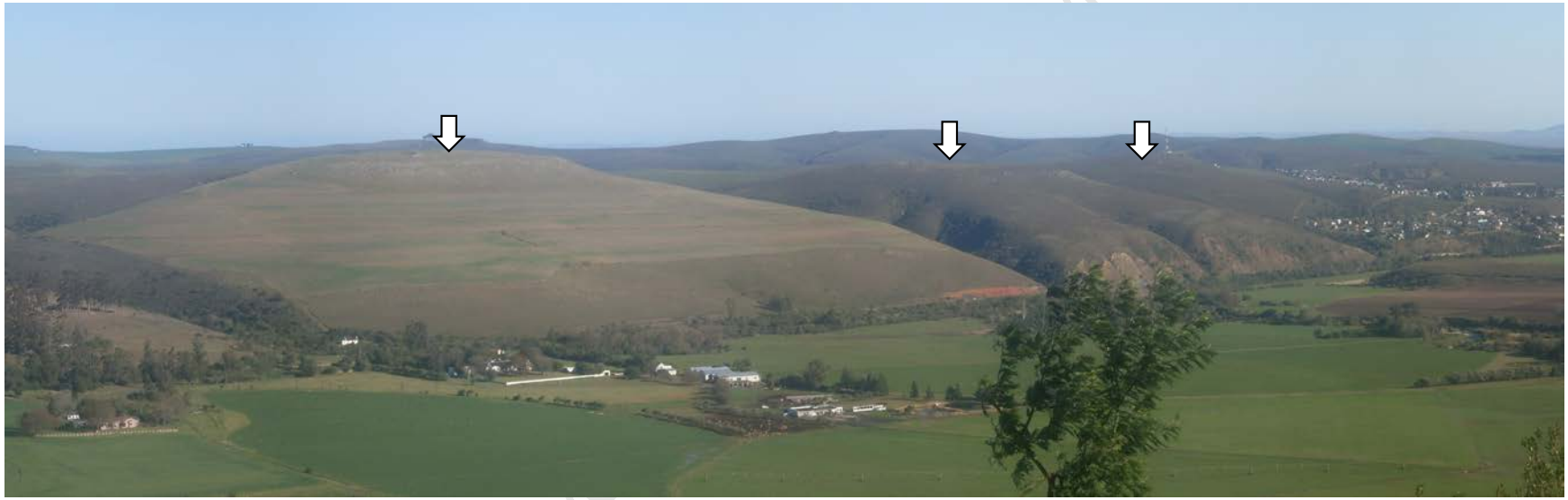

Figure 1.7: Landscape inversion within the river valley of the Buffeljags River, at the foot of the Langeberg Range of the coastal Cape Mountains. Fluvial deposits of quartzite boulders form a carapace on the hilltops (white arrows) which appears to preserve the elevation of the small hills while the surrounding land is lowered. However, no quantitative data exists as of yet to confirm this interpretation. In the foreground are the floodplains of the Buffeljags and Tradouw Rivers, in the right background is the small town of Zuurbrak. The view is towards the south-west.

Without an objective method with which to assess the exposure ages of these land surfaces or the rates at which they denude, traditional geomorphological studies continue to rely on field observation and the subsequent correlation of erosion surfaces in their attempts to unravel the evolutionary history of this landscape (e.g. van Zyl, 1982; Taljaard, 1949; Lenz, 1953; Twidale and van Zyle, 1981; Partridge and Maud, 1987). Inherent in these methods are difficulties in distinguishing observation from interpretation, a dearth of independent age constraints, and the doubts that surround the extrapolation and correlation of localised erosion surfaces over broad areas (Summerfield, 1996; Brown et al., 2000; Summerfield, 1985; Decker et al., 2011). In short, despite attracting the attention of geomorphologists for over a century, attempts to unravel the denudational chronology of the Cape Mountains' landscapes have been confounded by the lack of reliable, quantitative data for Earth surface processes in the region.

The relatively recent development of techniques such as apatite fission track analysis (AFTA), (U-Th)/He analysis and terrestrial cosmogenic nuclide analysis (TCN analysis) has provided a new quantitative means of evaluating the nature of landscape evolution (Brown et al., 1998; Farley, 2002; Dunai, 2010). AFTA and (U-Th)/He analysis are capable of assessing the timing, magnitude and rate of regional exhumation events over timescales of 10^6 – 10^8 years thus providing coarse resolution (regional to subregional scale) information on the long-term patterns of denudation rates across the subcontinent (Brown et al., 1998; Farley, 2002). TCN analysis, on the other hand, can be used to constrain denudation rates and surface exposure ages over timescales of 10^3-10^6 years from areas ranging in size from a bedrock outcrop tens of centimetres in width, to a high-order river catchment thousands of kilometres in extent (Dunai, 2010). Used in conjunction with one another, the different averaging timescales and spatial resolutions of these techniques are a powerful complement to each other, allowing geomorphologists to better constrain the timing, magnitude and nature of denudational processes that have shaped the coastal hinterland and southern Africa at large.

The value of these analyses is further increased when viewed in conjunction with sedimentation records. Off-shore basins bordering southern African contain a first-order proxy - albeit imperfect - of fluctuations in onshore erosion rates, provided that eroded material is efficiently transported from the landmass to the oceans and minimal redistribution of the sediment occurs after its deposition in the

offshore basins (Tinker et al. 2008a). Comparison of data from onshore AFTA and offshore sedimentary records has already been used in assessments of the relative magnitudes and timings of large-scale denudation events to have affected the southern coastal region (Tinker 2005, 2008a, 2008b), western coastal margin and interior (Brown et al., 1990) and the eastern escarpment (Flowers and Schoene, 2010) of southern Africa.

While the recent surge of geochronological studies has helped to identify regional patterns of denudation since the Cretaceous to present, little data exists for the coastal Cape Mountains. To be fully understood, the restricted regional extent of the coastal Cape Mountains requires data of higher spatial resolution than is offered by the regional AFTA and (U-Th)/He analyses. Furthermore, the scarcity of apatite in the quartzites of the Table Mountain Group from which the mountainous peaks are comprised has, to date, prevented direct application of these techniques in the peaks of these mountains (Tinker, 2005). Given the lack of unambiguous chronological data in the region, geomorphological studies have remained speculative. Key questions that remain unanswered include:

Age — How old is the topography of the Cape Mountains? Is the present-day landscape sculpted into an ancient topography excavated at the end of the Mesozoic, now slowly denuding under the gentle forcing of isostatic uplift (van der Beek et al., 2002; Gilchrist et al., 1994)? Alternatively, has the rugged topography been subject to landscape rejuvenation due to episodic epeirogenic uplift in the Mesozoic and Pliocene (Partridge and Maud, 1987; Moore, 1999; Moore and Blenskinsop, 2006), or sea level fluctuations of approximately +120–150 m ca. 20 ka to present and ± 1 m ca. 5 ka to present (Bintanja et al., 2005; Rohling et al., 2009; Waelbroeck et al., 2002; Carr et al., 2010; Siesser and Dingle, 1981; Ramsay and Cooper, 2002)?

Landscape preservation — If the Cape Mountains are an ancient, exhumed topography, to what can the long term preservation (>65 Ma) of this topography be attributed?

Canyon formation — If the topography of the Cape Mountains is young (post-Cretaceous exhumation), what constraints can be placed on the process and timing of canyon formation?

This study focuses on the ranges of the southern coastal Cape Mountains; subsequently, emphasis will be placed on the physical characteristics of this region from this point onwards.

1.3 Regional Setting

The geomorphic evolution of the coastal Cape Mountains must be viewed in the context of the landscape evolution of southern Africa. Knowledge of the regional topography of the subcontinent is therefore necessary to appreciate the models of landscape evolution that have been applied to southern Africa and which define the context in which these mountains have long been viewed.

1.3.1 Regional topography

Africa's topography is unique among the continents in that it is host to greatly elevated plateaux that are almost entirely surrounded (<90%) by extensional margins (Doucouré and de Wit, 2003; de Wit, 2007). Furthermore, Africa's topography has a bimodal distribution, with eastern and southern Africa characterised by high relief and high elevations of over 1000 masl, while central and western Africa have low relief and sit at elevations of less than 500 masl (Doucoure and de Wit, 2003 and references therein; de Wit, 2007). In southern Africa this topography dates from the late-Jurassic and has tentatively been linked to plume magmatism accompanying the break-up of Gondwana at 180 Ma (east) and 130 Ma (west). This same mantle upwelling is cautiously suggested as a possible origin of the high elevations of east Africa which arose much later, in the Cenozoic (30-50 Ma), due to mantle dynamics being spatially and temporally out of phase between southern and east Africa (Doucouré and de Wit, 2003).

Southern Africa is characterised by three main, geomorphologically distinct zones; namely a coastal plain, an inland plateau and the Great Escarpment which separates these two (Figure 1.2 and Figure 1.8). The coastal plain is a low-lying (~0-400 masl), highly dissected terrain that declines with gentle gradient from the foot of the Great Escarpment to the coastal margins. It is here, in the southern and south-western coastal plain, that the restricted geomorphic zone of the coastal Cape Mountains is located, its peaks rising ~1000 m to over 2000 masl. Where it

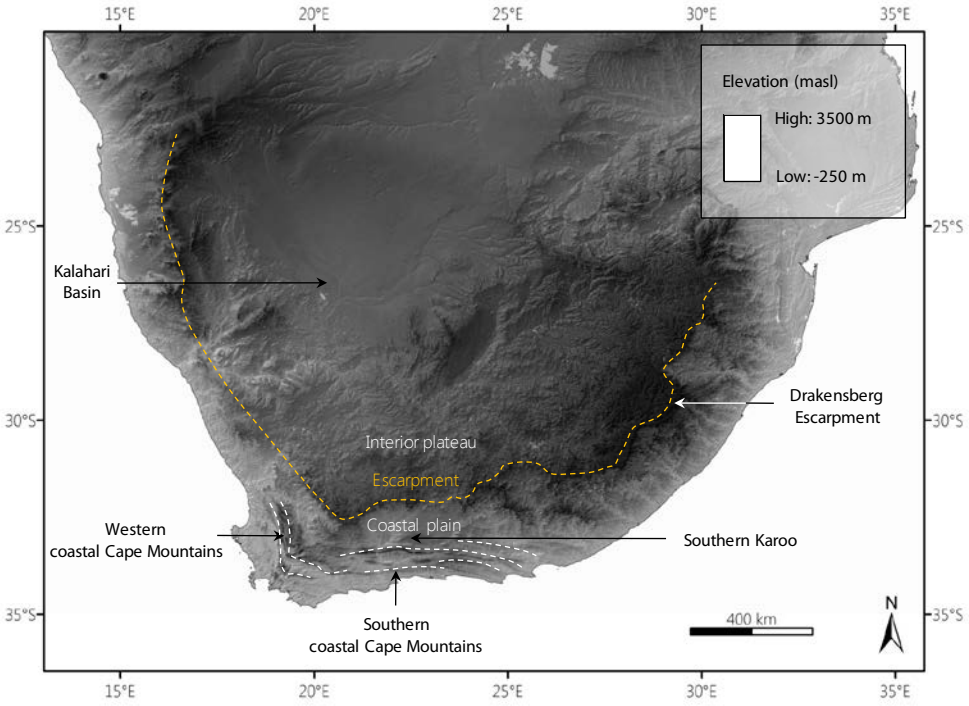

Figure 1.8: The geomorphological setting of the Cape Mountains. The topography of southern Africa can be divided into three main geomorphologically distinct zones, namely the inland plateau, the Escarpment and the coastal plain (cf. Figure 1.2). To the south and south west, the coastal plain is split by the coast-parallel ranges of the southern and western coastal Cape Mountains, respectively. Northwards of the inland plateau lies the Kalahari Basin. This figure was constructed using the SRTM 90 m digital elevation model, sourced from the AEON database.

lies, this fold belt divides the coastal plain in two, namely that sector of the coastal plain which lies seawards of the mountains, and that which lies inland of the mountains. Inland of the mountains, the coastal plain is of slightly higher elevation and comprises the plains of the southern Karoo.

The low-lying coastal plain is separated from the high-elevation interior plateau by the Great Escarpment, a narrow zone of high relief which forms a prominent step in the landscape. Elevations typically vary between 1-1.5 km along the west coast, increasing to 1-2 km along the south coast and reaching a maximum of ~3.4 km in the Drakensburg mountains along the east coast. The escarpment can be found to follow the trend of the shorelines some 100 to 150 km inland of the coast, from the rugged Drakensberg-Maluti mountains in the east to the less pronounced Namibian escarpment in the west. Inland of the escarpment lies the high-elevation (~1200-1500 masl), low relief terrain of the interior plateau which descends northwards into the depression of the Kalahari basin (~600-1000 masl).

1.3.2 Drainage networks

Drainage patterns of the inland plateau and coastal plain are distinctly different (Figure 1.9). River networks of the plateau are dendritic and dominated by the west-flowing Orange-Vaal river system which exits to the Atlantic via the western escarpment. The coastal plain, however, is dissected by parallel drainage networks which arise in the escarpment and flow towards the oceans in a somewhat counter intuitive trend that is perpendicular to both the regional structural grain of the coastal Cape Mountains (southern and south-western margins) and the coastlines of the subcontinent (all margins). Furthermore, where these rivers cut the coastal Cape Mountains, they do so in disregard for the strength of the quartz arenites of which the mountains are comprised.

Major rivers within the fold belt flow E-W between the parallel ranges, their paths dictated by local structure, before turning at right angles to meander through the mountains along exceptionally steep, narrow, sinuous gorges known locally as 'poorts'. An excellent example of this phenomenon is the Gamtoos River whose well-established meanders are entrenched ~1 km into the mature quartz arenites of the coastal Cape Mountains. The nature of these meanders have been disputed, however, with some authors suggesting that they are not true meanders but rather the result of headward erosion along regional joint plains (e.g. Lenz, 1953).

Stankiewicz and De Wit (2005) and Stankiewicz and De Wit (2008) have assessed the physical laws governing drainage pattern development in southern Africa. The reader is directed to these authors for further, detailed discussion of the river networks of southern Africa.

1.3.3 Climate

Climate in southern Africa is largely controlled by latitude, altitude, continentality, atmospheric circulation, ocean currents and substrate (Taljaard, 1994). South Africa is comprised of 15 climatic zones, as defined by the National Weather Bureau, with detailed descriptions of each available in Schulze (1994).

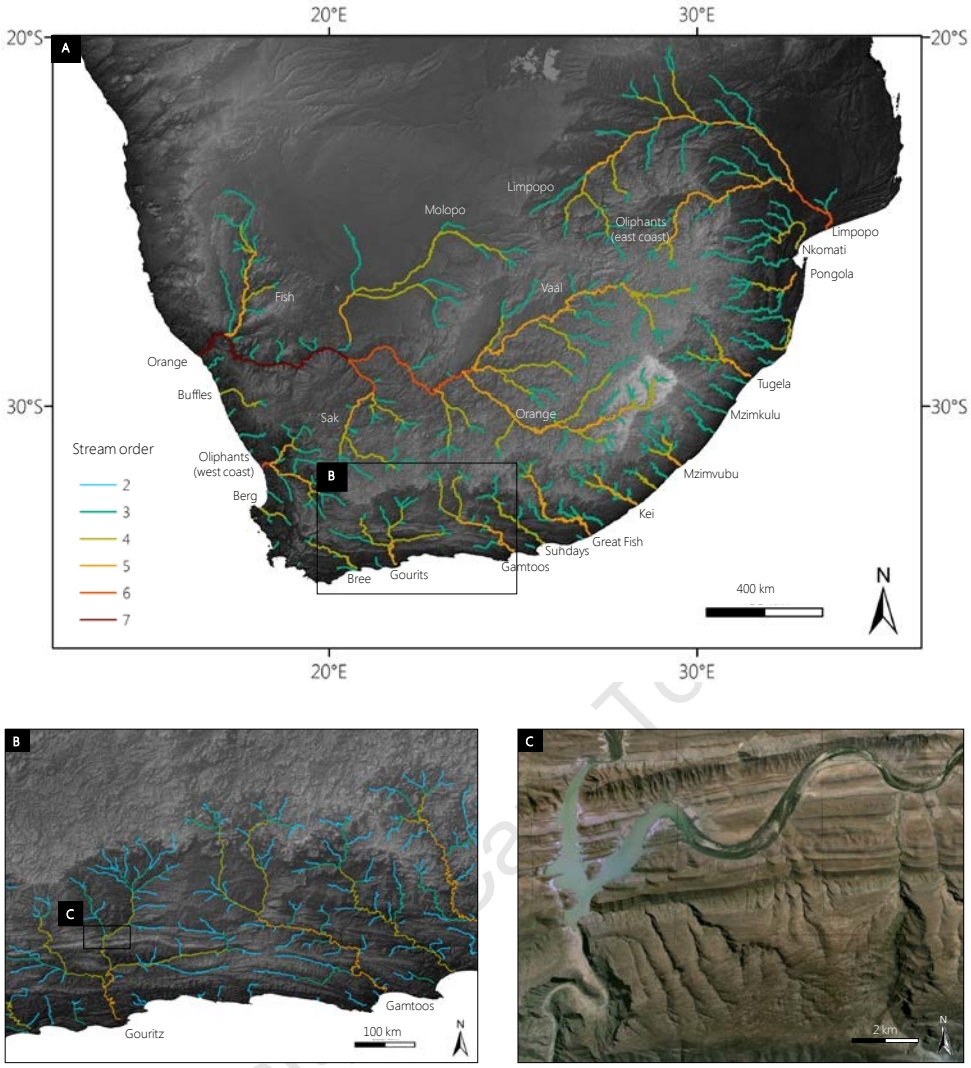

Figure 1.9: Drainage patterns of southern Africa. Figure A shows the dendritic drainage of the interior dominated by the westward-flowing Orange-Vaal River system. The trellis pattern typical of drainage in the coastal Cape Mountains can be seen in Figure B. The enlargement of the Gamtoos River (Figure C) shows the well-established meanders which have cut across the quartzites of the coastal Cape Mountains. Figures 1.9 A and B were constructed using the SRTM 90 m resolution digital elevation model and river network data sourced from the AEON database. Figure 1.9 C has been sourced from Google Earth.

Precipitation patterns of South Africa are dominated by a distinct rainfall gradient over the interior plateau (Figure 1.10). Mean annual rainfall increases from a minimum of ~38 mm along the north-west coast, to a maximum of 1250 mm on the seaward-facing slopes of the eastern Drakensburg escarpment (Taljaard, 1996b; Schulze, 2007). Small localised regions of anomalously high rainfall are located in the north east of South Africa. The southern and south-western coastlines, and with them the coastal Cape Mountains, are not subject to this gradient and instead

experience relatively constant, moderate to heavy, mean annual rainfall on their seaward-facing mountain slopes (Figure 1.10).

Rainfall intensity increases similarly from west to east; an effect which is felt along coasts more so than in the interior[1]. In addition to increased rainfall intensity, the southern and eastern coastal regions are subject to occasional downpours which measure 48-72 mm per hour (Taljaard, 1996b). These heavy rains have their origins either in strong south-easterly winds which can blow onshore under favourable conditions, or in tropical cyclones off the eastern shore of Africa which brush the eastern coastline approximately once in a decade or two.

Approximately 85% of the country (interior) receives summer rainfall, 12% (west coast) receives winter rainfall, and only 3% (south coast) shows no seasonal distribution (Figure 1.11) (Taljaard, 1996b; Schulze, 2007; Taljaard, 1994). The coastal Cape Mountains thus span two rainfall seasons, namely, the highly seasonal winter rainfall zone in the west and the aseasonal rainfall zone in the south. Within these zones, the mountains exert a strong orographic effect on precipitation. Drizzle and light to moderate rain are characteristic of the western and southern coastal plains with some of the highest mean annual rainfall figures recorded on the southern and south western slopes of the mountains. Conversely, some of the lowest figures are recorded on the inland-facing slopes of the coastal Cape Mountains – a clear rain shadow effect.

Surface temperature shows a strong negative correlation with altitude. Consequently, the coolest summer and winter temperatures are experienced in regions of highest-elevation. Within the coastal Cape Mountains, seasonal temperature fluctuations are moderate, with mean maximum January temperatures of ~22°C-30°C and a temperature range of ~22°C-14°C, and mean maximum June temperatures are 12°C-18°C with a temperature range of ~2°C-10°C (Taljaard, 1994; Taljaard, 1996a Schulze, 2007).

[1] The term 'interior' will be used throughout the text to refer to those regions inland of the Great Escarpment.

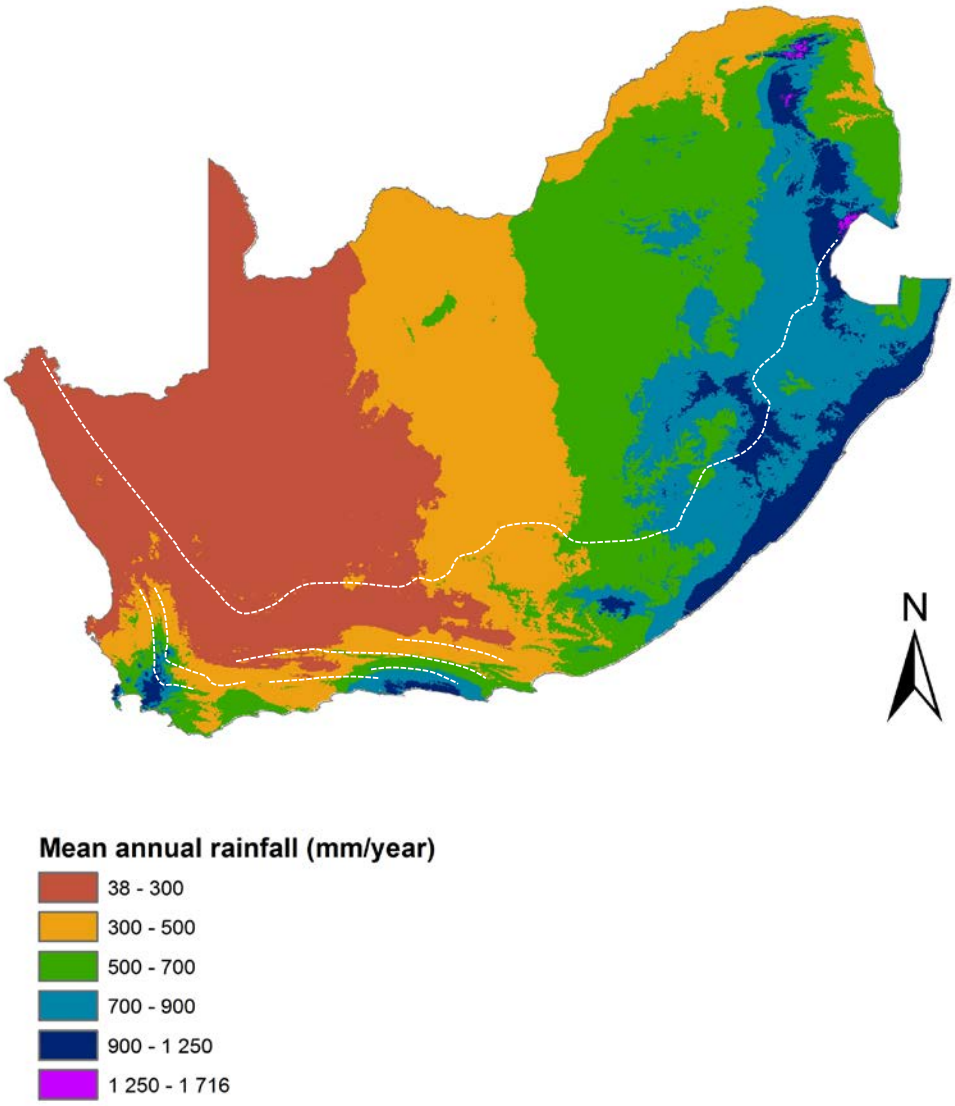

Figure 1.10: Rainfall patterns across southern Africa are dominated by an E-W rainfall gradient across the interior plateau. Figure 1.10 shows this rainfall gradient across South Africa and Lesotho. The approximate location of the Escarpment and coastal Cape Mountains are indicated by white stippled lines. This figure was constructed using public BioClim data with 1 km spatial resolution, available from www.worldclim.org, and the rainfall zones defined by Schulze (2007).

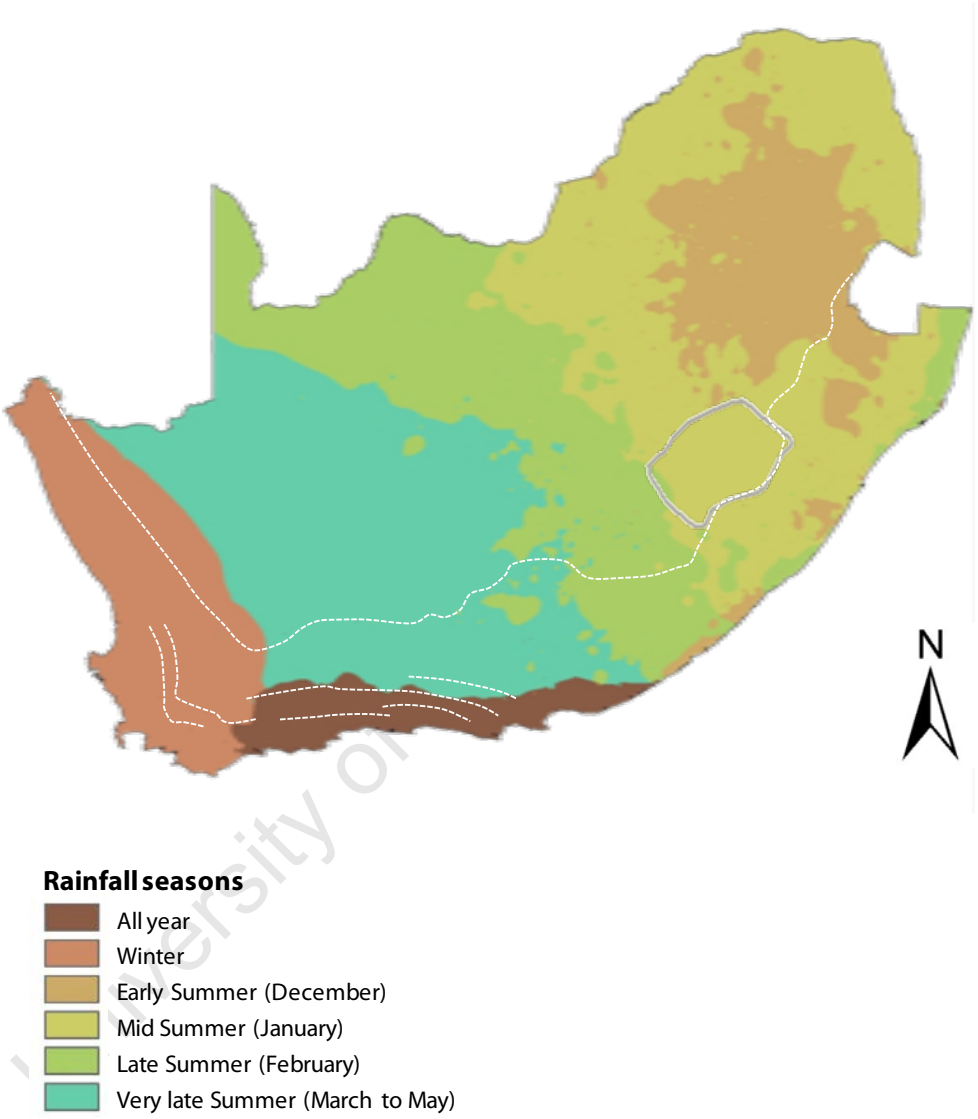

Figure 1.11: Distribution of rainfall seasons in South Africa. Approximate location of the Escarpment and coastal Cape Fold Belt ranges are indicated with white stippled lines. Data sourced from Schulze, 2007.

1.4 Theories of landscape evolution

Literature concerning the geomorphology of southern Africa is dominated by what will here be referred to as 'classical theories' of landscape development – models based largely on field observation and interpretation, with independent age constraints few and far between. Though beset with problems, such investigative methods were necessitated by the lack of analytical tools available to geomorphologists some 30 years, and more, ago. Authors such as Du Toit, King and Partridge wrote prolifically; their ideas simple, and their interpretations pleasing in so much that they were based on first-order field observations. Consequently, their proposed models were quickly accepted by the scientific community and have had a profound influence on the understanding of African landscapes up to the present day. If correct, the chronology of landscape evolution as laid out by these authors holds important implications for the development of the topography of the Cape Mountains. Furthermore, geomorphological investigations of the coastal Cape Mountains and their canyons have concerned themselves largely with the timing of canyon ('poort') formation, with such studies relying heavily on the datum surfaces and associated chronology laid out in classical landscape evolution models.

1.4.1 Classical landscape evolution models

Du Toit's 1933 paper on the evolution of the southern African landscape is certainly not the first paper to address the topic of landscape evolution in southern Africa but it serves as a suitable starting point for an introduction to classical landscape evolution models as it provides both an overview of the influential work of du Toit, as well as geomorphological science of the time. Du Toit (1933) considered the present-day landscape of southern Africa to be relatively young, dating no further back than the mid-Tertiary, which he attributed to isostatic uplift and crustal warping. In his 1933 paper, it was proposed that a low-lying subcontinent with elevations below 600 m - save for isolated montane regions - was elevated to its present position through isostatic uplift occurring in response to on-shore denudation. In support of this long-lived and on-going uplift, du Toit points to various marine deposits and wave-cut benches found within the western, southern and eastern coastal hinterland of southern Africa. The interior of the

subcontinent was said to have been most strongly affected by this uplift, pushed upwards in a dome whose zone of maximum flexure lay just seawards of the Great Escarpment and coincided with the location of the coastal Cape Mountains. While long-term denudation levelled the domed interior to an exceedingly flat plain standing 600 m above its original position, intense erosion in the zone of maximum flexure cut the exceptionally steep, narrow poorts characteristic of the present-day coastal Cape Mountains.

Uplift was considered slow and long-lived; however, Du Toit (1933) does not quantify this slow rate of uplift. Instead, he described the rate of uplift as being sufficiently slow to allow for the incision of meandering coastal rivers into the underlying coastal plain. However, a subsequent sudden increase in the rate of uplift in the late Tertiary caused the distal reaches of these rivers to stretch across the coastal plain toward the newly-established shoreline, resulting in the distinct linearity and deep canyons of these rivers as they approach the oceans perpendicularly to the coastline, e.g. Storms River of the Eastern Cape.

Five sub-parallel uplift axes located inland of the escarpment were cited as loci of maximum uplift in episodic epeirogenic events thought to have warped the interior of the subcontinent. Du Toit referred to these as the *Griqualand-Transvaal*, *Kalahari-Rhodesia*, *Zoutpansberg*, *Komas* and *Otavi* axes, and linked their activity to that of the Central African Rift System. Alternatively, stone implements found on abandoned river terraces are considered evidence of recent river incision and thus flexural uplift in the region of these axes.

King (1951, 1953, 1957, 1962) incorporated the uplift axes of Du Toit in his theory of cyclic landscape evolution which he brought to global popularity in the mid 1900's. In addition to the five axes of Du Toit, King added an additional *Escarpment Axis* which coincides largely with the position of the current Great Escarpment. King drew his inspiration from the 'stepped' appearance of the African landscape - a consequence of its dramatic escarpments which separate comparatively low-relief plains of differing altitudes. Influenced by the works of Penk (1924), Wood (1942), Hutton[2] and Dixey[2], King (1951, 1953, 1957, 1962) proposed a model in which composite four-element slopes (Wood, 1942) evolve

[2] King does not identify the particular publication to which he refers in the case of Hutton and Dixey, citing only the author names.

through scarp retreat (Penk, 1924) to form a low-relief pediment in all climatic regimes short of glacial, behaving today as they did in the geological past (Hutton). Repetition of this process through time results in a polycyclic landscape, namely a landscape comprised of the mappable remnants of numerous erosion surfaces (Dixey).

King considered southern Africa to be a polycyclic landscape comprising eight erosion cycles preserved at various stages of their development. The oldest are located at the highest altitudes at the tops of the coastal Cape Mountains and Drakensburg Escarpment, having been subjected to repeated uplift since their incursion, while the youngest are still in the phase of river incision and are limited to the coastal plain. In order of decreasing age, these surfaces are:

1. *Pre-Karoo Surface* of late-Carboniferous to Permian age
2. *Intra-Karoo Surface* of Triassic age
3. *Gondwana Surface* of late-Triassic to Jurassic age
4. *Post-Gondwana Surface* of Cretaceous age
5. *African Surface* of late-Cretaceous to mid-Cenozoic age
6. Miocene-Pliocene surface
7. Quaternary surface
8. Modern-day coastal deposits.

Of these, the *African Surface* is deemed the most important as it is the most pervasive, best developed and most easily identifiable surface across Africa. As such, it is considered a useful datum surface in mapping.

Almost no trace is said to remain of the *Pre-Karoo* and *Intra-Karoo Surfaces*. The *Gondwana Surface* is described as a surface of exceptional smoothness, bevelled across Gondwana during a period of continental stillstand, whose remnants lie at elevations of 1200-1500 m. The development of the *African Surface* is attributed to an extensive period of planation following the Mesozoic rifting of Gondwana. At the time of rifting, monoclinal warping is said to have occurred along the margins of southern African. These monoclines tilted outwards towards the oceans and stood with their strike perpendicular to the trend of major drainage lines. Once established, the uplifted margins retreated parallel to themselves to reach their present day positions approximately 120 km from the coastline, thus forming the Great Escarpment. Remnants of this surface are thought to lie across

Africa at elevations of 600-1200 m in the interior and 600-900 m in the coastal hinterland.

Subsequent falls in relative base level initiated new cycles of erosion that propagated through the landscape either through the parallel retreat of valley walls or through the parallel retreat of marginal scarps formed at the coastline. These erosion cycles are said to have left benches at 80-300 m alongside rivers of the coastal hinterland.

As the landscape evolved through parallel retreat and pedimentation, an escarpment came to separate the *Gondwana Surface* from the *African Surface*, and the *African Surface* from the succeeding mid- to late-Cenozoic surfaces. In support of his model, King points to the region of Natal where the Drakensberg, Ixopo-Pietermaritzburg-Greytown scarp and coastal hinterland scarp occur in a step-like series of escarpments aligned perpendicular to the regional drainage pattern and parallel to the coast.

Partridge and Maud (1987) modified the framework laid out by King by suggesting that three such erosional events occurred, forming the Mesozoic *African Surface*; mid-Miocene *Post-African I Surface* and the end-Miocene to early-Pliocene *Post-African II Surface* (see also Partridge, 1998; Partridge and Maud, 2000; and Partridge et al., 2006). This modified polycyclic landscape evolution model has become the most prevalent in the literature (van der Beek et al., 2002). To the axes outlined by Du Toit and King, Partridge and Maud (1987, 2000) have added another: the *Ciskei-Swaziland* axis along the eastern coastal hinterland of southern Africa, thought to have been active in the Plio-Pleistocene (Figure 1.12). Whilst the *Gondwana* and *African Surfaces* of Partridge and Maud (1987) coincide largely with those of King (1951, 1953, 1957, 1962), these authors disagree with King in two fundamental respects. Firstly, they do not support King's proposal that an erosion surface may be traced, unbroken, over the vast extent of Africa, let alone southern Africa. Secondly, they find no evidence of erosion surfaces predating the *African Surface* and thus do not support the *Pre-Karoo*, *Intra-Karoo*, *Gondwana* and *Post-Gondwana Surfaces* of King (1962).

In line with King, Partridge and Maud (1987) claim that the *African Surface* was the result of large-scale erosion following continental rifting at the end-Mesozoic. However, while King suggested the high-elevation escarpment to be the

result of monoclinal warping at the time of break up, Partridge and Maud propose that it was the high elevation of the African continent (~2400 m in Lesotho and 1500 m adjacent to the western interior) at the time of breakup that consequently formed a rift margin of considerable relief which evolved through scarp retreat and pedimentation to produce the Great Escarpment and accompanying *African Surface*. Claims of a high elevated subcontinent at the time of continental break-up are supported by offshore sedimentation records, onshore AFTA, and assessments of the extent to which Karoo volcanic and kimberlite diatreme facies have been eroded (Partridge and Maud, 1987; and Partridge, 1998). Note that rates of denudation and sedimentation determined by offshore sedimentary records and onshore AFTA are discussed in Section 1.4.2.

Up to 3 km of material was removed from the coastal hinterland by the end of the Cretaceous and considerably less from the continental interior as the African Surface was cut both seawards and inland of the migrating escarpment, reaching maturity by the end-Cretaceous. This split erosion surface was facilitated by the Orange-Vaal and Limpopo river systems that had breached the escarpment and consequently communicated the fall in base level to the interior (Figure 1.9). Today this *African Surface* is identified as isolated remnants of bevelled flat ground, capped with laterite and silcrete, and overlying a kaolinised weathered zone approximately 50 m in depth. Once again, its 'characteristic' morphology has engendered its use as a datum surface by which subsequent tectonic and erosional events have been assessed in the work of these authors.

The *Post-African I Surface* was initiated in the early-Miocene, ca. 20 Ma; the result of mild uplift focused along the eastern-margin of the subcontinent and contemporaneous warping along interior uplift axes. The age of this planation surface is based on field cut-off relationships, namely, the ages of strata underlying and overlying the proposed erosion surface. However, as discussed by Partridge and Maud (1987), the ages of these deposits are often uncertain. The greatest uplift was experienced around KwaZulu-Natal where the coastal plain was raised approximately 300 m (Figure 1.12). Intensity decreased towards the south coast where only 200 m of uplift occurred and reached a minimum along the west coast where uplift was a mere 150 m. The *Post-African I* erosion cycle was initiated, giving rise to a gently undulating surface cut some 100–300 m below the *African*

Surface. The modern coastal plain of southern Africa is attributed to this erosion cycle.

A second instance of Neogene uplift is said to have taken place in the Pliocene, between 3-5 Ma. Similarly to the Post-African I surface, the age of the Post-African II surface is based on cut-off relationships in the field. In particular, gravels, the estimated age of which was based on their stone artefact content. In addition to onshore cut-off relationships, offshore data is used to constrain the age of this surface. However, as offshore sediment basins do not strongly support the proposed timing of uplift, Partridge and Maud (1987) cite the work of Davies (1977) which shows a world-wide increase in deep-ocean basin sedimentation rates at the time of the proposed Pliocene uplift. However, Davies (1977) believed this global phenomenon was due to climate change.

Partridge and Maud (1987 and 2000) and Partridge (1998) attribute the high elevation of southern Africa to this uplift event, which was concentrated along the 'Ciskei-Swaziland axis' some 80 km inland from the coast, between Port Elizabeth and Swaziland. Intense uplift raised the eastern coastal hinterland by 700 – 900 m, the southern by 200 m and the western by 100-200 m (Figure 1.12). In support of their proposed Ciskei-Swaziland axis, Partridge and Maud (1987) and Partridge (1998) point towards convex river profiles and raised marine deposits found within the eastern coastal hinterland of the subcontinent; however, van der Beek et al. (2002) suggest that these observations could be the result of lithological control on landscape and isostatic uplift, respectively. This event is said to have caused the incision of valleys up to 500 m deep along the eastern coast, and rejuvenation of rivers along the western coast. Once again, flexure along the Griqualand-Transvaal axis is thought to have accompanied this event, as well as the formation of a hinge-line in the Western Cape along which the coastal plain was warped downwards. The *Post-African II Surface*, still in a stage of youth, is thought to occur within the coastal hinterland in the form of incised rivers and thus extensive dissection of the *Post-African I Surface*.

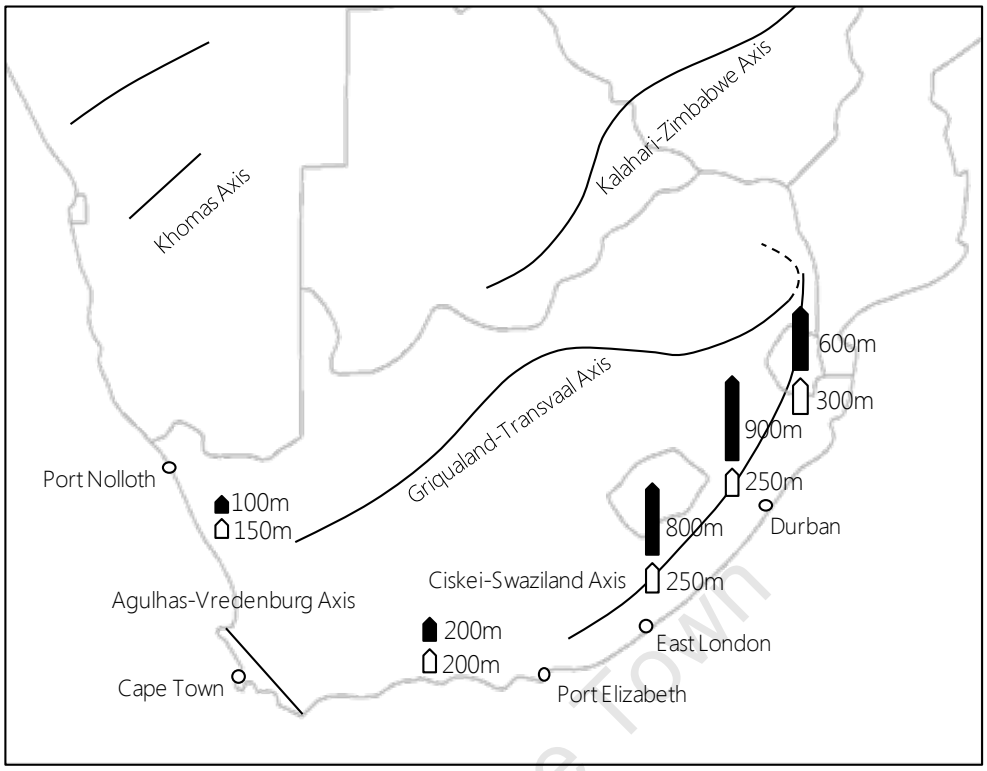

Figure 1.12: Proposed magnitudes of the uplift associated with the early-Miocene *Post-African I Surface* (white arrows) and the early- to mid-Pliocene *Post-African II Surface* (black arrows). Solid black lines delineate the onland epeirogenic flexure axes. Note that the Agulhas-Vredeburg Axis is a hinge-line along which the southwest coast is considered to have been down-warped. All other axes are axes of uplift. This diagram is modified from Partridge et al. (2006).

Partridge and Maud (2000) and Partridge et al. (2006) have linked the uplift events of the Neogene to the 'African Superswell' of Nyblade and Robinson (1994) - a region of high elevation that characterises the eastern interior. While the origins of this feature are not clearly understood, Partridge et al. (2006), Partridge and Maud (2000) and Partridge (1998) favour the interpretation offered by Su et al. (1994) that the elevation may be due to the 'Great African Superplume', a thermal anomaly centred below eastern and southern Africa and thought to extend into the lower lithosphere. However, the nature of this magnetic anomaly and whether it does in fact relate to a mantle plume is disputed (de Wit, 2007, and references therein). Furthermore, below southern Africa, this anomaly lies ~1-1.5 km below the lithosphere with the result that the temperature of the upper mantle below southern Africa is equivalent to the global average (de Wit, 2007 and references therein).

Moore (1999) assessed the work of previous geomorphologists in southern Africa, including Du Toit, King and Partridge, providing a concise summary of the axes of uplift proposed by previous authors and adjusting the proposed location and timing of these. Mention has already been made of the inference of these zones of uplift in the models of southern African landscape evolution. As these are not of primary importance here, they will not be discussed further, save to say that Moore supports the position and timing of the *Escarpment axis* and *Ciskei-Swaziland axis* as proposed by Partridge and Maud (1987, 2000), but proposes that the *Post African I* erosion cycle be early Tertiary in age and not Miocene as suggested by these authors.

1.4.2 Criticisms of classical landscape evolution models

Classic landscape evolution models have long been criticised for the lack of reliable age-constraints on these cyclic erosional surfaces that has necessitated their identification based on 'characteristic' morphological and sedimentary features, and the questionable reliability of correlating these surfaces over broad regions of the sub-continent (Brown et al., 2000; Summerfield, 1996; Summerfield, 1985 and references therein; Taljaard, 1948, van der Beek et al., 2002). Furthermore, Summerfield (1985) has raised doubts as to whether discrete uplift events would in fact cause regional erosion surfaces. King's model has received added criticism on its lack of a satisfactory geotectonic mechanism to explain the origins of the proposed uplift events (Summerfield, 1985).

Prior to the development of geochronology techniques such as ATFA, (U-Th)/He analysis and TCN analysis, classical landscape evolution models remained largely untested. However, the increasingly frequent application of these new analytical techniques to studies of southern Africa over the past two decades has placed quantitative constraints on the magnitude, timing and distribution of denudational events that have affected the subcontinent, thus providing a means of assessing the chronology and nature of landscape evolution. Studies include apatite fission track analysis (AFTA) (Brown et al., 1990, 2002; Gallagher and Brown, 1999; Tinker et al., 2008; Kounov, 2007, 2009), (U-Th)/He analysis (Flowers and Schoene, 2010), and terrestrial cosmogenic nuclide analysis (Fleming et al., 1999; Cockburn et al., 1999 and 2000; Bierman and Caffee, 2001; Van der Wateren and

Dunai, 2001; Kounov et al., 2007; Codilean et al., 2008; Dirks et al., 2010; Decker et al., 2011).

There is significant agreement between thermochronometry studies from the western, southern, and eastern margins of the subcontinent. The Cretaceous is identified as a period of large-scale regional denudation in which denudation rates were up to 2 orders of magnitude higher than in the Cenozoic (Table 1.2). Most of the subcontinent (particularly the coastal peripheries) was excavated during this period which was punctuated by two episodes of above-average denudation rates in the early-Cretaceous (~140-120 Ma) and mid-Cretaceous (~100-80 Ma) (Brown et al., 2000). These episodes of increased denudation rates have been linked to marginal rifting of Gondwana. Since the end-Cretaceous (~65 Ma), studies report a dramatic drop in denudation rates which are typically reported to range from 5 $m \cdot Myr^{-1}$ to 15 $m \cdot Myr^{-1}$ by the late-Cenozoic. These studies, their reported denudation rates, and the periods over which these rates average are listed in Table 1.2 and Figure 1.13.

Denudation was most intense within the coastal hinterland, from which 2.5-4.5 km of material has been removed (Kounov et al., 2009; Tinker et al. 2008b; Brown et al., 2002; Flowers and Schoene, 2010) in comparison to the interior which suffered a loss of only ~1-2 km (Kounov et al., 2009; Brown et al., 2002). Apatite fission track analyses and (U-Th)/He analysis have shown denudation of the subcontinent to be almost entirely confined to the Cretaceous with only minor excavation occurring in the Cenozoic. This would appear to discredit the classical landscape evolution models that suggest that intense neotectonism played an important role in reshaping the southern African land surface; however, the possibility of discrete Cenozoic uplift events cannot be discounted on the basis of AFTA data alone as the method is insensitive to shallow crustal excavation due to the closure temperature of apatite (~120-60°C) (Brown et al., 1998; Farley, 2002; Tinker, 2008b).

Cosmogenic nuclide analysis has proven a useful complement to thermochronometry techniques. Denudation rates reported from a variety of terrains, geomorphic elements, lithologies and climates across southern Africa are consistently low, and within the range predicted by AFTA for the post-Cretaceous (Table 1.3A and 1.3B, Figure 1.13 and Figure 1.14). Exceptions to the regional trend of low rates come from vertical surfaces prone to mass wasting.

Table 1.2: Average denudation rates for southern Africa and the time periods to which they apply, determined by apatite fission track analysis and, in the case of Flowers and Schoene (2010), by (U-Th)/He analysis. Note that the denudation rates cited for Kounov (2009) and Flowers and Schoene (2010) were calculated based on the estimated thicknesses of overburden removed during discrete time periods described by these authors.

Author	Analytical technique	Region	Location	Ave. time period (Ma)	Ave. denudation rate ($m \cdot Myr^{-1}$)
Gallagher and Brown (1999)	AFTA	South Africa – Namibia	Western coastal plain and interior	140-0	7-36
Cockburn et al. (2000)	AFTA	Namib Desert	Coastal hinterland	130-36	40
				36-0	5
			Interior	130-0	10
Brown et al. (2002)	AFTA	South Africa	East of Drakensberg escarpment	130-0	35
				91-69	95 ± 43
				~65-0	~14
			Inland of Drakensberg escarpment	78-0	15-28
				78-64	82 ± 43
				~65-0	~10
Tinker (2008)	AFTA	South Africa	Southern coastal hinterland	100-80	125-175
				80-0	10-15
Kounov (2009)	AFTA	South Africa	Western coastal hinterland	115-90	60-108
			Western interior	115-90	<40
Flowers and Schoene (2010)	(U-Th)/He	South Africa	Eastern Drakensberg escarpment	112-65	64
				65-0	13

Table 1.3A: Denudation rates reported from TCN analyses across southern Africa. Table continued overleaf.

Author	Region	Location	Sampling technique	Lithology	Averaging denudation rate ($m \cdot Myr^{-1}$)
Fleming et al. (1999)	Drakensberg escarpment, South Africa	Vertical face	Bedrock	Basalt	50 - 95
		Summit	Bedrock	Basalt	6
Cockburn et al. (1999)	Namib Desert	Inselberg summit	Bedrock	Biotite-granite	5.07 ± 1.1
Cockburn et al. (2000)	Namib Desert	Escarpment vertical face and ridges	Bedrock	Granite-gneiss	10
		Gamsberg (escarpment summit)	Bedrock	Quartzite	0.4 ± 0.1
		Coastal bornhardts	Bedrock	Biotite-granite	5.1 ± 1.1
Bierman and Caffee (2001)	Namib Desert and escarpment	Inland of the escarpment	Bedrock	Granite, quartzite. gneiss, pegmatite, granite gneiss	3.2 ± 1.5
		Coastal plain	Bedrock	Granite, quartzite., gneiss, pegmatite, granite gneiss	3.6 ± 1.9
		Escarpment (small streams)	River sediment	-	16
		Interior (small streams)	River sediment	-	5
		Coastal plain (small streams)	River sediment	-	8
		Large rivers	River sediment	-	3-9

Table 1.3B: Denudation rates reported from TCN analyses across southern Africa. Continuation of Table 1.3A.

Author	**Region**	**Location**	**Sampling technique**	**Lithology**	**Averaging denudation rate ($m \cdot Myr^{-1}$)**
Van der Wateren and Dunai (2001)	Namib Desert	Pediment	Vein quartz	Vein quartz in schist	0.1 ± 0.0 - 1.0 ± 0.0
		Depositional terrace	Amalgamated pebble samples	Quartz pebbles	0.2 ± 0.0 - 0.7 ± 0.1
		Gaub River; river bed	Vein quartz	Quartz veins in bedrock	1.4 ± 0.1
		Kuiseb River (inferred incision rate)	-	-	40-160
Kounov et al. (2007)	Southern and south-western coastal escarpment and interior plateau	Escarpment summit	Bedrock	Quartzite	1-2.1
		Interior plateau, escarpment summit, interior 'koppie' summit	Bedrock	Dolerite	1.5-3
Codilean et al. (2008)	Namib Desert	Gaub River subcatchments	River sediment	-	7.9 ± 0.5 – 14.1 ± 0.9
Dirks et al. (2010)	South Africa (near Malapa Cave, Gauteng Province)	Plateau ('African Surface')	Quartz veins	Quartz veins in chert breccia	3.6 ± 1.1
		Grootvleispruit River	Bedrock	Chert breccia	53 ± 9
Vermeesch et al. (2010)	Western southernAfrica	Orange River catchment	River Sediment	-	4.0 ± 0.9
Decker et al. (2011)	South-central Karoo, South Africa	Various vertical, horizontal, subhorizontal and inclined surfaces	bedrock	Dolerite	4

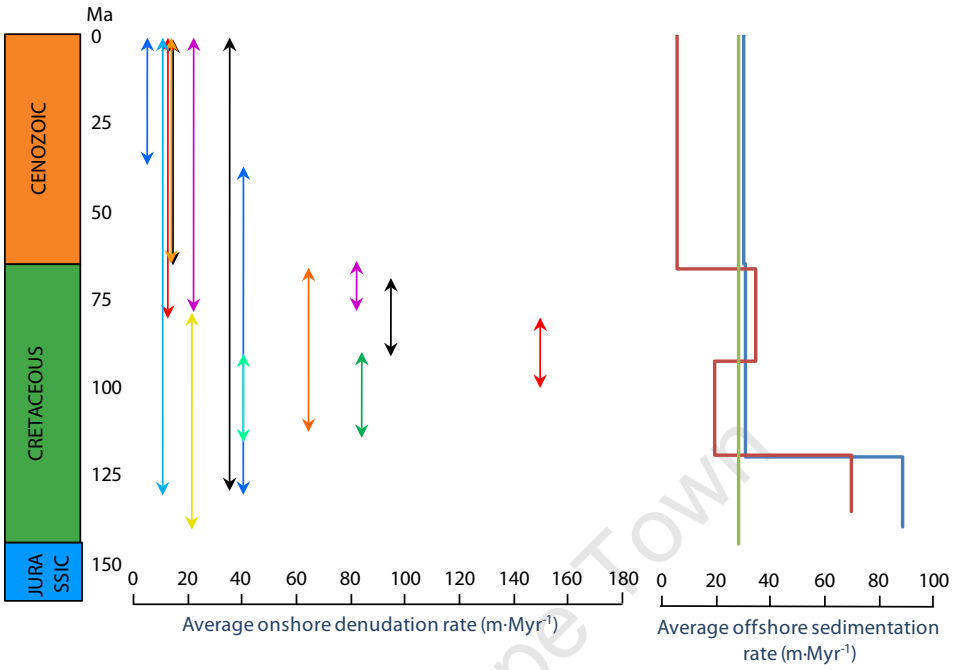

Legend: AFTA

- Tinker et al. (2008b): Southern coastal hinterland
- Brown et al. (2002): East of Drakensberg escarpment
- Brown et al. (2002): Inland of Drakensberg escarpment
- Kounov et al. (2009): Western coastal hinterland
- Kounov et al. (2009): Western interior
- Flowers and Schoene (2010): Eastern Drakensberg escarpment
- Cockburn et al. (2000): Coastal hinterland
- Cockburn et al. (2000): Interior
- Gallagher and Brown (1999): Western coastal plain and interior

Legend: Offshore sedimentation rates

- Rust and Summerfield (1990)
- Tinker (2005, 2008a)
- Martin (1987)

Figure 1.13: A comparison of onshore denudation rates estimated by apatite fission track studies, with offshore sedimentation rates. Onshore denudation rates are as reported in Table 1.2. Where Table 1.2 reports a range of values, the mid-point of this range was plotted. Averages of offshore sedimentation rates are taken from Tinker (2005). Both onshore denudation rates and offshore sedimentation rates are reported to decline dramatically from the Cretaceous to the Cenozoic.

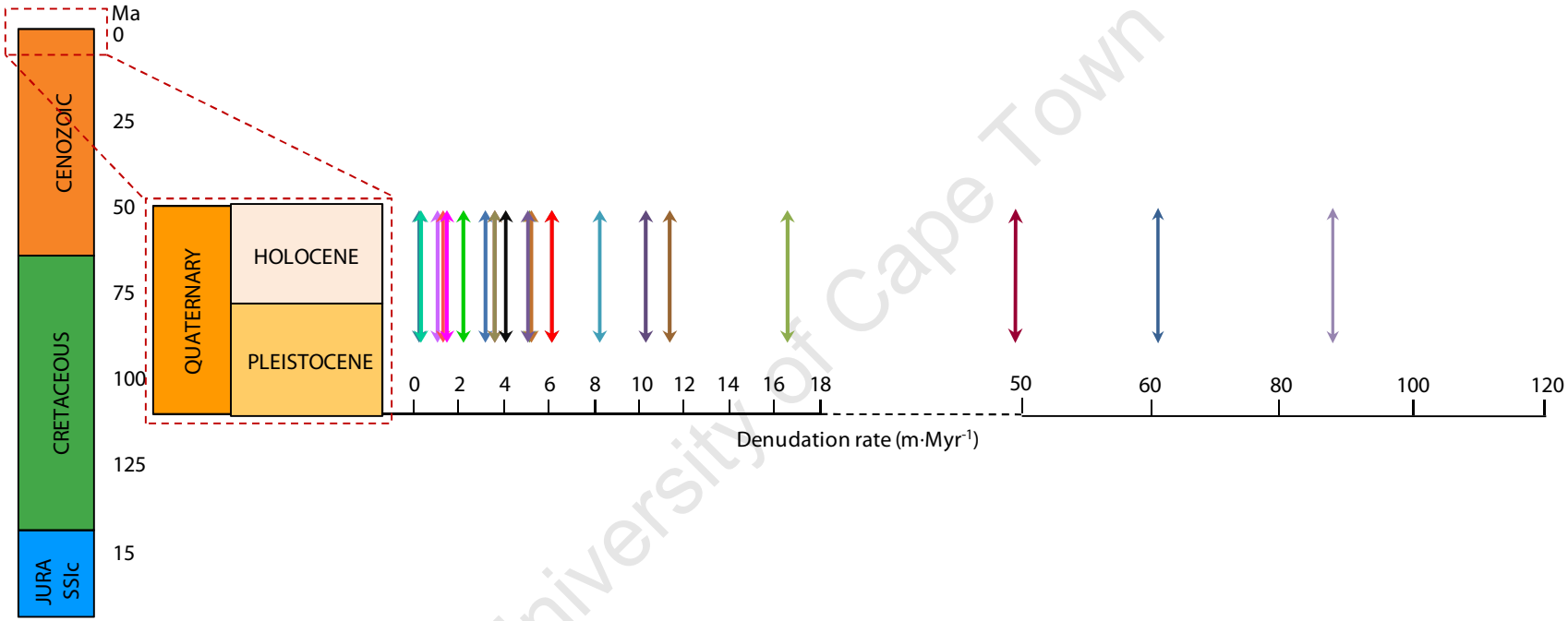

Figure 1.14: A comparison of averaged onshore denudation rates across southern Africa, determined by means of TCN analysis. Denudation rates are as reported in Tables 1.3a and 1.3b. Where a study reported a range of values, the mid-point of the range was plotted. The low rates for the past 10^3-10^6 year are in agreement with both the results of AFTA and offshore sedimentation analyses (cf. Figure 1.13) in that they are largely below 20 m $\cdot$ Myr^{-1}. The length of the arrows indicates the averaging timescale of the denudation rates reported from cosmogenic nuclide analysis, namely, 10^3-10^6 years. Legend overleaf.

Figure 1.14 Legend: southern African studies incorporating TCN analysis

Furthermore, the studies of Fleming (1999), Bierman and Caffee (2001), Van der Wateren and Dunai (2001) and Decker (2010) have shown denudation rates of land surfaces to preclude their preservation over the time periods suggested by King (1962) and Partridge and Maud (1987). TCN analysis studies for southern Africa and their reported denudation rates are listed in Table 1.3A, Table 1.3B and Figure 1.14.

Geomorphic steady state has been inferred for the landscape of western southern Africa based on the invariance of denudation rates between various lithologies and landforms sampled (Bierman and Caffee, 2001; Van der Wateren and Dunai, 2001). This contradicts the classical landscape evolution models which suggest recent neotectonic rejuvenation of the southern African landscape (Van der Wateren and Dunai, 2008). Close agreement between denudation rates determined over the long term through AFTA and over the short term through TCN analysis is cited as further evidence for steady-state conditions (Bierman and Caffee, 2001). A similar agreement between AFTA and TCN analysis in southern Africa is evidenced by the work of AFTA work of Tinker (2008b) and TCN analysis work of Decker et al. (2011) (Table 1.2 and Table 1.3B, Figure 1.13 and Figure 1.14).

The spatial and temporal changes in offshore sedimentation are closely related to that of onshore denudation. Data on sediment accumulation rates in the basins adjoining the south-western, southern and south-eastern margins of the subcontinent show that periods of accelerated offshore accumulation are largely coincident with periods of accelerated onshore denudation as determined by AFTA and (U-Th)/He analysis for the south-western, southern, and south-eastern margins (Figure 1.13 and Figure 1.14)

A number of studies have characterised the changing sedimentation rates off the west coast. Rust and Summerfield (1990) show increased sedimentation rates in the late-Cretaceous and early-Cenozoic, in close agreement with the periods of increased onshore denudation reported by the fission track data of Brown (1990) for the west coast. From the Eocene onwards, sediment accumulation rates remain low.

Off the south coast Tinker et al. (2008a) have reconstructed the changing sediment accumulation rates in the Outeniqua Basin in complement to the onshore AFTA of the southern Cape by Tinker et al. (2008b). While the relative timing of

events agrees closely between the onshore and offshore data, the volume of sediment preserved offshore is less than that predicted to have been denuded. This discrepancy is attributed to uncertainties in the aerial extent of onshore denudation, the loss of onshore material through dissolution, the loss of sediment to the deep ocean basins in the early-Cretaceous and the redistribution of sediment by ocean currents subsequent to its deposition. The work of Tinker et al. (2008a) shows that sedimentation rates peaked in the early and mid- to late-Cretaceous and has remained low throughout the Cenozoic.

Off the south-east coast, the work of Martin (1987) shows the sediment deposits of the Natal basin to be much thinner than off the south coast, and suggests that ~0.5-1 km of material has been removed from the catchment areas over the last 100 Ma. Sedimentation rates for the past 5 Ma are shown to be 6% higher than for the geological average. Recently the work of McMillan (2003) suggests a trend of declining sedimentation rates in the Natal Basin, from Cretaceous to present. Whilst McMillan acknowledges that recent offshore sedimentary deposits have been somewhat eroded, he suggests that Cenozoic sedimentation off the south-east coast of southern Africa could not have exceeded a few hundred meters. Flowers and Schoene (2010) have cited the work of McMillan in support of their (U-Th)/He analysis data which return similar trends for onshore denudation in the region (Table 1.2).

Little conclusive evidence exists offshore to support the major Miocene and Pliocene uplift events described by Partridge and Maud (1987). These authors have attributed this to redistribution of sediment by ocean currents and cite the work of Davies (1977) that shows a vast increase in sedimentation rates of the Atlantic and Indian Ocean Basins since the mid-Miocene and a notable hike in sedimentation rates since the Pliocene. Davies, however, noted that deep ocean basins reflect the sediment supply from all continental landmasses and suggests that a simultaneous increase in sedimentation rates in these basins is likely due to global climatic fluctuations. It should also be noted that recent work by Willenbring and von Blanckenburg (2010) has shown global chemical weathering and physical erosion rates to have remained fairly constant over the past 10 Ma. These authors have attributed the apparent highs in sedimentation rates commonly reported for the past 5 Ma to sampling bias. Furthermore, Summerfield (1985) points out that there is little agreement between the stratigraphic ages of

unconformities in the offshore sedimentary records of Dingle (1982) and the suggested timing of King's major erosion cycles.

1.4.3 Canyons of the coastal Cape Mountains

The peculiarity of deeply incised, meandering rivers that transect the coastal Cape Mountains at right angles to its structural grain has been ascribed to antecedence, superimposition and headward erosion of streams by various authors over the past century. Further uncertainty exists regarding the timing of canyon formation, with ages varying from Cretaceous to Pleistocene throughout the literature. Despite numerous geomorphic investigations into the timing and nature of canyon development, the drainage evolution in the coastal Cape Mountains remains a topic of controversy due, mainly, to the lack of reliable age constraints on topographic elements of the region.

The theory of superimposition was supported by Rogers (1903) who believed that, after the uplift of the mountains, the intermontane valleys were filled with the products of erosion in the form of the Uitenhage Group which partially buried the coastal Cape Mountains. Rogers looked at the Gourtiz river system in particular and proposed that these N-S oriented rivers, whose headwaters arose in the Escarpment, proceeded to meander across the gentle surface provided by the Uitenhage deposits and consequently, over the coastal Cape Mountains. In doing so, the rivers were rapidly lowered through this newly deposited, unconsolidated material and succeeded in superimposing their well-developed river courses on the underlying quartzites of the Cape Mountains by the late-Cretaceous to early-Cenozoic.

King (1951) supported Rogers in the belief that deposits of the Uitenhage Group filled the intermontane valleys of the coastal Cape Mountains and extended over the mountains to their north-bounding intermontane basins, e.g. the Little Karoo basin. King describes how the meandering nature of rivers such as the Gamtoos and Gourits suggests that they were superimposed from a previous plain of low gradient, possibly provided by the Enon deposits. The lateral tributaries of these rivers are, however, said to be structurally controlled and thus of younger age.

Du Toit (1954) cites Rogers (1903) in support of his account of drainage evolution where, once again, it is suggested that Cretaceous deposits filled the intermontane valleys of the coastal Cape Mountains, over which ran the E-W flowing rivers of the time. Du Toit suggests that down-faulting to the south of the anticlinal ranges of the Cape Mountains resulted in cross-warping which partitioned the intermontane valleys into separate, adjacent synclines and likewise caused synclinal warping of the mountain ranges. The E-W directed rivers are then thought to have been redirected through these N-S synclines, and have since superimposed their drainage onto the underlying quartzites as described in Rogers (1903).

Davis (1906a, 1906b) favoured headward extension of rivers as the most probable mode of drainage development in the south-western coastal Cape Mountains, including the well-established Gamtoos and Gouritz so often cited in favour of the superimposition theory. He does, however, mention that those rivers that have succeeded in breaching the full mountain belt might have developed through antecedent drainage, but acknowledges that this is only a hypothesis for which there is no field evidence. Davis does not attempt to assign ages to the various rivers and canyons in the south-west Cape Mountains, claiming that not enough is known of the area to do so. He does, however, intimate that the present-day drainage may have developed post-Cretaceous and possibly in the mid-Cenozoic, about which time Davis suspected cyclic erosion to have created a peneplain descending from the interior of the subcontinent to the coast.

Whilst recognising the short-comings of field observations that rely on the correlation of erosion surfaces, Taljaard (1948, 1949) makes use of the abundant gravel-capped erosion surfaces in the region of the Little Karoo in an attempt to gauge the ages of the canyons and associated river systems amongst the ranges of the coastal Cape Mountains, though taking care to mention that his correlations are based on visual observation and not extensive mapping. Taljaard was largely in favour of drainage development by means of headward extension along master joint sets for most river valleys of the region, even the Gamka and Gourtiz rivers (Figure 1.9) whose incision is commonly attributed to superimposition (e.g. Rogers, 1903 and King, 1951), using the same Enon deposits that inspired Rogers' 1903 theory of superimposition to argue against such theories. Taljaard's work placed the ages of many canyons in the south-western Cape Mountains in the early- to mid-Cenozoic. Few, such as the Tradouw, Prins, Buffels and Seven Weeks Rivers

were considered mid- to late-Cenozoic in age or, like the Touws River and Gamka-Gouritz drainage system, mid- to late-Cretaceous in age.

Lenz (1957) was the only author to base his model of drainage evolution on detailed field mapping, having mapped and subsequently correlated erosion surfaces. Lenz, a student of Taljaard, held similar views to his mentor and considered all canyons of the south-western Cape Mountains to have developed through headward extension along joint sets. Rivers which meander through the quartzitic mountains (e.g. Gamtoos River through the Swartberg Range, cf. Figure 1.9 C) and those which are linear and have not yet breached the mountains, are considered to have one and the same origin, namely headward erosion along joint patterns. Breachings of the mountains were dated as follows:

Pleistocene	Prins Pass, Garcia's Pass, Tradouw Pass, Jagberg (Olifants portion) Pass
Miocene-Pliocene	Kogmanskloof Pass, Buffels Pass
Eocene-Oligocene	Aasvoelberg Pass, Gamka Pass, Jagtberg (Gamka portion) Pass
Late Cretaceous	Gourtiz river system

The chronology suggested by Lenz is based on cut-off relationships with gravel deposits in the field. Lenz identifies what he terms the 'Higher Surface' and 'Lower Surface', both of which are gravel deposits found regionally. Lenz considers the Higher Surface to be Eo-Oligocene in age and the Lower Surface to be Mio-Pliocene in age, but mentions that he finds no evidence with which to constrain the ages of these surfaces, within his study area. Instead, he has correlated his Higher and Lower Surfaces with similar depositional surfaces found south of the Langeberg Range on the basis of similar elevation (accounting for a decline in elevation in a downstream direction) and stratigraphy. According to Lenz, "various authors" have assigned ages to the Higher Surface south of the Langeberg Range, based on their cut-off relationships in the field with coastal deposits. Lenz further mentions that the ages of these coastal deposits is disputed, and that he resorted to "assuming" an age for these coastal deposits based on the arguments in literature.

This author assigns the formation of the Lower Surface to an incursion of the sea, dated Mio-Pliocene in age; however, his reason for doing so is not clear from his text. According to Lenz, the absence of the Lower Surface on both the northern and southern side of the mountains indicates that the river had not cut through the mountains at the time that the Lower Surface was being deposited regionally.

The gravel deposits mentioned by Lenz and Taljaard were investigated by Marfarlane (1949) who infers a late-Pleistocene age for those deposits within the Breede River valley of the Western Cape, between Napier and Riversdale, due to the presence of stone tools in these deposits. Macfarlane does not mention whether the tools occur throughout the gravel deposits or are confined to the surface. Based on his paleontological age constraint, Macfarlane further suggests that the lower 45-150m of the coastal Cape Mountain canyons in the region were carved out since at least the late-Pleistocene, that is to say since ~2 Ma.

Maske (1957) was similarly in favour of drainage evolution through headward extension processes, as popularised by Taljaard and Lenz. In his review paper, Maske points out that the relative age of the Cape Fold Belt Orogeny (Permo-Triassic) and that the age of the deposits which these rivers overlie (Late Cretaceous) refutes the theory of antecedent drainage. Furthermore, the peculiar incised N-S drainage of the Cape Mountains must post-date the Enon deposits over which they in places flow, according to the work of De Villiers (1944) and Du Preez (1944). Given the lack of evidence in support of a Cretaceous covering of the Cape Mountains Maske, similarly to Taljaard and Lenz, dismisses Rogers' theory of superimposition. Instead, he considers the main drainage of the region at mid-Cretaceous time to have been E-W and structurally controlled, with N-S drainage arising though the headward extension of streams that were tributary to the main E-W flowing rivers in the Cretaceous, and their capture of drainage to the north. This N-S drainage developed post-Enon deposition, and owes its origin to intense E-W normal faulting at the time of Gondwana's break-up which caused N-S warping within the mountain ranges.

Van Zyl (1982), however, returns to the superimposition theory for Prins Poort, which both Lenz and Taljaard attributed to headward extension, suggesting that Prins Poort (and similarly, all major drainage lines of the area) is pre-Tertiary in age as opposed to the young ages assigned to it by Lenz (Pleistocene) and Taljaard (Late Tertiary). Van Zyl considers Prins Poort to be inherited from a Cretaceous

erosion surface, and to have existed as a deeply incised gorge by the Oligocene or early-Miocene. The timing of incision was based on the relative ages of the *African* and *Gondwana Surfaces* in the area.

Twidale and Van Zyl (1988) furthered the theory of headward extension, suggesting that most drainage in the area developed in the mid-to-late Cretaceous in this manner, and was inherited from overlying, conformable rocks of varying resistance. This differs from the work of Lenz in that Lenz suggested a variety of ages for different poorts and an origin through headward extension of rivers within the same rock type.

Apatite Fission Track Analyses (AFTA) by Tinker (2004, 2005) has shown the coastal Cape Mountains to be the excavated remnants of the Permo-Triassic Cape Fold Belt which lay buried beneath approximately 2-7 km of Karoo (and possibly younger) deposits. Excavation took place as two discrete events in the early-Cretaceous (140-120 Ma) and mid-Cretaceous (100-80 Ma), with 1-2.6 km of overlying material removed during the former and 2.1-3.5 km during the latter event. While Tinker's work was not primarily concerned with drainage development within the coastal Cape Mountains, passing commentary was made as to the possible implications of these results. Tinker points out that superimposition of meandering drainage patterns - such as those of the Gamtoos and Gourtiz - across the coastal Cape Mountains may well have been possible, given the evidence that nearly 2 km of material once overlay these mountains. Furthermore, if these through-cutting river courses are the result of superimposition from overlying Karoo (or younger) strata, the poorts by which these rivers traverse the mountains are likely to be late-Cretaceous in age.

1.5 Synthesis

The Cape Mountains of southern Africa display a dramatic landscape of meandering rivers incised hundreds of meters into robust quartzite, whose high relief and steep hillslopes appear at odds with the passive margin setting in which they are placed. Investigations into the timing and nature of landscape development of the coastal Cape Mountains have long been based within the context of cyclic landscape evolution models for southern Africa; however, within the region of the coastal Cape Mountains no reliable age constraints are provided

by these models. This has lead to disagreement between the nature and timing of canyon formation concluded by various authors and consequently the origins of the present-day landscape remains unresolved.

The recent development of AFTA and (U-Th)/He analysis has allowed reliable constraints to be placed on the long-term regional patterns of denudation across southern Africa for time periods spanning the early Cretaceous to Present. However, these techniques have not yet been directly applied to the coastal Cape Mountains as apatite is scarce in the quartzites of which this mountain belt is largely comprised. Furthermore, the resolution of AFTA is not sufficient to discount or support the proposition that neotectonic uplift events have rejuvenated the landscape of southern Africa. The technique of TCN analysis is of a higher spatial and temporal resolution than both AFTA and (U-Th)/He analysis and can be applied to the materials of these mountains; although, as of yet, no such analysis has been undertaken within the coastal Cape Mountains.

This study assesses the geomorphic evolution of the present-day landscape of the costal Cape Mountains through the analysis of quartz-hosted *in situ*-produced cosmogenic ^{10}Be. River sediment is analysed to constrain the regional denudation rates within the quartzites of the mountains, while 'spot' bedrock analysis allows a comparison of regional rates with the variation of local denudation rates within the catchments. Sampling of depth profiles through alluvial terraces should allow a comparison of both regional and local denudation rates with paleodenudation rates within the area. Viewed in conjunction with one another, these three techniques allow one to assess the geomorphic processes operating within the mountains since the late-Pleistocene. The implications of the results are then discussed in the context of classical landscape evolution models and the more recent understandings of the denudational history of southern Africa provided through AFTA, (U-Th)/He analysis and offshore sedimentation records.

An attempt will be made to address three key questions regarding the landscape:

Hillslope processes	What are the denudational processes currently operating within the coastal Cape Mountains and what is the pace at which they proceed?

Age of the landscape	Can any constraint be placed on the timing of canyon formation within these mountains?
Landscape preservation	If no evidence is found to suggest that neotectonics have rejuvenated the landscape of the coastal Cape Mountains, to what can the rugged terrain of these mountains possibly be attributed?

Chapter 2:

Controls on denudation rates

2.1 Introduction

Topography is the expression of interplay between tectonic and climatic forcings, and lithologic and structural controls that dictate the spatial and temporal distribution of denudation rates across a landscape. In the context of the geomorphological evolution of the Cape Mountains, understanding the forces that drive landscape denudation and the mechanisms by which they operate, namely chemical weathering and mechanical erosional processes, is fundamental to identifying the processes responsible for its present-day landscape.

The term 'denudation' refers to the removal of materials of the land surface under the combined actions of physical erosion and chemical weathering. Despite a considerable amount of geological research dedicated to the elucidation of denudation rates and their environmental controls, quantitative relationships between the two remain poorly defined. This is largely due to the interdependent nature of these forcings, such that the presence of one moderates the expression of another in a complete feed-back mechanism. Variation of environmental conditions between study sites introduces additional uncertainty as conditions cannot be reproduced, often preventing independent verification of results. Furthermore, up until the recent advent of cosmogenic nuclide analysis, no objective technique existed with which to measure denudation rates over a timescale that is relevant to general geomorphological processes, ~10^3–10^6 years (Figure 2.1) (Dunai, 2010; von Blanckenburg, 2005).

Traditional methods such as direct measurement of erosion rates on slopes, landslide mapping, gauging of river loads and of deposition rates in sediment sinks, measure denudation rates on the 10–100 year scale (Hewawasam, 2003; von Blanckenburg, 2005). As such, they are particularly sensitive to recent conditions

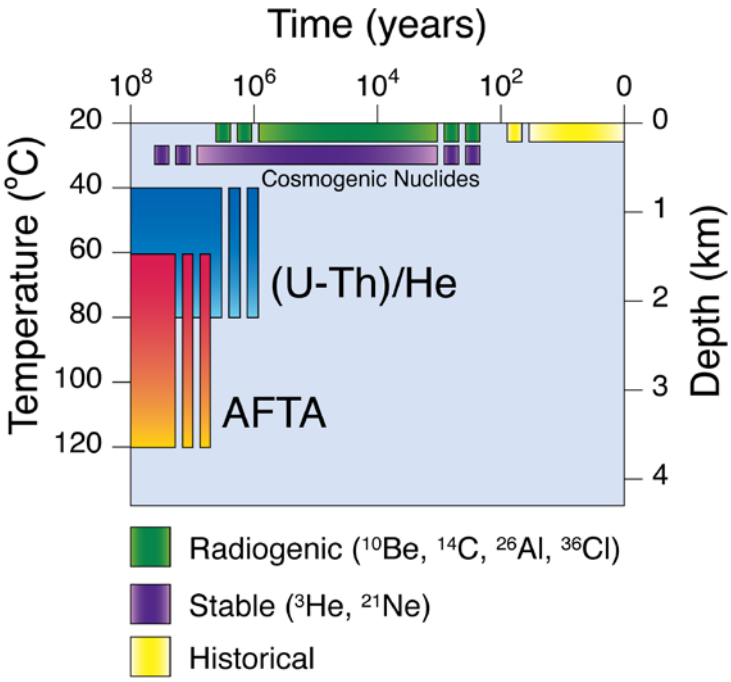

Figure 2.1: A comparison of the averaging timescales of thermochronometry (AFTA, (U-Th)/He), cosmogenic nuclide analysis (radiogenic and stable nuclides) and historical methods of quantifying denudation rates. This diagram is courtesy of Dr. A.T. Codilean (GFZ-Potsdam).

and anthropogenic influences (Hewawasam, 2003) and often do not account for low frequency, high intensity events which may play an important role in landscape development. Methods such as zircon and apatite fission track analysis and (U-Th)/He dating allow one to gauge the large-scale denudation histories of landscapes over the 10^6–10^8 year timescale (Brown et al., 1998); however, these methods tend to average out the effects of many possible shorter-lived environmental forcings. Cosmogenic nuclide analysis averages over a timescale which is intermediate to that of other techniques, yet long enough to average over episodic fluctuations in sediment flux and reflect natural, background denudation rates (Vanacker et al., 2007; von Blanckenburg, 2005; Brown et al., 1995). As such, cosmogenic nuclide analysis can provide a link between these techniques and their respective timescales, facilitating the comparison between geomorphological processes and the interpretation of landscape development across all three timescales (Kirchner et al., 2001; Binnie et al., 2008; Vanacker et al., 2007).

In spite of these shortcomings in the study of denudation rates and their environmental controls, there is broad agreement on the qualitative relationships between denudation rates (and by proxy, topography) and tectonics, climate,

lithology and structural geology, basin morphometrics and anthropogenic influences. In the natural world, these elements work in concert to sculpt the landscape, often as a complex feedback-system, and should not be considered as discrete forcings disconnected from one other. Chapter 2 reviews the current literature on denudation controls, discussing the present-day understanding of control mechanisms in Section 2.2, followed by a chapter summary in Section 2.3.

2.2 Control mechanisms

Denudation rates have been positively correlated with five main controls; namely tectonics, climate, local lithology (including structure), basin morphometrics and anthropogenic influences. For ease of discussion, each of these five will be discussed as an independent phenomenon, though an attempt has been made to highlight their interdependencies, where applicable.

2.2.1 Tectonics

Tectonic activity[1] is widely agreed to be the dominant control on rates of denudation, even in intraplate settings where crustal disturbances are often mild and discontinuous (Anhert, 1970; Koppes and Montgomery, 2009; Pinet and Souriau, 1988; Quigley et al., 2007b; Riebe et al., 2004; von Blanckenburg, 2005; Binnie et al., 2008; Montgomery, 2003; Safran et al., 2005). Subtler influences such as climate and lithology can easily be obscured in the presence of a tectonic forcing, adding further challenges to the study of denudation rates and their controls (Riebe et al., 2004; Safran et al., 2005). There is a stark contrast in denudation rates of tectonically active versus inactive areas, with active regions measuring ca. 100-1000 $m \cdot Myr^{-1}$ and inactive regions up to two orders of magnitude lower at ca. 1-20 $m \cdot Myr^{-1}$. This clearly illustrates the strong impact that crustal disturbances can have on rates of down-wearing (Quigley et al., 2007b; Koppes and Montgomery, 2009).

In areas that undergo a relative drop in base level, trunk streams will experience an increase in potential energy that translates to an increase in their erosive power

[1] The term 'tectonic activity' is here used to refer to active crustal warping or faulting, and not passive movements such as isostatic rebound. Areas affected by isostatic uplift alone are here considered to be tectonically inactive.

(Anhert, 1970; Peizhen et al., 2001). Accelerated down-wearing initially concentrated at the locus of base level drop may generate a knickpoint whose progressive back-wearing conveys the impulse of rejuvenation up the channel network. Knickpoint development and propagation is referred to as a 'bottom-up' erosive process and is characteristic of the early stages of an orogeny. Furthermore, it reflects disequilibrium in the landscape as those areas downstream of the knickpoint have responded to the relative drop in base level while those areas above the knickpoint have not yet felt the effects of the change in base level (Bishop, 2007). Conversely, those channels in a developed orogen with sufficient relief and rainfall may undergo a fairly instantaneous (on a geological timescale) lowering to the newly established base level by means of 'top down' erosional processes in which hillslopes throughout the catchment deliver sediment to the channel under the highly erosive conditions of intense rainfall and seismic activity (Bishop, 2007). In both situations the hillslopes keep pace with channel lowering through steepening of their slope angles. Accordingly, steep slopes are associated with rapid river incision.

Physical erosion and chemical weathering are complimentary mechanisms in that chemical weathering aids erosion by weakening bedrock and forming regolith, and mechanical erosion facilitates the removal of regolith and its assimilation into soil, thus exposing fresh, reactive mineral grains to chemical weathering both in soil horizons and on rock surfaces (Riebe et al., 2004; Riebe et al., 2001a; Riebe et al., 2001b; von Blanckenburg, 2005; Summerfield and Hulton, 1994). The strong coupling between physical erosion and chemical weathering is such that rates of chemical weathering increase proportionally according to a power function of the supply rate of fresh, reactive mineral surfaces supplied by means of physical erosion under a given climatic regime. Consequently, tectonic forcing is also a strong control on rates of chemical denudation (Riebe et al., 2004; Riebe et al., 2001b; Summerfield and Hulton, 1994; von Blanckenburg, 2005; Montgomery, 2003).

Tectonic activity which results in crustal uplift can thus incite landscape rejuvenation by increasing the erosional capacity of river networks which subsequently drives hillslope adjustments and associated chemical weathering. Furthermore, brittle deformation of the crust associated with tectonic activity (faulting and fracturing) both weakens and fragments bedrock up to depths of ~10-

20 km (Molnar et al., 2007; Selby, 1980; Pettifer and Fookes, 1994). Bedrock is thus more susceptible to physical erosion (both break-down and transport) upon arrival at the earth's surface (Molnar et al., 2007). The pervasive system of fractures imparted to the rock serves as a network of pathways for fluid movement, thus facilitating chemical weathering by increasing the reactive surface area of rock exposed to weathering agents (Molnar et al., 2007).

Tectonics, high relief, steep slopes and elevated denudation rates are inherently linked through process and form; the result of a dynamic natural system where valley floors and hilltops are coupled through drainage networks (e.g. Burbank et al., 1996; Roering et al., 2007; Quigley et al., 2007a; Tucker and Whipple, 1999). It therefore comes as no surprise that the morphometric parameters of a drainage basin and the spatial distribution of the denudation rates therein reflect its tectonic history.

2.2.2 Basin morphology

As the primary mode of denudation in tectonically active and post-orogenic regions is physical erosion (White and Blum, 1995; Montgomery, 2003) it stands to reason that the main morphometric controls on the rate of denudation will be hillslope and hillslope curvature (von Blanckenburg, 2005; Burbank et al., 1996; Harrison, 2000; Roering et al., 2007) as these features have a bearing on the rate of mass wasting at low slope angles, and the internal sheer stress of bedrock responsible for rockfalls at high slope angles. Both hillslope and hillslope curvature are found to correlate well with rates of denudation. By association, mean basin relief and mean basin elevation also show statistically significant relationships with denudation rates and have often been used as proxies for hillslope and hillslope curvature in geomorphic investigations (von Blanckenburg, 2005; Harrison, 2000; Summerfield and Hulton, 1994). Summerfield and Hulton (1994) have suggested that the relationship between relief and erosion rates may not be due to hillslope alone, but also associated factors such as increased seismic activity and extensive jointing of rocks, both of which are common in high-relief (1000-1500 m) terrain characteristic of tectonically active regions (Montgomery and Brandon, 2002).

Early literature advocates a direct proportionality between denudation rates and mean basin relief and hillslope. Gilbert (1909) theorised that convex hilltops in

mature terrains experience what he termed 'dynamic equilibrium'. In such an equilibrium, the rate of soil production is matched by the rate of soil degradation which is constant at all points along the convex hilltop. In order to sustain this equilibrium, it is necessary for the rate of removal to increase proportionally with hillslope. Anhert (1970), amongst others, reported this positive linear relationship following his analysis of mid-latitude drainage basins; noting that high relief is related to steep slopes which he proposed facilitated the 'speedy' downhill transport of material. Further support for this positive linear correlation came from Pinet and Souriau (1988), who described their use of mean basin elevation as a proxy for relief in a study that concluded two linear relationships, namely one of steeper gradient for basins belonging to orogenies younger than 250 Ma and a second of lower gradient for those belonging to older events. The difference in gradient between the steeper and shallower functions was interpreted to reflect the presence and absence of tectonic activity, respectively. More recent work, such as that of McKean et al. (1993) and Small et al.(1999), have found the linear slope dependent model to be justified in so much that it describes the relation of rate of soil creep to slope steepness on low-angle, soil-mantled convex hillslopes where conditions of dynamic steady state are likely to prevail.

Further refinement of the hillslope-relief-denudation rate relationship has shown the linear model to be an inadequate description of processes occurring in areas of active uplift. Non-linear or asymptotic functions are better suited to these environments (Binnie et al., 2007; Montgomery and Brandon, 2002; Montgomery and Schmidt, 1995; Burbank et al., 1996; Montgomery et al., 2001; Montgomery, 2003; Harrison, 2000; Ouimet et al., 2009; Roering et al., 2007; Roering et al., 2001; DiBiase et al., 2010). While denudation rates scale linearly with hillslope gradient at low slope angles, they increase exponentially as slopes steepen, eventually becoming decoupled above a given threshold angle commonly reported as approximately 30°-35° (Binnie et al., 2007; Montgomery and Brandon, 2002; Ouimet et al., 2009; Roering et al., 2007; Roering et al., 2001). This critical angle denotes the maximum steepness which the hillslope can attain and is dependent on the mountain-scale rock strength of the slopes. At threshold slope the gravitationally induced sheer stress acting on internal planes of weakness in the rock equal the mechanical strength of the slope face, with the result that further steepening leads to slope failure (Montgomery and Schmidt, 1995; Ouimet et al.,

2009; Roering et al., 2007; Korup, 2008). Under these conditions the rate of hillslope denudation is controlled by the frequency of landsliding, which in turn is dictated by the rate of tectonically driven river incision, with the result that small increases in hillslope bring about large increases in hillslope denudation rate (Montgomery and Brandon, 2002; Binnie et al., 2007; Montgomery, 2003; Roering et al., 2007; Korup, 2008).

These threshold slopes, attributed to rapid river incision, are noted to occur at uplift and/or denudation rates of approximately 0.2 $mm \cdot yr^{-1}$ and above (Jansen et al., 2010; Ouimet et al., 2009) at which point the rate of exhumation exceeds the rate of soil production resulting in a change from soil-mantled to bedrock-dominated landscapes (Ouimet et al., 2009). It should be noted, however, that Gabet et al. (2011) have linked high mean annual rainfall to reduced hillslope angles in the Himalayas. These authors attribute this phenomenon to high pore pressures and increased chemical weathering brought on by the increased rainfall, which together lower rock strength and reduce threshold slope angles in an actively uplifting orogen where rock strength is not the limiting factor on hillslope angle. Overall denudation rates were seen to remain constant despite the lowering of threshold slope angles.

Binnie et al. (2007) concisely illustrate this transition from a linear slope-denudation rate correlation at low slope angles to slope-denudation rate decoupling at critical slope angles, identifying the 0°-18° hillslope range as transport-limited slopes, 18°-33° as intermediate slopes and 32° and above as detachment-limited slopes (Figure 2.2). This agrees with Montgomery and Brandon (2002) who find a linear slope–denudation rate relationship up to 25°, a steeper linear relationship from 25°-30° that they ascribe to slope angles reaching a steepness that can support debris flows, and no correlation above the threshold limit of 30°. Similarly, Ouimet et al. (2009) report this positive linear correlation between slope values of 5°-20°, with a dramatic increase in denudation rates as threshold slopes of approximately 32° are reached. It should be noted that, although threshold slope angles are commonly reported to lie in the range of 30°-35° , it is not strictly correct to infer from a slope angle of ~30° that a given slope sits at its threshold inclination. As threshold slope angles are dictated by mountain-scale lithologic

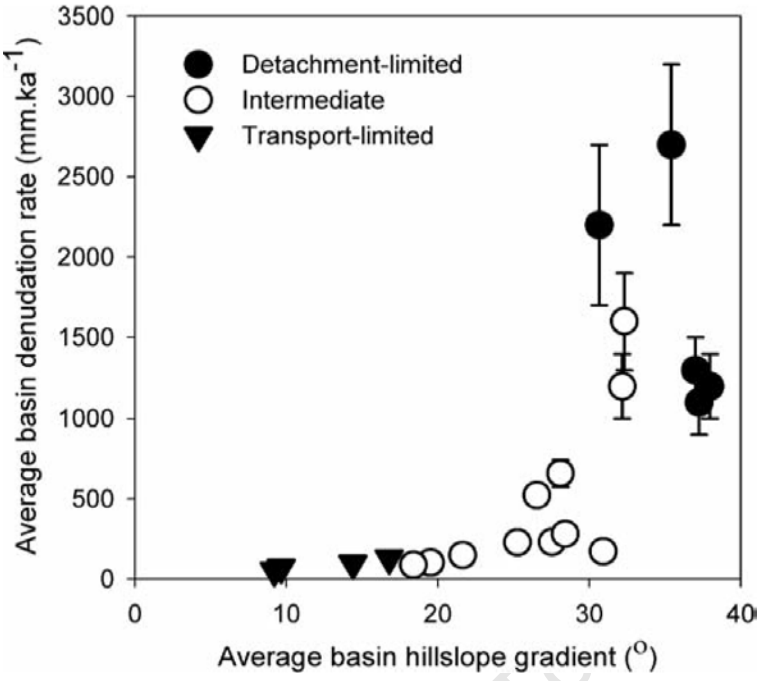

Figure 2.2: The hillslope gradient–denudation rate relationship is described by a linear positive correlation at low slope angles and an exponential positive correlation at high slope angles. Low slope angles are associated with transport-limited rivers; high slope angels are associated with detachment-limited rivers; and intermediate slope angles are associated with rivers whose behaviour is intermediate to these two. Transport-limited rivers are those in which the sediment supply exceeds the sediment carrying capacity of the river. Detachment-limited rivers are those in which the sediment carrying capacity of the river exceeds the sediment load. This graph is taken from Binnie et al. (2004).

strength, slope values will vary between rock types, as well as between similar rock types which have undergone varying degrees of tectonism and thus display varying degrees of jointing and fracturing (Korup, 2008). Varying degrees of brittle deformation will thus lower the internal cohesion of the rock to varying degrees, causing variation in threshold slope angles between slopes.

The implications of this non-linear hillslope-denudation rate function are two-fold. Firstly, hillslope plays an important role in dictating rates of denudation on interfluves. Given the close association of relief and hillslope, catchment-averaged relief is also found to correlate strongly with rates of denudation (Summerfield and Hulton, 1994). Secondly, mountain-scale rock strength can impose an upper limit on relief by dictating the angle of threshold slopes in a catchment (Montgomery and Brandon, 2002; Montgomery and Schmidt, 1995; Burbank et al., 1996; Summerfield and Hulton, 1994; Montgomery, 2003; Ouimet et al., 2009).

Rates of river incision not only dictate hillslope angles, but also channel gradients. Similar to hillslope, steeper channels allow fluvial action to exceed the threshold shear stress required for entrainment of bedload and river incision more frequently than occurs at low channel gradients. Consequently, channel steepness can reflect the rate of incision and as such, variations in channel steepness across a landscape reflect variations in denudation rate and its controls within that landscape (e.g. Kirby and Ouimet, 2011; DiBiase et al., 2010; Snyder et al., 2000; Kirby and Whipple, 2003; Kirby et al., 2007).

River profiles are commonly described by Flint's Law (Flint, 1974) shown in Equation 2.1.

$$S = k_s A^{-\theta} \qquad 2.1$$

In the above equation, S is the local channel steepness, A is the drainage area upstream of the point of interest, k_s is an indication of channel steepness, referred to as the 'channel steepness index', and θ is the 'concavity index' which measures the rate at which channel steepness changes as drainage area changes. To facilitate the comparison of steepness indices between rivers of varying drainage area, steepness indices must be normalised for the effects of drainage area. Consequently, channel steepness is conventionally described by the 'normalised channel steepness index (k_{sn})' of a river, which reports the channel steepness calculated using a reference concavity - usually approximately 0.45 in uplifting orogens (Kirby and Ouimet, 2011). These k_{sn} values are valid over a stretch of river with constant channel steepness. As channel steepness varies throughout a river profile, it is likely that different k_{sn} values will apply to different stretches of a river.

Numerous studies have shown strong positive correlations between normalized channel steepness index and both rock uplift rates and denudation rates e.g. (Safran et al., 2005; Kirby and Ouimet, 2011; Snyder et al., 2000; Ouimet et al., 2009; DiBiase et al., 2010). While some studies support a linear relationship between erosion rates and normalised channel steepness index (e.g. Safran et al., 2003; Wobus et al., 2006), others describe a non-linear positive correlation much like the revised hillslope-denudation rate relationship for actively uplifting areas.

However, where slopes reach threshold angles, channel gradients continue to steepen with increasing denudation rates, only reaching their threshold angles at much higher denudation rates. Channel steepness indices can thus provide us with a more sensitive indicator of incision rates in rapidly denuding terrains (Ouimet et al., 2009; DiBiase et al., 2010).

2.2.3 Climate

Climate encompasses both temperature and precipitation, which in turn influence the physical and chemical removal of surface material by moderating factors such as vegetation, run-off, mechanisms of physical erosion and rates of chemical weathering (Anhert, 1970; Riebe et al., 2001b; White and Blum, 1995; Montgomery and Brandon, 2002; Summerfield and Hulton, 1994; Montgomery et al., 2001; Montgomery, 2003; Harrison, 2000).

The influence of temperature and precipitation on both erosion and weathering are mutually moderating to such a degree that the one cannot be discussed without the other. Precipitation is consistently reported to be the dominant climatic control on denudation rates given its direct control on both rates of chemical weathering and mechanical erosion (von Blanckenburg, 2005; Summerfield and Hulton, 1994; Riebe et al., 2001a and 2001b, Riebe et al., 2004). This is in contrast to temperature whose effects on denudation rates are not as strongly felt and extend only to chemical weathering where it influences the rate of rock dissolution (Harrison, 2000; Riebe et al., 2004; von Blanckenburg, 2005). In addition, rates of chemical weathering are strongly coupled to rates of physical erosion (Riebe et al., 2004; Riebe et al., 2001a and 2001b; Summerfield and Hulton, 1994; von Blanckenburg, 2005). These interdependencies are illustrated in Figure 2.3.

Studies of river solute loads and chemical fluxes, and their comparisons with river sediment flux have traditionally been used to assess the influence of climate on denudation rates (e.g. Summerfield and Hulton, 1994; Harrison, 2000; White and Blum, 1995; Pinet and Souriau, 1988). Recently, however, Riebe et al. (2004),

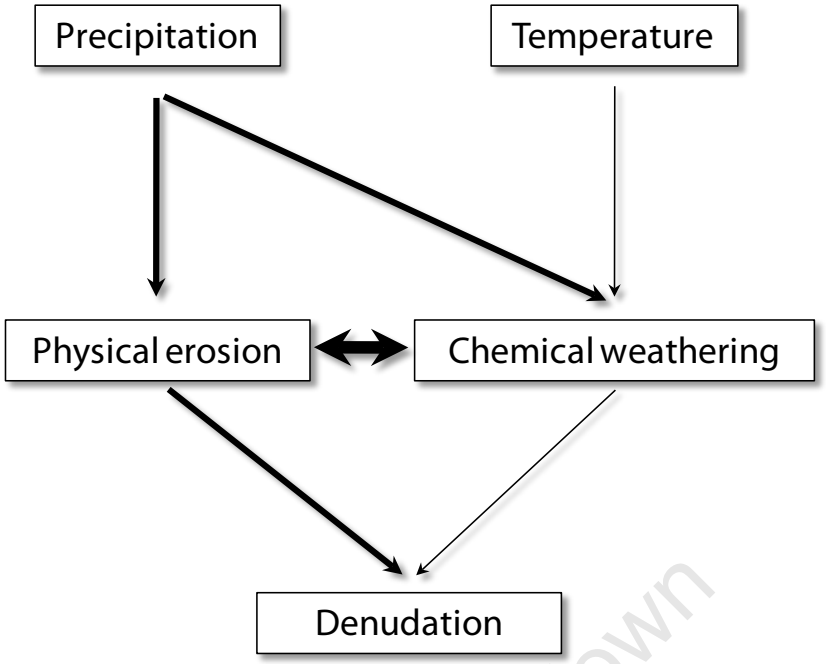

Figure 2.3: Both precipitation and temperature can affect overall denudation rates through their influence on the rates of physical erosion and chemical weathering. The relative strengths of influences ('forcings') are indicated by arrow thickness, with greater thickness indicating greater influence. The effects of precipitation on overall denudation rates are more strongly felt than those of temperature. Furthermore, precipitation is able to influence both physical erosion and chemical weathering, whereas the influence of temperature is largely limited to the rate of chemical dissolution. It is important to note that chemical weathering scales primarily with rates of physical erosion to the extent that any climatic influence can be obscured. Any external forcing which governs the rate of physical erosion will thus govern the rate of chemical weathering. See main text for discussion.

Riebe et al. (2001a) and Riebe et al.(2001b) have developed an accurate method to distinguish the proportion of physical erosion from the proportion of chemical weathering contributing to the overall denudation rates of granites.

These studies have drawn conflicting conclusions regarding the nature of the climate-denudation rate relationship. Pinet and Souriau (1988) find that rates of chemical weathering are unrelated to basin morphology but increase proportionally with an increase in mean annual precipitation. Similar findings were reported by White and Blum (1995) who show rates of silicate weathering to be unrelated to rates of physical erosion, but to increase linearly with precipitation at a given temperature and nonlinearly, according to an Arrhenius-type equation, as temperature increases. Harrison (2000) likewise reports a non-linear relationship

between chemical dissolution and temperature. In contrast, Summerfield and Hulton (1994) find that chemical weathering rates are poorly governed by climate but correlate well with rates of physical erosion. The methods developed by Riebe et al. (2001a), Riebe et al. (2001b) and Riebe et al. (2004) and reviewed by von Blanckenburg (2005) agree with Summerfield and Hulton (1994) in that they find no correlation between climate and rates of denudation but instead find that rates of chemical weathering and physical erosion are strongly coupled (Figure 2.4). However, Riebe (2004) and Riebe (2001a and 2001b) note that the proportion of chemical weathering to overall denudation, termed the 'chemical depletion fraction' or 'CDF', is governed by climate. CDF increases with an increase in precipitation, and also with an increase in temperature if the effects of precipitation are accounted for (Figure 2.4). These authors suggest that their observed lack of correlation between climate and denudation rates is likely due to the strong coupling between chemical weathering rates and physical erosion rates, which obscures the climate-denudation rate relationship. The effects of climate on overall denudation rates may only be noticeable if one normalises for the effects of physical erosion - which are largely governed by tectonic activity - or if an investigation is carried out in a region with little to no active tectonic input (e.g. Bierman and Caffee, 2002; Kounov et al., 2007)

The relationship of precipitation to physical erosion is likewise debatable. An incongruity exists between those studies which report a positive correlation between mean annual precipitation and physical erosion (e.g. Summerfield and Hulton, 1994; Harrison, 2000) and those which conclude 'storminess' (variability of rainfall and rainfall intensity) to be the controlling factor on physical erosion (e.g. Anhert, 1970; Molnar and England, 1990; Pinet and Souriau, 1988; Bierman and Caffee, 2002, Tucker and Bras, 1999).

Anhert (1970) advocates that it is not the magnitude of mean annual precipitation that influences erosion rates, but rather the seasonal variation of rainfall. He suggests that both wet and dry climates are equally capable of denuding a landscape, with aridity favouring physical erosion and humidity favouring chemical dissolution. Anhert proposes that a variation between these conditions – seasonality – can increase rates of denudation as dry spells leave the earth exposed prior to the rain season, whose run-off subsequently removes the

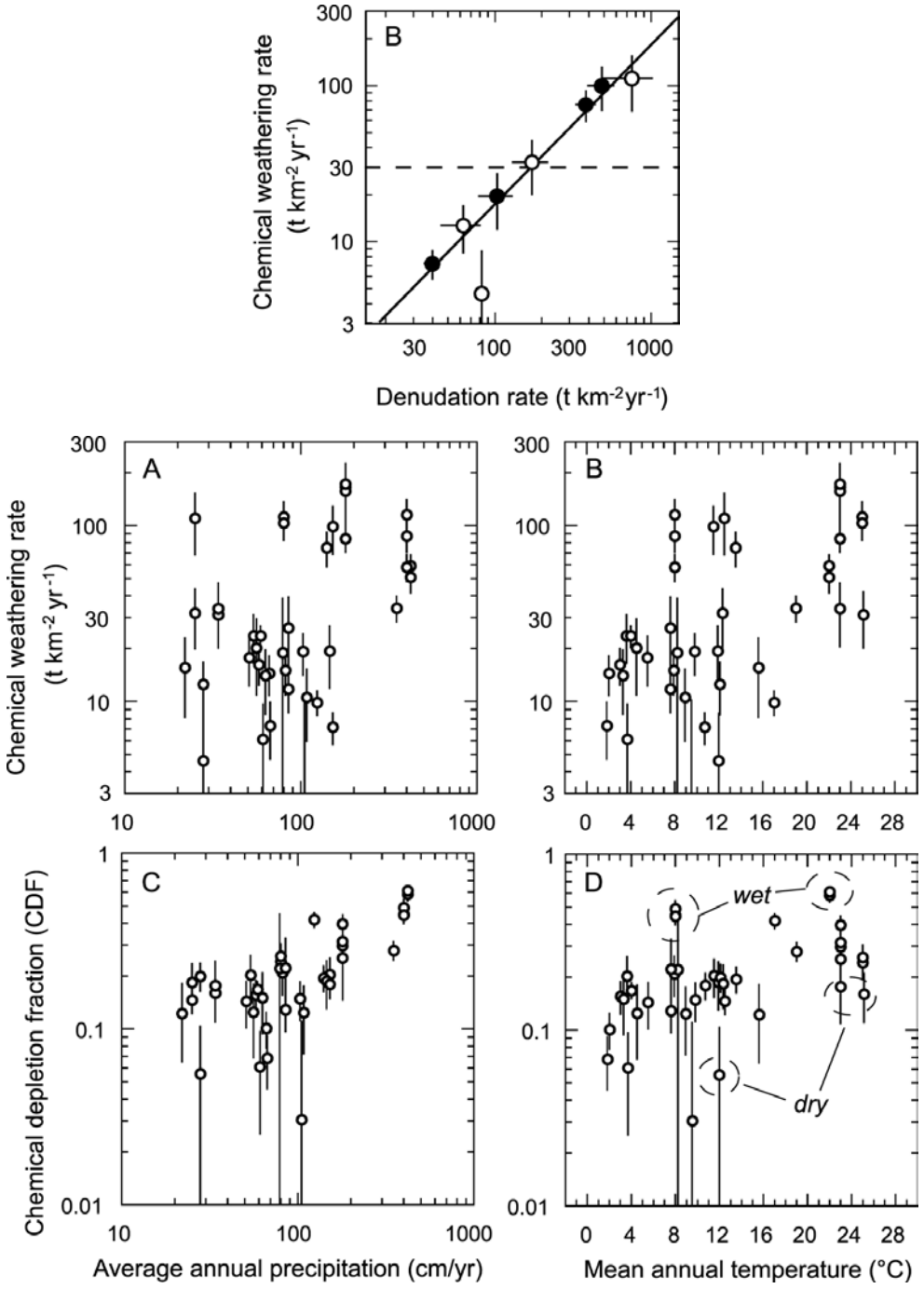

Figure 2.4: Examples of the climate-denudation rate relationships reported from literature; graphs taken from Riebe et al. (2004). Top centre: Chemical weathering rates are strongly coupled to overall denudation rates. Middle row: Chemical weathering rates show no clear correlation with either average annual precipitation (A) or mean annual temperature (B). Bottom row: Chemical depletion fraction shows a positive correlation with average annual precipitation (C) and mean annual temperature (D). Note that although CDF increases with an increase in mean annual temperature, values will be elevated in wet regions relative to dry regions.

unprotected material. Similarly, Molnar and England (1990) have suggested that an increase in 'storminess' due to global cooling in the late-Cenozoic may in part be responsible for the apparent global increase in denudation rates since ca. 5 Ma. It must be noted, however, that Willenbring and von Blanckenburg (2011) find no evidence for the apparent increase in global denudation rates reported by several authors, and attribute this 'phenomenon' to sampling bias. The findings of Pinet and Souriau (1988) and Bierman and Caffee (2002) are in partial agreement with Anhert (1970) and Molnar and England (1990) in that they find no relation between mean annual precipitation and physical erosion rates. Tucker and Bras (1999) have provided a more convincing argument for the importance of rainfall variability and rainfall intensity through their use of the Channel-Hillslope Integrated Landscape Development (CHILD) model which shows that an increase in rainfall intensity is accompanied by increased sediment flux in rivers, increased incision and steepening in first-order streams, and a decrease in the gradient of main valley rivers. By contrast, the correlation analyses of Summerfield and Hulton (1994) and Harrison (2000) yield strong relationships between mean annual run-off and both physical and chemical erosion, but only weak correlations between run-off variability (and thus 'storminess') and mechanical denudation rates.

Anhert may well be correct in his hypothesis that both dry and wet climates are equally competent in denuding a landscape. The studies of Riebe (2004); Riebe et al. (2001a and 2001b), and Kounov (2007) likewise appear to suggest this. It is also well known that a dearth in vegetation assists the removal of unprotected bedrock, soil and regolith (Kounov et al., 2007; Anhert, 1970; Harrison, 2000; Riebe et al., 2001b; Hooke, 2000). However, precipitation is directly correlated to run-off (Summerfield and Hulton, 1994); the intensity of which dictates the size of particles entrained in the run-off, the speed with which they are transported and the erosional potential of rivers (Jansen et al. 2010; Tucker and Bras, 1999). One is thus obliged to acknowledge that the intensity of precipitation, and not just seasonality, may have a bearing on rates of physical erosion in the manner described by Tucker and Bras (1999). This conclusion finds support in the work of Harrison (2000) and Summerfield and Hulton (1994), where run-off and annual precipitation are shown to correlate with rates of mechanical and chemical erosion. However, this relationship breaks down when annual precipitation exceeds ca. 360

$mm \cdot year^{-1}$ as erosion rates are retarded by the shielding effects of increased vegetation cover (Tucker and Bras, 1999; Harrison, 2000). To the knowledge of the author, the relative importance of mean annual precipitation versus seasonality has not yet been clearly defined. As such, their relationship will simply be considered here as complimentary, in that both have a bearing on denudation rates that is greatest when rainfall is both high and seasonal.

Temperature and precipitation also dictate the distribution and type of vegetation, which is considered to play a role in both chemical weathering and physical erosion; however, the dynamics of the vegetation–denudation rate relationship are ill-resolved (White and Blum, 1995; Riebe et al., 2001b). Distribution of plant life is largely dictated by climate and it has been suggested that its overall effect might already be accounted for in the precipitation and temperature correlations that exist (White and Blum, 1995). Nevertheless, vegetation has been noted to significantly reduce the rate of physical erosion by shielding the underlying material from physical erosion, as well as promoting the development of soils which reduce bedrock exposure (Tucker and Bras, 1999; Vanacker et al., 2007; Harrison, 2000; White and Blum, 1995, and references therein; Anhert, 1970). In addition, plant growth has the potential to aid chemical weathering. By protecting clay minerals from erosion, vegetation promotes the retention of water which can then be used in the weathering processes in the absence of rainfall. The production of carbon dioxide and organic acids by roots, associated organisms, and the decay of plant matter, further promotes the hydrolysis of silicates (White and Blum 1995; Moulton and Berner 1998).

2.2.4 Lithology and structure

The varied mechanical and chemical properties amongst the different rock types results in a range of susceptibilities to weathering and erosion and a consequent variability in denudation rates (Anhert, 1970). Intergranular cohesion, chemical composition and structural fabric as dictated by fractures, joints, faults and bedding planes are collectively responsible for rock mass-strength on the mountain-scale (Korup, 2008; Selby, 1980).

Internal grain-to-grain cohesion of rock determines its tensile strength; dictating its resistance to fluvial abrasion and, in detachment-limited settings[2], to slope failure (Sklar and Dietrich, 2001; Korup, 2008). Abrasion experiments of Sklar and Dietrich (2001) have shown erosion rate to be inversely proportional to the square of bedrock tensile strength. This tensile strength - also referred to as 'critical shear stress' - is particularly relevant to landscape adjustment, causing up to a factor-of-20 difference in the relief decay-time of various lithologies in post- and non-orogenic landscapes, and dampening denudation rates in both high-relief and high-rainfall regions (Baldwin et al., 2003; von Blanckenburg et al., 2004). The high-strength characteristics of quartzites, especially relevant to work in this study, have been noted (Jansen et al., 2010; Sklar and Dietrich, 2001; Selby, 1980 and references therein). In 2010, Jansen et al. reported an erosional potential for quartzites three times lower than that of surrounding lithologies, with a resultant control on regional topography that saw areas of high-ground and steep slope located on this crystalline metamorphic rock. The observations of Jansen et al. (2010) echo those of Clayton and Shamoon (1998) who found that varying resistance of lithologies to denudation was, to a large extent, responsible for the relative relief of the British Isles, with areas of highest elevation comprised of quartz-rich rocks. Both these authors, however, were preceded by Selby (1980), whose work in developing a classification scheme for rock strength also led to the observation that stronger lithologies tend to exhibit steeper slopes, and that quartzite is amongst the hardest of rocks.

The robust properties of quartzites results in reduced ability of rivers to efficiently erode channel beds and walls comprised of this rock type. Rivers flowing through quartzites tend to be steeper and narrower than those flowing through neighbouring lithologies (Jansen et al., 2010). Abrasion experiments carried out by Sklar and Dietrich (2001) showed quartzites to have the highest tensile strength – and consequently lowest erosion rates – out of a selection of rock types that included (in order of increasing resistance to erosion) sandstone, greywacke, limestone, welded tuff, andesite and quartzite. Selby (1980) tabulated relative rock strengths of common rock types, using data accumulated from various authors cited in his text. Quartzite, dolerite and gabbro are considered to be

[2] A detachment-limited setting is one in which the sediment carrying capacity of a river exceeds the sediment load of the river.

amongst the strongest lithologies. Within the coastal Cape Mountains and present study area, much of the present-day morphology has been attributed to the strength of the quartzites of which these mountains are largely comprised (King, 1962; Moon, 1982).

It is not only the grain-to-grain cohesion of rock that affects erodibility, but its structural fabric as well. Joints and fractures weaken a rock face, promoting early slope failure, lowering critical slope angles and increasing susceptibility to removal through fluvial action or seismic disturbance (Burbank et al., 1996; Quigley et al., 2007a; Korup, 2008; Molnar et al., 2007; Selby, 1980). The detailed investigation of Korup (2008) into the relationship between slope angles, erosion rates and landsliding places particular emphasis on the ability of joints and fractures to weaken rock and lower critical slope angles.

Joints serve to weaken rock and increase erodibilty in three ways. Firstly, the internal cohesion of rock is destroyed along the fissure. Friction may still exist where opposing joint faces are in contact with one another but this, too, is lost where joints are widely open. Consequently, the effective rock mass strength is destroyed and the outcrop is made more susceptible to erosion (Selby, 1980). Secondly, together with bedding surfaces, fractures and joints allow moisture to infiltrate the rock face thus becoming loci of increased erosion and chemical weathering, encouraging the production of saprolite (e.g. Bierman and Caffee, 2002; Burbank et al., 1996; Jansen et al., 2010; Selby, 1980). Thirdly, these planes of weakness are further exploited through various mechanisms of physical erosion (such as fire spallation, frost shattering and plant roots, amongst others) which reduce solid rock outcrops to smaller fragments, transportable under the action of fluvial or gravitational processes (Small et al., 1997). Naturally, joint spacing is also of consequence to denudation rate, as the closer spacing of joints implies a rock mass that is more finely divided and thus more easily eroded, as well as greater exposure to chemical weathering (Selby, 1980; Molnar et al., 2007).

Both grain-to-grain cohesion and structural fabric have a bearing on the size and abundance of river bedload material, which in turn affects the rate of river incision and channel slope (Sklar and Dietrich, 2001; Gilbert, 1877; Turowski et al., 2007). In transport-limited rivers (i.e. those in which the sediment load of the river exceeds sediment carrying capacity of the river) a profusion of sand or gravel in the river channel can armour the channel bed, effectively shielding it from

erosion. In detachment-limited rivers (i.e. those in which the carrying capacity of the river exceeds the sediment load of the river) no such armouring occurs and sediment supplied to the river can effectively be used to erode channel floors and walls. Under these conditions, both channel width and incision rate are functions of bedrock erodibility.

Abrasion occurs most efficiently when the river is supplied with an amount of sediment that is moderate in comparison to the maximum transport capacity of the stream (Gilbert, 1877), as low sediment supplies rob the channel of the tools required for abrasion, while high sediment supplies will blanket the channel floor thus minimising abrasion through grain-to-grain impact. Turowski et al. (2007) have shown that erosion rates increase with an increase in river bedload up to a threshold point, after which the sediment load exceeds the transport capacity of the river and sediment begins to blanket the channel floor and shield it from abrasion. As the channel floor is progressively shielded by the excess sediment load, the erosion rate due to channel abrasion decreases asymptotically towards zero. A gradual change from a tool-dominated environment in the proximal reaches of a river to a cover-dominated environment in the distal reaches of a river, is observed.

Grain size is also important, as shown by Sklar and Dietrich (2001). Sand-sized particles are light and tend to travel in suspension and impart little damage to the channel floor when the two occasionally collide. Sand therefore serves solely to abrade channel walls and protrusions above the channel floor (Sklar and Dietrich, 2001, and references therein), with grains smaller than 2 mm (coarse-grained sediment) effecting negligible abrasion. Intermediate grain size particles are the most efficient at scouring, as they are heavy enough to travel as bedload but still light enough to be transported by the stream. Larger sediment clasts, approximately 35 mm in diameter (very coarse grained gravel), are heavy and tend to form a protective, immobile armouring on the channel floor. As such, their contribution to bedrock erosion is limited to occasional flood events, when stream flow is powerful enough to move this heavier material.

Lithology is also thought to have a dominant effect on chemical weathering in watersheds, due to varying reactivity amongst minerals. White and Blum (1995) describe a 'reactivity series' based on the work of previous authors, in which relative mineral reactivity decreases in the order of carbonates, mafic silicates,

feldspars and finally quartzites. Flint (1963) also noted that rocks rich in chemically less-reactive quartz generally occupy higher altitudes than rocks more prone to chemical weathering, such as carbonates.

As with climate, rock strength and structure are considered secondary controls on denudation rates, subordinate to the effects of tectonics (Safran et al., 2005). The influence of hillslope-scale lithological strength on denudation rate is further lessened in large drainage basins that encompass a variety of lithologies as the individual lithologic effects are averaged over. Smaller drainage basins which host only one or two rock types, however, are likely to experience a more pronounced lithologic control on denudation rates (Anhert, 1970).

2.2.5 Anthropogenic influences

In addition to the natural, long-standing influences of climatic and tectonic regimes and lithological strength, the recent advent of industrialised civilization has had a remarkable effect on erosion rates to the extent that humans are now considered the primary agent of denudation (Hooke, 2000; Wilkinson and McElroy, 2007). Large-scale agriculture, deforestation and construction remove natural vegetation, rendering the underlying soils vulnerable to erosion (Vanacker et al., 2007). The resultant increase in soil erosion on slopes and interfluves is comparable to that seen in actively uplifting mountain ranges (Anhert, 1970; Koppes and Montgomery, 2009; von Blanckenburg, 2005; Vanacker et al., 2007), with soil erosion rates in areas of extensive agricultural practice exceeding soil production rates by up to two orders of magnitude (Hewawasam, 2003; Dale et al., 1998; Farnsworth and Milliman, 2003; Decker et al., 2011; Milliman et al., 1987). This extensive erosion not only removes current soil deposits but decreases soil production rates, resulting in a disequilibrium which will ultimately strip the Earth's surface of a non-renewable resource if these rates continue unimpeded (Decker et al. 2011).

2.3 Summary

Steeper hillslopes and channel gradients support increased rates of downhill sediment transport (Anhert, 1970; Harrison, 2000; Roering et al., 2007). All else held constant, the relative magnitude of denudation rates will scale primarily with

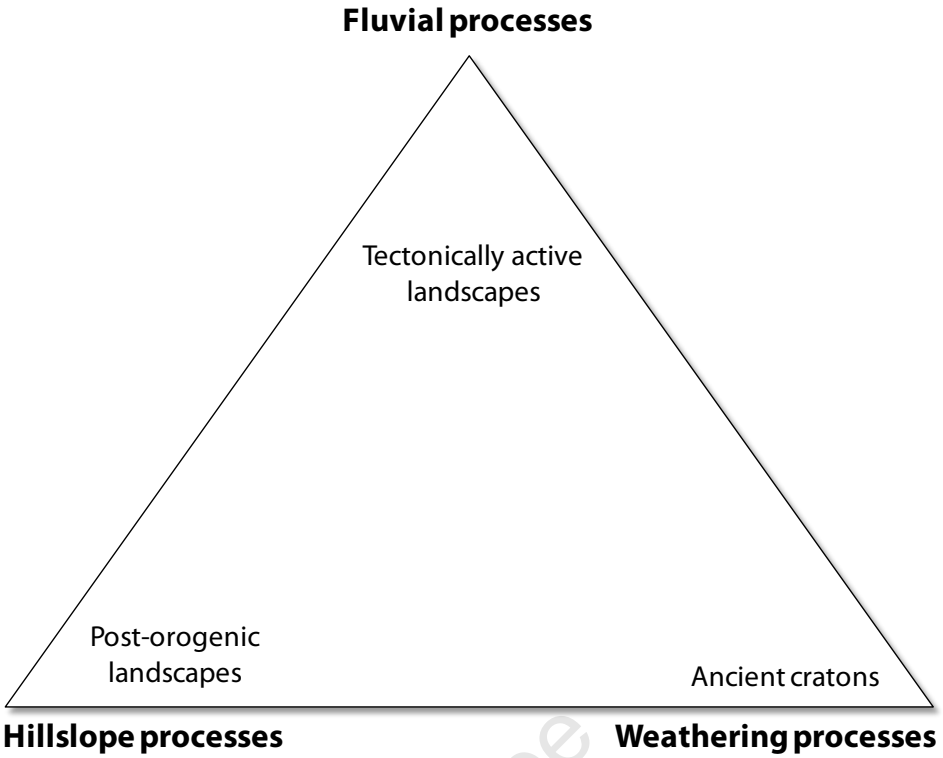

Figure 2.5: The relationship between geological setting and the dominant controls on denudation rates. This figure is modified from Montgomery (2003).

hillslope and channel gradient such that rugged terrains yield higher denudation rates than gentle terrains (Summerfield and Hulton, 1994; Safran et al., 2005). The absolute magnitudes of denudation rates, however, are influenced by controls such as tectonic activity, climatic regime, and lithologic properties. Of these, tectonic activity exerts the strongest control, inciting high denudation rates which often mask the subtler influences of climate and lithology (Safran et al., 2005).

Based on topography and principal denudational mechanisms, landscapes can be broadly grouped into three categories as illustrated in Figure 2.5 (Montgomery, 2003):

Cratons — These stable, ancient landscapes have subdued topography and experience minimal tectonic input. Here, chemical weathering dominates over physical erosion (Montgomery, 2003; Montgomery and Brandon, 2002).

Post-orogenic landscapes — Low hillslope and channel gradients characterise the gentle, often soil-mantled topography of post-orogenic landscapes. In the absence of active tectonic uplift (e.g. epeirogenic uplift or upward

displacement due to faulting) river incision ceases and denudation rates on hillslopes exceed rates of down-wearing by rivers. This spatial imbalance in denudation rates causes a decline in relief over time until a topographic steady state is established, at which point all elements of the landscape will denude at similar rates. Hillslope-processes dominate over river incision and the slope-denudation rate relationship is described by a positive, linear function. Changes to climatic or tectonic regimes will be accommodated by adjustments in hillslope and channel gradients. (Montgomery, 2003; Roering et al., 2001; Roering et al., 2007)

Active orogens

Active orogens are characterised by high relief, steep channel gradients and hillslopes at or approaching their angle of repose. River incision dictates the pace of landscape lowering, which is accommodated on hillslopes through debris flows and landslides. Detachment-limited conditions prevail and the landscape responds to variations in uplift with an adjustment in the frequency of slope-failure events. Under these conditions, an exponential curve characterises the hillslope-denudation rate relationship, which fails to hold once threshold slope angles are achieved. (Montgomery, 2003; Roering et al., 2007; Roering et al., 2001; Burbank et al., 1996; Montgomery and Brandon, 2002).

Denudation rates alone offer little information on a landscape other than the spatial distribution of average rates of surface excavation and the minimum time periods (cf. Figure 2.1) over which these averages apply. However, with an understanding of landscape behaviour, the spatial distribution of denudation rates can be used to identify the denudational processes operating within a landscape. This allows one to constrain the nature, timing and extent of denudational episodes responsible for the geomorphic evolution of the landscape. An understanding of the environmental forcings that govern denudation rates, and the nature in which a landscape will respond to each, is thus crucial for an accurate interpretation of both regional and local patterns in denudation rates.

Chapter 3

In situ-produced cosmogenic nuclide analysis

3.1 Introduction

Chapter 3 provides an introduction to the principles behind *in situ*-produced cosmogenic nuclide analysis, with emphasis on the radionuclide ^{10}Be. The origins of cosmogenic nuclides are discussed in Section 3.2 and their rates of production, in Section 3.3. Section 3.4 reviews the scaling regimes and shielding factors in common use. A discussion of the applications of in situ produced cosmogenic ^{10}Be analysis that are relevant to this study of the coastal Cape Mountains is presented in Section 3.5. A chapter summary is provided in Section 3.6.

3.2 The cosmic ray flux

Cosmogenic nuclides are isotopes formed in the atmosphere and surface of the Earth through the interactions of cosmic ray particles with atomic nuclei native to the atmosphere and minerals of the Earth's surface. Those which form in the atmosphere are called meteoric cosmogenic nuclides, while those which form in the Earth's surface are called *in situ*-produced cosmogenic nuclides or terrestrial cosmogenic nuclides (TCN) and occur only in trace quantities in the upper meters of the Earth's surface (Dunai, 2010).

The cosmic rays responsible for the formation of these nuclides arise within our solar system through supernova events and consist largely of protons (87%) and alpha-particles (12%) with energies ranging from a few MeV to hundreds of MeV (Simpson, 1983; Masarik and Reedy, 1995; Niedermann, 2002; Dunai, 2010). Electrons, positrons and heavy nuclei are responsible for the remaining 1% of the

particles; however, these are not relevant to the production of cosmogenic nuclides (Masarik and Reedy, 1995).

Upon entering the Earth's atmosphere, particles of the primary cosmic ray flux interact with atmospheric atomic nuclei (target nuclei) to produce secondary cosmic ray particles (Dunai, 2010). The high energies of primary cosmic ray particles far exceed the binding energies of atomic nuclei (7-9 MeV); consequently, these extraterrestrial particles impart sufficient energy to the atmospheric target nuclei for nucleons to escape the target nucleus. Secondary nucleons produced in this manner possess sufficient energy to induce similar reactions in surrounding atmospheric atomic nuclei. The result is a chain-reaction of nucleon production referred to as a 'nuclear cascade' (Figure 3.1). The principal reaction occurring in the upper atmosphere is therefore spallation whereby atmospheric atomic nuclei are broken down into the three components of the secondary cosmic ray flux which ultimately reach the Earth's surface; namely, the nucleonic component, the mesonic component and the electromagnetic component. It is the nucleonic and mesonic components of the secondary cosmic ray flux that are responsible for the production of TCNs. The intensity of the nuclear cascade is greatest in the upper atmosphere where both primary and secondary cosmic ray particles have the highest energy. Successive interactions of secondary particles with surrounding atmospheric nuclei will reduce their energies so that nucleons which reach the Earth's surface do so with energies of 100 MeV or less, while muons that reach the Earth's surface have an average energy of approximately 4 GeV (Dunai, 2010).

In addition to a reduction in energy the secondary cosmic ray flux undergoes a change in composition along its path through the atmosphere. At the top of the atmosphere the secondary cosmic ray flux is dominated by protons and alpha-particles; however, at the Earth's surface it consists primarily of neutrons and muons (Lal and Peters, 1967). This change is a result of protons having a greater potential for interaction with their environment due to their charge, than neutral neutrons. Muons are noted for their weak interactions with matter, being the least 'reactive' of these three particles. As muons have far weaker interactions with matter than do neutrons, they dominate the secondary cosmic ray flux at the Earth's surface (Lal 1988).

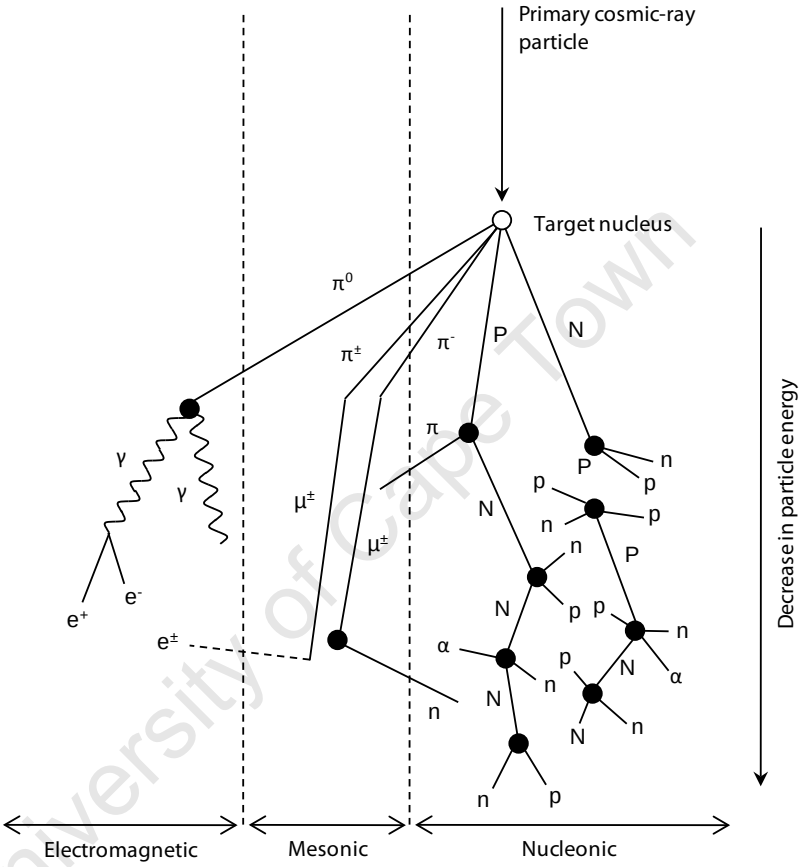

Figure 3.1: A schematic diagram depicting the propagation of the nuclear cascade through the atmosphere. This diagram is modified from Dunai (2010), after Simposon and Fagot, (1953). A primary cosmic ray particle interacts with a target nucleus in the upper atmosphere by means of spallation. The secondary cosmic ray particles which result have sufficient energy to induce similar reactions in the surrounding atmospheric atomic nuclei, thus producing the 'nuclear cascade' effect. Abbreviations: n - neutron, p – proton, $e^{\pm}$ - electron or positron, γ – photon, μ - muon, π – pion. Upper case letters indicate particles which propagate the nuclear cascade.

3.3 Factors affecting the cosmic ray flux

3.3.1 Electric and magnetic fields

The primary cosmic ray flux is comprised largely of positively charged particles (protons and alpha-particles) and will consequently be deflected when passing through a magnetic field of sufficient strength. The degree to which particles are deflected is dependent on particle kinetic energy and the size of the angle between the particle velocity vector and the magnetic field line vector (Masarik and Reedy, 1995; Masarik and Beer, 1999; Dunai, 2010). Both greater angle and lower kinetic energy result in greater deflection.

The term 'rigidity' is used to describe a particle's resistance to deflection by a magnetic field and is described by Equation 3.1, where R is the rigidity, p is the particle momentum, c is the speed of light and e is the particle charge (Dunai, 2010). Rigidity is thus particle momentum per unit charge expressed in units GV (Masarik and Reedy, 1995; Niedermann, 2002). In this respect, the magnetic fields of the Sun and Earth are important as they dictate the energy spectrum of the primary cosmic ray particles which enter the Earth's atmosphere.

$$R = \frac{pc}{e} \qquad 3.1$$

The magnetic field of the sun will deflect any particles with energies below 10 MeV so that only those of higher energy may approach the Earth (Masarik and Reedy, 1995; Masarik and Beer, 1999). The strength of this magnetic field varies with solar activity, which waxes and wanes according to a number of cycles whose periodicities range from 11 years up to a possible 2300 years (Lifton et al., 2005 and references therein; Niedermann, 2002). Fluctuations in solar modulation will cause the intensity of the primary cosmic ray flux incident upon the Earth's upper atmosphere to likewise fluctuate with the solar activity cycles.

The effects of fluctuations in solar modulation are born largely by the low-energy end of the cosmic ray spectrum which is confined to high geomagnetic latitudes. Their impact on geological applications of cosmogenic nuclide analysis is, however, often dampened as the exposure times dealt with in geological

investigations generally exceed the periodicity of the solar fluctuations. As a result, common geological samples experience the average of these fluctuations (Niedermann, 2002). This is not the case for nuclides such as ^{14}C, where the short half-life of the nuclide prevents it from accumulating over time periods that are sufficiently long to average the effects of fluctuating solar modulation on production rate. Solar modulation should thus be accounted for in the accurate analysis of short-lived cosmogenic nuclides.

The Earth's magnetic field will similarly moderate the incident cosmic ray flux. The rigidity required to penetrate the Earth's magnetic field is termed the 'cut-off rigidity' (Masarik and Reedy, 1995; Masarik and Beer, 1999; Gosse and Phillips, 2001; Niedermann, 2002; Dunai, 2010). If the Earth's magnetic field is approximated to a dipole field this cut-off rigidity can be described by Equation 3.2, where M is the dipole moment of the geomagnetic field ($7.9{\cdot}10^{22}\mathrm{Am}^2$), c is the speed of light ($3 \cdot 10^8 \mathrm{m} \cdot \mathrm{s}^{-1}$), R is the radius of the Earth ($6.37{\cdot}10^6\mathrm{m}$), μ_0 is the magnetic permeability of free space ($4\pi\mathrm{x}10^{-7}\mathrm{Vs{\cdot}Am}^{-1}$), and λ_m is the geomagnetic latitude (Niedermann, 2002).

$$P_c = \frac{M\mu_0 c}{16\pi R^2}\cos^4 \lambda_m \qquad 3.2$$

Particles with sufficient energy to penetrate the Sun's magnetic field and approach the Earth's surface are aligned predominantly along the vertical. Maximum flux intensity is thus aligned perpendicular to the geoid and decreases as the angle of incidence increases (Dorman et al., 1999). The major proportion of incident cosmic ray particles which approach the Earth's geomagnetic equator are therefore aligned perpendicularly to the Earth's magnetic field lines, while those which approach the geomagnetic poles are aligned parallel to the magnetic field lines. Those particles incident on the geomagnetic equator will thus experience a stronger deflecting force than particles which approach the geomagnetic poles (Dunai, 2010). Higher particle energy is therefore required to resist deflection and approach the Earth's geomagnetic equator. As a result, the average energy of the cosmic ray flux decreases from a maximum in equatorial regions to a minimum at 60° geomagnetic latitude. Conversely, the magnitude of the cosmic ray flux increases from the geomagnetic equator to a maximum at 60° geomagnetic latitude

(Dunai, 2010; Niedermann, 2002). Due to solar modulation, nearly all impingent cosmic ray particles possess sufficient energy to penetrate the Earth's magnetic field at a geomagnetic latitude of 60° and no further increase in the magnitude of the cosmic ray flux or decrease in the energy of cosmic ray flux is experienced beyond this point.

As the primary cosmic ray flux is responsible for the production of the secondary cosmic ray flux which in turn is responsible for TCN production, TCN production rates are seen to vary with geomagnetic latitude. Greater production rates occur in geomagnetic polar regions and decrease with decreasing geomagnetic latitude (Dunai, 2010).

The intensity and direction of the dipole and non-dipole components of the Earth's geomagnetic field fluctuate over periods of 10^1-10^6 years, resulting in further variations in the cosmic ray flux (Niedermann, 2002 and references therein). For periods of 10-20 ka, dipole fluctuations average out and are of little consequence to the geological applications of cosmogenic nuclide analysis (Merrill et al., 1998; Dunai, 2000; Niedermann, 2002). The variance in position of the geomagnetic pole becomes important when investigating geological features that have been exposed for less than 1 ka (Niedermann, 2002). The magnitude of fluctuations in field intensity are less well-understood; however, their influence on the production rate of cosmogenic nuclides is limited to low latitude regions (0°-10°) where the cut-off rigidity of the Earth's magnetic field strongly moderates the incident flux intensity (Masarik et al. 2001; Niedermann, 2002). Mid-latitude regions (30°-40°) are minimally affected while high-latitude regions (>40°) are not affected at all as the cut-off rigidities in these regions are too low to influence the cosmic ray flux.

3.3.2 Interactions with matter

3.3.2.1 Attenuation of the cosmic ray flux

The secondary cosmic ray flux is attenuated exponentially with depth through matter (Niedermann, 2002; Dunai, 2010). This decline in flux intensity is described by Equation 3.3, where I_0 is the incident particle flux (neutrons or

muons), d is depth within a given material (cm) and Λ is the attenuation length of the neutrons or muons ($g \cdot cm^{-2}$) in the given material.

$$I(d) = I_0 e^{\frac{-d}{\Lambda}} \quad 3.3$$

Attenuation length describes the exponential decrease of the cosmic ray flux with depth in any material (Gosse and Phillips, 2001). This parameter can be considered to reflect the probability of particle interactions occurring between a given particle flux and the medium through which it is passing; higher attenuation lengths indicate a lower probability for interaction and vice versa. Attenuation length is specific to the energy of the cosmic ray flux concerned. The neutron flux and muon flux are therefore characterised by different attenuation lengths. Further differentiation can be made between the attenuation lengths of fast, slow, thermal, and epithermal neutrons; as well as between that of fast and slow muons.

The quotient obtained by dividing the attenuation length of the particle flux (Λ) by the density of the material through which it passes (d), is termed the 'attenuation path length (z^*)'. This parameter describes the distance 'z^*' into a material of density 'd' that the cosmic ray flux of attenuation length 'Λ' must penetrate in order for it to be attenuated to 33% of its original strength. This distance is measured perpendicularly to the surface through which the cosmic rays penetrated. In a horizontal, unshielded silicate rock, z^* is approximately 60 cm (Lal 1991).

At the boundary between the atmosphere and solid Earth, the neutron flux does not display the expected exponential decrease with depth but instead remains steady for 10-20 $g \cdot cm^{-2}$ on either side of the air-surface boundary (Masarik and Reedy, 2005). This zone of constant neutron flux is due to the reflection of neutrons from the solid surface into the atmosphere and the production of thermal neutrons in the surface of a material which diffuse to the air-surface boundary and atmosphere beyond (Niedermann, 2002; Phillips et al., 2000).

Within the atmosphere, the attenuation lengths of secondary cosmic ray particles vary according to altitude and geomagnetic latitude. Dependence on altitude is due to the decrease in particle energies with increasing atmospheric depth, while the dependence on geomagnetic latitude is due to the moderating influence of cut-off rigidity on the energies of the incident primary cosmic ray

particles (Dunai, 2010). Typical attenuation lengths for fast neutrons at the surface of the Earth range from 150-180g $\cdot$ cm^{-2} (Masarik and Reedy, 1995; Lal, 1991; Dunai, 2010 and references therein; Gosse and Phillips, 2001 and references therein). For muons, the attenuation length is longer due to their weak interactions with matter and typically range from 800-1500g $\cdot$ cm^{-2} (Gosse and Phillips, 2001; Dunai, 2010). The attenuation length of fast muons is longer still with an approximate value of 5300 g $\cdot$ cm^{-2} (Braucher, 2003). For surface production, attenuation lengths of 150-170 g $\cdot$ cm^{-2} yield similar results (Gosse and Phillips, 2001); consequently, a value of 160 g $\cdot$ cm^{-2} is commonly used in geomorphological applications of cosmogenic nuclides.

3.3.2.2 Production mechanisms

The nature of the reaction which occurs when a secondary cosmic ray particle interacts with an atomic nucleus is dependent on the energy of the cosmic ray particle. The rate at which these reactions occur is dependent on the intensity of the secondary cosmic ray flux. Reactions which give rise to TNCs include spallation, thermal neutron absorption, slow-muon absorption, and fast-muon induced photoneutron reactions.

At the surface of the Earth production is dominated by spallation reactions between fast neutrons (~0.1-10 MeV) and target nuclei in the materials of the Earth's surface, despite muons being the largest contributor to the secondary cosmic ray flux (Dunai, 2010). The fast neutron flux is directional, moving solely in a downward direction. As these particles collide with surrounding target nuclei in spallation reactions their energies are reduced to that of thermal neutrons (0 eV-0.5 eV) and their trajectories randomised (Phillips et al. 2001; Niedermann, 2002; Dunai, 2010). The resultant thermal neutrons are captured by surrounding atomic nuclei. This process causes the excitation of the 'captor' nucleus, which subsequently disintegrates to produce the resultant TCN. Thermal neutron adsorption does not play a major role in the production of all TCNs but is important for the production of ^{14}C, ^{36}Cl, ^{41}Cl and ^{3}He (Dunai 2010, Lal, 1988; Phillips, 2001).

The strong interactions between neutrons and matter, as compared to muons and matter, results in the rapid attenuation of the neutron flux in comparison to

the muon flux. This is evidenced in the short attenuation length of neutrons (~150-180 $g \cdot cm^{-2}$; Masarik and Reedy, 1995; Lal, 1991; Dunai, 2010 and references therein; Gosse and Phillips, 2001 and references therein) compared to the longer attenuation lengths of slow muons (1500 $g \cdot cm^{-2}$; Gosse and Phillips, 2001 and references therein; Dunai, 2010 and references therein) and fast muons (5300 $g \cdot cm^{-2}$; Braucher, 2003). Consequently, production by muon interactions dominates at depth (~200-300 $g \cdot cm^{-2}$; Figure 3.2) where the neutron flux is much reduced (Lal and peters 1967; Gosse and Phillips, 2001 Niedermann, 2002; von Blanckenburg, 2005 Braucher et al. 2003, Dunai, 2010).

Low energy ('stopped') muons can be captured by atomic nuclei and taken up into the atomic nucleus. A combination of neutrinos, alpha-particles, protons, and neutrons are subsequently lost from the atomic nucleus to accommodate the additional energy which the absorption of a muon brings to the atomic nucleus, thus producing the cosmogenic nuclide (Heisinger et al. 2002b; Dunai, 2010). Fast muons are the only particles to penetrate to depths of a few tens of meters, that is to say ~$10^6 g \cdot cm^{-2}$ (Masarik and Reedy, 1995). The deceleration of these particles by surrounding atomic nuclei produces Bremsstrahlung which can incite the release of photoneutrons from surrounding atomic nuclei in the rock (Groom et al, 2001; Heisinger and Nolte, 2002). These high energy photoneutrons can go on to react with surrounding atomic nuclei in a similar manner to fast neutrons, thus producing TCNs (Dunai, 2010; Niedermann, 2002).

3.3.2.3 *In situ*-produced cosmogenic ^{10}Be

In situ-produced cosmogenic ^{10}Be is a radionuclide with a half-life of 1.387 ± 0.012 Myr (Korschinek et al., 2009; Chmeleff, 2010) and a sea level, high latitude production rate of 5.14 ± 0.53 $atom \cdot g^{-1} \cdot year$ (Balco et al., 2008). Given its long half-life, ^{10}Be is well suited for the investigation of geologic phenomena over the Quaternary and late-Pliocene.

Its production mechanisms are dominated by spallation reactions with oxygen, thus making quartz an ideal target mineral, while the ubiquitous nature of quartz makes sampling viable in nearly any geological setting (Dunai, 2010; von Blanckenburg, 2005, Niedermann, 2002). This spallation reaction is shown in

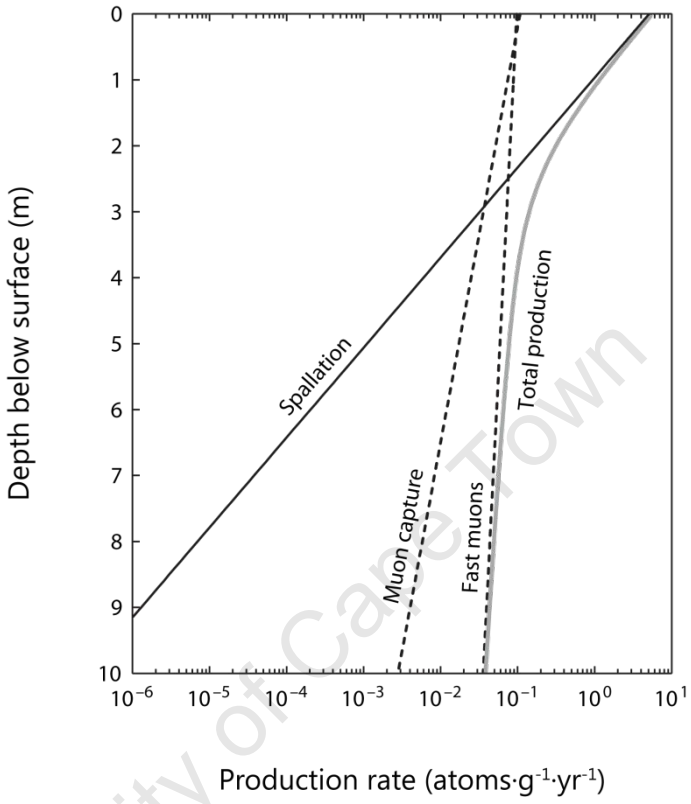

Figure 3.2: Exponential decrease of *in situ*-produced cosmogenic ^{10}Be production rate with depth in a silicate rock of density 2.7 g·cm^{-3}. This figure is modified from Dunai (2010) who modelled production rates and their attenuation according to Heisinger et al (2002a, 2002b). The neutron flux attenuates at a faster pace with depth through a substrate than the muon flux. Similarly, the slow muon flux attenuations at a faster pace than the fast muon flux. Production is thus dominated by muon interactions at depth, with fast muons penetrating deeper than slow muons.

Equation 3.4, where *n* symbolises 'neutron' and *p* symbolises 'proton'. ^{10}Be decays to stable ^{10}B by means of beta minus decay, as shown in Equation 3.5 where e^- symbolises 'electron', $\overline{\nu_e}$ symbolises 'antineutrino', superscript integers indicate the mass number of an atom and subscript integers indicate the atomic number of an atom.

$$^{16}O(n, 4p3n)^{10}Be \quad 3.4$$

$$^{10}_{4}Be \rightarrow {}^{10}_{5}B + e^- + \overline{\nu_e} \quad 3.5$$

As ^{10}Be is typically hosted in quartz, it can be efficiently chemically extracted from the sample material without the tedious hand-picking of target mineral grains that is required for the analysis of noble gas nuclides (Dunai, 2010). A major risk of contamination for *in situ*-^{10}Be is meteoric ^{10}Be whose production rate is three orders of magnitude greater than that of *in situ*-^{10}Be and is easily adsorbed onto the target mineral surfaces (Dunai, 2010; Gosse and Phillips 2001). This necessitates the removal of the outer surface of the quartz grains; however, this is easily achieved through a series of acid leachings (Kohl and Nishiizumi, 1992).

The simple sampling methods and analytical techniques required to extract ^{10}Be from its target mineral, the ubiquitous nature of the target mineral, the low risk of contamination, the well constrained production rates and the long half-life of *in situ*-produced ^{10}Be, make this TCN the nuclide of choice for the analysis of the coastal Cape Mountains. Further discussion of *in situ*-produced cosmogenic nuclide analysis will deal only with those aspects that are relevant to the analysis of *in situ*-produced ^{10}Be and the sampling techniques applied to the analysis of the coastal Cape Mountains.

3.4 TCN production rates: Scaling factors and shielding factors

The rate of TCN production at a point of interest is dependent on the intensity of the secondary cosmic ray flux incident on that point (Lal, 1991; Dunai, 2010). At any given location on the Earth's surface this incident cosmic ray flux has been moderated by the magnetic fields of both the Sun and the Earth, and attenuated on passing through the atmosphere. In the case of a subsurface sample, the incident cosmic ray flux has been further attenuated by the materials of the Earth's surface. Site-specific moderations of the incident cosmic ray flux are due to shielding of the sample site from the full spectrum of secondary cosmic ray irradiation:

Topographic shielding
: A large geomorphic feature can obstruct part of the incoming cosmic ray flux and prevent the full angular spectrum of cosmic rays from impinging upon the sample site (Dunai, 2010; Dunne et al, 1999).

Self-shielding
: In an inclined surface, the up-dip portion of the surface may shield the lower down-dip portion from the full angular spectrum of cosmic rays. In a sample whose thickness exceeds 10 cm the cosmic ray flux attenuates exponentially with depth. The overlying material therefore shields the underlying material by reducing the intensity of the cosmic ray flux passing through the underlying material (Dunai, 2010; Dunne et al, 1999).

Burial
: In the case of buried sample material (e.g. soil cover on a bedrock surface) the cosmic ray flux is attenuated on passing through the overburden. Consequently, that cosmic ray flux which passes through the underlying sample surface does so with reduced intensity. Self-shielding due to sample thickness is a 'special case' of burial shielding (Dunai, 2010; Dunne et al, 1999).

Geological applications of cosmogenic nuclide analysis require an accurate knowledge of nuclide production rates at the geological sampling sites, without which exposure ages and denudation rates cannot be reliably calculated. The effects of these moderating influences on the cosmic ray flux must therefore be accounted for if an accurate production rate is to be determined (Lal, 1991).

3.4.1 Altitudinal and latitudinal scaling factors

Production rates have been established for the analytically-useful TCNs and are reported normalised to the standard conditions of sea level and high latitude (SLHL). To this end, three techniques have been used, namely, modelling of the cosmic ray flux and its interactions with Earth materials based on physical principles, irradiation experiments, and geological calibration. Modelling of production rates based on physical principles is hindered by the currently incomplete knowledge of neutron-reaction cross-sections which necessitates the use of certain assumptions whose inherent inaccuracies may be as much as 25%. Irradiation experiments which subject a pure target to an artificial particle beam do not account for the full energy spectrum that a target will encounter in nature; while those which expose a target to natural radiation do so for periods of time too short to account for the effects of solar modulation on production rates. Geological calibration determines the TCN content of a sample whose age has been accurately determined through independent geochronometric methods, and is naturally only as accurate as the independent age determination. Of these three methods, geological calibration yields the most reliable production rates. (Dunai, 2010)

The production rate determined for each of the calibration sites is dependent on the secondary cosmic ray flux at the location of the calibration site, which in turn is dependent on the geomagnetic latitude and atmospheric depth of the calibration site. In order to make these production rates applicable to geological sampling sites elsewhere on Earth a latitude-altitude scaling factor is used to account for the effects that the change in geomagnetic latitude and atmospheric depth between SLHL and the geologic sampling site in question, would have on production rate. Numerous latitude-altitude scaling factors exist which predict the change in secondary cosmic ray flux with differing accuracy. In any geological

study one should use the same scaling factors to scale the SLHL production rate to the sampling site, as were used to scale the production rate from the calibration site to conditions of SLHL (Niedermann, 2002; Dunai, 2010).

Commonly used scaling factors include those of Lal (1991), Dunai (2000, 2001a), Stone (2000), Desilets and Zreda (2003) and Desilets (2006), and Lifton et al. (2005). The important differences between these scaling regimes relate to how atmospheric depth and the geomagnetic field are accounted for, and whether or not they account for variations in the geomagnetic fields of the Earth and Sun (Dunai, 2010). In this study, the scaling regimes of Dunai (2000) were applied as they accurately account for the effects of atmospheric pressure.

3.4.1.1 Lal (1991)

The scaling factors of Lal (1991) were the first developed and are still the most widely cited in the literature. Using geographic latitude as a proxy for geomagnetic latitude and altitude as a proxy for atmospheric depth, Lal (1991) proposed that the production rate of ^{10}Be in quartz can be calculated according to Equation 3.6, where *P(L,y)* is the production rate as a function of geomagnetic latitude *(L)* and altitude *(y)* and the coefficients *a*, *b*, *c* and *d* are dependent on latitude. The values for the coefficients are given in Table 3.1. Equation 3.6 applies to spallation reactions with nucleons of energy greater than 40 MeV at any point between the altitudes of 0-10 km.

Lal's scaling factors approximate the Earth's magnetic field to an axial geomagnetic dipole. Under these conditions geomagnetic and geographic latitudes coincide and can thus be used interchangeably in Equation 3.6. This assumption, however, over-simplifies the Earth's geomagnetic field leading to inaccuracies in production rate calculation (Dunai, 2000; Desilets and Zreda, 2003). In addition, fluctuations in the geomagnetic field are not accounted for, although Lal (1991) acknowledges that variations in the Earth's magnetic field will affect cut-off rigidities and thus the secondary cosmic ray flux and resultant production rates.

The use of altitude as a proxy for atmospheric depth is based on the US standard atmosphere relationship and assumed to be applicable to all areas on the Earth's surface. This assumption overlooks local air pressure anomalies and can lead to production rate errors of 2-10% for places with anomalously low or high

Table 3.1 Coefficients for Equation 3.4 (Lal, 1991).

Geomagnetic latitude	Polynomial coefficients			
	a	b	c	d
0	3.511	2.547	0.915125	0.18608
10	3.360	2.522	1.0668	0.18830
20	4.0607	2.734	1.2673	0.22529
30	4.994	3.904	0.9739	0.42671
40	5.594	4.946	1.3817	0.53176
50	6.064	5.715	1.6473	0.68684
60 -90°	5.994	6.018	1.7045	0.71184

$$P(L,y) = a(L) + b(L)y + c(L)y^2 + d(L)y^3 \qquad 3.6$$

pressure and up to 30% in Antarctica (Stone, 2000). A further criticism is the use of attenuation lengths determined for altitudes of 3-3.5 km. Subsequent to the publication of Lal (1991) further nuclear data has shown that the energy spectrum for cosmic ray particles, assumed by Lal (1991) to be constant between altitudes of 0-12 km for particles with energies of 400 MeV, does in fact soften with increasing atmospheric depth (Desilets and Zreda, 2003). As a result, the attenuation lengths given by Lal (1991) are likely an overestimate of those found at sea level (Dunai, 2000).

3.4.1.2 Stone (2000)

The scaling factors of Stone (2000) are a reformulation of those by Lal (1991) designed to accurately account for variations in air pressure on local production rates. Most places on Earth deviate from the US standard atmosphere assumption applied by Lal (1991) to his scaling factors and consequently experience local

production rates that are 3-4% higher or lower than those predicted using the standard atmosphere assumption. In regions of long-lived high or low atmospheric pressure, error is increased to approximately 6-10%, while the prevalence of a large low pressure over Antarctica leads to an underestimation of production rates by 25-30%. In all regions other than Antarctica, the errors are smaller than the uncertainty associated with the scaling factors of Lal (1991). The value of Stone's reformulated scaling factors therefore lies in their ability to accurately model the anomalous atmospheric pressure – altitude relationship in Antarctica. It must be noted, however, that most scaling schemes succeeding those of Lal (1991) have incorporated atmospheric pressure instead of altitude as a proxy for atmospheric depth. Any of these can be successfully applied to Antarctica if the correct atmospheric pressure – altitude relationship is used.

Stone modelled the spallation production rate as a function of atmospheric pressure and geographic latitude according to Equation 3.7. Production by muon-capture is similarly modelled as a function of atmospheric pressure and geographic latitude, as shown by Equation 3.8. Coefficients are listed in Table 3.2. Equation 3.9 gives the total production by both spallation and muonic interactions, where f_{sp} is the proportion of spallogenic production relative to total production in a surface at sea level. In the case of Antarctica, Stone (2000) supplies an additional formula for the determination of the pressure value, P, to be used in Equations 3.7-3.9. This pressure formulation is not provided here and the reader is directed to Stone (2000).

$$S_\lambda(P) = a + be^{-P/150} + cP + dP^2 + \mathrm{e}P^3 \qquad 3.7$$

$$M_\lambda(P) = M_{\lambda,1013.25}\, e^{[(1013.25-P)/242]} \qquad 3.8$$

$$F_\lambda(P) = f_{sp} S_\lambda(P) + \left(1 - f_{sp}\right) M_\lambda(P) \qquad 3.9$$

Table 3.2: Coefficients for Equation 3.7 (Stone, 2000).

Geographic latitude	a	b	c	d	e	$M_{\lambda 1013.25}$
0	31.8518	250.3193	-0.083393	$7.4260 \cdot 10^{-5}$	$-2.2397 \cdot 10^{-8}$	0.587
10	34.3699	258.4759	-0.089807	$7.9457 \cdot 10^{-5}$	$-2.3697 \cdot 10^{-8}$	0.600
20	40.3153	308.9894	-0.106248	$9.4508 \cdot 10^{-5}$	$-2.8234 \cdot 10^{-8}$	0.678
30	42.0983	512.6857	-0.120551	$1.1752 \cdot 10^{-4}$	$-3.8809 \cdot 10^{-8}$	0.833
40	56.7733	649.1343	-0.160859	$1.5463 \cdot 10^{-4}$	$-5.0330 \cdot 10^{-8}$	0.933
50	69.0720	832.4566	-0.199252	$1.9391 \cdot 10^{-4}$	$-6.3653 \cdot 10^{-8}$	1.000
60 -90	71.8733	863.1927	-0.207069	$2.0127 \cdot 10^{-4}$	$-6.6043 \cdot 10^{-8}$	1.000

3.4.1.3 Dunai (2000 and 2001)

The scaling factors of Dunai (2000) are fundamentally similar to those of Lal (1991) but differ with respect to the way in which it models the Earth's geomagnetic field, the attenuation lengths used and the proxy used to describe atmospheric depth. Furthermore, while Lal (1991) only accounts for spallogenic reactions, Dunai (2000) accounts for muonic interactions as well. These differences are as follows:

Geomagnetic field

While Lal (1991) approximates the Earth's geomagnetic field as a dipole, Dunai (2000) draws attention to the fact that the Earth's magnetic field incorporates a large non-dipole component that contributes 10-25% to the magnetic field (Dunai, 2000 and references therein). This non-dipole component is spatially variant.

To accurately constrain the production rate in a localised region (e.g. a geological sampling site) it is necessary to account for the non-dipole effects on the cosmic ray flux in that region. To achieve this, the scaling factors of Dunai (2000) use

geomagnetic field inclination as a proxy for geomagnetic latitude.

The scaling factors of Dunai (2000) do not take into account variations in the geomagnetic field strength through time and are thus applicable to the present-day field strength only.

Attenuation length

Dunai (2000) and Lal (1991) have used similar data sources in their determination of attenuation lengths at various latitudes and altitudes; however, their manipulation of this data differs. While Lal (1991) uses attenuation lengths that are applicable at 3-3.5 km altitude to describe nuclear interactions at the Earth's surface, Dunai uses values determined for 0-700 m altitude. As attenuation length varies with elevation, those used by Dunai (2000) are more applicable to reactions occurring at the surface of the Earth, while those used by Lal (1991) are likely to overestimate the actual attenuation length at the Earth's surface and consequently lead to higher production rates.

Despite using attenuation lengths that are more applicable to the altitude at which sampling occurs, Dunai (2000) does not incorporate the variation of attenuation length with altitude into the proposed scaling factors but instead assumes a constant neutron flux between 0 km and 4 km altitude at low latitude (Desilets and Zreda, 2003; Desilets et al., 2001).

Atmospheric depth

The dependence of cosmic ray flux on atmospheric depth is modelled with a simple altitude-atmospheric pressure relationship by Lal (1991). This allows one to use altitude as a proxy for atmospheric depth under the assumption that atmospheric depth decreases linearly with altitude. However, this simple altitude-atmospheric pressure assumption is not applicable to all points on the Earth's surface. Dunai (2000) thus uses atmospheric pressure as a proxy for atmospheric depth.

Dunai (2000) models neutron flux as a function of magnetic field inclination and atmospheric pressure, and provides Equation 3.10 for cosmogenic nuclide production by protons and secondary neutrons, and Equation 3.11 for production by all components of the cosmic ray (nucleons and muons).

$$N(z,I) = N_{1030}(I) \cdot e^{z(h)/\Lambda(I)} \tag{3.10}$$

$$N(z,I) = N_{1030}(I) \cdot e^{\frac{z(h)}{\Lambda(I)}} \cdot (1-x) + N_{1030}(I) \cdot e^{\frac{z(h)}{\Lambda_\mu}} \cdot x \tag{3.11}$$

In Equations 3.10 and 3.11, $N_{1030}(I)$ and $\Lambda(I)$ are defined by Equations 3.12 and 3.13. $N_{1030}(I)$ is the nuclide production rate at sea level (1030 $g \cdot cm^{-2}$) as a function of geomagnetic inclination (I). $\Lambda(I)$ is the attenuation length at geomagnetic field inclination I. $N(z,I)$ is the nuclide production rate at geomagnetic field inclination I and atmospheric depth z, where z is the difference in atmospheric depth between sea level and the point of interest, calculated according to Equations 3.14 - 3.17. x is the fraction of production by muons and Λ_μ is the attenuation length of muons in the atmosphere. Parameters A, B, C (Equation 3.12) and a, b, c (Equation 3.13) are given in Table 3.3.

$$N_{1030}(I) = Y + \frac{A}{\left[1 + e^{-\left(\frac{I-X}{B}\right)}\right]^C} \tag{3.12}$$

$$\Lambda(I) = y + \frac{a}{\left[1 + e^{-\left(\frac{I-x}{b}\right)}\right]^c} \tag{3.13}$$

Table 3.3: Coefficients for Equations 3.12 and 3.13 (Dunai, 2000).

Coefficients for $N_{1030}(I)$		Coefficients for $\Lambda(I)$	
A	0.4450	a	19.85
B	4.1703	b	-5.430
C	0.3350	c	3.590
X	62.698	x	62.050
Y	0.5555	y	129.55

In Equations 3.14-3.17, d_0 is the atmospheric depth at sea level and d is the atmospheric depth at the point of interest ($g \cdot cm^{-2}$), p is the long-term atmospheric pressure (mbar), g_0 is gravitational acceleration at sea level (9.80665 $m \cdot s^{-2}$), p_0 is the atmospheric pressure at sea level (1013 mbar), β_0 is the decrease in temperature with altitude (6.5 $mK \cdot m^{-1}$), h is altitude (m), T_0 is the temperature at sea level (288.15K), and R_d is the gas constant (287.05 $J \cdot kg^{-1} \cdot K^{-1}$).

$$z(h) = d_0 - d \tag{3.14}$$

$$d = \frac{10p}{g_0} \tag{3.15}$$

$$d_0 = \frac{10p_0}{g_0} \tag{3.16}$$

$$p = p_0 \left(1 - \frac{\beta_0 h}{T_0}\right)^{\frac{g_0}{R_d \beta_0}} \tag{3.17}$$

The geomagnetic field inclination is related to geomagnetic latitude according to Equation 3.18, where I is field inclination and λ is geomagnetic latitude. Over periods of 10-20 ka the average geomagnetic field approximates to a geocentric axial dipole field and geomagnetic latitude approximates to geographic latitude. This allows geographic latitude to be substituted for geomagnetic latitude in Equation 3.11.

$$\tan I = 2tan\lambda \qquad 3.18$$

The discrepancies between the scaling factors of Dunai (2000) and Lal (1991) are largest at high altitudes and at sea level between latitudes of 20° and 40°. Deviation at high altitude is a result of the different attenuation lengths used in the two scaling regimes; consequently, production rates calculated using the scaling factors of Dunai (2000) are up to 30% higher than those calculated using the scaling factors of Lal (1991). The variance at mid-latitude is related to the non-dipole field effects which Dunai (2000) accounts for but Lal (1991) does not, resulting in an 18% variance between the two scaling factors. The use of atmospheric pressure to model atmospheric depth in the scaling factors of Dunai (2000) further reduces the inaccuracy in scaled production rates by 5-10%.

Desilets et al. (2001) have criticised Dunai (2000) on several points including the limited neutron data used to construct attenuation lengths; the assumption that attenuation lengths are constant between 0 km and 4 km elevation; the absence of a data correction for instrumental bias; using an over simplified model of the magnetic field which allows for the use of magnetic field inclination instead of vertical cut-off rigidity as a proxy for geomagnetic latitude; the assumption that solar modulation does not affect the secondary cosmic ray flux near the Earth's surface; and the questionable suitability of the geological samples used to test the scaling factors of Dunai (2000). These criticisms are addressed by Dunai (2001b) in support of his methodology.

The scaling factors of Dunai (2000) were later revised to produce those of Dunai (2001a) which take into account the effects of variations in the geomagnetic field strength through time. The revised scaling factors are analogous to those of Dunai (2000) and require detailed geomagnetic records from within 1000-2000 km of the region under study for their implementation.

In this study of the coastal Cape Mountains, the scaling regime of Dunai (2000) was applied. The work of Dunai (2000) was favoured over the preceding work of Lal (1991) as it accounts for the non-dipole components of the Earth's magnetic field, and uses atmospheric pressure instead of altitude as a proxy for atmospheric depth. The scaling regime of Dunai (2000) is likewise favoured over

that of Stone (2000) as both Dunai (2000) and Stone (2000) model production rates as a function of atmospheric pressure; however, the scaling regime of Dunai (2000) is more simply applied. The succeeding scaling regimes of Dunai (2001a), Desilets and Zreda (2003), Desilets et al. (2006) and Lifton et al (2005) incorporate the effects of variance in the Earth's magnetic field; however, over the exposure times applicable to the coastal Cape Mountain samples, variance in the Earth's magnetic field will likely not be of consequence and thus these scaling regimes were not used.

3.4.1.4 Desilets and Zreda (2003) and Desilets et al. (2006)

The scaling factors of Desilets and Zreda (2003) account for the effects of solar modulation, geomagnetic dipole variance and fluctuations in air pressure over time. Those of Desilets et al. (2006) are an adaptation of Desilets and Zreda (2003) for application to low geomagnetic latitudes. As the attenuation length of spallation reactions is energy dependent, these authors have developed scaling factors which differentiate between production rate by thermal and fast neutrons. This required a recalculation of attenuation lengths associated with high-energy spallation reactions and thermal neutron absorption reactions. Consequently, intricate scaling factors were formulated whose use is only justified for: young samples in which TCN content will reflect the effects of solar modulation and geomagnetic dipole variance; those cosmogenic nuclides where production by thermal neutrons contributes a significant portion to the overall production rate (e.g. ^{36}Cl); and low latitude regions where the difference between the attenuation length of spallation reactions and those of thermal neutron absorption reactions differ the most. Within these models, atmospheric depth is described in terms of shielding depth ($g \cdot cm^{-2}$) and geomagnetic latitude in terms of effective vertical cut-off rigidity, 'R_c' (GV).

3.4.1.5 Lifton et al. (2005)

The scaling factors of Lifton et al (2005) were developed with the intention of accurately accounting for the effects of solar modulation which causes fluctuations of 10-20% in the secondary cosmic ray neutron flux at sea level, high latitude and less than 7% at sea level, low latitude. The muon flux is less affected by solar

modulation and varies only by 4-6% at sea level, high latitude. The scaling factors of Lifton et al. (2005) account for the effects of fluctuations in air pressure and geomagnetic field, and differentiate between production by fast and slow muons. No differentiation is made between thermal and epithermal neutrons. Geomagnetic latitude is expressed in terms of effective cut-off rigidity (R_C) and atmospheric depth is expressed in terms of shielding depth ($g \cdot cm^{-2}$).

3.4.2 Shielding

Production rate in a substrate is dependent on the cosmic ray flux passing through the substrate. Consequently, any material which blocks or attenuates the cosmic ray flux will effectively shield the substrate from the full cosmic ray spectrum, thus reducing production rates in the substrate. For this reason, a number of correction factors exist to deal with different forms of shielding. Shielding corrections dealt with below are a brief summary of the corrections applicable to samples from the coastal Cape Mountains. For an exhaustive review of shielding factors, the reader is referred to Gosse and Phillips (2001) and Dunne et al. (1999).

3.4.2.1 Topographic shielding

An exposed surface receives cosmic rays incident from all angles. Due to atmospheric attenuation, the strongest flux is that which is aligned along the vertical, with flux strength decreasing as the angle of incidence increases. A horizontal, unobstructed surface will receive the full angular spectrum of cosmic ray radiation and thus be subjected to the maximum secondary cosmic ray flux. This maximum flux can be calculated according to Equation 3.19, where F is the maximum cosmic ray flux and $I(\theta,\phi)$ is the cosmic ray intensity, θ is the inclination angle measured from the horizontal, and ϕ is the azimuthal angle of incoming radiation seen from the perspective of the irradiated surface (Figure; Dunne et al., 1999).

$$F = \int_{\phi=0}^{2\pi} \int_{\theta=0}^{\pi/2} I(\theta,\phi) cos\theta d\theta d\phi \qquad 3.19$$

For the case of $\theta = 0$, cosmic ray intensity is likewise zero; however, for the case of $\theta \geq 0$ Equation 3.20 applies, in which I_0 is the maximum intensity and m is a constant commonly taken to be 2.3. Substituting Equation 3.20 into 3.19 gives a simple formula for maximum flux incident on a horizontal, unshielded surface as shown in 3.21.

$$I(\theta, \phi) = I_0 sin^m(\theta) \quad 3.20$$

$$F_{max} = \frac{2\pi I_0}{m+1} \quad 3.21$$

If the horizon is not clear but instead marked with an obstruction thick enough to stop cosmic rays from passing through (i.e. a thickness of at least one attenuation length), then the intensity of the cosmic ray flux incident on the surface will be reduced and with it, the production rate in the surface. The effective attenuation length of the incident cosmic ray flux will also be affected by topographic shielding; the interested reader is directed to Equations 7 and 9 and Figures 2 and 3 of Dunne et al. (1991) for further explanation.

Formulae exist to account for shielding by one or more rectangular obstructions (Equation 3.22) and one or more triangular obstructions (Equation 3.23) (Dunne et al. 1999). In both cases it is the height and width of the obstruction, as seen from the view point of the shielded surface, that determine the degree to which the obstruction shields the surface. The height of the obstruction can be described by its inclination θ, above the horizon and its width by its azimuthal width of ϕ, both of which are illustrated in Figure. Equation 3.22 is the 'shielding factor' which is effectively a ratio of the reduced cosmic ray intensity to the maximum cosmic ray intensity (Dunne et al., 1991). The shielding factor can be multiplied with the production rate to account for the effect of cosmic ray shielding on the surface rate of production.

$$f_{topo} = 1 - \frac{1}{360^0} \sum_{i=1}^{n} \Delta\phi_i \, sin^{m+1}\theta_i \quad 3.22$$

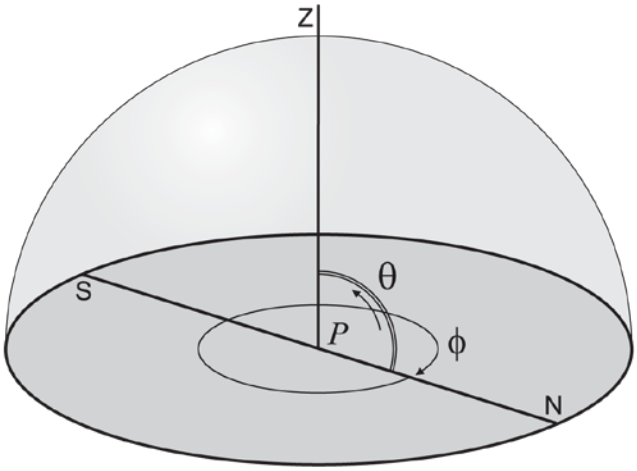

$$F_{Received} = F_{Max}$$

Figure 3.3: A horizontal, unshielded substrate at point P is subjected to the maximum secondary cosmic ray flux. The maximum cosmic ray flux is the sum of secondary cosmic ray particles incident from all angles, as described by the inclination angle θ and the azimuthal angle ϕ. This figure is taken from Codilean (2008).

The shielding effect of a triangular obstruction can be calculated by approximating the triangular object to a rectangular object of equivalent shielding effect (Dunne et al., 1991). Equation 3.22 can be used and θ substituted for θ_R of Equation 3.23 where θ_T is the inclination (degrees) of the apex of the triangle. If the zenith angle of the triangle is less than 50°, θ_R can be substituted with $0.62\theta_T$.

$$\theta_R = 0.62\theta_T - (6.5 \cdot 10^{-4})\theta_T^2 \qquad 3.23$$

Certain applications of cosmogenic nuclide analysis require the determination of topographic shielding for large areas and complex topography; for example, in the determination of catchment-averaged denudation rates where the effects of topographic shielding must be quantified for an entire catchment. In such a case, the use of Equation 3.22 is not feasible due to the complexity of shielding variations throughout the catchment. Complex topographic shielding effects can be calculated using a GIS-based model developed by Codilean (2006) which uses relief shadow modelling to compute the topographic shielding experienced by each

cell in a DEM of the respective study region. From this the average topographic shielding for the catchment can be calculated.

3.4.2.2 Self-shielding

A sample may shield itself from cosmic rays due to its being inclined, or due to its thickness. In the case of an inclined surface, the upper portion may shield the lower portion from cosmic rays; with the degree of shielding varying in a complex manner with azimuthal angle (Dunne et al., 1999). Self-shielding only becomes prominent when the inclined surface is large, with a width of several meters.

The total cosmic ray flux experienced by a sample situated a distance z below a surface with a dip of α, is given by Equation 3.24, where $I(\theta, \phi)$ is the intensity of the cosmic ray flux from a direction (θ, ϕ) relative to the sample point, and d is the flux penetration distance (**Error! Reference source not found.**; Dunne et al., 1999). The flux penetration distance for a sample located a distance z perpendicularly below the inclined surface is the straight-line distance through the subsurface that a cosmic ray must travel from its point of incidence on the surface to the sample point below the surface, as described by Equation 3.25 (Dunne et al., 1999). In Equations 3.24 and 3.25, γ is the surface inclination in the direction of ϕ, where ϕ has a value of 0 in the direction of maximum slope inclination. Equation 3.25 is only valid if θ is greater than γ (Dunne et al., 1999). Equation 3.24 can be solved to give the self-shielding scaling factor of Equation 3.26, where α is the surface dip, z is the perpendicular distance of the sample below the sloped surface, Λ is the attenuation of production rate in the subsurface (Dunne et al. 1999).

$$F = \int_{\phi=0}^{2\pi} \int_{\theta=\gamma}^{\frac{\pi}{2}} I(\theta,\phi) e^{-d/\lambda} \cos\theta \, d\theta d\phi \qquad 3.24$$

$$d = \frac{z \cos\gamma}{\cos\alpha \sin(\theta - \gamma)} \qquad 3.25$$

$$s(z,\alpha) = (1 - 3.6 \cdot 10^{-6} \alpha^{2.64}) e^{-\left(\frac{z}{\Lambda}\right)\left(1+\frac{\alpha^2}{5000}\right)} \qquad 3.26$$

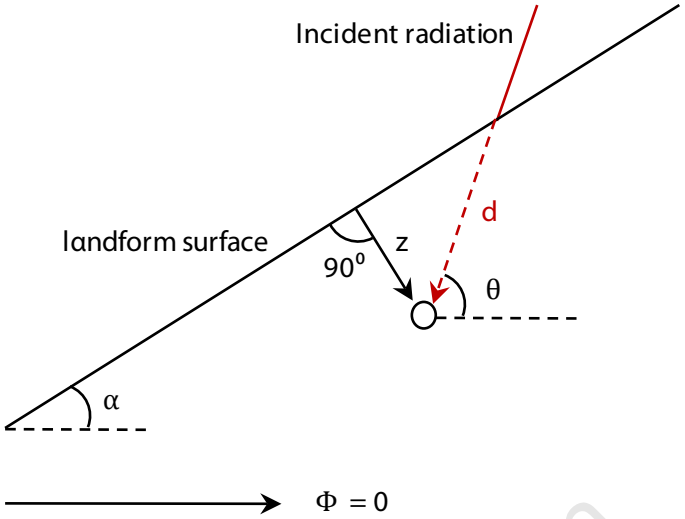

Figure 3.4: Relevant angles for the determination of self-shielding in a sloped surface. This figure is modified from Dunne et al. (1999). The surface has a maximum inclination of α in the direction of $\phi = 0$. The target at point P lies a perpendicular distance of z below the surface of the substrate. The secondary cosmic ray flux travels a distance of d from its point of incidence on the substrate surface to the target situated below surface. For an azimuth angle other than $\phi = 0$, the angle of inclination is described by γ (not visible in the figure).

Shielding due to sample thickness is the result of the attenuation of the cosmic ray flux as it passes through the subsurface. For samples that do not exceed 10 cm thickness, and for nuclides whose production is dominated by spallogenic interactions, this form of self-shielding with depth can be corrected for by applying Equation 3.27 in which the attenuation length used is that for spallation reactions (Dunai, 2010). Due to the attenuating affect of the subsurface, surface samples should ideally not exceed 5 cm in thickness (Dunai, 2010).

$$f(z) = e^{-z\rho/2\Lambda} \qquad 3.27$$

In the case of a sample subject to both topographic shielding and self-shielding due to inclination, Equations 3.22 and 3.26 can only be applied to the sample as separate scaling factors if the topographic obstructions are situated down-slope of the inclined surface. If this is not the case, Equations 3.19 and 3.24 must be solved using the case-specific integration limits (Dunne et al. 1999).

3.4.2.3 Mass shielding

Similar to self-shielding with depth in which the cosmic ray flux incident on a subsurface sample is attenuated when passing through the overlying material, any semi-permanent overburden will likewise shield the underlying surface from the full cosmic ray flux, e.g. soil cover on a bedrock surface (Dunai, 2010). Self-shielding by means of sample thickness can be considered a 'special case' of mass shielding. To correct a spallation-dominated production rate for the shielding effects of intermittent surface burial, Equation 3.28 can be applied. *F(z)* is the shielding factor, z is the depth of burial, ρ is the density of the overburden, and Λ is the attenuation length of spallation reactions.

$$f(z) = e^{-z\rho/\Lambda} \qquad 3.28$$

3.5 Applications of cosmogenic nuclide analysis

TCNs accumulate within the upper meters of the Earth's crust at a rate that decreases exponentially with depth, and which is dependent on geomagnetic latitude, local atmospheric depth, and sample-specific cosmic ray shielding. Interpretation of the TCN content of target mineral grains is therefore dependent on site-specific conditions.

If the sampled surface has neither been denuded nor buried and none of the TCN content of the target mineral grains is due to a previous exposure to cosmic rays (no 'inherited' TCN content) then the TCN concentration is directly proportional to exposure time of the surface.

In the case of surface burial, the radionuclide content of the target mineral grains will decay according to the half-life of the radionuclide. The differential decay rates of two radionuclides (e.g. ^{10}Be and ^{26}Al) can be used to determine the burial history of the surface. This is commonly referred to as 'burial dating'. Alternatively, if the material in question is a clastic deposit, the exponential decrease in production rate with depth of one TCN can be used to constrain the minimum age of the deposit, the paleodenudation rate which gave rise to the clastic material of which the deposit is comprised and in the case of an actively

denuding depositional surface, the rate at which the surface is denuding. This will be referred to as 'depth profiling' in this text. For a surface subject to steady-state denudation, the TCN content of the target mineral grains will reflect the rate at which the surface is denuding.

The following discussion of the applications of cosmogenic nuclide analysis to geologic sciences will be limited to those techniques used in this investigation of the coastal Cape Mountains. These include bedrock surface exposure age dating, both localised bedrock and catchment-averaged denudation rate determination, and depth profiling.

3.5.1 Exposure age dating

Exposure age dating is used to determine the length of time for which a substrate has been exposed at the surface of the Earth. In an exposed, non-eroding (or negligibly eroding) surface, target minerals will slowly accumulate ^{10}Be over time; however, as ^{10}Be is a radionuclide it will be simultaneously lost at a rate determined by its half life (Brown et al., 1995; Dunai, 2010). Over time, the rate of accumulation will come to equilibrate with the rate of loss and the ^{10}Be concentration in the substrate becomes time invariant (Brown et al., 1995; Dunai, 2010). At this point the TCN content of the substrate (e.g. an exposed bedrock surface) will no longer reflect the exposure time of the surface, but rather the rate of ^{10}Be loss (flat portion of the graphs in **Error! Reference source not found.**). Provided this steady-state has not yet been reached (inclined portion of the graphs in **Error! Reference source not found.**) the nuclide concentration in a surface is directly proportional to the exposure age if the surface material contains no inherited cosmogenic nuclide concentration.

This exposure age is equivalent to the age of formation of the surface if the surface has experienced neither denudation nor burial, and if the surface was formed over a period of time that is brief in comparison to the time for which it has been exposed to cosmic rays. Under these circumstances, the total ^{10}Be concentration at any point on or below the surface is described by Equation 3.29, where C_{total} is the total nuclide concentration, C_{inh} is the inherited nuclide concentration, z is depth, t is exposure time, P is the production rate as per

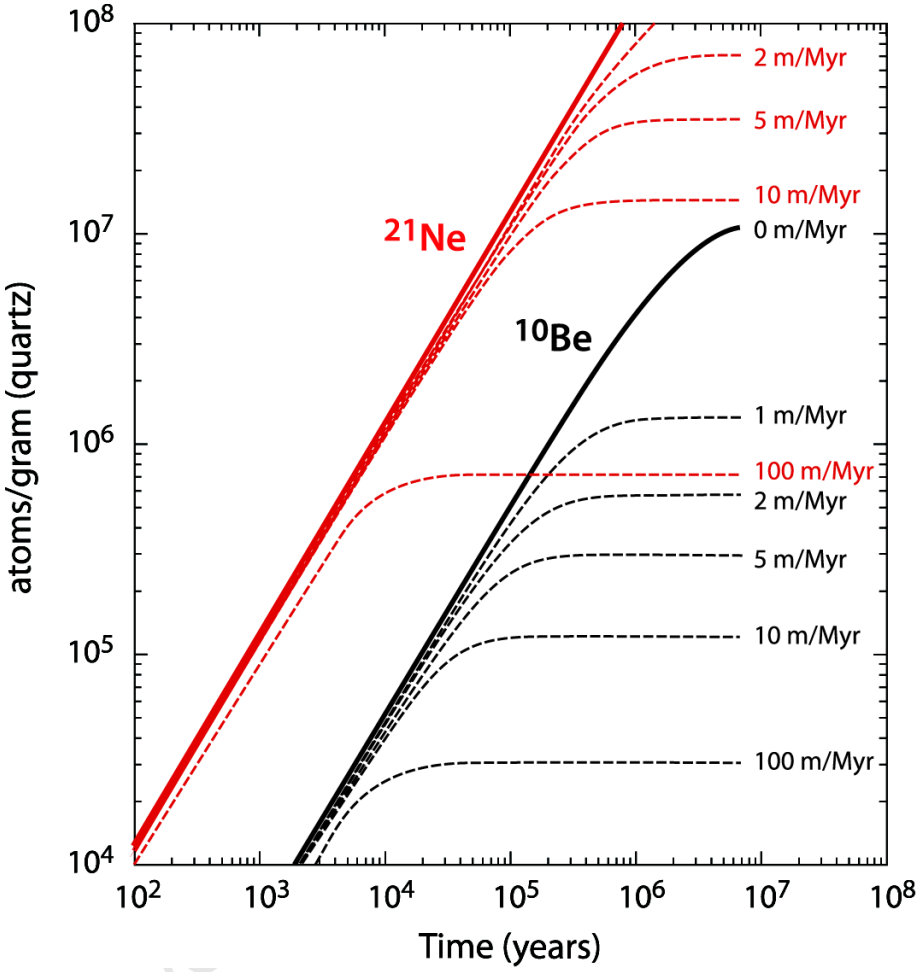

Figure 3.5: Accumulation of in situ-produced cosmogenic ^{10}Be and ^{21}Ne in quartz, assuming no inherited TCN content. This figure has been taken from Codilean (2008). The solid lines show the accumulation of the nuclides in a surface which is not denuding. The nuclides are produced by cosmic ray interactions with the quartz and, in the case of ^{10}Be, lost through radioactive decay. If given sufficient time ($<10^6$), these two processes will come to equilibrate and the ^{10}Be concentration will become time invariant. The stippled lines show the effects of varying denudation rates on the nuclide production rates. As denudation increases the rate of nuclide removal, equilibrium between production and loss is reached more quickly. Once equilibrium is reached, the nuclide concentration no longer reflects the exposure age of the surface, but instead its denudation rate and the minimum age required for steady-state denudation rates to be reached.

Equation 3.30, the subscript i indicates the production rate associated with various production mechanisms (e.g. spallation, thermal neutrons, fast muons and slow muons), ρ is the density of the substrate and λ is the decay constant of ^{10}Be (Lal, 1991; Niedermann, 2002).

$$C_{total}(t,z) = C_{inh}(z)e^{-t\lambda} + \sum_i \frac{P_i(z)}{\lambda}(1 - e^{-t\lambda}) \qquad 3.29$$

$$P_i(z) = P_i(0)e^{\frac{-z\rho}{\Lambda_i}} \qquad 3.30$$

Equation 3.29 can be rearranged to give the exposure time of a surface sample under the assumption of no inheritance, burial or erosion (Equation 3.31) (Lal, 1991, Niedermann 2002).

.

$$T_{exp} = -\frac{1}{\lambda}\ln\left(1 - \frac{C_{total}(z, T_{exp})\lambda}{\sum_i P_i(z) \cdot e^{-\rho z/\Lambda_i}}\right) \qquad 3.31$$

Ideally a horizontal surface should be sampled to avoid corrections for self-shielding. To avoid further complications due to the attenuation of the secondary cosmic ray flux with depth through the surface, samples should be limited to a thickness of less than 5 cm (Dunai, 2010). Doing so ensures that sampled material is sourced from the zone of constant neutron flux.

Production rates are sensitive to the amount of matter per volume, i.e. density, as described by the attenuation length of the cosmic ray flux. Consequently the removal of any material overlying the point of interest, whether by mechanical erosion or chemical weathering, will affect production rates at the point of interest. If the rate of denudation is known and no more than 10 cm of material has been eroded, the minimum exposure age can be calculated by correcting for the effects of denudation according to Equation 3.32 and 3.33, which are applicable solely to spallation reactions (Dunai, 2010).

$$T_{\exp(corrected)} = f_\varepsilon T_{exp} \quad 3.32$$

$$f_\varepsilon = 1 + \frac{\frac{\varepsilon T_{exp}\,\rho}{\Lambda_{sp}}}{2} \quad 3.33$$

If, however, the denudation rate is not known, the exposure age determined without correction for the unknown rate of denudation will translate to a minimum exposure age for the surface (Dunai, 2010). This is because the removal of material from the upper layers of the sample substrate will expose mineral grains from deeper below the surface which have only been subjected to an attenuated cosmic ray flux and thus a reduced production rate. Consequently, these mineral grains will have a lower TCN concentration. At the surface a lower TCN concentration will be interpreted as a shorter exposure age if one is not aware of the denudational history of the substrate.

3.5.2 Denudation rate determination

Continuous denudation which proceeds at a constant pace for a time period that far exceeds the averaging timescale of the denudation rate is referred to as 'steady-state denudation'. The 'averaging timescale' refers to the time required to remove a depth of one absorption path length of material from the denuding surface at the given denudation rate. This parameter is the quotient of the attenuation path length (z*) and the denudation rate. For ^{10}Be, the averaging timescale typically varies between 10^2 and 10^6 as seen in Figure 3.6 (von Blanckenburg, 2005).

Under conditions of steady-state denudation the rate of TCN production has had time to equilibrate with the rate of TCN loss through denudation and decay. Consequently, the TCN content in the target mineral grains is time invariant and no longer reflects the absolute age of the surface (Brown et al., 1995; Dunai, 2010). It is, however, inversely proportional to the rate at which the surface is denuding and can thus be used to determine the denudation rate, as well as the minimum exposure age of the surface (Lal 1991; Brown et al., 1995; Bierman and Steig 1996; von Blanckenburg 2005). This is well illustrated in Figure, where the inclined portions of the graphs indicate a system approaching steady-state conditions, while

the flat portions of the graphs indicate a system in which steady-state denudation has been established.

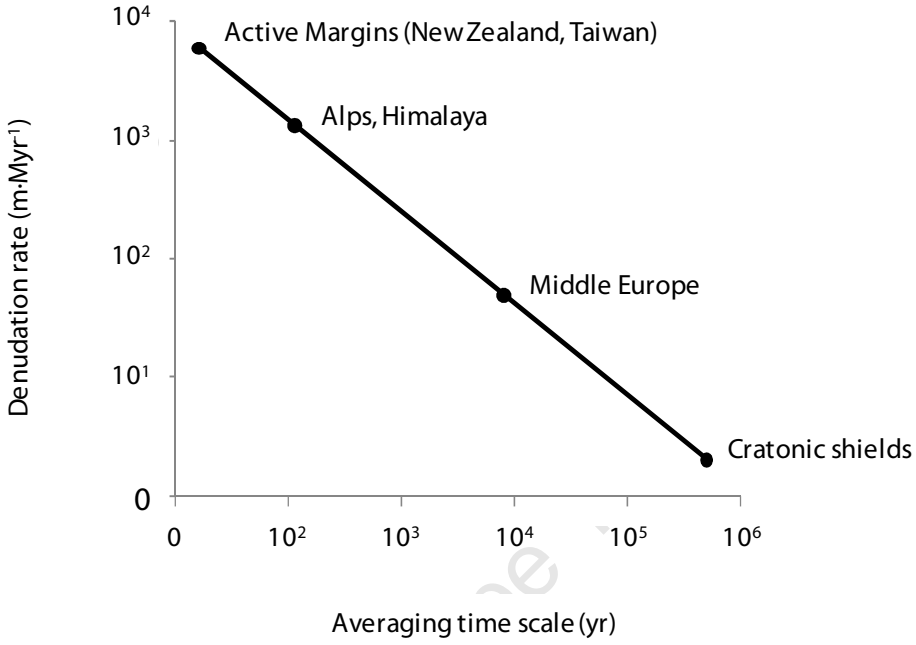

Figure 3.6: Averaging timescale as a function of the denudation rate for various tectonic settings of the world. This image was modified from von Blanckenburg (2005).

Steady-state denudation further implies that the denuding surface is slowly lowered through time under the action of granular disintegration, spallation of thin rock layers, or both. In the case of ^{10}Be the half-life of the nuclide provides the lower limit of the denudation rates to which this steady-state relationship can apply (Brown et al., 1995). At denudation rates below 1 $m \cdot Myr^{-1}$ ^{10}Be is primarily lost through decay and not denudation; therefore, the ^{10}Be concentration will reflect the age of the surface and not its denudation rate.

Equation 3.34 describes the TCN content C, in a denuding surface at a depth z and time t, before equilibrium between ^{10}Be production and loss is established. The initial depth below surface (when $t = 0$) is labelled z_0, the denudation rate is given by ε, and the exposure age by t (Lal, 1991; Niedermann, 2002). Under conditions of steady-state and in the absence of an inherited TCN component, Equation 3.34 reduces to Equation 3.35 (Lal, 1991). For a surface sample where production is dominated by spallation reactions, Equation 3.35 simplifies to

Equation 3.36. Equation 3.36 can be rearranged to form Equation 3.37, which allows one to calculate the denudation rate.

$$C_{total}(t,z) = C_{inh}(z)e^{-t\lambda} + \sum_i \frac{P_i(z)}{\lambda + \frac{\rho\varepsilon}{\Lambda_i}} e^{\frac{-\rho(z_0-\varepsilon t)}{\Lambda_i}} \left(1 - e^{-\left(\lambda+\frac{\rho\varepsilon}{\Lambda_i}\right)t}\right) \quad 3.34$$

$$C_{total}(z) = \sum_i \frac{P_i(z)}{\lambda + \frac{\rho\varepsilon}{\Lambda_i}} \quad 3.35$$

$$C(0) = \frac{P(0)}{\lambda + \rho\varepsilon/\Lambda} \quad 3.36$$

$$\varepsilon = \left(\frac{P(0)}{C(0)} - \lambda\right) z^* \quad 3.37$$

Equation 3.37 is applicable to a horizontal, unshielded surface. In the case of an inclined surface the attenuation length of the cosmic ray flux passing through the surface is reduced relative to that passing through a horizontal surface (Dunne et al., 1999). Consequently, the production rate within the inclined surface is reduced which in turn has a bearing on the denudation rate calculated. The actual erosion rate (ε), which is oriented perpendicular to the inclined surface, is related to the apparent erosion rate (ε^*) according to Equation 3.38, where α is the angle of inclination (Hermanns et al., 2004).

$$\varepsilon^* = \varepsilon\left(1 + \frac{\alpha^2}{5000}\right) \quad 3.38$$

3.5.3 Catchment-averaged denudation rates

Sediment in the main channel of a catchment is an amalgamation of rock fragments sourced from all surfaces within the catchment (Figure 3.7). A denudation rate determined from river sediment is therefore a catchment-averaged denudation rate weighted according to the various 'local' denudation rates found within a catchment and the areas over which they apply. Sampling of river

sediment thus allows one to determine the average denudation rate of a landscape in a cost effective and time efficient manner (Brown et al., 1995; Bierman and Steig, 1996; Granger et al., 2006).

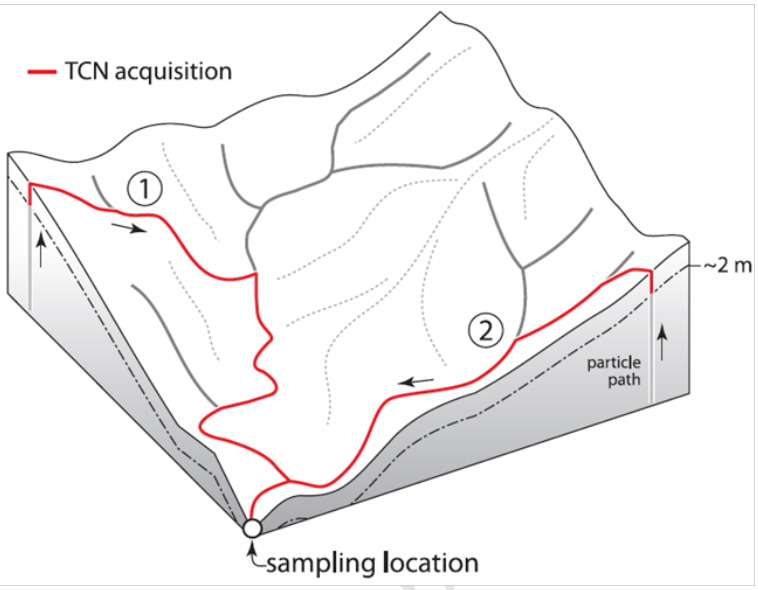

Figure 3.7: River sediment is an amalgamation of grains sourced from all regions in the catchment. This schematic diagram shows the paths travelled by two grains sourced from different regions in the catchment, to the trunk stream. In each case the exposure history is unique to the grain in question, with transport times, burial times, and possibly even denudation rates at the point of origin, differing for each grain. The TCN content of a sediment sample collected from the trunk stream returns and average of these processes operating in the catchment.

Catchments suitable for sampling must adhere to the following prerequisites:

Isotopic steady state Nuclide production and loss within the catchment must be in equilibrium; this is referred to as isotopic steady state. Isotopic steady state requires that all points eroding within the catchment be in denudational steady state although erosion rates need not be spatially uniform throughout the catchment (Bierman and Steig, 1996).

^{10}Be loss The primary means of ^{10}Be loss must be from erosion and not radioactive decay, i.e. the catchment must be eroding at a rate higher than 1 m $\cdot$ Myr^{-1} (Brown et al., 1995).

Well-mixed sediment

The sediment must be well mixed through hillslope and fluvial processes. Thorough mixing ensures that all sediment samples will report the same average TCN content and no sample will be biased to material from a particular area of the catchment (von Blanckenburg, 2005; Bierman and Steig, 1996).

If one area supplies material to the main river channel at a rate that is out of proportion for the average denudation rate of that area, this assumption is violated, e.g. landsliding (von Blanckenburg, 2005; Dunai, 2010). However, in a catchment of sufficient size the effects of landsliding can be averaged out (Niemi et al., 2005; Dunai, 2010; von Blanckenburg, 2005). Larger catchments are required to average over the effects of landsliding as the frequency of landsliding increases. The catchment size required to account for the effects of mass wasting has been modelled by Niemi et al. (2005) according to Equation 3.39 in which ε is the catchment-averaged denudation rate.

$$A_{ave}\, km^2 = \frac{100\, km^3 \cdot Myr^{-1}}{\varepsilon\, km \cdot Myr^{-1}} \qquad 3.39$$

Minimal sediment storage

The time that sediment spends in the catchment must be small in comparison to the averaging timescale of the denudation rate (Granger et al., 1996; Bierman and Steig, 1996; Brown et al., 1995; von Blanckenburg, 2005). If sediment is quickly transported through the catchment the TCN content of its grains reflect the denudation rates operating on the catchment slopes as minimal TCN content is lost to decay or gained through exposure to cosmic rays during transport.

Distribution of target mineral	The target mineral must be present in all lithologies in the catchment so that the sample is representative of processes occurring in all lithologies in the catchment. Furthermore, if the abundance of the target mineral varies between the lithologies of a catchment, a particular lithology may be over or under-represented in the sample (Bierman and Steig, 1996; Dunai, 2010).
Size of target mineral	The mineral size of a sediment sample should be representative of the mineral sizes in the lithologies of the catchments and independent of erosional processes (Bierman and Steig, 1996; von Blanckenburg, 2005; Dunai, 2010). Given two lithologies, one with grain size twice that of the other, sampling only the smaller grain size will exclude information from the lithology with greater grain size. Similarly, sampling only sand and ignoring pebbles will exclude the mechanism by which pebbles are denuded from the catchment-averaged denudation rate.
Minimal chemical weathering	The production of TCN in target mineral grains is sensitive to the amount of material above the mineral grain. If material is removed from below the mineral through deep weathering, the TCN concentration will not reflect this (Dunai, 2010). Furthermore, in compositionally heterogeneous rocks, the preferential dissolution of certain minerals relative to others (e.g. feldspar relative to quartz) will result in sediment samples comprised of the more resistant mineral, thus reflecting lower denudation rates as denudation by means of

chemical dissolution is not accounted for (Bierman and Steig, 1996; von Blanckenburg, 2005; Dunai, 2010).

Averaging timescale of denudation rates

The averaging timescale of the denudation must be short in comparison to the half life of the radionuclide. In the case of ^{10}Be, analysis is limited to catchments eroding faster than 0.3 m $\cdot$ Myr^{-1} (von Blanckenburg, 2005; Dunai, 2010).

The TCN content of the target minerals is accumulated over the time period taken for the mineral to move from a depth of one attenuation path length, to the surface. The target mineral thus arrives at the surface with a TCN content that is representative of the rate of denudation which prevailed during the time taken to excavate the target mineral. The underlying assumption of this calculation is that the denudation rate has remained constant for the duration of the averaging time period and is thus accurately reflected by the TCN content of the mineral. However, constant denudation rates do not always apply. If a change in denudation rate occurs, this change will not be immediately reflected in the TCN content of the mineral grains. The rock surface must be denuded to a depth of one attenuation pathlength (60 cm in a horizontal, silicate rock) to remove all 'memory' of the previous denudation rate, before the new denudation rate is accurately reflected by the TCN content of the mineral grains. Alternatively, the TCN content accumulated under a past denudational regime must be lost through radioactive decay. Given the long half-life of ^{10}Be, the former is applicable to almost all situations (Granger and Riebe, 2007).

Short lived fluctuations in denudation rate cannot be resolved; instead, the TCN content of the mineral grains will tend to 'smooth' over these fluctuations and report a TCN content that is an approximate average of these fluctuations (Bierman and Steig, 1996; Schaller et al., 2002; von Blanckenburg et al., 2004; Niemi et al., 2005; Binnie et al., 2008). When a sudden change in denudational regime occurs, the TCN content of the target minerals will asymptotically approach the new concentration representative of the new denudation rate (Figure 3.8). The time required for the TCN concentration in the target minerals to

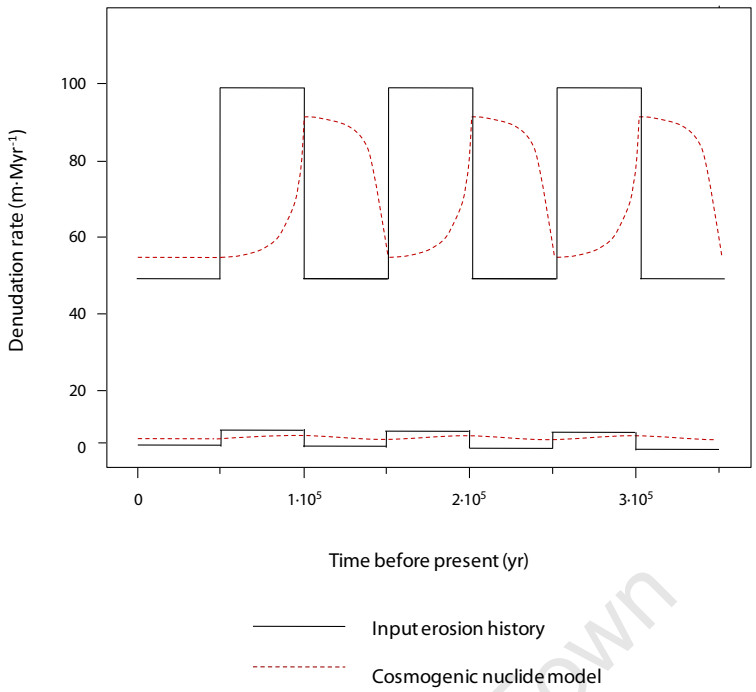

Figure 3.8: A theoretical model of fluctuating denudation rate modified from von Blanckenburg (2005). The black lines show the changes in denudation rate and red stippled lines show the adjustment of the TCN concentration to these fluctuations. In the upper graph, denudation rates fluctuate between 50 m · Myr^{-1} and 100 m · Myr^{-1}, while the lower graph rates fluctuate between 5 m · Myr^{-1} and 10 m · Myr^{-1}. At high denudation rates the associated averaging timescale is short enough for the fluctuations in denudation rate to be resolved. At low denudation rate these fluctuations cannot be resolved and an average denudation rate is reported.

to the new denudation rate is governed by the half-life of the nuclide and the rate of denudation. Adjustment to high denudation rates take on the order of 10^1ka, while at low denudation rates adjustment may take as long as 10^2 ka (Bierman and Steig, 1996). For a detailed discussion on the adjustment of TCN concentration to variations in denudation rates, the reader is directed to Bierman and Stieg, (1996) and Granger and Riebe (2007).

3.5.4 Depth profiles

In the case of a depositional surface, the exponential decrease in production rate with depth can be used to determine the exposure age of the surface and the inherited TCN component which accumulated during exhumation and transport of the clastic material prior to its deposition (Braucher et al., 2003). In this case the inheritance is that TCN content in the sampled material which was accumulated during its erosion, transport and storage en route to its current position, as well as

that which the clasts may have accumulated during a previous episode of exposure in the case of recycled clasts (Anderson et al., 1996).

The clasts of a depositional terrace originate from various regions within a catchment and therefore have varying exhumation and transport histories. In order to represent the average of all processes operating within the catchment, each sample should comprise several clasts sampled from the same location within the terrace. Repka et al. (1994) and Hancock et al. (1999) advise that at least 30 clasts be collected to constrain the mean TCN concentration to within an accuracy of 5%.

Anderson et al. (1996) and Repka et al. (1997) present the simplest correction for inheritance in the age determination of a depositional terrace using two amalgamated samples, one collected at the surface of the terrace and the other some depth below. In the case of a non-eroding terrace, the material at the base of the terrace is representative of the inheritance of the terrace material, having not been exposed to cosmic rays since its deposition. The difference between the ^{10}Be concentration of the surface and lower-most sample is representative of the exposure age of the terrace as it is the ^{10}Be content accumulated in the surface deposit since terrace deposition (Anderson et al 1996, Repka et al. 1997, Hancock et al., 1999). This simple calculation of $TCN_{surface\ sample} - TCN_{lowest\ sample}$ for the average inheritance makes the assumption that inheritance is constant throughout the terrace and that the terrace was deposited over a period of time that is short in comparison to the time for which it has been exposed to cosmic rays (Anderson et al., 1996). Furthermore, this calculation should not be applied to deep samples where TCN production by muons becomes significant.

For both a stable nuclide and a radionuclide whose half-life is far greater than the age of the deposit, the exposure age of the depositional surface can be calculated using Equation 3.40. In the case of a radionuclide that does not meet the above requirement, Equation 3.41 can be used. In both Equations 3.40 and 3.41 T_{exp} is the exposure age of the surface, the subscript *0* indicates a depth of 0 m, i.e. the surface, and the subscript z denotes the sampling depth below the surface (Anderson et al., 1996; Repka et al., 1997).

$$T_{exp} = \frac{P_0 - P_Z}{N_0 - N_Z} = \frac{\Delta P}{\Delta N} \quad 3.40$$

$$T_{exp} = \frac{1}{\lambda} \ln\left(\frac{\Delta P}{\Delta P - \lambda \Delta N}\right) \quad 3.41$$

By collecting a number of samples over a vertical distance within the same sedimentary horizon (~6 samples within a vertical distance of 1.5 m) the exponential decrease in production rate with depth can be determined with greater accuracy than by the two-sample method (Hancock et al., 1999; Repka et al., 1997). The multiple-sample method reconstructs the actual decline in sample TCN concentration with depth (Figure 3.9) whereas the two-sample method only allows one to approximate the shape of the exponential decline in production rate with depth. Any violation of the assumptions under which the investigation is carried out (i.e. no surface erosion of the terrace, no post-depositional burial of the terrace, no post-depositional reworking of the terrace, negligible TCN decay) will result in a divergence from the predicted exponential curve (Hancock et al., 1999).

In the case of a denuding terrace, chi-squared inversion techniques can be used to determine the depth profile and the best fit combination of present-day denudation rate and exposure age to explain the TCN content of the sampled terrace material at their respective depths of sampling, assuming the deposit has only undergone one exposure and has not been reworked since deposition (Siame et al., 2004; Carretier et al., 2006; Braucher et al., 2009).

At constant denudation rate, the exposure age and denudation rate of the terrace can be determined from a multiple-sample depth profile due, mainly, to the very different attenuation lengths of neutrons, negative and fast muons (Braucher et al., 2003; Siame et al., 2004; Braucher et al., 2009). Under conditions of steady-state erosion, the nuclide concentration at the surface of a deposit behaves just as in a surface rock sample, equilibrating with the rate of nuclide removal from the system and thus reflecting denudation rates. Production by muons which dominates at depth, however, takes far longer to reach equilibrium due to its much longer attenuation length. The concentration of production at depth due to muons will

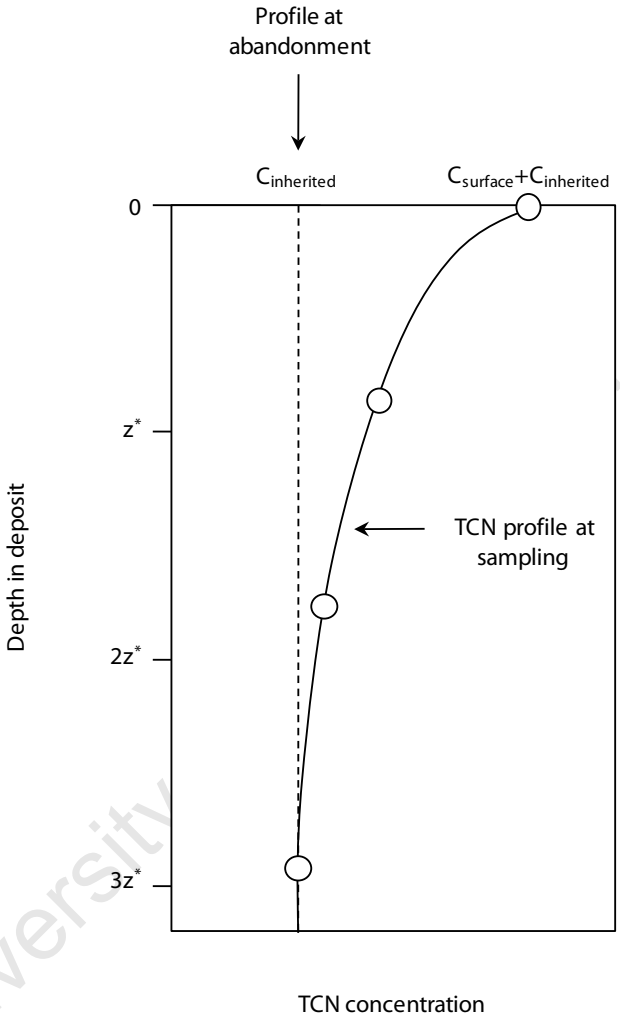

Figure 3.9: A schematic diagram of the depth profile of TCN content within a clastic deposit at two time intervals, namely, at the time of deposition (stippled line) and some time after deposition (solid black line). At the time of deposition the TCN content of the clasts is equivalent to that accumulated during their excavation and transport prior to deposition. After an amount of time, clasts near the surface of the deposit would have accumulated further TCN content, with the rate of accumulation decreasing exponentially with depth in the deposit. At depth, no further accumulation of TCNs occurs as the material is sufficiently shielded by the overlying material. Analyzing amalgamated samples at various depths within the deposit (open circles) allows for the concentration-depth profile of the deposit to be determined.

thus reflect the exposure time of the terrace while the TCN content produced at the surface by spallation has equilibrated to the steady-state erosion rate, thus reflecting the erosion rate of the terrace. The calculation, when solved for conditions of constant denudation rate and constant production rate, taking into account the varying production rates associated with spallogenic, fast muon and slow muon reactions, yields a four-term equation that allows one to account for TCN concentration due to inheritance, spallogenic reactions at surface, slow muon interactions in the deep subsurface, and fast muon interactions in the deepest subsurface. The equations involved are not presented here and the reader is instead directed to Siame et al. (2004) for further information.

Theoretically, in a depth profile which is deep enough for production by muons to be significant, there exists only one exposure time-denudation rate pair which can explain the decrease in ^{10}Be concentration with depth. In practice, sample ^{10}Be concentrations are associated with an uncertainty, thus allowing a narrow range of exposure time-denudation pairs to be applied to the depth profile. The chi-squared inversion model tests for the exposure time-denudation pair which yields the lowest value for the sum of the chi-squared values for each sample depth and concentration. In Equation 3.42, C_i is the analysed ^{10}Be content of a sample at depth z_i and σ_i is its uncertainty, while $C(z_i, \varepsilon, t)$ is the ^{10}Be concentration calculated using for a sample at depth z_i with a given exposure age and denudation rate (Siame et al., 2004; Braucher et al., 2009). The goodness-of-fit of the Chi-squared value is then tested to determine its applicability to the depth profile.

$$\chi^2 \equiv \sum_{i=1}^{n} \left(\frac{C_i - C(z_i, \varepsilon, t)}{\sigma_i} \right)^2 \qquad 3.42$$

For chi-squared inversion modelling of a depth profile, 6 samples are required over a depth of 2 – 4 m (Braucher et al., 2009). With fewer than 6 samples, one may not be able to discern anomalies from the general trend. For old terraces where production of ^{10}Be has equilibrated with removal of ^{10}Be, a 2 m depth profile will suffice. If equilibrium has not yet been reached, however, a depth profile of ~4 m is

sufficient providing that the ^{10}Be concentrations of the samples can be determined with an uncertainty of less than 5%.

3.6 Summary

In situ-produced cosmogenic nuclides are trace amounts of isotopes produced by the interaction of cosmic rays with materials of the Earth's surface. The nuclide of interest in this study is the quartz-hosted radioisotope ^{10}Be. The rate of nuclide production at the surface of the earth is dependent on the intensity of the cosmic ray flux. This, in turn, is affected by the Sun's magnetic field, Earth's magnetic field, variations in these magnetic fields, and particle interactions with materials of the Earth's atmosphere. However, over time periods greater than 10-20 ka, the rate of nuclide production at the surface of the earth varies primarily with altitude and geomagnetic latitude. Higher production rates are found to occur at higher altitudes and latitudes.

The dependence of cosmogenic nuclide production rates on latitude and altitude necessitates the use of an appropriate latitude-altitude scaling regime to determine the rate of nuclide production in a horizontal, unshielded surface at the sampling locality. The scaling regime of choice in this study is that of Dunai (2000). Shielding factors are used to account for the effects of topographic shielding, self-shielding and shielding by burial on production rates at individual sample sites.

At its very simplest, cosmogenic nuclide analysis requires an accurate knowledge of the nuclide production rate at the sampling locality, as well as the sample nuclide concentration. These two quantities allow one to constrain the exposure ages and denudation rates of a variety of geomorphic features. This study applies three sampling techniques to a study of the coastal Cape Mountains, namely bedrock sampling, river sediment sampling and alluvial terrace depth profiling, which take advantage of this simple principle to place quantitative constraints on the denudational processes operating within the mountains.

Chapter 4:

Study Area

4.1 Introduction

Chapter 4 presents an outline of the rationale for the selection of study area in Section 4.2, and proceeds in Section 4.3 with an overview of the geology, geomorphology, climate, soils and vegetation of the region. The specifics of sample sites are dealt with under Section 4.4, which is in turn followed by the chapter summery of Section 4.5.

4.2 Rationale for the selection of study area

Previous studies have shown that the rates at which landscapes denude correlate with tectonic setting, climate and lithological strength on the hillslope scale (Chapter 2). As this study uses denudation rates as a proxy for tectonic activity to investigate the geomorphic evolution of the South African coastal hinterland, the study area was selected with the aim of minimising variation in both climate and lithology. Doing so facilitates the interpretation of the data by eliminating noise that might be introduced by variations in lithology and climatic conditions within the study area. This allows one to infer a tectonic control on geomorphic processes, should denudation rates be comparable to those of tectonically active ranges elsewhere in the world. Conversely, denudation rates that are low compared to what is expected for the steep topography of the coastal Cape Mountains would imply that the present-day steep topography is unrelated to neotectonics and thus likely the result of either climate or lithology in the area (Chapter 2).

The potential accelerating influence that a warm, wet climate may have on erosion rates was reduced by limiting the study to the coastal Cape Mountains of

the Western Cape. In contrast to the hot and humid Eastern Cape, the cooler, drier climatic conditions of the Western Cape are less likely to give rise to elevated rates of denudation (Chapter 2). Within the Western Cape, study was confined to the W-E oriented ranges flanking the south coast some 50 km inland from the sea, to the exclusion of the N-S oriented ranges of the west coast. Those mountains paralleling the Atlantic seaboard are subject to highly seasonal rainfall with a precipitation-high in winter, in contrast to the year-round precipitation experienced along the south coast. As seasonality is argued to be an influential factor in determining denudation rates (Chapter 2), an attempt was made to eliminate this potential complicating climatic influence by restricting sampling to the non-seasonal coastal ranges of the south. Under these conditions, one can assume that any high rates which the data may present are not likely to be strongly influenced by climatic conditions.

Within this region, the Langeberg and Swartberg Ranges - whose highest peaks stand 1710 m and 2325 m above sea level, respectively - were chosen as easily accessible representatives of the fold belt (Figure 4.1). These ranges are subject to similar rainfall and temperature conditions as affect the southern limb of the western coastal Cape Mountains at large, while the coast-parallel strike of lithologies and repetition of lithological units due to thrust-stacking and folding result in the exposure of identical lithological units in both mountain ranges (Chapter 1). These units are not only continuous along strike within the Langeberg and Swartberg mountains but also throughout most of the western and eastern coastal Cape Mountains. They are thus considered characteristic rock types of this mountain belt.

Three factors were considered when selecting sampling sites within the study area:

Catchment lithologies — The coastal Cape Mountains and its intermontane valleys are comprised of the siliciclastic Cape Supergroup rocks with quartzites and sandstones dominating the high-relief areas of interest to this study, while siltstones and shales lie in the intermontane valleys (Chapter 1). Due to the natural distribution of rock types, quartzite and sandstone were sampled within the mountain ranges. Given the potential influence of lithology on erosion rates, with less

competent rocks often reported to erode faster than more competent rocks of the same area (Chapter 2), rivers draining similar lithological units were sampled. This was easily accomplished due to tectonic-induced repetition of units throughout the mountain belt. Sediment was sampled where the rivers exited the mountains, rather than in the floodplains, to avoid sampling sands which have had their quartz content diluted by the addition of shaley clasts and muddy material. Sampling of diluted material would require the collection of a much larger sample, creating logistical difficulties in the field.

River profiles — All rivers sampled were of the short, steeply-incised, linear nature that is characteristic of the Cape Mountains. Rivers that breeched the mountains were largely avoided, as they traverse a wide variety of lithologies outside of the coastal Cape Mountains and it was not known how sediment carried from these outer regions would affect the analysis. This sampling prerequisite was waved in the case of Tradouw River, which provided the unique opportunity of sampling river sediment, alluvial terraces, bedrock benches in the modern day river and bedrock from interfluves; as well as in the case of Seven Weeks River.

Spatial spread of data — Catchments were sampled throughout the Langeberg and Swartberg Ranges so as to provide a fair reflection of erosion rates within the western sector of the southern limb of the coastal Cape Mountains. The final selection of catchments was, however, a compromise between even-distribution and accessibility in the field.

Of the ten rivers sampled, focus was given to Tradouw River along whose course fluvial terraces and benches are preserved. The river winds its way through the canyon of Tradouw Pass where fluvial benches lie exposed in the present-day river channel, a plethora of percussion marks across their surface. Above the river channel on the interfluvial slopes, exposed bedrock provides an excellent sampling opportunity. Upon exiting the Pass to the south, the river flows past remnants of associated pebbly alluvial terraces. Two of these terraces were accessible for profile-sampling; one exposed as a road cutting at the entrance to the Pass and the

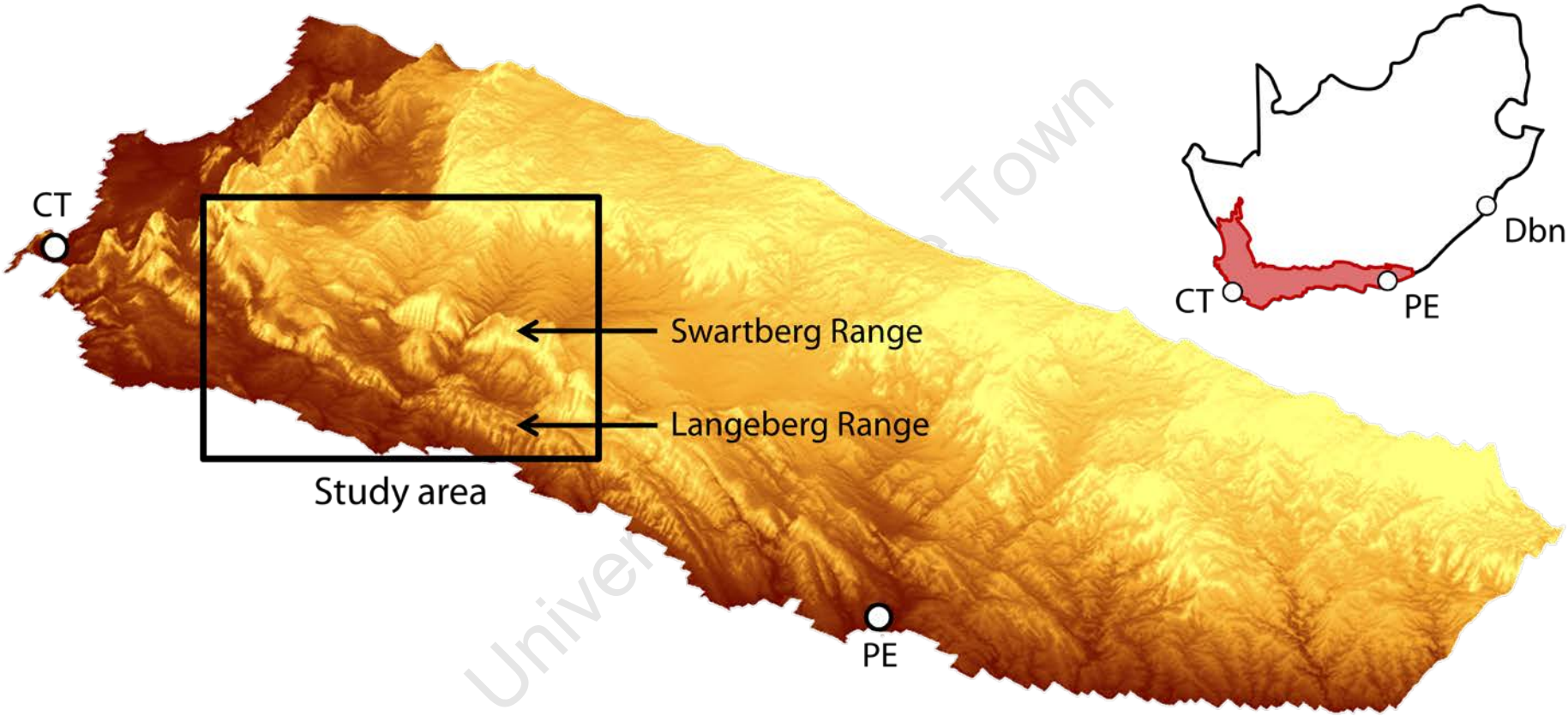

Figure 4.1: Study area within the western sector of the southern coastal Cape Mountains. This study is confined to the Langeberg and Swartberg Ranges. This image was constructed using the SRTM 90 m resolution digital elevation model sourced from the AEON database.

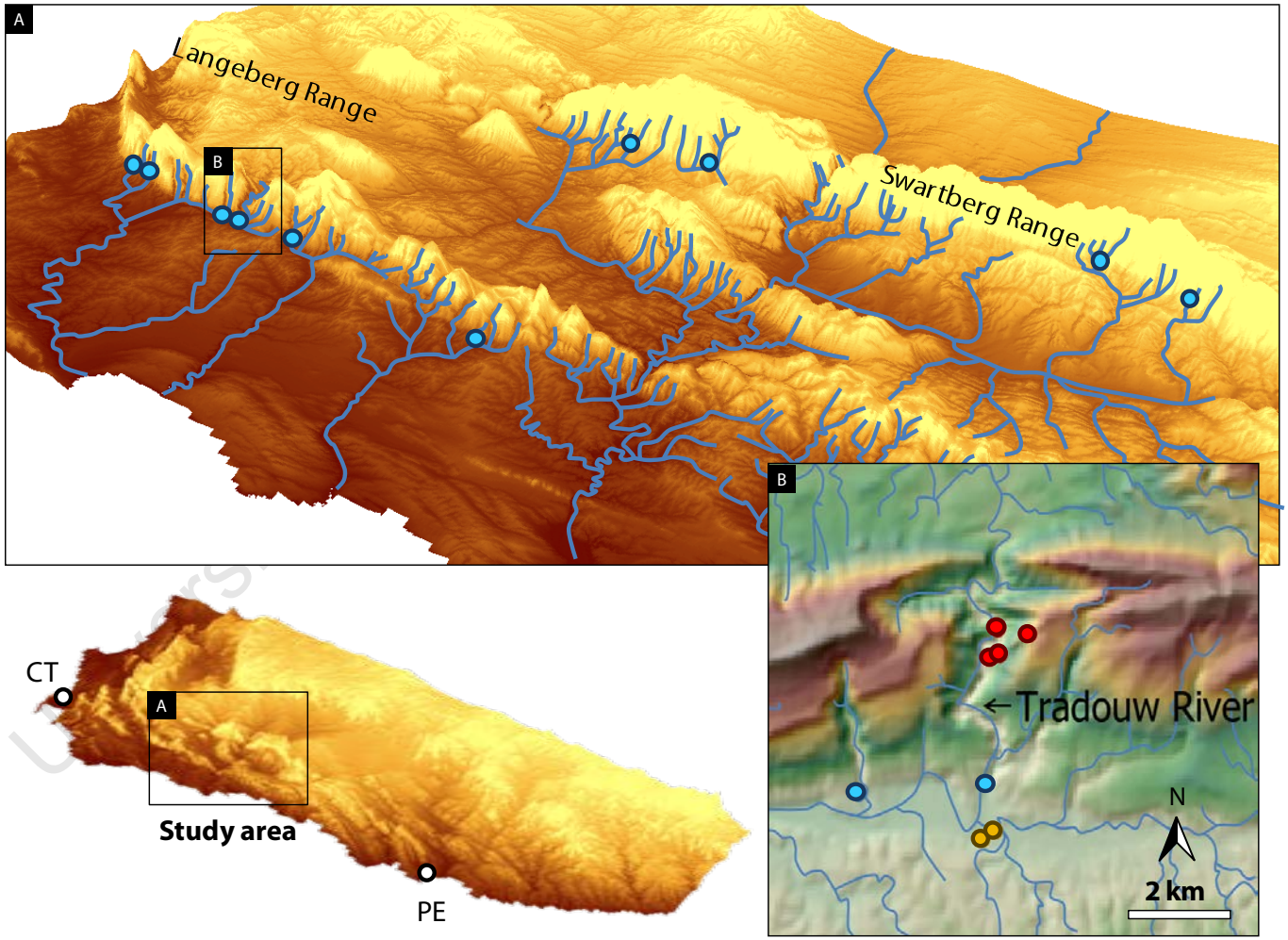

Figure 4.2: Sampling points within the study area. Insert shows the location of the study area within the coastal Cape Mountains enclosed in box A (cf. Figure 4.1). All figures were constructed using the SRTM 90 m resolution digital elevation model, sourced from the AEON database.

Figure 4.2A: The distribution of river catchments sampled (blue points) within the Langeberg and Swartberg Ranges which enclose the Little Karoo intermontane basin. Tradouw River Canyon is enclosed in box B, and shown enlarged in Figure B.

Figure 4.2B: An enlargement of box B seen in Figure 4.2A. This image shows the distribution of bedrock sampling sites (red points) and alluvial terrace sampling sites (yellow points) in the vicinity of Tradouw River Canyon.

other as a vertical wall along the banks of the river. In the case of the river cutting, organic matter overlying the river terrace material provided an opportunity for radiocarbon dating. Tradouw River thus provides the unique opportunity of using four sampling techniques; namely river sediment, bedrock samples and depth profile samples, and radiocarbon sampling, to investigate the geomorphic evolution of the area.

Based on the above, a field area of some 30 000 km^2 spanning the magisterial districts of Swellendam, Riversdale, Ladysmith, Caltizdorp and Oudtshoorn, was defined. Within this area, ten rivers were sampled of their sediment, while bedrock was collected from two fluvial benches and three outcrops along interfluvial slopes (Figure 4.2). Pebbles were collected from two depositional terraces, with a sum total of seven samples removed from the profiles. In the case of the river-cut terrace, three radiocarbon samples were collected from the overlying muddy silts.

4.3 Field setting

4.3.1 Geology

The Cape Supergroup is subdivided into the Table Mountain, Bokkeveld and Witteberg Groups, of which only the Table Mountain and Bokkeveld Groups outcrop in the studied river catchments. The arenaceous Table Mountain Group consists largely of metasandstones and quartzites, while the argillaceous Bokkeveld Group comprises cyclic alternations of mudrock, siltstone and fine-grained sandstone (Newton et al., 2006; Kent, 1980). Resistant sandstones and quartzites of the Table Mountain Group often form the high-lying peaks of the mountains which rise up approximately 1–2 km above sea level, while the Bokkeveld shales and sandstones form low-relief foothills and intermontane basins which sit approximately 300–500 m above sea level.

High relief and steep slopes characterise the coastal Cape Mountains and contrast it with the surrounding low-lying coastal hinterland. Both relief and elevation increase to the west with peaks reaching a maximum elevation of 2325 m in Seven Weeks Pass (Stankiewicz and De Wit, 2005). The mountain slopes are marked by short, deeply-incised valleys drained by underfit and occasionally,

ephemeral rivers. In places, the larger of these rivers have breached the mountains while maintaining their coastward flow at right angles to both the structural fabric of the rock and the strike of the mountain belt (Stankiewicz and De Wit, 2005; Stankiewicz and De Wit, 2008; Chapter 1).

4.3.2 Climate, soils and vegetation

Two climatic regimes occur within the study area, namely that of the Langeberg Range and adjacent coastal plain to its south, and that of the intermontane Little Karoo basin and Swartberg Range to its north (Schulze, 1994; Taljaard, 1996a and 1996b).

The Langeberg-coast region lacks seasonal rainfall and is instead characterised by gentle fluctuations in the annual rainfall pattern that give rise to maxima during the months of November and March and minima during the months of December and June. So mild are these fluctuations that they rarely deviate more than 10% from the norm. A similar rainfall regime characterises the Swartberg-Little Karoo region, with the exception that the temporal fluctuations in annual rainfall are more pronounced. Maxima occur in November and March and minima in the December-January and June-August periods. (Schulze, 1994; Taljaard, 1996b)

In both regions the distribution of precipitation is largely dictated by orographic barriers. The Langeberg-coast zone sees an increase in mean annual precipitation from ~400-500 mm in the low-lying coastal plain to over 1100 mm along the south-facing slopes of the Langeberg Range. Further north, in the rain shadow of the Langeberg Range, the semi-arid to arid Little Karoo basin experiences annual precipitation values that barely exceed 250 mm. The rising slopes of the Swartberg mountains to its north, however, herald an increase in rainfall, with these south-facing slopes experiencing mean precipitation values in excess of 750 mm. (Schulze, 1994; Taljaard, 1996b)

The Langeberg-coast zone experiences an average of 8–10 rain days per month. Precipitation commonly takes the form of drizzle and light showers, though up to 10 thunderstorms occur per year. Hail is an uncommon form of precipitation that occurs on average 0.5–1 days per year, while frost barely affects the region at all. Snow is restricted to the peaks of the Langeberg Range where it can be spotted up

to twice a year during the winter and spring seasons (Schulze, 1994; Taljaard, 1996b).

Juxtaposing the comparatively wet Langeberg-coast zone is the drier Swartberg-Little Karoo zone where only 1-3 rain days per month are expected in the mountains. Thunderstorms are more common in this region, with 10–20 storm events affecting the Little Karoo per year. Hail, frost and snow likewise occur more frequently in this region. While hail can still be considered a rare phenomenon, frost is expected between the months of June and August. Snow occurs solely within the Swartberg mountains where it may blanket the peaks up to 5 times a year (Schulze, 1994).

Temperatures within the Langeberg-coast region are mild to hot, with mean maximum monthly temperatures ranging from 26°C in January to 19°C in July. The corresponding minima are 15°C and 7°C, respectively. The Swartberg-Little Karoo region is characterised by large temperature fluctuations, both on a seasonal and on a daily basis. Mean maximum monthly temperatures decrease from 32°C in January to 18°C in June, while the corresponding minima decrease from 15°C to 5°C (Schulze, 1994).

Throughout the study area vegetation patterns mirror rainfall, with south-facing slopes densely populated by fynbos while north-facing slopes are host to grasses and sparse shrubbery. Natural woodlands populate valleys and, in designated conservation areas, the south-facing slopes of the ranges. The open basins of the Little Karoo are host to succulents and hardy shrubbery adapted to the low rainfall conditions. Soils of the coastal Cape Mountains are sandy, shallow and infertile in the high mountains where metasandstones and quartzites of the Table Mountain and Witteberg Groups form the underlying bedrock (Fey, 2010). Foothills, however, are mantled by colluvial soils which tend to greater thickness and fertility than the thin mountain soils (Fey, 2010).

4.4 Sample Sites

4.4.1 River sediment samples

Sample sites were identified with the aid of 1:50 000 and 1:250 000 topographic and 1:250 000 geologic maps of the Riversdale, Ladismith and Oudtshoorn areas. Of the ten rivers selected, six drain the Langeberg Range and four, the Swartberg Range (Figure 4.3).

Bare bedrock channels predominate in the mountains and gravelly, boulder-filled bedrock channels are characteristic of the foothills. Sandy-banked alluvial channels meander through the floodplains and here too, riverbeds are characteristically gravelly and host to pebbles and boulders. The bedload derives from quartz veins, quartzites, sandstones, siltstones and shale units forming the bounding hillslopes of the river valleys. River gravel is typically representative of all lithologies in a catchment and comprises subangular to angular clasts whose sizes range from millimetres to centimetres in diameter. Pebbles are subangular to angular discs that, like the well-rounded boulders, consist of sandstone or quartzite whose surface is littered with percussion marks. Individual sampling sites are described in Table 4.1 and Table 4.2A, B and C.

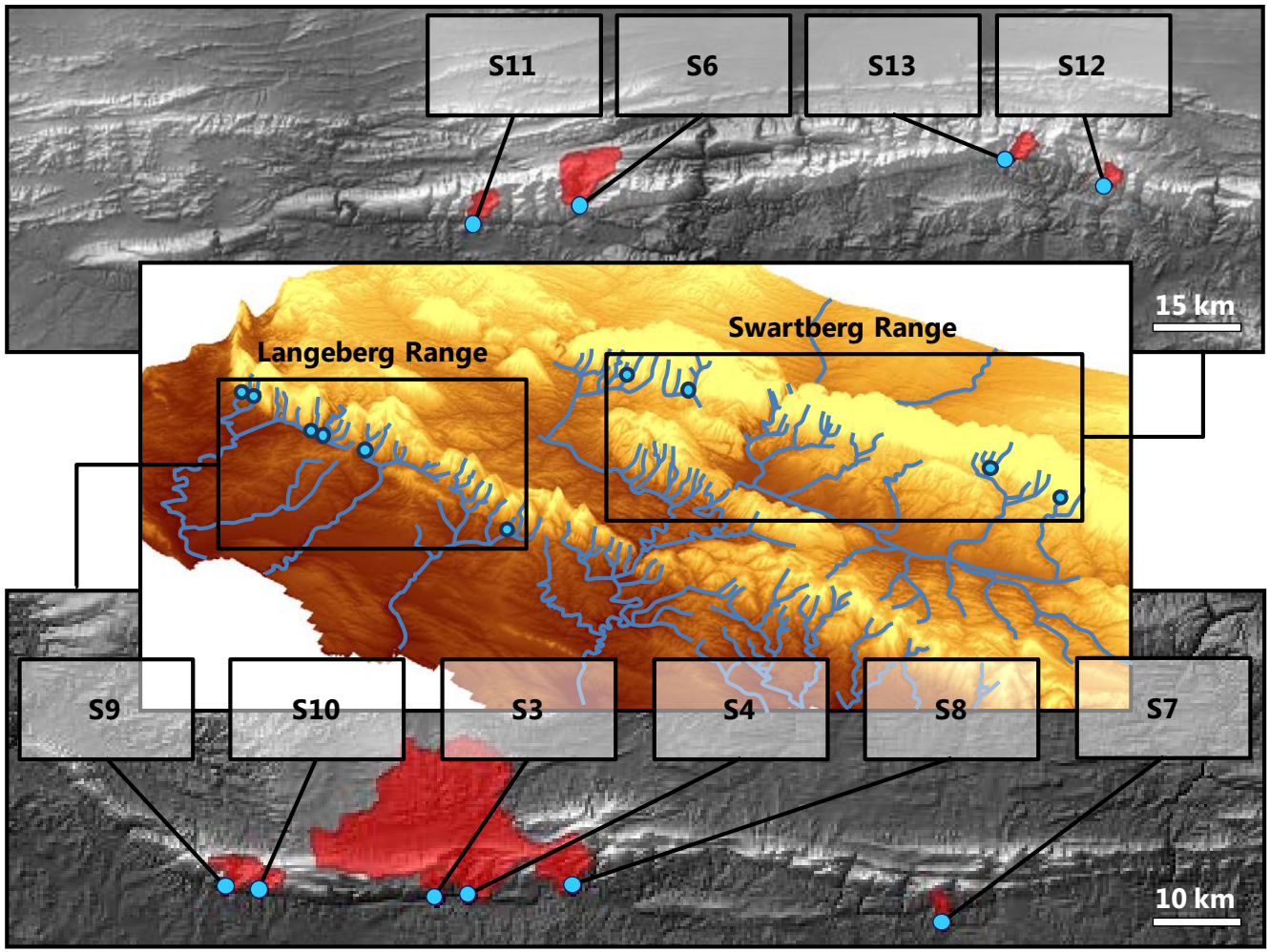

Figure 4.3: River sediment sample sites across the Langeberg and Swartberg Ranges of the coastal Cape Mountains. River catchments are represented by red polygons. Sample points are represented by blue circles.

Table 4.1: River sediment sampling sites.

Sample ID	Lat. (deg.)	Long. (deg.)	Elev. (masl)	River Name	Gorge Name
S3	-33.99541	20.66277	119	Unnamed river,	unnamed gorge
S4	-33.99296	20.70459	129	Tradouw River,	Tradouw Pass
S6	-33.43325	21.40669	619	Seven Weeks River,	Seven Weeks Pass
S7	-34.02089	21.35044	194	unamed river,	Tierkloof
S8	-33.98339	20.84508	247	Duiwenshoksrivier,	unamed gorge
S9	-33.98122	20.37606	211	Keurboomsrivier,	Wolfkloof
S10	-33.98514	20.42211	230	Kliprivier,	unamed gorge
S11	-33.46236	21.215	529	Buffleskloofrivier,	Buffelskloof
S12	-33.39631	22.357	747	Tributary of the Groot Rivier,	unnamed gorge
S13	-33.35956	22.179	737	Hoeksrivier,	Grootkloof

Table 4.2A: Physical description of sample sites. Table continued overleaf.

Sample ID	Site Description
S3	Sediment-poor, gravel-rich bedrock river sampled between quartzite cliffs. Gravel bars occur intermittently along the walls of the gorge. Bedload material comprises sandstone, quartzite and vein quartz clasts ranging in size from gravel to large boulders over a meter in diameter. River sediment is quartz-rich. Catchment is underlain by rocks of the Table Mountain Group (Peninsula, Cedarberg, Goudini and Pakhuis Formations). See Figure 4.4.
S4	Gravelly river bed with sandy, heavily vegetated banks. Bedload material comprises sandstone, quartzite and vein quartz clasts, usually in the form of pebbles a few centimetres in diameter. Gravelly sand bars occur throughout the river. River sediment is quartz-rich. Catchment overlies the Table Mountain Group (Peninsula, Cedarberg, Pakhuis, Goudini, Skurweberg and Rietvlei Formations) and the Bokkeveld Group (Gydo, Voorstehoek, Hex River, Tra-Tra, Boplaas, Waboomberg and Adolphspoort Formations). See Figure 4.5.
S6	Sediment-poor, shallow stream, sampled between quartzite cliffs. The river bed is heavily armoured with discoid, subangular to subrounded pebbles of quartzitic sandstone and occasionally greywacke that occur in a variety of sizes, as well as grit. River banks are notably sandier though still gritty, and heavily vegetated. River sediment is quartz-rich. Catchment overlies the Table Mountain Group (Peninsula, Cedarberg, Pakhuis, Goudini, Skurweberg, and Rietvlei Formations) and the Bokkeveld Group (Gydo, Gamka and Voorstehoek Formations). See Figure 4.6.

Table 4.2B: Physical description of sample sites continued from Table 4.2A. Table continued overleaf.

Sample ID	Site Description
S7	Pebbly, gravel-laden river bed, ~2 m wide. Bedload comprises quartzite, vein quartz, shale and siltstone clasts of various sizes and similar in dimensions to that seen in previous rivers. Gravel clasts are angular to subangular, while boulders are subrounded. Muddy river banks ~3 m high exhibit internal stratification as shown by horizontal pebbly layers within the mud. Close inspection shows these dark muds to be filled with quartz sand grains. The abnormally sandy nature of this river in comparison to others in the region, together with evidence for undercutting along the banks, suggest that a fair amount of sediment and gravel found in the river is likely reworked material sourced from the muddy river banks. River catchment overlies the Table Mountain Group (Peninsula Formation), Bokkeveld Group (Boplaas Formation), and coastal deposits (Uitenhage Group, Kirkwood Formation). See Figure 4.7.
S8	The river is dominated by pebble and gravel clasts of various sizes. Bedload material comprises sandstone, quartzite, vein quartz and minor amounts of mudrock. Gravel clasts are angular to subangular, while pebbles are angular to subrounded. River sediment is quartz-rich. Banks are ill-defined, broad, gravel and pebble-rich deposits. The sample site lies within a steep gorge whose cliff-tops are heavily vegetated. Catchment overlies the Table Mountain Group (Peninsula, Cedarberg, Pakhuis and Goudini Formations), Bokkeveld Group (Gydo Formation) and the Grahamstown silcrete Formation. See Figure 4.8.
S9	Pebble- and gravel-laden bedrock river located between quartzite cliffs. Sediment is quartz-rich and scarce. Catchment overlies the Table Mountain Group (Peninsula, Cedarberg, Pakhuis, Goudini and Skurweberg Formations). See Figure 4.9.

Table 4.2C: Physical description of sample sites continued from Table 4.2B.

Sample ID	Site Description
S10	Sediment-poor bedrock river located between heavily vegetated quartzite cliffs. Bedload comprises sandstone, quartzite, vein quartz and shale clasts which take the form of pebbly and gravelly deposits both on the banks and within the river bed where it occurs alongside large boulders. Quartz-rich river sediment was sifted out from amongst the gravel deposits within the river. Catchment overlies the Table Mountain Group (Peninsula, Cedarberg, Pakhuis, Goudini and Skurweberg Formations). See Figure 4.10.
S11	Shallow, pebble- and gravel-filled dry river bed. The majority of clasts consist of quartzitic sandstone with a smaller fraction comprised of pink feldspathic sandstone. Low trees and shrubs line the flat, poorly developed banks. Catchment overlies the Table Mountain Group (Peninsula, Goudini, Cedarberg, Pakhuis, Skurweberg and Rietvlei Formations) and Witteberg Group (Wagendrift Formation). See Figure 4.11.
S12	River sediment was sifted out from amongst the pebbles and gravels filling a broad, deep rock pool located at the foot of Rust and Vrede waterfall. River sediment is quartz-rich and abundant in comparison to the majority of sampling sites. Catchment overlies the Table Mountain Group (Peninsula Formation) and Kango Group, (Groenefontein Formation). See Figure 4.12.
S13	Bedrock river whose bedload comprises quartz-rich sediment, gravel clasts and pebbles of predominantly sandstone, but also quartzite and vein quartz. Catchment overlies the Table Mountain Group (Peninsula, Cedarberg, Pakhauis and Skurweberg Formations) and Kango Group (Groenefontein Formation). See Figure 4.13.

Figure 4.4: Sample site S3. Backpack for scale, ~60 cm high.

Figure 4.5: Sample site S4.

Figure 4.6: Sample site S6. This photo is courtesy of Dr. Samuel Niedermann (GFZ-Potsdam).

Figure 4.7: Sample site S7. Spade for scale, ~1.3 m in length.

Figure 4.8: Sample site S8. Spade for scale, ~ 1.3 m in length.

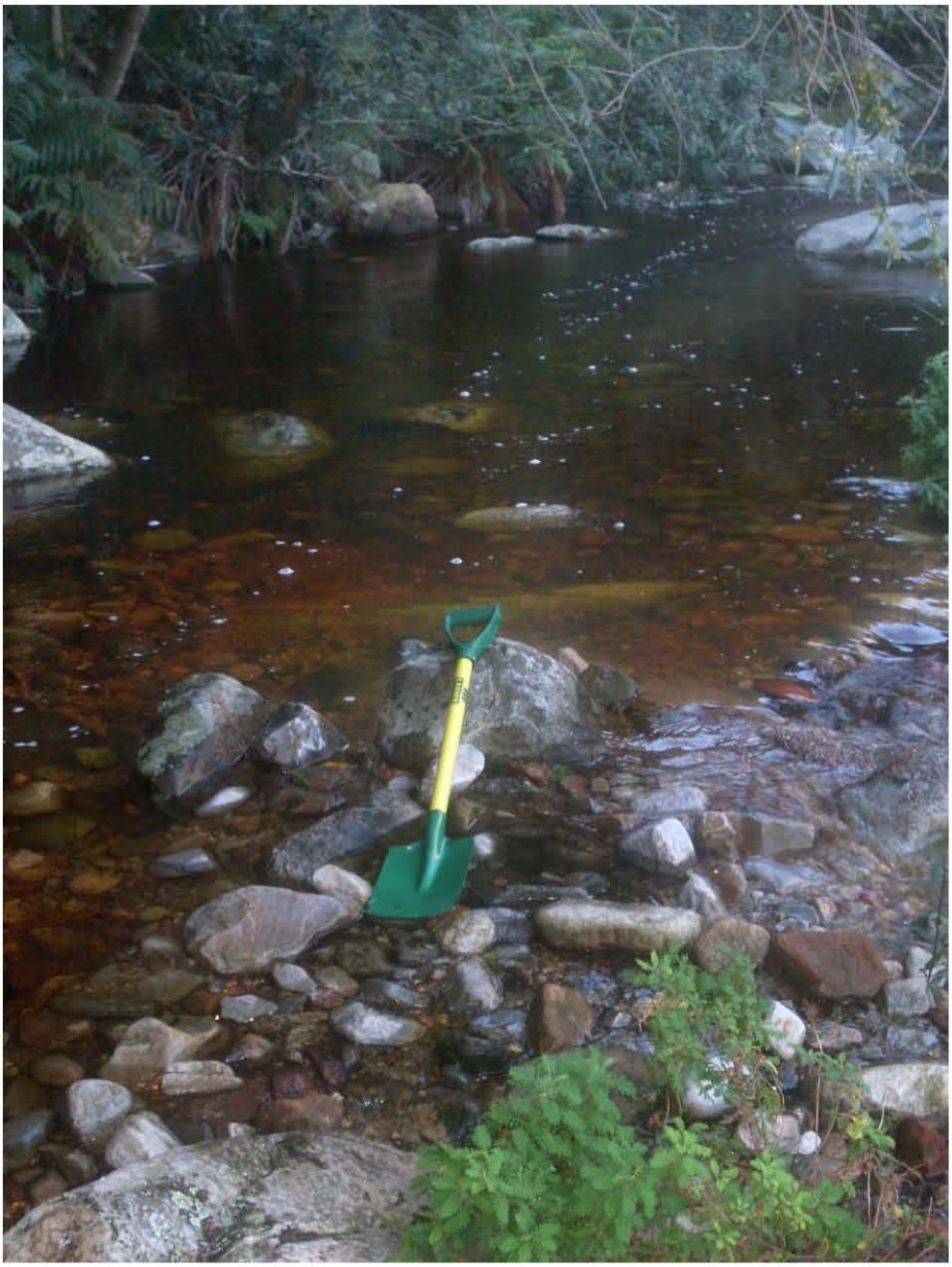

Figure 4.9: Sample site S9. Spade for scale, ~1.3 m in length.

Figure 4.10: Sample site S10. Spade for scale, ~1.3 m in length.

Figure 4.11: Sample site S11. Spade for scale, ~1.3 m in length.

Figure 4.12: Sample site S12. Spade for scale, ~1.3 m in length.

Figure 4.13: Sample site S13. Spade for scale, ~1.3 m in length.

4.4.2 Bedrock samples

Bedrock samples were collected along Tradouw Pass, from the Tradouw River channel and the interfluvial slopes above (Table 4.3 and Figure 4.14).

Within the channel, two bedrock ledges with a vertical separation of 5.5 m were sampled out of a series of four, just above the present-day water-level (Figure 4.15). These ledges are near-horizontal, in accordance with the local bedding orientation, and comprised of the particularly robust quartzitic sandstone belonging to the Peninsula Formation, Table Mountain Group, with quartz veins cross-cutting their surfaces. Percussion marks were visible on all benches, well-pronounced on the lower-most bench and becoming progressively fainter on the above-lying surfaces. The presence of these percussion marks was interpreted to indicate that minimal denudation has affected the surfaces since their formation.

Overlooking Tradouw River are heavily vegetated spurs which exhibit graded concave-upwards profiles or stepped profiles. The sampled surfaces follow the local dip of bedding which is to the south. Atop these spurs, the bedrock outcrops are few and far between and exhibit extensive jointing and fragmentation. Clear signs of surface lowering by means of both spallation and incremental down-wearing are present. In places these outcrops are saprolitic, their rot attributed to the retention of water by the dense vegetation that in places covers these platforms.

Table 4.3: Locations and lithologies of bedrock samples.

Sample ID	Lat. (deg.)	Long. (deg.)	Elev. (masl)	Lithology sampled
S5.1	-33.95593	20.70795	232.00	Quartzite of the Peninsula Formation and vein quartz.
S5.2	-33.95593	20.70809	226.50	Quartzite of the Peninsula Formation and vein quartz.
S15	-33.96211	20.70775	489.00	Quartzite of the Peninsula Formation.
S17	-33.95719	20.71817	811.00	Quartzite of the Peninsula Formation.
S18	-33.95706	20.71817	815.00	Quartzite of the Peninsula Formation.

The tops of the spurs are littered with rock spall: typically blocky fragments ranging from a few centimetres to nearly a meter along their long axis. Four bedrock samples were collected from one such spur with a stepped profile, in order to constrain erosion rates within the interfluvial slopes (Figure 4.16 and Figure 4.17)

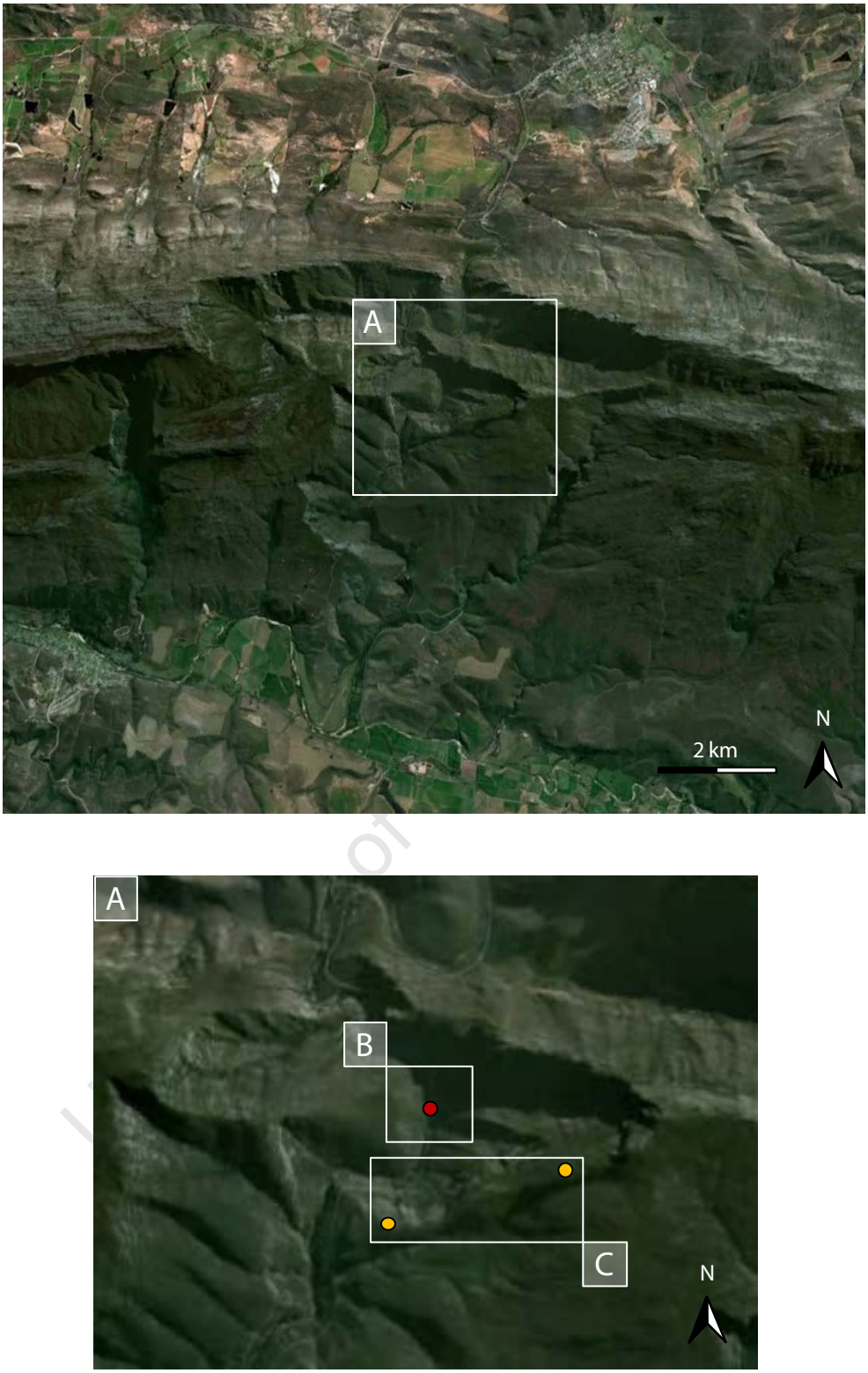

Figure 4.14: Top image: Areal view of Tradouw Pass, within the Langeberg Range of the coastal Cape Mountains. Enlargement A shows the apex of the Langeberg Range with the location of bedrock sampling points S5.1 and S5.2 at the base of the canyon (red point) and bedrock sampling points S15, S17 and S18 on the interfluves (yellow points). Box B shows the location of Figure 4.15 and box C shows the location of Figure 4.16. The background satellite images were captured from Google Earth.

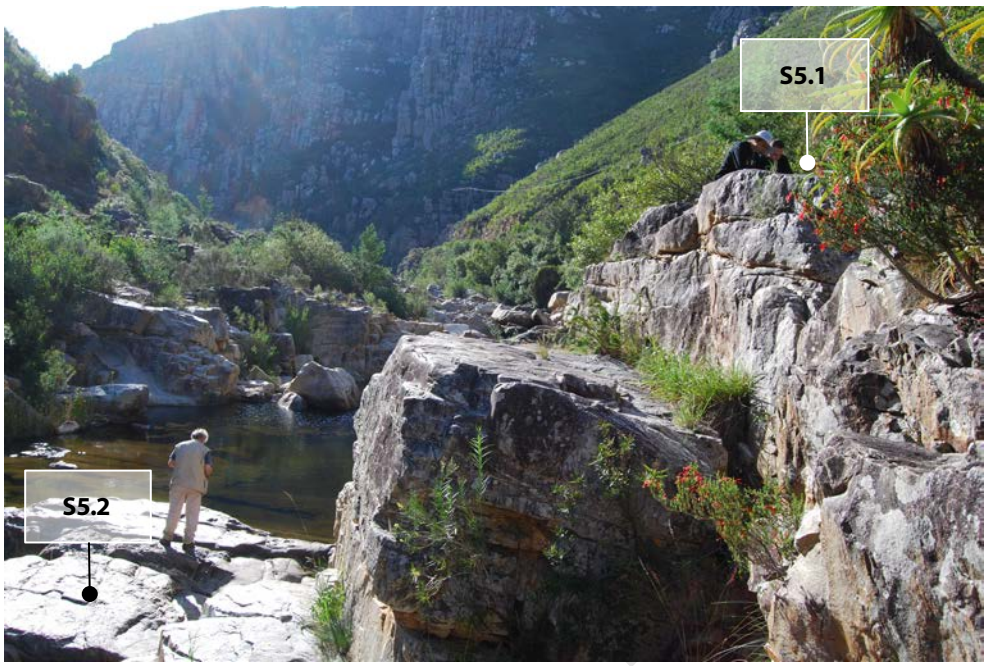

Figure 4.15: Bedrock benches S5.1 and S5.2 at the base of Tradouw River Canyon. The view is to the north. This photo is courtesy of Dr. Samuel Niedermann (GFZ-Potsdam).

Figure 4.16: A stepped spur in Tradouw Canyon, where samples S15, S17 and S18 were taken. The view is to the north. This photo is courtesy of Dr. Samuel Niedermann (GFZ-Potsdam).

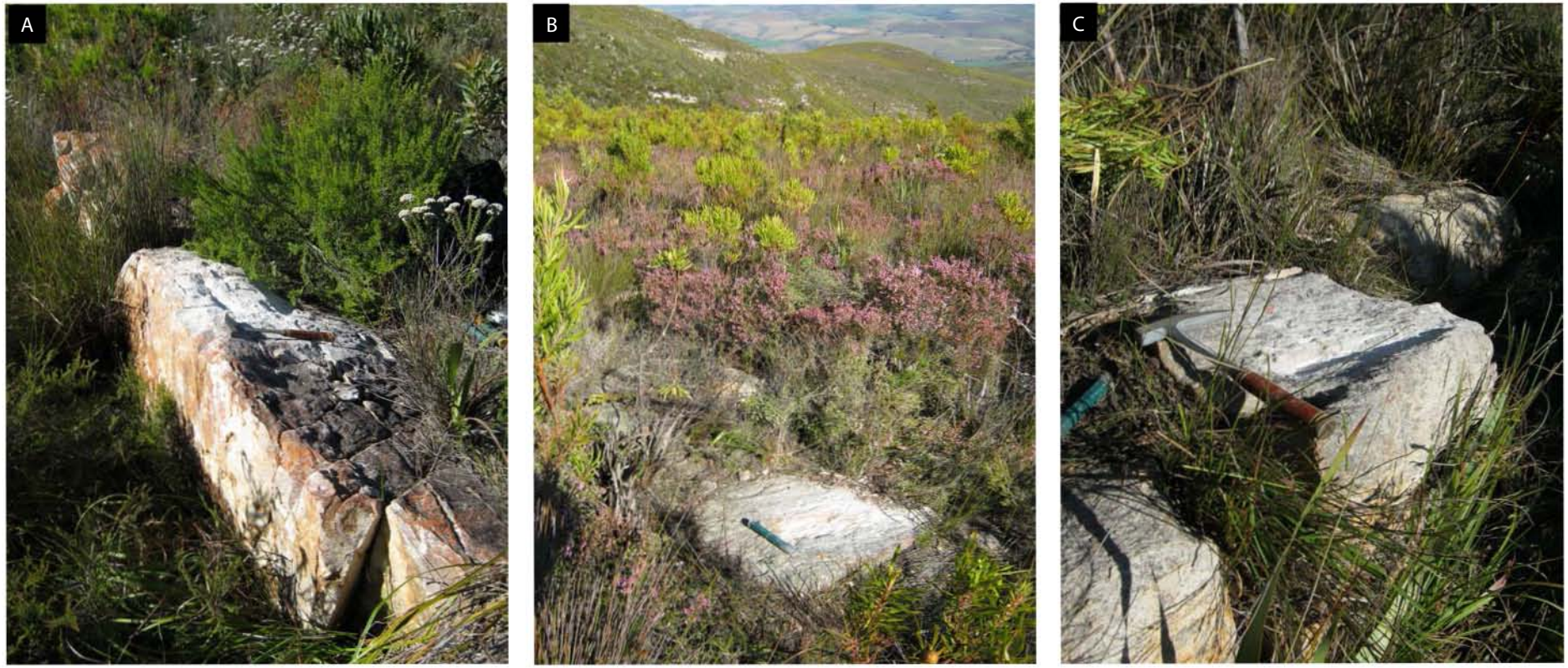

Figure 4.17: Sampled bedrock outcrops on the interfluves, S15 (A), S17 (B) and S18 (C). Geological hammer (~40 cm) and chisel (~17 cm) for scale.

4.4.3 Alluvial terrace and radiocarbon samples

Two alluvial terraces were sampled at the base of Tradouw Pass, where they lie exposed in road and river cuttings (Table 4.4 and Figure 1.18). These are moderately to poorly sorted, weakly stratified terraces of imbricate pebbles in a gritty matrix. Pebbles and grit are similar in size, shape and lithology to that found in the present-day river channels. Along the fresh road cutting, the exposed face of terrace S2 exceeds 4 m in depth and is overlain by 60 cm of soil (Figure 4.19 and Figure 4.20). 4 m is considered a suitable depth to accurately constrain the exposure age and denudation rate of a terrace by means of depth profiling (Braucher et al., 2009; Chapter 3). This terrace may have been related to either the Tradouw River or the Grootvarderbos River, as it lies near the junction between the two. Along Tradouw River, terrace S1 is exposed to a depth of 1.3 m and overlain by 3.8 m of sand and mud (Figure 4.21). While 1.3 m is less than the desired depth for depth profile sampling, it may be sufficient if the terrace is old enough for TCN concentrations to have reached steady state or if post-depositional erosion rates affecting the terrace were high enough to allow steady state to be reached prior to burial (Braucher et al., 2009; Chapter 3). Three samples of carbon-rich material (possibly charcoal) were removed from the overlying muds for radiocarbon dating (Table 4.5).

Table 4.4: Location of alluvial terrace samples.

Sample ID	Lat. (deg.)	Long. (deg.)	Elev. (masl)	Locality	Sampling depth (m)
S1.2	-34.00639	20.70333	122	River cutting	3.82 - 3.92
S1.3	-34.00639	20.70333	122	River cutting	4.02 - 4.12
S1.4	-34.00639	20.70333	122	River cutting	4.32 - 4.42
S1.5	-34.00639	20.70333	122	River cutting	4.82 - 5.02
S2.3	-34.00458	20.70661	135	Road cutting	0.6 - 0.75
S2.2	-34.00458	20.70661	135	Road cutting	2.94 - 3.04
S2.1	-34.00458	20.70661	135	Road cutting	3.58 - 3.78

Table 4.5: Location of radiocarbon samples.

Sample ID	Lat. (deg.)	Long. (deg.)	Elev. (masl)	Locality	Burial depth (m)
R1.1	-34.00639	20.70333	3.82	Overlying S1	3.82
R1.2	-34.00639	20.70333	3.02	Overlying S1	3.02
R1.3	-34.00639	20.70333	1.72	Overlying S1	1.72

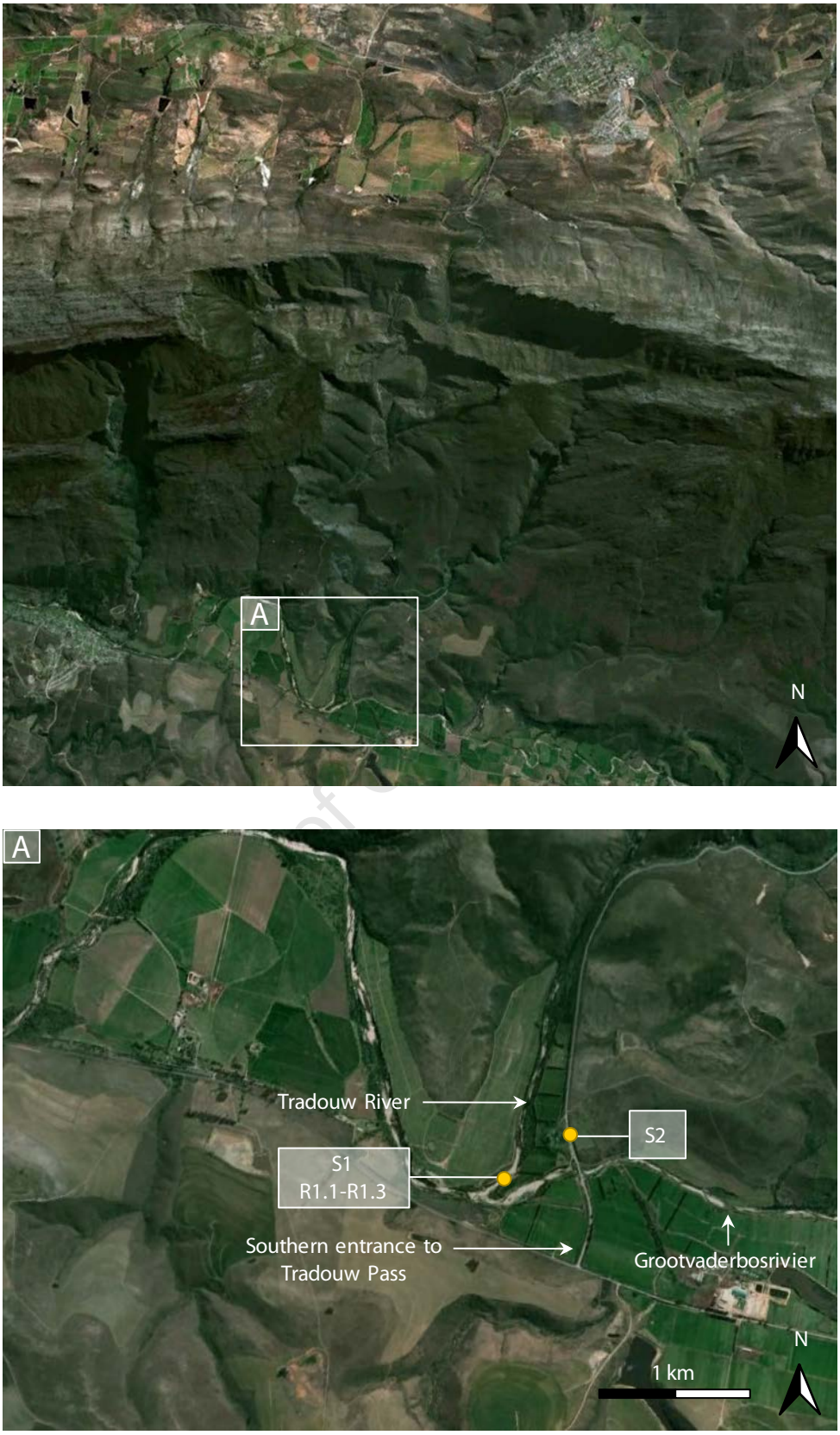

Figure 4.18: Location of alluvial terrace sampling sites at the southern foot of the Langeberg Range. Background satellite images were captured from Google Earth.

Figure 4.19: Terrace S2, exposed in a road cutting at the entrance to Tradouw Pass. The view is towards the north-east. The white box is shown enlarged in Figure 4.20. This photo is courtesy of Dr. Samuel Niedermann (GFZ-Potsdam).

Figure 4.20: An enlargement of Figure 4.19. Terrace S2 exposed along a road cutting. The terrace comprises weakly stratified pebbles and boulders and is overlain by 60 cm soil.

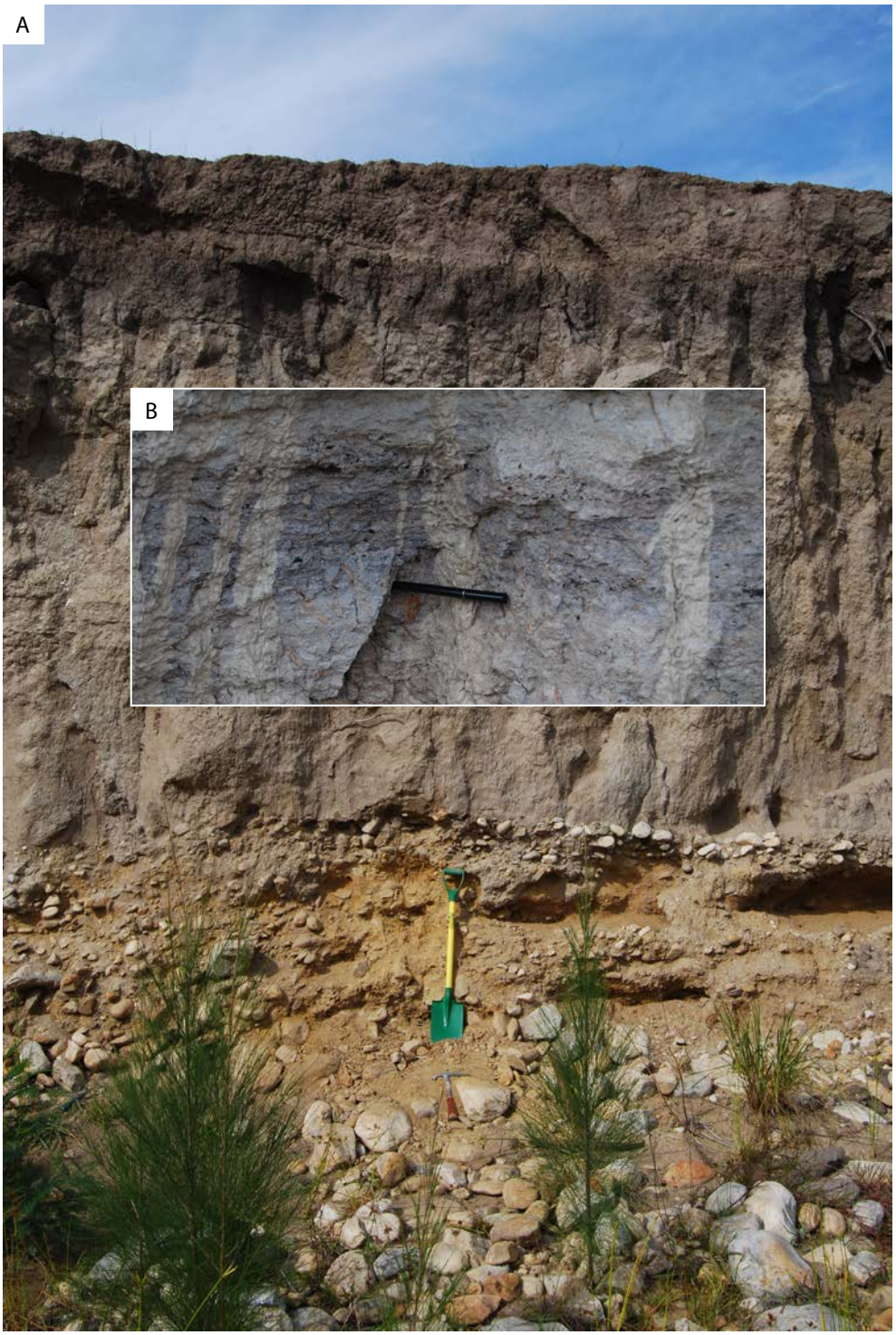

Figure 4.21: Terrace S1, exposed in a river cutting (A). The terrace is overlain by a 4 m mud deposit from which organic matter (possibly charcoal) was sampled for radiocarbon dating. Insert B shows an enlargement of this mud as it occurs overlying the pebbly terrace, in which the dark organic matter is visible. Photo A is courtesy of Dr. Samuel Niedermann (GFZ-Potsdam) and photo B courtesy of Prof. de Wit (NMMU).

4.5 Summary

Parallel to the southern coast of the Western Cape, the Langeberg and Swartberg Ranges are representative of the southern coastal Cape Mountains with respects to lithology and topography and form the sampling foci of this study. Both mountain ranges comprise quartzites and metasandstones and are characterised by deeply incised, undersized rivers that flow through canyons perpendicular to the structural fabric of the rock. Within these mountains, tectonically induced repetition of stratigraphic units allows for sampling of identical stratigraphic units in both ranges

Quartz-rich sediment was collected from ten rivers distributed throughout the two mountain ranges, with the intent of quantifying the averaged denudation rates within each catchment. Focus was then given to the canyon of Tradouw River where, in addition to river sediment, quartzite samples were collected from the interfluves above the river and bedrock benches along the river, two depth profiles were sampled in pebbly depositional terraces located at the river's exit from the mountains, and radiocarbon samples were collected from muddy silt overlying a pebbly depositional terrace.

Chapter 5:

Methods of field and laboratory work

5.1 Introduction

Chapter 5 outlines the methods of sample collection and analysis. Field techniques were based on Gosse and Philips (2001) and are detailed in Section 5.2. The protocol for sample cleaning, ^{10}Be extraction and target preparation is a modification of the techniques developed by Kohl and Nishiizumi (1992) and procedures developed by von Blanckenburg et al. (2004) and von Blanckenburg et al. (1996). Full laboratory procedures are discussed in Section 5.3. The specifics of accelerator mass spectrometry (AMS) analysis are dealt with in Section 5.4. A chapter summary is provided in Section 5.5.

Initial processing of samples took place at the University of Cape Town, South Africa, in preparation for quartz separation and ^{10}Be extraction that were carried out at the GFZ in Potsdam, Germany. The final ^{10}Be targets were analysed at the Laboratory of Ion Beam Physics, ETH, Zurich, Switzerland. Radiocarbon analysis was carried out at the University of Cologne.

5.2 Sampling methods

Of initial concern in sampling was the avoidance of 'complex' outcrop and catchment geometries. Complex outcrop geometry is here defined as any non-planar surface, or planar surface of non-negligible dip, whose geometry may influence the cosmic ray flux incident on the material sampled (Chapter 3). Complex catchment geometry refers to the basins of those rivers that have cut through the coastal Cape Mountains and now drain the intermontane regions in addition to the mountain slopes. In the case of bedrock samples, the effects of outcrop geometry can be accounted for in production rate calculations. Each of these mathematical adjustments, however, introduces an error into the final calculation, which may ultimately affect the accuracy of the minimum erosion rates and maximum exposure ages calculated. For this reason, outcrops with simple 2 D, near-horizontal geometries were sampled where available. In the case of complex catchments, material carried in from the intermontane basins may affect the final ^{10}Be concentrations. For this reason, first order catchments were favoured, namely the steeply-incised, near-linear drainage basins characteristic of the slopes of the Cape Mountains, thus avoiding input from the intermontane basins where shales dominate. In all sampling scenarios, the geographic position of the sampling site was noted with a Garmin 60CSx hand-held GPS.

5.2.1 Bedrock samples

A simple chisel and rock hammer were used to collect bedrock fragments, whose thickness was kept below 5 cm to remain within the zone of constant neutron flux that exists at the air-rock surface interface (Niedermann, 2002; Masarik and Reedy, 1995; Chapter 3). Sampling small chips of bedrock avoids the need to later trim samples to size, a procedure which can be both labour intensive and a potential source of sample contamination. Sampling widely across a bedrock surface ensures that the material collected is representative of the surface under investigation. As the edges of an outcrop are exposed to cosmic rays from multiple directions, complicating the calculation of cosmic-ray flux incident on these areas, all samples were collected a minimum distance of 10 cm from the outcrop margins. Where available, surfaces of negligible dip were targeted to avoid later corrections for self-shielding or adjustments

to the cosmic ray flux, as discussed by Gosse and Philips (2001), Lal and Chen (2005); Hermanns et al. (2004) and Dunne et al.(1999). Approximately 200 g of rock were collected per sample.

5.2.2 River sediment samples

Mobile sediment was collected from the river channels by means of a common garden trowel and sifted on site to isolate the 250-500 µm grain size fraction. In addition to being the inherent grain size of sediment in these rivers, targeting this particular grain size excludes finer material that may be eolian in origin and thus foreign to the catchments studied. To ensure that each sample was representative of its respective channel's sediment, material was collected from a number of points within each channel at the given sample locations. Sediment was collected from the river channel instead of the river banks to avoid the unknown influence of sediment storage on the final ^{10}Be concentrations calculated. Approximately 300 g of sediment were collected per sample.

5.2.3 Depth profile samples

Sampling of alluvial terraces involved measuring, to the nearest centimeter, the depth of the exposed terrace face and defining zones of approximately 10 cm depth, at depth intervals of approximately 20 cm, along which pebbles were hand-picked. Pebbles of sandstone, quartzite and vein quartz were preferentially picked due to their high quartz content. All clasts had similar dimensions, measuring 3-4 cm on their long axis and 2-3 cm on their short axis. The nature and thickness of further deposits overlying the terrace was also recorded. Each sample comprised 30 quartz-rich clasts collected over a distance of roughly 1 m along the strike of the terrace, at the given sampling depth.

5.2.4 Radiocarbon samples

Three carbon-rich samples were removed from the mud deposit overlying the alluvial terrace of sample site S1. From each, approximately 10-20 g of carbonaceous material was hand-picked, and the material sent to the University of Cologne, Germany, for radiocarbon analysis.

5.3 Cosmogenic nuclide analysis

Cosmogenic nuclide analysis requires the extraction of the *in-situ* produced radiogenic ^{10}Be from the sample material in a form suitable for the practical procedure of target packing. AMS analysis of the resultant targets determines the ^{10}Be/^{9}Be ratio of each sample, from which the corresponding ^{10}Be concentrations can be derived. These concentrations are required for the determination of the minimum exposure ages and maximum erosion rates of the sampled material.

The procedure for target preparation consists of two stages; the first being quartz separation and the second, isotope extraction. The purpose of quartz separation is to convert the raw sample taken in the field into a purified concentration of monomineralic quartz grains from which ^{10}Be can be chemically extracted without the risk of contamination by meteoric ^{10}Be or *in situ*-produced ^{10}Be produced in minerals other than quartz (Chapter 3). For the samples in question, quartz separation involved crushing of bedrock samples and terrace clasts to release the monomineralic quartz grains, rinsing of all samples to remove fines and organic matter, and a series of acid leachings to remove contaminant minerals, precipitates and meteoric ^{10}Be. The isotope extraction which follows (stage 2) is a multi-step chemical procedure carried out on the ultra-pure quartz separates prepared by the quartz-separation procedure (stage 1).

5.3.1 Stage 1: Quartz separation

A number of physical and chemical methods can be used to selectively remove contaminant minerals and precipitates from a sample. Commonly used techniques include, amongst others, magnetic separation by means of a Frantz magnetic separator, for the removal of ferromagnetic and paramagnetic minerals; froth floatation, for the removal of feldspars and micas; density separation by means of heavy liquids, for the removal of minerals whose density differs notably from that of quartz (e.g. mafic silicates and oxides); leaching with HCl and HNO_3, for the removal of carbonates and metal precipitates; and leaching with HF, for the removal of feldspar and meteoric ^{10}Be. The often heterogeneous nature of rock and sediment commonly requires the use of more than one of these techniques for the effective

cleaning of a sample, the choice of which is dictated by the sample's composition. The relatively clean nature of the coastal Cape Mountains samples which consist almost exclusively of quartz with only minor amounts of feldspar and titaniferous minerals, made it possible to remove all macroscopic contaminants through a series of acid leachings. Carbonates, aluminum and ferrous mineral coatings were removed with hydrochloric acid (HCl), while a mixture of hydrofluoric acid (HF) and nitric acid (HNO_3) was used to preferentially dissolve the non-quartz silicate minerals such as feldspars and micas.

Prior to leaching, all samples were reduced to sand-sized particles in order to release the monomineralic quartz grains from the rock matrix. The use of monomineralic grains in the clean-up procedure exposes individual grain surfaces to etching by acid, thus allowing for the thorough removal of meteoric ^{10}Be from quartz and the quick and efficient removal of contaminant minerals. Bedrock and alluvial terrace samples were cut, crushed and ground to sand-sized grains by means of a rock splitter, jaw crusher and grinding mill. The material was subsequently sifted to separate the 250-500 µm grain size fraction, which was kept for analysis. Given that the quartzites and alluvial pebbles sampled were on average medium-grained, the collection of this size fraction effectively retained the largest monomineralic quartz grains derived from the original samples.

Grain size is important in the leaching process. Quartz is resistant to corrosion by acids, except in the presence of fluoride (Kohl and Nishiizumi, 1992). This phenomenon is due to the stability of the hexaflourosilicate ion (SF_6^{2-}) in acid medium (Potts, 1987a). The solutions of HF used in the cleaning procedure will attack the quartz in addition to other silicate minerals, albeit at a slower pace, causing samples in the 250-500 µm grain-size range to lose up to 20-30% of their material through dissolution. Smaller grain sizes are difficult to leach as they tend to react violently with HF (Bierman et al., 2002) and one runs the risk of losing excessive amounts of material. Analytical practicality has therefore placed a lower limit on grain-size, should one wish to leach with HF. Similarly, practicality often dictates the upper limit of grain size as acid digestion of large grains can be a time consuming process. However, this is not a concern when working with medium-grained sediment such as

that which is found in the rivers of the coastal Cape Mountains. For these samples, the upper limit (500 µm) was set by the grain size of the parent rock from which the sample was derived.

Sediment samples were passed through a sample splitter to homogenize the sample, ensuring that an aliquot from any given sample would consist, in equal parts, of material from all sampling points within the respective river channel. The end-products of the crushing, sieving and homogenization procedures were then rinsed with water to remove fines and organic matter, and left over night in a drying oven set to 70°C. Once dry, 100 g of material was removed from each sample and placed in a labeled 500 ml glass beaker.

Initial acid leachings were done in 10% HCl solution. The primary purpose of an HCl leach is to remove carbonates (Equation 5.1) and ferrous oxides (Equation 5.2) prior to the addition of HF, the benefits of which are two-fold. Firstly, although both HF and HCl are effective in removing carbonates and metal oxides, HF attacks quartz whereas HCl does not. The use of HCl in this step allows for the removal of surficial contaminants whilst leaving the quartz intact. Secondly, as the reaction of acids with carbonates is often energetic and accompanied by the release of CO_2, the reaction is carried out in uncovered glass beakers to allow the rapidly exsolving gas to escape. Given the toxicity of HF, an open-system containing this acid is an unnecessary health-risk in the lab when an equally suitable acid of lesser toxicity could be used.

$$2HCl_{(l)} + CaCO_{3(s)} \rightarrow CaCl_{2(aq)} + CO_{2(g)} + H_2O_{(l)} \qquad 5.1$$

$$3HCl_{(l)} + Fe_2O_{3(s)} \rightarrow FeCl_{3(aq)} + 3H_2O_{(l)} \qquad 5.2$$

The coastal Cape Mountains samples contained little to no carbonate and these initial leachings served mainly to remove the surficial coatings of iron oxide on the mineral grains. In this procedure, glass beakers were filled with the acid solution and placed in a fume cupboard over night, on a hotplate set to 105°C. The purpose of the hotplate is to increase the temperature of the sediment-acid mixture, thereby

increasing reaction rates. Once the acid solution had reached saturation with respect to $Fe^{3+}_{(aq)}$ ions, marked by a deep orange-brown discolouration of the solution, the liquid was drained and the sample rinsed with deionized water. In the absence of deionized water, tap water will suffice. Acid, rinsings and any fines suspended in the rinsings were discarded in a designated HCl waste bottle. Each sample was subjected to three leachings of this kind, at which point the solutions were no longer discoloured by the presence of $Fe^{3+}_{(aq)}$ ions and the samples were considered relatively free of iron oxide.

Following the removal of carbonates and metal oxides, samples were transferred from the glass beakers to uniquely labeled HDPE wide-mouth bottles for the second stage of leaching, during which a mixture of HF and HNO_3 was used to remove unwanted silicates and remaining metal oxides from the samples. The tendency of HF to attack silica in glassware necessitates the use of plastic apparatus made from linear polypropylene or polytetraflouroethylene for all procedures in which this acid is used (Potts, 1987a). High density polyethelene (HDPE) bottles were considered most suitable for this procedure given their resistance to corrosion by acids and tendency to retain their form and leak less than low density polyethelene (LDPE) bottles, when heated.

Although HF attacks all silicate minerals, the slower rate of quartz dissolution allowed for the preferential dissolution of non-quartz silicate minerals, while the high concentration of quartz in the samples meant that only a fractionally small amount of this mineral was lost during the procedure. Upon addition of HF, the reaction proceeds to the right of Equation 5.3 with the release of gaseous silicon tetraflouride (SiF_4) and any other volatile fluoride which may be present (Potts, 1987a). The addition of the HNO_3 is required to overcome the low solubility which certain fluoride salts of the major elements (such as calcium and potassium) experience in HF (Potts, 1987a). In addition to solvation, nitric acid assists in maintaining a high H^+ molarity in the solution, promoting the forward reaction and consequently increasing the rate of reaction.

$$4HF_{(l)} + SiO_{2(s)} \rightarrow SiF4_{(g)} + 2H2O_{(l)} \quad 5.3$$

Samples were covered with a 2% HF/HNO_3 solution[1] and placed horizontally on heated rollers, where they were left to rotate slowly throughout the night at an elevated temperature of approximately 35°-40°C. Continuous rotation of the bottles ensured the thorough mixing of sediment and acid solutions. Once the leach was complete, the acid solution was drained, diluted and discarded in a designated HF waste bottle. Samples were rinsed with deionised water to remove any remaining silicon fluorides and the rinsings discarded in the HF waste container. The concentrated HF/HNO_3 leach was performed in triplicate on all samples.

The final acid leachings were carried out using a 4% HF/HNO_3 solution. The increase in acid concentration allows for faster grain dissolution, promoting a speedier clean-up procedure. As with the previous leachings, the sediment-acid mixture was left to rotate over night on heated rollers. This procedure was repeated until all non-quartz silicate minerals were dissolved and the samples had been reduced to their quartz contents only. This translated to four leachings per sample. Once the last leach was complete, samples were thoroughly rinsed in milli-Q water and left over night in a drying oven set to 70°C.

Following the clean-up procedure, the purity of the remaining quartz was assessed by means of ICP-OES analysis (Figure 5.1). A sufficiently clean sample should have an Al content of below 100 ppm as higher concentrations indicate the presence of contaminants such as feldspars. A 200 mg aliquot was removed from each sample and transferred to a labeled 7 ml Savillex beaker. 2 ml of HF stock solution and 1 ml of HNO_3 stock solution were added, the beakers sealed and the quartz left to dissolve overnight on a hotplate set to 125°C. Once dissolution was complete, the solutions were evaporated overnight at 90°C and the residues taken up in 1 ml of 3 M HNO_3 stock solution. After all residue had dissolved, the 1 ml 3 M HNO_3 was pipetted into

[1] The specific concentration of the acid mixture is not significant. Concentrations between 2% and 5% are commonly used as 1% is too weak to be effective and greater than 5%, excessive.

15 ml centrifuge tubes and diluted to 0.3 M HNO_3 solution by the addition of 9 ml of milli-Q water. All tubes were centrifuged once to separate any solids, and the liquid pipetted into a clean 15 ml centrifuge tube for analysis.

5.3.2 Stage 2: Isotope separation

Isotope separation is carried out in a clean laboratory. The room is supplied with filtered air to prevent the introduction of environmental contaminants to the samples. All chemistry was carried out in metal-free laminar-flow work stations likewise supplied with filtered air.

In this stage of target preparation the cosmogenically produced ^{10}Be and ^{26}Al isotopes are chemically extracted from the ultra-pure quartz prepared in Stage 1, precipitated as hydroxides, and oxidized in preparation for target packing. This process comprises three steps; namely, 'Step 1: carrier addition and sample digestion', in which the ultrapure quartz separates were doped with a known quantity of ^{9}Be prior to their dissolution; 'Step 2: chromatography', in which contaminant ions were removed from the sample solutions and the Be and Al ions separated from one another; and 'Step 3: oxidation and sample packing', in which the Be was oxidized and packed for AMS analysis. Given the large amount of material to be analysed, the 24 samples were processed in two batches of 12, namely Batch 1 and Batch 2, each with its own procedural blank. Procedural blanks were subject to full isotope separation procedures whilst carrying no sample material and thus no ^{10}Be other than the known ^{10}Be inherent in the carrier solution itself.

5.3.2.1 Step 1: Carrier addition and sample digestion

Prior to isotope separation, the ultra-pure quartz separates were subjected to a final two-stage leach in HF and aqua regia. This is a precautionary step intended to remove any remaining feldspars and meteoric ^{10}Be still present in the samples. Etching in HF removes feldspars as well as the upper layer of the quartz grains in which meteoric ^{10}Be may reside, while aqua regia performs the dual function of dissolving the remaining oxides and removing the fluorides which may have formed during the preceding reactions with HF.

30 g of ultra-pure quartz were removed from each sample and placed in a 220 ml Savillex beaker of known weight, bearing the sample's unique ID number. The samples were covered in HF stock solution and left at 120°C for an hour, after which the cooled samples were drained of acid, rinsed in Milli-Q water and covered with r.a. grade aqua regia. The mixture was again left at 120°C for an hour, this time with the beaker lids slightly ajar for the first 30 minutes to allow the evolving gas to escape. Once complete, the acid was drained and the remaining quartz rinsed thoroughly with Milli-Q water, dried over night on a hotplate and the precise weight of the samples recorded. During the drying procedure care was taken to cover the beakers with a loosely-fitted lid as static is a common problem in the lab, causing grains to jump about in a manner that could potentially contaminate neighboring samples. Once dissolution is complete, the use of high analytical grade reagents, distilled acids and Milli-Q water in all succeeding steps of the protocol is essential for ensuring the purity of the final BeO produced for AMS analysis.

Following the two-stage acid leach, samples were doped with a known quantity of ^{9}Be carrier solution of precisely known concentration. This solution is the in-house GFZ carrier as of 01/10/2010, with a ^{9}Be concentration of 372.5 ± 3.5 ppm. The addition of ^{9}Be is necessitated primarily by the low natural abundances of Be in *in situ*-irradiated samples. As AMS analysis does not determine the absolute concentration of an isotope but rather the ratio of one isotope to another, the Be content of a sample is recorded as a ratio of its ^{10}Be to ^{9}Be content. Natural *in situ*-produced ^{10}Be concentrations are exceedingly low, commonly in the order of 10^{-6}-atoms·g^{-1} of quartz (Southon et al. 1983; von Blanckenburg 2004; von Blanckenburg et al. 1996), and are not capable of producing an ion beam of reasonable strength during AMS analysis. In addition to low ion beam strength, these exceptionally low concentrations would result in Be samples too small to be handled if no external Be were added to the system (Southon et al., 1983). Samples are thus spiked with a known quantity of the stable ^{9}Be isotope, increasing the total Be concentration whilst leaving the natural ^{10}Be concentration undisturbed. A ^{10}Be/^{9}Be ratio measured is therefore a ratio of the *in-situ* produced cosmogenic ^{10}Be inherent in the sample and the stable ^{9}Be isotope with which the sample is spiked; any ^{9}Be occurring naturally in a sample is present in such small quantities that its contribution to the ^{10}Be/^{9}Be ratio

is considered negligible (Blanckenburg et al. 1995; Tera et al. 1986). One further advantage of this procedure is afforded by the identical chemical behavior of the ^{10}Be and ^{9}Be isotopes. By increasing the total Be concentrations in the samples to detectable levels, and behaving in a chemically identical manner to ^{10}Be, the addition of ^{9}Be allows one to track the movements of Be through all stages of the chemistry by means of ICP-OES analysis.

In accordance with the requirements of the ETH-AMS facility, Zurich, Switzerland, samples were doped with 0.15 mg of ^{9}Be through the addition of 400 µL of carrier solution with a ^{9}Be concentration of 372.5 ± 3.5 ppm. Thereafter, a total 90 ml of 48% HF stock solution was added in two stages for sample dissolution. Initially, 40 ml was added and the uncovered, unheated Savillex beakers left to stand for 1.5 hours. Thereafter a further 50 ml was added and the uncovered, unheated beakers left to stand for one hour. Finally, the beakers were filled with HF stock solution, sealed and placed over night on a hotplate set to 100°C [2]. Once dissolution was complete, the lids were removed from the beakers and the hotplate temperature increased to 135°C to evaporate the HF solution. By the end of this procedure SiO_2 is lost from the system in the form of $SiF_{4(g)}$, leaving behind a residue of those chemical species which were initially trapped within the quartz grains prior to their dissolution.

The residue which remained was taken up in aqua regia and the resultant solution likewise evaporated off over a 4-5 hour period at an elevated temperature of 105°C. Once dry, a further 10 ml of 6 M HCl were added to the precipitate, which was left to dissolve over night. The successive addition and evaporation of aqua regia and HCl facilitates the removal of fluorides as HF and contaminant metal ions in the form of metal-chloride complexes. The resulting solution was transferred to a 10 ml acid-cleaned centrifuge tube, taking care to leave any remaining insoluble impurities behind in the Savillex beaker, and centrifuged for 5 minutes at 3500 rpm. A fine, dirty-white precipitate of titanium oxide (TiO_2) collects at the bottom of the tube below a clear, yellow supernate. Discolouration of the supernate is due to the presence of $FeCl_3$ in solution. This solid contaminant is removed before the samples are introduced to the

[2] Further HF was added where necessary. HF and silica react in a 4:1 ratio (Equation 5.3) and one can approximate the quantity of HF required (in millilitres) as four times the mass of quartz (in grams).

ion-exchange columns of Step 2, as solid particles can clog the resin and reduce flow rates in the columns (McAlister and Horwitz, 2005).

At this point, the sample solution contains the cosmogenic ^{10}Be inherent in the sample, ^{9}Be both inherent in the sample and acquired through the addition of carrier solution, and contaminant metal ions in the form of metal-chloride complexes, metal-chloride ion pairs or neutral species. These contaminants are removed in Step 2 through the consecutive use of an anion-exchange column followed by a cation-exchange column; a process which also serves to isolate the ^{10}Be and ^{26}Al fractions from one another. Prior to column chemistry, however, the purity of the samples is determined by means of ICP-OES analysis (Figure 5.2). For this procedure, 100 µl of the sample solution is pipetted into a clean centrifuge tube, and 10 ml of 0.3 M HNO_3 added to each 100 µl aliquot. Samples were centrifuged a further 5 minutes at 3500 rpm to ensure that no droplets have clung to the walls of the centrifuge tubes before being analysed.

5.3.2.2 Step 2: Chromatography

Chromatography facilitates the removal of contaminant ions in solution through ion-exchange. A fluid phase containing the unwanted, charged chemical species is introduced to a porous, stationary solid phase in the form of a resin containing counter ions of similar polarity to the contaminants in solution. The counter ions on the dry resin become mobile in solution, able to diffuse in and out of the resin matrix. These counter ions will be replaced by the contaminant ions in solution if the aqueous species has a greater affinity for the resin than the counter ions or occur in greater abundance. Those chemical species which are not of suitable polarity will pass through the ion-exchange column unaffected. Once the ion-exchange procedure is complete, the contaminant ions can be eluted from the column by introducing ions of higher affinity for the resin or a high concentration of ions of similar or lower affinity. These resin filled columns have a maximum capacity, termed 'exchange capacity', which is descriptive of the maximum number of ions which can be loaded onto a column. Clean ion-separation is only possible if the number of ions introduced into

the system remains below 50% of the exchange capacity, and preferably below 10%. (Potts, 1987b)

An ion's affinity for a resin in a particular aqueous medium is expressed by the equilibrium distribution coefficient (Kd) of the ion. The Kd value can be considered a ratio of resin-bound ions to free ions in solution and reflects the susceptibility of an ion to elution by a particular fluid medium. Equation 5.4 provides a full definition of the equilibrium distribution coefficient. (Gupta, Carolina, and Strelow, 1960)

$$Kd = \frac{\text{amount of ion on resin} \times \text{volume of water phase (ml)}}{\text{amount of ion in water phase} \times \text{weight of dry resin (g)}}. \qquad 5.4$$

Kd is variable and dependent on the ion in question, the nature of the resin, the composition and concentration of the fluid phase at a given temperature and pressure, and the ion to resin ratio of the system. The significance of Kd lies in its ability to predict the behavior of an ion during column chemistry and determine the 'separation factor' of two ions which one may wish to elute separately. Ions of considerably different Kd values will have a large separation factor, implying that the two ions are easily separable by means of elution due to their very different affinities for the resin. Column chemistry is therefore based on the knowledge of Kd values and their variation in response to changes in the aqueous phase (e.g. composition and concentration) of the system. Careful choice of eluates and the order in which they are introduced to an ion-exchange column can allow one to separate unwanted contaminant ions from those ions of interest to an investigation.(Gupta et al., 1960)

Both anion- and cation-exchange columns are employed in the chromatographic clean-up procedure of Step 2. The anion-exchange column facilitates the removal of contaminant Fe and Ti ions that exist as anionic metal-chloride complexes within the sample solution at the end of Step 1, while cation-exchange columns remove residual cationic Ti, Na and Fe. The anionic coordination compounds formed by the reaction with HCl at the end of Step 1 (e.g. $FeCl_4^-$, $FeCl_5^{2-}$, $FeCl_6^{3-}$ and $TiCl_6^{2-}$) bind to the resin of the anion-exchange column and remain within the upper few millimeters of

the column while Be^{2+} and Al^{3+}, which do not form such strong complexes, proceed through the column unhindered (Strelow et al. 1965). In addition to anionic $TiCl_6^{2-}$, however, titanium may take the form of Ti^{4+}, Ti^{3+}or neutral Ti; all of which are unaffected by anion-exchange column chemistry (Strelow et al. 1965). These contaminant forms of Ti are expelled from the column together with the Be and Al and require the subsequent use of a cation-exchange column to remove them along with residual Na, Fe and Al ions in solution (von Blanckenburg et al. 1996).

Initially, samples were passed through a 15 ml anion-exchange column containing 2 ml Biorad 1-X8 in the Cl^- form, 100-200 mesh. The resin was washed with 10 ml of 0.3 M HCl, conditioned with 6 ml of 6 M HCl, and the samples loaded. Given their notably low Kd values in concentrated HCl (Gupta et al., 1960), Be^{2+} and Al^{3+} were eluted from the column with the addition of 6 ml of 6 M HCl and the rinsings collected in an acid-cleaned Savillex beaker. Once elution was complete, the anion-exchange column was washed a second time with 10 ml of 0.3 M HCl before being filled with Mili-Q water and sealed.

The rinsings containing Be and Al were evaporated and the precipitate taken up in 4 ml of 0.4 M oxalic acid ($C_2O_4H_2.2(H_2O)$). Those trivalent cations still remaining in the solution will complex with the oxalic acid forming anionic metal-oxalate complexes (e.g. $[Fe(C2O4)3]^{3-}$) while di- and monovalent cations remain largely unaltered (von Blanckenburg et al. 2004; Strelow et al. 1972). The large difference in the Kd values of the oxalate complexes and free cations facilitates their separation in the cation-exchange procedure to follow (Blanckenburg et al. 2004).

Prior to the use of cation-exchange columns, the total cation load of each sample was determined by means of ICP-OES analysis and an appropriately sized column selected in order to avoid exceeding the exchange capacity of the resin (Figure 5.3). 7.5 ml cation-exchange columns containing 1 ml of Biorad AG50-X8 resin in the H^+ form, 200-400 mesh were prepared by washing with 5 ml of 5 M HNO_3. The nitric acid was rinsed from the column with the addition of 5 ml Mili-Q water, and the resin conditioned with 5 ml of 0.4 M oxalic acid. The sample solutions were centrifuged for 5 min at 3000 rpm and the supernatant added to the ion-exchange columns. Al^{3+},

Fe^{3+} and Ti^{4+} are flushed from the column in the form of metal-oxalate complexes while di- and monovalent cations, which form oxalate complexes of less stability, bind to the resin (von Blanckenburg et al. 1996; Strelow et al. 1972). Stepwise addition of 12 ml 0.4 M oxalic acid removed Al, Ti and Fe from the column, with the elution of Al and Fe delayed with respect to that of Ti (von Blanckenburg et al. 1996). Once the Al fraction had been collected the oxalic acid was washed from the column with 3 ml Milli-Q water. 8 ml of 0.5 M HNO_3 was then added to the column to wash Na^+ from the column. The low Kd value of Na^+ in 0.5 M HNO_3 (12.7) contrasts with that of Be^{2+} (52) and ensures that no Be^{2+} is lost when Na^+ is removed (Strelow et al. 1965). Thereafter, 11 ml of 1 M HNO_3 was used to extract the Be fraction whose Kd value decreases to 14.8 in 1 M HNO_3 (Strelow et al. 1965). Metals of similarly low partition coefficients (i.e. Kd values below 30) such as K and Mg, as well as minor amounts of Zn, Cu, Ni and Co, will elute with Be if they are present in the sample solution (von Blanckenburg et al. 1996). This Be-fraction was collected and kept separate from that containing Al. The column was cleaned with 10 ml 5 M HNO_3 and rinsed with 5 ml Milli-Q water. For storage, the columns were filled with Milli-Q water and sealed. Figure 5.5 illustrates the cation exchange process.

A sample of the Be-containing eluate was sent for ICP-OES analysis, the remaining liquid evaporated and the precipitate taken up in 1M HNO_3 (Figure 5.4). At the end of column chemistry samples are largely free from contaminant ions, most importantly Fe and Ti, which tend to reduce currents during AMS analysis.

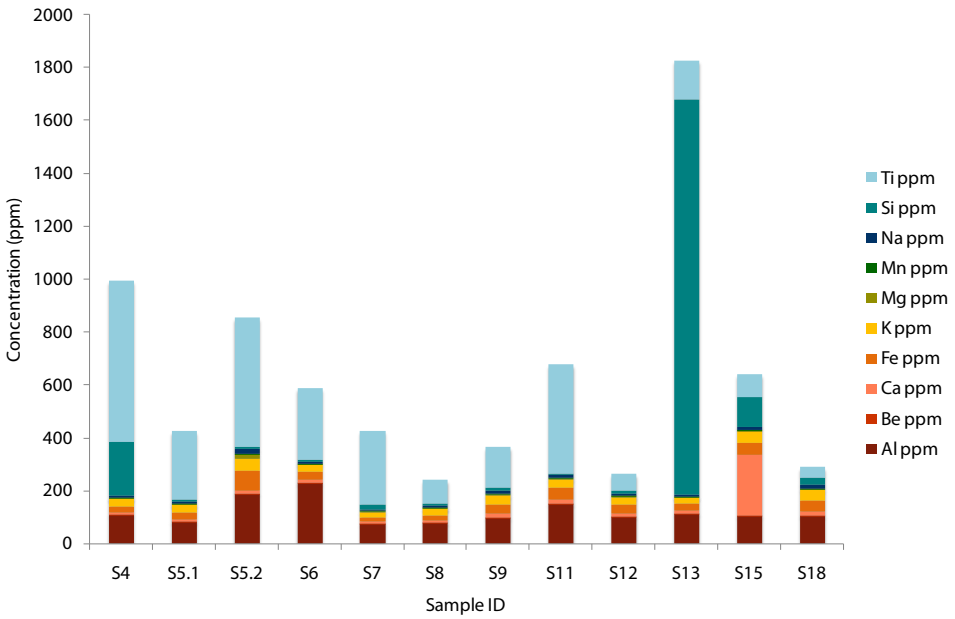

Figure 5.1: The ICP-OES analysis of Batch 1 samples at the completion of Stage 1: Quartz separation and prior to Stage 2: Isotope separation. Compare with Figure 5.2.

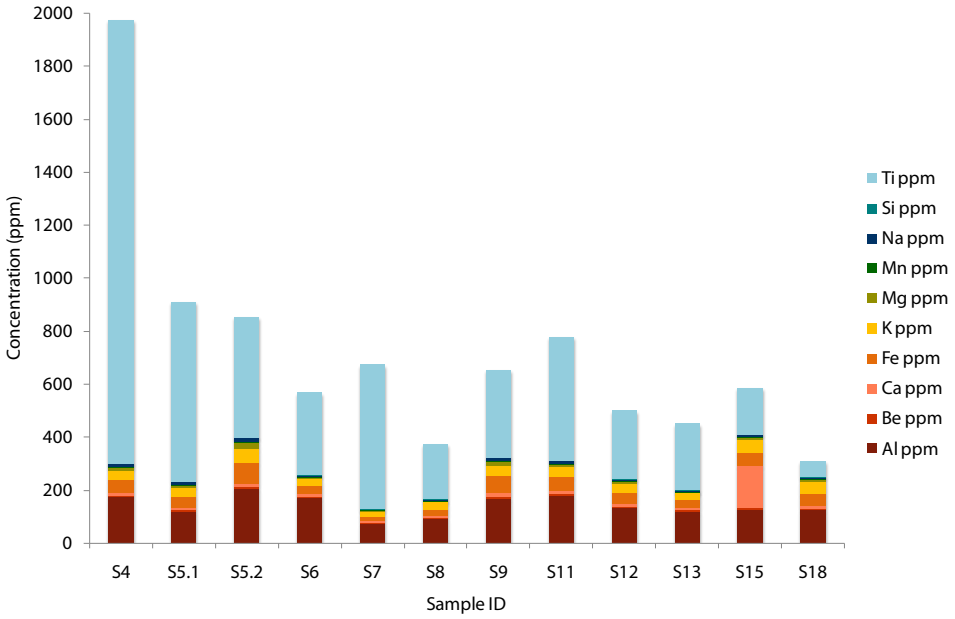

Figure 5.2: Results of ICP-OES analysis for Batch 1, following the addition of ^{9}Be carrier solution and the successive addition and evaporation of aqua regia and HCl. Note that, in comparison to Figure 5.1, the samples have notably reduced silica (Si) and calcium (Ca) contents.

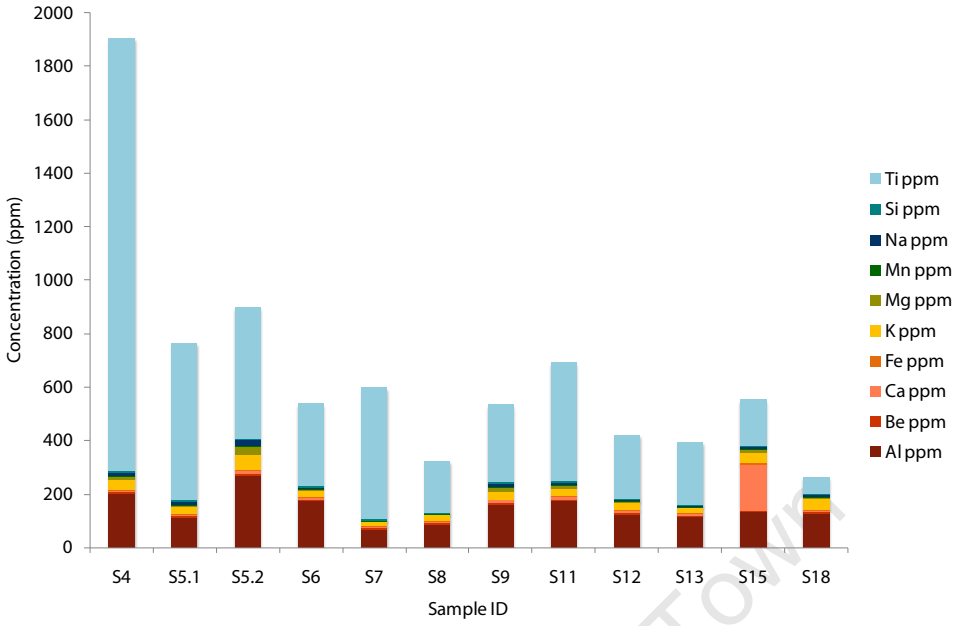

Figure 5.3: The results of ICP-OES analysis for Batch 1 after passing through the anion-exchange column. Note the significant reduction in sample iron (Fe) content in comparison to Figure 5.2.

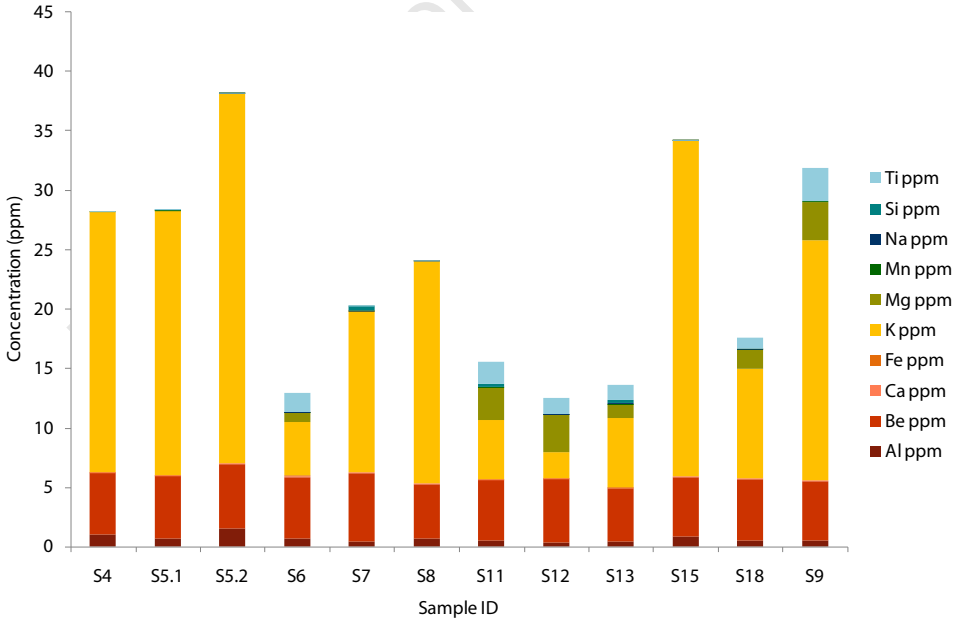

Figure 5.4: The results of ICP-OES analysis for Batch 1 samples, after passing through the cation-exchange column. Note the significant reduction of contaminant metals ions, in comparison to Figure 5.3. The trace amounts of Be now form a major component of the sample composition.

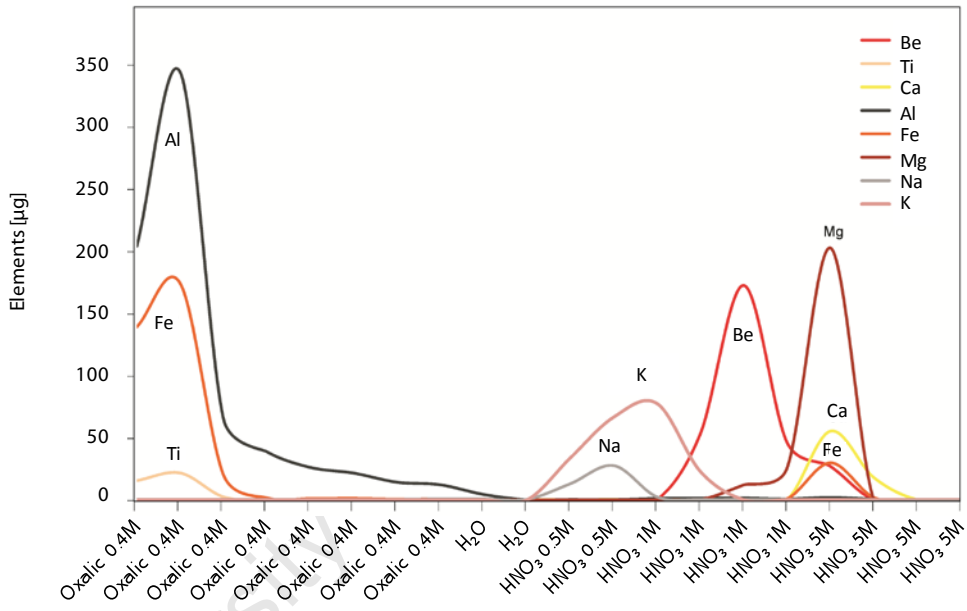

Figure 5.5: Cation-exchange column elution curve, courtesy of Hella Wittmann (GFZ-Potsdam). Al, Fe and Ti are removed by an initial addition of 12 ml 0.4 M oxalic acid. Na is eluted by the addition of 8 ml 0.5 M HNO_3. Be is eluted thereafter, by the addition of 11 ml 1 M HNO_3. Finally, the cation-exchange column is cleaned of remaining Mg, Ca and remaining Fe by rinsing with 10 ml 5 M HNO_3.

5.3.2.3 Step 3: Oxidation and sample packing

In Step 3, $Be(OH)_2$ is precipitated out from the final Be-hosting eluate collected from the cation-exchange column of Step 2. Silver is added to the precipitate, the mixture oxidized, and the resultant oxide packed into discoid copper targets for AMS analysis.

Beryllium hydroxide ($Be(OH)_2$) is an amphoteric substance which precipitates out when the pH exceeds 7 but redissolves at a pH of 12 to form isopolyanions of the form $[(HO)_2\{Be(\mu\text{-}OH)_2\}_nBe(OH)_2]^{2-}$ and with further addition of alkali, beryllate anions of the form $[Be(OH)_4]^{2-}$ (Greenwood and Earnshaw, 1997). With the use of a Pasteur pipette a 1:1 solution of suprapure NH_4OH in Milli-Q water was added to the samples, gradually increasing the pH to between 8 and 10. The solution was left to stand for a few minutes and centrifuged, separating the white, gel-like precipitate of $Be(OH)_2$ from the supernate. Be coprecipitates with any Fe, Al, Ti, Zr, U, Cr, Cu, Ni, Zn, Co, Pb and rare-earth elements which may be present in the sample while Mg, Mn, Na, K and Ca remain in solution (von Blanckenburg et al. 1996; von Blanckenburg et al. 2004). Following chromatographic clean-up, however, the concentration of these potential contaminants should be negligible. The supernate was then pipetted off, leaving the $Be(OH)_2$ intact at the base of the centrifuge tube. The process was repeated by redissolving the precipitate in 5 ml of 1 M HNO_3, reprecipitating with NH_4OH, and once again separating the precipitate from its supernatant liquid by means of centrifugation. The final precipitate was washed with Milli-Q water whose pH was adjusted to 9 by the addition of NH_4OH, and the rinsings pipetted off.

AMS analysis requires the addition of silver (Ag), copper (Cu) or niobium (Nb) to the samples as stipulated by the respective AMS facility. ETH processes samples that have been mixed with either copper or silver (Kubik and Christl, 2010). The addition of these metals increases the volume of the final samples for ease of handling, and promotes high negative ion yields during AMS analysis (Southon et al., 1983). The respective metal can be physically mixed in powder form with the final beryllium oxide or, where the chemistry allows, added chemically to the beryllium hydroxide prior to its oxidation. In the case of the Cape Mountains samples, Ag was chemically mixed with Be by the addition of $AgNO_3$ to the $Be(OH)_2$ precipitate and the two oxidized simultaneously.

Chemical mixing has several advantages over the physical alternative. As it is not necessary to manually crush and mix the final BeO with Ag powder, processing times are reduced. The method is also far more efficient than manual mixing and ensures the homogeneous dispersal of BeO throughout the Ag matrix. This eliminates the risk of secondary ion emissions which may plague the analysis of a poorly-mixed sample. The presence of Ag in the samples prior to and during their oxidation ensures that the Ag acts as a binder in the final product, both curbing the release of toxic BeO into the atmosphere and lending friability to the samples which aids in target pressing. Chemical mixing also results in a more voluminous final product than is obtained by physical mixing. Consequently, less ^{9}Be is required to bulk a chemically mixed sample (approximately 0.1 mg ^{9}Be as compared to 0.2-0.3 mg ^{9}Be required for a physically mixed sample). This reduction in ^{9}Be causes an increase in the $^{10}Be/^{9}Be$ ratio of the sample and a resultant increase in the precision of AMS analysis (Stone et al., 2004).

Whether manually or chemically mixed, the addition of a thermally and electrically conductive metal to the final BeO plays an important role in the AMS analysis. By forming a continuous conductive matrix in which the BeO is embedded, Ag prevents a build-up of charge on the surface of the target during sputtering (Stone et al., 2004). Following the work of Hedges et al. (1980) on the production of C^- beams in AMS analysis, it has also been suggested by Southon et al. (1983) that Ag is likely to promote high negative ion beam current during the AMS analysis of Be. Hedges et al (1980) described how the reduced thermal conductivity of carbon samples under the *in vacuo* conditions of AMS analysis results in a decrease in the amount of C^- ions produced by sputtering due to uncontrolled increase in sample surface temperature. Southon et al. (1983) suggest that if sufficient Ag is present in the sample, the high thermal conductivity of the metal will buffer this effect, moderating surface temperatures and encouraging the production of BeO^- ions.

A solution of $AgNO_3$ was prepared by dissolving 157 mg of $AgNO_3$ in 10 ml of 5 M HNO_3, and added to the $Be(OH)_2$ in sufficient quantity to produce a Ag:Be ratio of 20:1. This ratio has been shown by Stone et al. (2004) to be optimal for the production of negative ion beams during analysis, and sufficient to produce a BeO-Ag mixture that is adequately brittle for sample packing. In the case of the Cape

Mountains samples, 0.15 mg of ^{9}Be carrier required the addition of approximately 300 µl $AgNO_3$ solution to each sample in order to achieve this 20:1 ratio. The Ag:Be mixture was transferred to round-bottomed quartz crucibles and placed on a hot plate set to 70°C for 30 minutes, whereafter the heat was increased to 120°C for dry-down.

Using platinum-coated tongs each crucible was placed within a gas flame with temperatures in excess of 1000°C, first along its periphery for approximately 30 seconds and then within the eye of the flame for approximately one minute. This process oxidizes the $Be(OH)_2$ and $AgNO_3$ to BeO and Ag_2O, respectively. The amount of time spent in the eye of the flame can be varied but it is worth noting that prolonged baking produces a more brittle product which is easier to crush and compact into an AMS target (Stone et al., 2004). At temperatures in excess of 155°C, the Ag_2O reduces to form a matrix of Ag metal around the BeO (Stone et al., 2004), with the final product appearing as a silver to white coating along the walls of the glass crucibles.

Inhalation of BeO can lead to scaring of the lung tissue, a condition referred to as 'chronic beryllium disease' (McAlister and Horwitz, 2005). Target packing was therefore carried out behind the lowered safety glass of a fumehood and a dust-mask was worn at all times. To prevent the scattering of the fine BeO by strong air currents, the fumehood was turned off. In accordance with the requirements of ETH, samples were loaded into discoid copper targets, each approximately 25 mm in diameter with a 1 mm-diameter hole in its center into which the BeO was compressed.

Prior to sample loading, targets were cleaned by soaking in 1 M HCl for one minute and rinsing in acetone. All equipment used in the target packing process was likewise wiped down with acetone. The BeO-Ag mixture was scraped from the walls of the glass crucibles with the aid of a spatula and the fine powder brushed into position on the target. Using a steel pin and hammer the oxide was gently compressed until the 1 mm-diameter holes were filled to approximately two thirds of their capacity. The remaining volume was filled with 63 µm p.a. quality copper powder to create a flush surface on the face of the target.

5.3.3 AMS analysis

Samples were analysed on the EN tandem accelerator of the Laboratory of Ion Beam Physics, ETH, Zurich, Switzerland, without the involvement of the author. All results were normalized to the in-house secondary standard S2007N, with a nominal $^{10}Be/^{9}Be$ ratio of 28.1 x 10^{-12}. S2007N is calibrated to the primary standard ICN 01-5-1, determined to have a nominal $^{10}Be/^{9}Be$ ratio of 2.709 x 10^{-11} assuming a ^{10}Be half-life of 1.387 ± 0.012 Myr (Kubik et al., 2009). The resultant $^{10}Be/^{9}Be$ ratios of Batch 1 and Batch 2 samples were corrected by their respective procedural blanks. For a detailed description of the AMS facility and analysis procedure, the reader is referred to Synal et al. (1997) and Kubik and Christl (2010).

5.4 Radiocarbon analysis

Radiocarbon analysis was carried out at the University of Cologne without the involvement of the author. Pretreatment of samples involved the standard acid-alkali-acid (AAA) extraction (Rethemeyer et al., 2011). In brief, the AAA-extraction method comprises three chemical treatments, each of which is followed by thorough sample rinsing in Milli-Q water (Brock et al., 2010; Schwabedissen and Freundlich, 1966). Initial acid treatment with HCl extracts contaminant fulvic acid from the organic sample matter. Subsequent alkali treatment with NaOH is used to remove contaminant humic acid, which is then precipitated out by again treating with acid. After the removal of fulvic and humic acids, that insoluble residue which remains is termed 'humin'. The remaining humin is treated a second time with HCl and subsequently dried, combust, and graphitized prior to AMS analysis

5.5 Summary

Bedrock, river sediment and alluvial terrace material were collected for the analysis of *in situ*-produced cosmogenic ^{10}Be. Quartzite and vein quartz were targeted for the sampling of bedrock and alluvial terrace samples, while fine-medium grained sand was collected in the sampling of river sediment. Buried organic material (possible

charcoal) was sampled for radiocarbon dating. In each case the sample location, elevation, inclination, burial and shielding were noted where appropriate.

^{10}Be extraction and sample packing were carried out by the author at the GFZ, Potsdam, Germany, according to a two-stage method. Stage 1 comprised the separation of ultra-pure quartz from the crushed samples by means of repeated acid leachings. Stage two comprised the chromatographic separation of ^{10}Be, its subsequent oxidation, and target packing for AMS analysis. Prepared ^{10}Be targets were analysed at the Laboratory of Ion Beam Physics, ETH, Zurich, Switzerland.

Organic (charcoal) material was hand-picked from the radiocarbon samples and sent to the University of Cologne for AMS analysis. Pretreatment of the samples included the acid-alkali-acid extraction method; and was followed by combustion, graphitization, and AMS analysis of the samples.

Chapter 6

Results

6.1 Introduction

Chapter 6 presents the reduced AMS data for the river sediment, bedrock, alluvial terrace and radiocarbon samples described in Chapter 5, as well as the results of channel steepness index analysis across the coastal Cape Mountains. ^{10}Be inventories are tabulated in Section 6.2, along with the production rates, maximum denudation rates, minimum exposure ages, paleodenudation rates and terrace abandonment ages derived from the nuclide inventories. Original AMS data for *in situ*-produced cosmogenic ^{10}Be analysis can be viewed in Appendix A.1-A.3, along with the physical parameters of the samples analysed. Uncalibrated radiocarbon ages and 'most-probable' calibrated radiocarbon ages are presented in Section 6.3. The full results of radiocarbon analysis can be found in Appendix A.4. Normalised channel steepness indices are presented in Section 6.4, followed by a chapter summary in Section 6.5.

6.2 Cosmogenic nuclide analysis

Site-specific production rates were determined assuming a ^{10}Be SLHL production rate of 5.14 ± 0.53 atom·g^{-1}·yr^{-1} (Balco et al., 2008) and applying a catchment-averaged correction factor for topographic shielding determined according to Codilean (2006). The latitude-altitude scaling scheme of Dunai (2001) was used to scale the SLHL production rates to the latitudes and altitudes of the respective sample sites. In the case of inclined bedrock, erosion rates were calculated according to Hermanns et al. (2004) and found to be negligibly affected.

Uncertainties in catchment-averaged production rates were taken to be the standard deviation of local point-production rates within the catchment. Doing so

ensured that uncertainties in catchment-averaged denudation rates were not underestimated, as the standard deviation proved to be larger than the error in SLHL production rate. Uncertainties in sample site production rates used for bedrock outcrops were determined by multiplying the sample site production rate with the percentage error in SLHL production rate, namely 10.4%. Uncertainties in denudation rates, exposure ages and terrace abandonment ages were calculated with the use of standard error propagation which incorporates the error in production rate and ^{10}Be concentration.

6.2.1 Results of river sediment and bedrock analysis

Catchment-averaged denudation rates are notably low throughout the study area, with a mean of 4.6 ± 1.1 m·Myr^{-1} and median of 4.7 ± 1.1 m·Myr^{-1}. There appears to be no significant spatial variation in the rate at which these catchments denude. The catchment-averaged denudation rates for the 10 sampled catchments can be viewed in Table 6.1 and Figure 6.1.

Analysis of bedrock samples S15, S17 and S18 indicate that the interfluvial slopes of Tradouw Canyon are denuding at an average pace of 3.0 ± 0.3 m·Myr^{-1}, a pace remarkably similar to the catchment-averaged denudation rates determined within the study area. Note that these bedrock denudation rates appear slightly lower than the catchment-averaged denudation rates for the same region. This discrepancy between bedrock- and sediment-determined denudation rates is a common phenomenon (Portenga and Bierman, 2011) and reflects the fact that sediment-determined denudation rates are representative of denudative processes throughout the catchment, whereas bedrock-determined denudation rates reflect only localised processes. The protocol for the sampling of bedrock dictates that horizontal, exposed surfaces be sampled. Outcrops of this nature are likely to be eroding at a minimum pace for the catchment due to their low gradients and the absence of soil coverage which would otherwise promote the chemical weathering of bedrock (Portenga and Bierman, 2011). Bedrock samples S5.1 and S5.2 were analysed for exposure ages rather than denudation rates as the sampled surfaces had been negligibly eroded (Chapter 4). The exposure ages of samples S5.1 and S5.2, as well as the denudation rates of samples S15, S17 and S18, are tabulated in Table 6.2. Figure 6.2 shows the spatial distribution of bedrock denudation rates.

Table 6.1: Catchment-averaged denudation rates of the sampled catchments. All uncertainties are reported to one sigma level.

Sample ID	Lat. (deg.)	Long. (deg.)	^{10}Be measured (10^5·atoms·g^{-1})	Production rate (atoms·g^{-1}·yr^{-1})	Denudation rate (m·Myr^{-1})
S3	-33.99541	20.66277	8.57 ± 0.27	8.05 ± 2.04	5.4 ± 1.4
S4	-33.99296	20.70459	9.21 ± 0.29	6.75 ± 1.24	4.1 ± 0.8
S6	-33.43325	21.40669	16.81 ± 0.53	10.88 ± 2.41	3.6 ± 0.8
S7	-34.02089	21.35044	14.71 ± 0.46	5.72 ± 0.94	2.0 ± 0.3
S8	-33.98339	20.84508	13.34 ± 0.42	7.38 ± 1.60	3.0 ± 0.7
S9	-33.98122	20.37606	8.43 ± 0.27	8.41 ± 1.56	5.7 ± 1.1
S10	-33.98514	20.42211	7.59 ± 0.24	8.98 ± 2.45	6.8 ± 1.9
S11	-33.46236	21.215	9.98 ± 0.31	11.59 ± 3.15	6.7 ± 1.8
S12	-33.39631	22.357	21.85 ± 0.69	12.37 ± 2.28	3.1 ± 0.6
S13	-33.35956	22.179	12.72 ± 0.40	11.77 ± 2.34	5.3 ± 1.1

Table 6.2: Maximum denudation rates and minimum exposure ages of bedrock samples. All uncertainties are reported to one sigma level.

Sample ID	Lat. (deg.)	Long. (deg.)	^{10}Be measured (10^5 atoms $\cdot$ g^{-1})	Production rate (atoms$\cdot$g^{-1} $\cdot$ yr^{-1})	Denudation rate (m $\cdot$ Myr^{-1})	Exposure age (kyr)
S5.1	-33.95593	20.70795	3.08 $\pm$ 0.11	4.84 $\pm$ 0.50	-	64.6 $\pm$ 7.1
S5.2	-33.95593	20.70809	0.49 $\pm$ 0.03	4.84 $\pm$ 0.50	-	10.2 $\pm$ 1.2
S15	-33.96211	20.70775	16,29 $\pm$ 0.51	5.82 $\pm$ 0.61	1.9 $\pm$ 0.2	301.6 $\pm$ 32.8
S17	-33.95719	20.71817	10.28 $\pm$ 0.32	7.48 $\pm$ 0.78	4.1 $\pm$ 0.4	142.2 $\pm$ 15.45
S18	-33.95706	20.71817	13.78 $\pm$ 0.43	7.48 $\pm$ 0.78	3.0 $\pm$ 0.3	193.2 $\pm$ 21.0

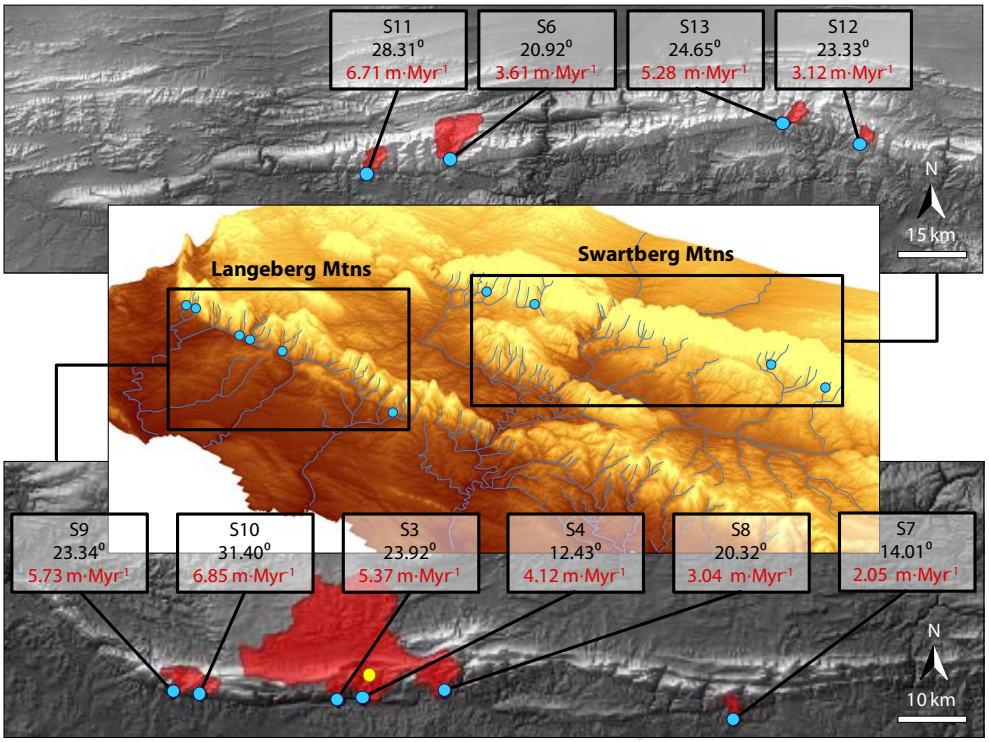

Figure 6.1: Distribution of catchment-averaged denudation rates across the study area. Blue points indicate sample sites while the single yellow point indicates the location of Figure 6.2. Catchments are indicated by red polygons. White boxes list the sample ID, catchment-averaged slope angle and catchment-averaged denudation rate with uncertainties omitted for the sake of clarity. This figure was constructed using the SRTM 90 m resolution digital elevation model, sourced from the AEON database.

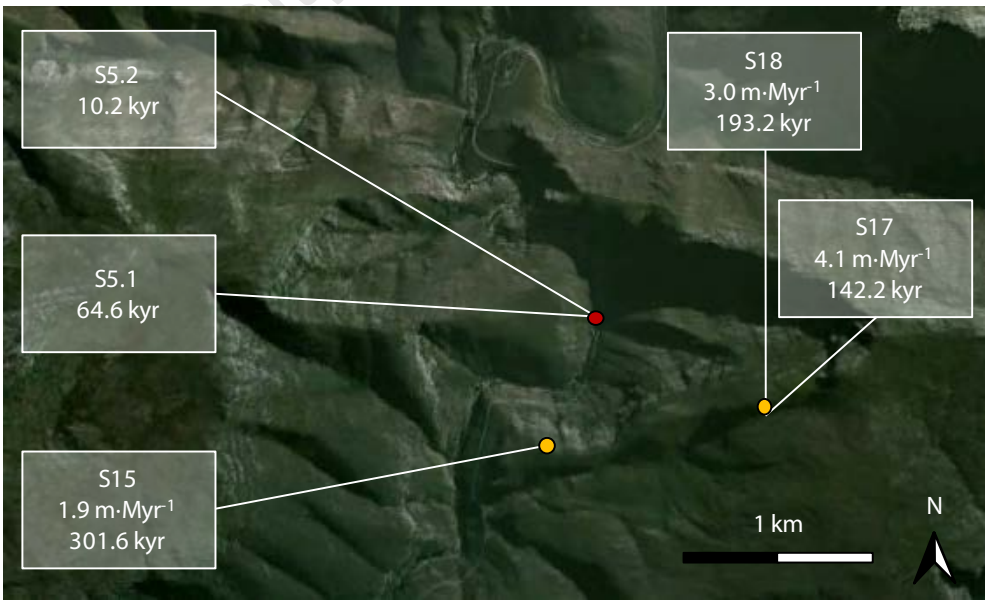

Figure 6.2: The spatial distribution of bedrock samples within Tradouw Canyon (cf. Figure 6.1). White boxes list, from top to bottom, the sample ID, maximum denudation rate and minimum exposure ages of the samples. Uncertainties have been omitted for the sake of clarity. The background satellite image was captured from Google Earth.

6.2.2 Results of alluvial terrace analysis

Two depositional terraces were analysed, namely terrace S1 and terrace S2. Four samples were removed from terrace S1 (S1.2-S1.5), one of which produced a beam current too low to be measured. Of the three remaining samples, no relationship between sample ^{10}Be concentration and sample burial depth was detected (Figure 6.3). The three samples analysed from terrace S2 (S2.1-S2.3) show decreasing TCN concentrations with increasing sample burial depth but the relationship is poorly described by an exponential curve (Figure 6.4). The spatial distribution of the terrace data is reviewed in Figure 6.5.

Uncertainties surrounding the burial and erosion of terrace S2, as well as the limited number of data points available, inhibited the use of a chi-squared inversion method (Chapter 3) to determine the paleodenudation rate and abandonment age of the terrace (further discussed in Chapter 7). The paleodenudation rate and abandonment age reported in Table 6.3 are thus based on the two-sample method of Anderson et al. (1996) and Repka et al. (1997), whilst taking into consideration the shielding effect of the overlying soil horizon (Chapter 3).

Table 6.3: Paleodenudation rates and abandonment ages of alluvial terraces. All uncertainties are reported to one sigma level.

Sample ID	Lat. (deg.)	Long. (deg.)	^{10}Be measured (10^6 atoms·g^{-1})	Production rate† (atoms·g^{-1}·yr^{-1})	Paleodenudation rate (m·Myr^{-1})	Terrace age (kyr)
S1.2	-34.00639	20.70333	0.38 ± 0.02	4.38 ± 0.46		
S1.3	-34.00639	20.70333	1.43 ± 0.08	4.38 ± 0.46		
S1.4	-34.00639	20.70333	0.41 ± 0.01	4.38 ± 0.46	—	—
S1.5	-34.00639	20.70333	CURRENT TOO LOW	4.38 ± 0.46		
S2.1	-34.00458	20.70661	0.20 ± 0.01	4.40 ± 0.46		
S2.2	-34.00458	20.70661	0.33 ± 0.01	4.40 ± 0.46	7.2 ± 1.1	128.0 ± 18.9
S2.3	-34.00458	20.70661	0.51 ± 0.03	4.40 ± 0.46		

†Production rates are surface production rates, uncorrected for burial shielding. The paleodenudation rate and terrace age of terrace S2 were calculated by correcting the surface production rate for burial shielding by 0.6 m of soil. Then density of the overlying soil was taken to be 1.52 g·cm^{-3}.

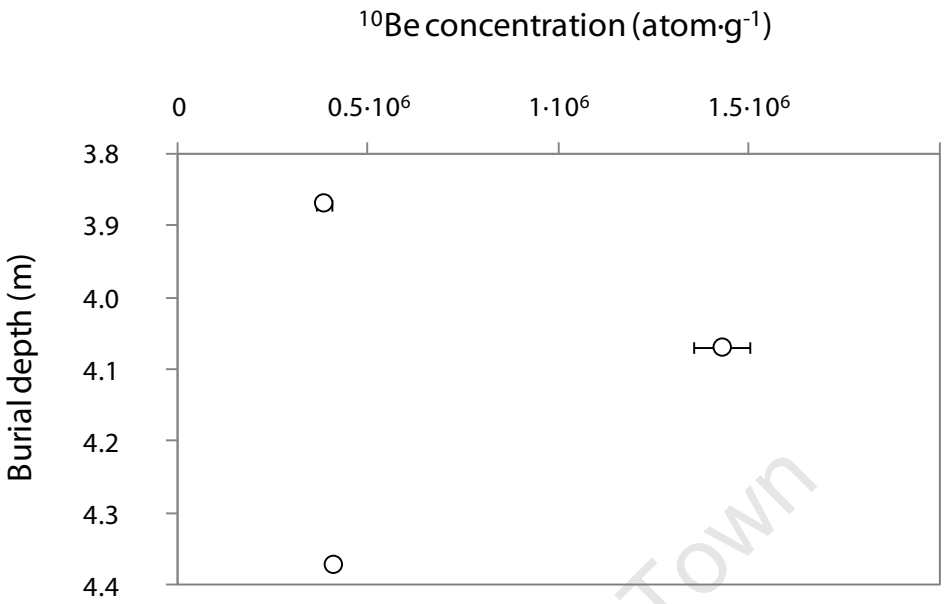

Figure 6.3: Depth profile of terrace S1. Sample ^{10}Be concentrations do not show any relationship to sample burial depth.

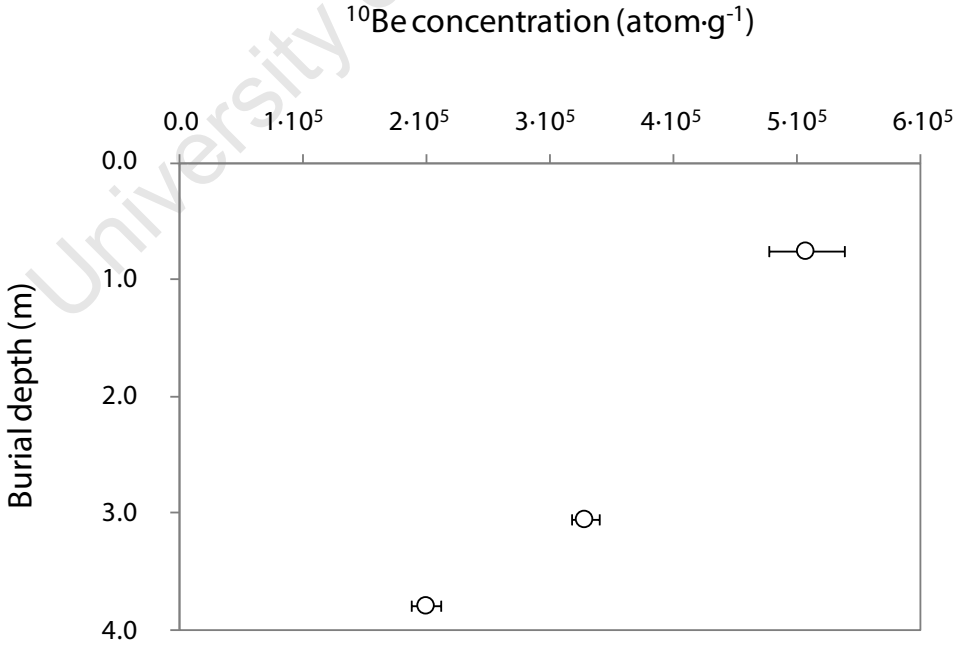

Figure 6.4: The ^{10}Be concentration-depth profile of terrace S2 is not well described by a decreasing exponential curve.

Figure 6.5: A bird's eye view of the southern foot of the Langeberg Range, at the southern entrance to Tradouw Pass, showing the spatial distribution of alluvial terraces and radiocarbon samples (cf. Figure 4.18). White boxes include the sample ID, paleodenudation rate and terrace abandonment age of terrace S2; and the sample ID and minimum abandonment age of terrace S1, constrained by radiocarbon ages of overlying organic-rich deposits. The background satellite image was captured from Google Earth.

6.3 Radiocarbon analysis

Radiocarbon samples were collected from an approximately 4 m thick muddy silt deposit overlying terrace S1 (cf. Figure 6.5). Radiocarbon concentrations reported in percent modern carbon, and conventional radiocarbon ages reported in years before present, were calculated according to Stuiver and Polach (1977). Both conventional radiocarbon ages and calibrated radiocarbon ages were determined with the use of Oxcal v4.17 (Bronk Ramsey et al., 2010; Bronk Ramsey, 1995). Calibrated radiocarbon ages were calibrated with the internal calibration curve IntCal09 (Riemer et al., 2009). The results of radiocarbon analysis can be viewed in Table 6.4.

Table 6.4: Radiocarbon ages of charcoal samples removed from the silt deposit overlying terrace S1. Uncertainties are reported to one sigma level.

Sample ID	Lat. (deg.)	Long. (deg.)	Depth (cm)	^{14}C (pmC)	CRA† (BP)	calBP‡ (95.4%)
R1.1	-34.00639	20.70333	3.82	64.15	3567 ± 31	3980 – 3820 (84.5%)
R1.2	-34.00639	20.70333	3.02	67.00	3217 ± 30	3490 – 3370 (93.8%)
R1.3	-34.00639	20.70333	1.72	68.56	3032 ± 30	3350 -3250 (95.4%)

†Conventional radiocarbon age.

‡Calibrated radiocarbon age in years BP, within a 95.4% certainty range. Each sample analysed returned more than one radiocarbon age which meets this criterion; therefore, the ages tabulated above are those which had the highest relative likelihood of being correct. The relative likelihood is reported as a percentage value, enclosed in parenthesis, adjacent to calBP age.

6.4 Channel steepness index analysis

Normalised channel steepness indices (k_{sn} values) were calculated according to Whipple et al. (2007) using the batch profiler code of these authors, ArcGIS 9.3, MATLAB R2011A and the 90 m SRTM DEM (http://srtm.csi.cgiar.org/). The batch profiler code allows the k_{sn} values for all stream segments within a defined catchment to be calculated simultaneously.

Parameters used in the analysis of the 10 sampled catchments, as well as the analysis of major catchments across the entire of the coastal Cape Mountains, are presented in Table 6.5. Rivers are defined as having a minimum drainage area of 10^6 m^2 in accordance with Tucker and Whipple (1999) and Montgomery and Foufoula-Georgiou (1993) who note that the cross-over between colluvial channels and bedrock channels occurs in the range of 10^5-10^6 m^2. A Theta Ref value of 0.45 is considered descriptive of areas undergoing active tectonic uplift (Tucker and Whipple, 1999). Theta Ref was set to a value of 0.45 in order to facilitate the comparison of k_{sn} values in the coastal Cape Mountains with those published for uplifting orogens (e.g. Kirby and Whipple, 2003; Ouimet et al., 2009). Normalised channel steepness index data can be viewed in Table 6.6 and Figure 6.6.

Table 6.5: The parameters required for the batch profiler code of Whipple et al. (2007), as defined in this study.

Parameters for batch profile analysis	Settings used in this study
Theta Ref	0.45
Remove Spikes?	Yes
Step Remover?	No
Smooth Profile?	No
Smoothing Window	N/A
Sampling interval (m)	20
Auto k_{sn} Window (km)	1
Search Distance (pixels)	10
Minimum Accumulation (pixels)	10

Table 6.6: Normalised channel steepness indices averaged per catchment sampled. All uncertainties are reported to one sigma level.

Sample ID	Lat. (deg.)	Long. (deg.)	Normlised channel steepness index (k_{sn})
S03	-33.99541	20.66277	111.2 ± 84.4
S04	-33.99296	20.70459	57.9 ± 43.5
S06	-33.43325	21.40669	92.7 ± 70.3
S07	-34.02089	21.35044	73.5 ± 25.1
S08	-33.98339	20.84508	92.5 ± 43.3
S09	-33.98122	20.37606	132.4 ± 101.9
S10	-33.98514	20.42211	241.1 ± 197.6
S11	-33.46236	21.215	221.5 ± 134.4
S12	-33.39631	22.357	116.2 ± 46.2
S13	-33.35956	22.179	113.1 ± 36.6

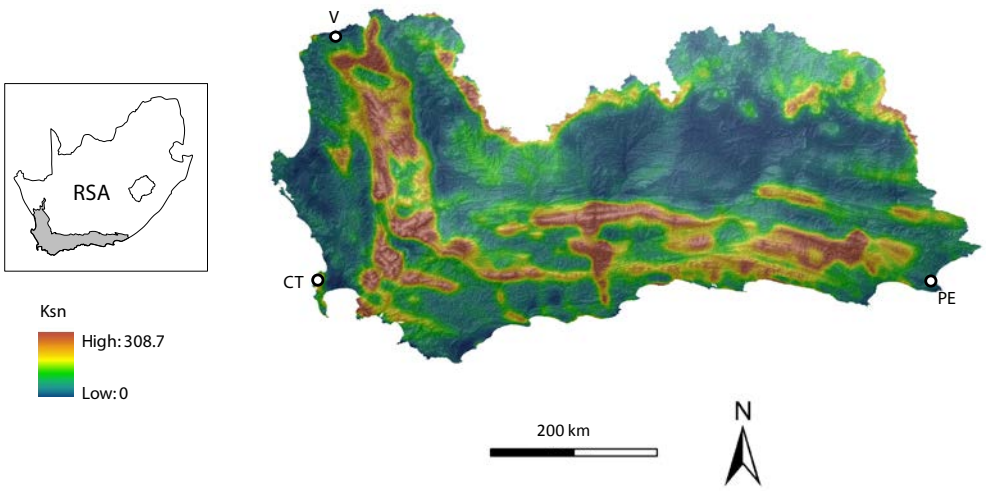

Figure 6.6: Graphical representation of the distribution of normalised channel steepness indices across the coastal Cape Mountains. Insert shows the distribution of the coastal Cape Mountains across South Africa. Towns are indicated by acronyms: V – Vanrhynsdorp, CT – Cape Town, PE – Port Elizabeth.

6.5 Summary

Sampled catchments report an averaged denudation rate of 4.6 ± 1.1 m·Myr^{-1} and are indistinguishable between the Langeberg and Swartberg Ranges. Bedrock denudation rates are comparable to catchment-averaged denudation rates.

Alluvial terrace samples do not show an exponential decrease in ^{10}Be content with increasing sample depth. Consequently, calculations of paleodenudation rate and terrace abandonment age were only possible for terrace S2 which returned a paleodenudation rate of 7.23 ± 1.1 m·Myr^{-1} and an abandonment age of 128.0 ± 18.9 kyr. Radiocarbon samples show a trend of increasing radiocarbon age with increasing burial depth. CalBP ages lie between 4 kyr and 3 kyr. As the radiocarbon samples overlie terrace S1, the lowest sample constrains the minimum abandonment age of terrace S1 to at least 4 kyr.

Calculation of the normalised channel steepness indices within the coastal Cape Mountains shows a uniform distribution of k_{sn} values from the western to the eastern limits of the mountain belt. High k_{sn} values are confined to the high-lying mountain ranges.

Chapter 7:

Discussion and conclusions

7.1 Introduction

The results presented in Chapter 6 are some of the first quantitative data available for the coastal Cape Mountains. Chapter 7 presents an interpretation of these results in Section 7.2. The implications of these results are discussed in the context of the coastal Cape Mountains, southern Africa and global geomorphology in Sections 7.3, 7.4 and 7.5, respectively. The findings of this study are concluded in Section 7.6.

7.2 Interpretation of results

7.2.1 Bedrock and river sediment samples

Catchment-averaged denudation rates from the Langeberg and Swartberg Ranges include among them some of the lowest catchment-averaged denudation rates in the world (cf. Portenga and Bierman, 2011), with a minimum of 2.1 m·Myr^{-1} (S7) and a maximum of 6.9 m·Myr^{-1} (S11). Furthermore, there is close agreement between the average denudation rates of the 10 catchments sampled, which differ by as little as 0.1 m·Myr^{-1} in the case of S3.1 (Langeberg Range) and S13 (Swartberg Range) and by as much as 4.7 m·Myr^{-1} in the case of S7 (Langeberg Range) and S11 (Swartberg Range).

These low rates coupled with low variability are particularly surprising when one considers:

1. The strong correlations seen globally between relief, hillslope angle, channel steepness and catchment-averaged denudation rates (Chapter 2), and in view of the roughness of the coastal Cape Mountains' terrain, which is comparable to that of some of the fastest denuding areas on earth (relief varies between 905 m and 1544 m amongst the sampled catchments, six of which have catchment-averaged slope angles between 20° and 30°).
2. The low variability appears scale invariant as it does not reflect the two orders of magnitude variation in the size of sampled catchments.
3. This low variability occurs despite the large spatial separation between the respective catchments (an approximate maximum of 120 km).

Assuming steady-state erosion, such low and spatially uniform denudation rates indicate a tectonically quiescent landscape where stability has prevailed on the mountain slopes, in the very least, since the late-Pleistocene. The definition for averaging time scale as described in Chapter 3, namely the time period over which cosmogenic nuclide data averages, is revisited here in Equation 7.1.

$$T_{ave} = \frac{z^*}{\varepsilon} \qquad 7.1$$

T_{ave} is the averaging time scale over which the denudation rates apply, z^* is the absorption length in a silicate rock and ε is the denudation rate measured (Dunai, 2010). Substituting 0.6 m for z^* (Dunai, 2010; Gosse and Phillips, 2001), 2.1 m·Myr^{-1} for a minimum value of ε and 6.9 m · Myr^{-1} for a maximum value of ε, a minimum averaging timescale of 0.1 Myr-0.3 Myr is obtained.

Maximum bedrock exfoliation rates obtained from samples S15 (1.9 ± 0.2 m·Myr^{-1}), S17 (4.1 ± 0.5 m · Myr^{-1}) and S18 (3.0 ± 0.3 m · Myr^{-1}) on the interfluves of Tradouw River Canyon are very similar to catchment-averaged denudation rates throughout the study area in the coastal Cape Mountains, either overlapping

with the lowest catchment-averaged denudation rates or being slightly lower than these values. As such, these bedrock denudation rates are considered closely representative of the dominant denudational processes operating on slopes within these catchments. Field observation suggests that such processes include spalling of highly jointed and fractured bedrock on the interfluves, where fragments centimetres in thickness may be lost instantaneously; comminution of regolith in transit down slope; and chemical weathering where dense vegetation (particularly *Leucadendron eucalyptifolius* of the genus of *Proteacea*, which grows prolifically on the wet, south-facing slopes) promotes the retention of water, as evidenced by saprolitic rock outcrops in densely vegetated areas. A reader unfamiliar with these processes may wish to refer to Sparks (1960).

The ^{10}Be inventories of bedrock samples S5.1 and S5.2, sampled just above the present-day Tradouw River, are representative of the surface exposure ages. Chatter marks preserved on these bedrock benches are evidence that the surfaces of these outcrops have been negligibly affected by erosion since the time of their formation. Calculations of surface exposure age return ages of 64.6 ± 7.1 ka and 10.2 ± 1.2 for S5.1 and S5.2, respectively (Chapter 6). As these two bedrock benches are separated by a vertical distance of 5.5 m, one can calculate the time it took Tradouw River to incise from S5.1 to S5.2, by dividing their vertical height difference (5.5 m) by their difference in surface exposure age (~54.4 ± 7.2 ka). Doing so yields an incision rate of 101.1 ± 7.2 m·Myr^{-1}.

The incision rate determined from S5.1 and S5.2 does not agree with catchment-averaged denudation rates but instead implies a localised denudation rate that is higher than any other denudation rate determined in this study area of the coastal Cape Mountains. It was noted in the field that the orientation of S5.1 and S5.2 and the accompanying, unsampled bedrock benches coincided with what is either the local bedding orientation, or the orientation of stacked thrust fault planes (Chapter 4). Given the common occurrence of large (on the meter scale) tabular rock slabs in the bedrock channels of the cliff-bounded upper reaches of the rivers, and the thick-bedded nature of the Peninsula Formation quartzite, a likely explanation could be loss of large masses of rock which are dislodged from the bedrock along the inherent weaknesses that are bedding, fault and joint planes

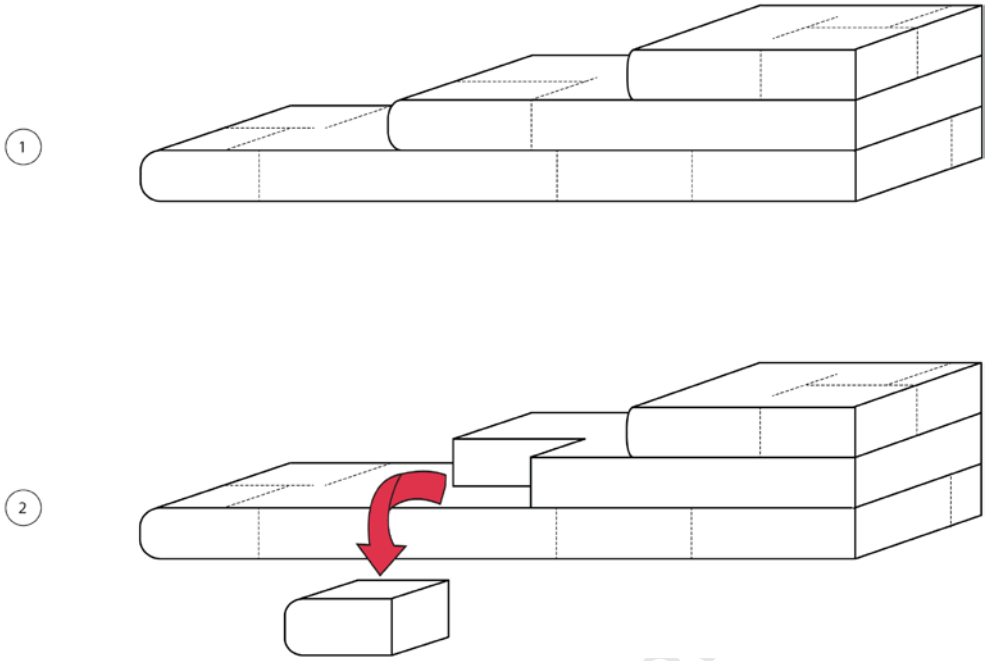

Figure 7.1: The density and orientation of bedding planes, fault planes, joint planes and fracture planes can have a large influence on rock mass strength and erodibility (Chapter 2). Where these planes of weakness intersect, the bedrock is particularly susceptible to erosion. Large bedrock benches such as S5.1 and S5.2, which indicate an anomalously high local incision rate, may be rapidly formed by the instantaneous loss of large blocks of bedrock that have been 'loosened' through the intersection of joints and bedding. These large blocks may be dislodged during episodes of increased stream flow (e.g. flash flood) where the turbulent waters have a greater potential to pluck and redistribute the rock mass. A similar process may operate on the near vertical canyon walls; however, gravity is likely to be the force which displaces the rock mass. In the above diagram, the stippled lines represent joint and fracture planes and the solid lines represent bedding and fault planes.

(Figure 7.1). The low catchment-averaged denudation rates reported throughout the study area are an indication that these events are infrequent occurrences.

The incision rate obtained from S5.1 and S5.2 is thought to reflect these rare episodes of rapid, large rock mass loss. This is not to say that S5.1 and S5.2 do not represent true strath terraces of Tradouw River. Simply put, the formation of straths such as S5.1 and S5.2 is likely due to the erosive action of infrequent high-power flood events acting on inherent structural weaknesses within the bedrock. The plethora of percussion marks across their surface must similarly owe their origin to infrequent flood events as the present-day Tradouw River does not have

the power to move the gravel that blankets its channel, let alone the coarse bedload of pebbles and boulders which are likely responsible for such markings.

A denudation rate determined from river sediment returns a catchment-averaged denudation rate that is weighted according to the various 'local' denudation rates within the respective catchments, and the areas over which these 'local' denudation rates apply (Brown et al., 1995; Bierman and Steig, 1996; Granger et al., 1996; Chapter 3). Bedrock denudation rates reported by S15, S17 and S18 were all particularly low, lower than or overlapping with the lowest of the catchment-averaged denudation rates in the region. These rates were interpreted to reflect the rates of spallation of thin sheets of rock ('exfoliation'), chemical weathering and granular disintegration of the bedrock. In contrast, S5.1 and S5.2 report a localised incision rate that far exceeds all catchment-averaged denudation rates determined for the region by this study, and is interpreted to represent the infrequent loss of massive rock spalls. The catchment-averaged denudation rate of Tradouw River is therefore a weighted average of these slow rates of gradual bedrock down-wearing (S15, S17, S18) and rapid rates of bedrock mass wasting (S5.1, S5.2). The close agreement between rates of gradual bedrock denudation and catchment-averaged denudation rates indicate the continued and pervasive action of incremental down wearing of bedrock within the catchments, while the significant difference between rates of mass wasting and catchment-averaged denudation rates may indicate the infrequent occurrence of mass wasting events and their confinement to the bedrock river channels and bounding steep, near vertical bedrock walls. This conceptual model infers that granular disintegration and exfoliation of thin rock layers contributes to the production of catchment sediment far more frequently than do mass spallation, rock falls or plucking of bedrock.

Alternatively, one could reason that the loss of such a large amount of bedrock so as to create a localised incision rate of 101.1 ± 7.2 $m \cdot Myr^{-1}$ may occur as frequently as other forms of mass wasting. In order to account for the consistently low catchment-averaged denudation rates measured from river sediment throughout the region, despite such frequent episodes of rapid erosion, it is necessary to infer that the rock mass lost remain in the river channel as one of the massive tabular boulders described, for an indefinite amount of time during which

it slowly accumulates a higher TCN concentration and gradually loses mass through abrasion during infrequent events of increased stream flow. However, if this were the case, the upper reaches of the catchments would be choked with boulders and the debris of rock falls. This is not seen in the field and consequently this hypothesis is rejected. As the mean of catchment-averaged denudation rates for the region are skewed to low values such as those reported from S15, S17 and S18 rather than high values as reported from S5.1 and S5.2, slow incremental down-wearing of bedrock is considered to dominate over uncontrolled mass wasting in terms of sediment production. However, as slope failure is capable of redistributing much larger quantities of rock and sediment in a much shorter space of time than is possible with incremental bedrock down-wearing (Niemi et al., 2005), the morphology of these catchments may be largely governed by the frequency and spatial distribution of mass wasting events.

A short-fall of this conceptual model is the small sample area and the limited number of samples. Only 5 bedrock samples were collected within Tradouw River catchment. Systematic sampling of bedrock surfaces from hillslope and bedrock channel environments throughout the coastal Cape Mountains is required to test the hypothesis outlined above. Increasing the number of samples would allow one to clearly discern outliers from the general trend of bedrock erosion rate and the spatial distribution of the various denudational mechanisms operating within the catchments. Furthermore, increasing the number and type of bedrock environments sampled within the Cape Mountains will likely increase the accuracy of estimations of the relative contributions of incremental bedrock down-wearing and rapid mass wasting to overall catchment-averaged denudation rates.

7.2.2 Paleodepositional terraces

Depth profiles were sampled from two alluvial terraces (S1 and S2) flanking the Tradouw River. Samples collected from an undisturbed paleodepositional terrace should show an exponential decline in TCN content with an increase in sample burial depth; a relationship which allows for the determination of the paleodenudation rate and exposure age. Exposure age is here taken to be synonymous with the abandonment age of the terrace (Chapter 3).

In the case of terrace S1, sample ^{10}Be concentration does not appear to correlate with sample burial depth. This may indicate post-depositional reworking of the terrace material (Hancock et al., 1999; Chapter 3); a hypothesis supported by the field observations that the present-day Tradouw River has incised approximately 5 m from the top of the soft clays overlying the terrace material, and that meander scars appear in the vicinity of the sampling site. These two points underscore the dynamic, as opposed to static, behaviour of Tradouw River in its floodplain. Alternatively, the scatter in the data might be due to outliers which cannot be discerned from the main data trend with so few data points.

In the case of terrace S2, the sample ^{10}Be concentration-burial depth relationship is poorly described by an exponential curve. Furthermore, calculations of paleodenudation rate and terrace abandonment age for terrace S2 were hindered by the limited number of data points with which to model these parameters, and by uncertainties regarding the potential burial and erosion of the deposit.

It was noted in the field that terrace S2 is mantled by 60 cm of soil, the age of which is unknown. Shielding by overlying soil can decrease TCN production rates in the underlying terrace material by attenuating the cosmic ray flux passing through the shielded subsurface. This scenario could lead to an underestimation of the terrace abandonment age, should the overburden be significant. Furthermore, deposits in the vicinity of terrace S2 commonly display signs of mass creeping, cautioning that terrace S2 may have experienced similar erosion in the recent past. However, the present-day soil atop terrace S2 indicates that mass creep is not currently operating to a large extent on terrace S2 and thus may be an episodic occurrence. Erosion would remove the upper layers of terrace material in which the highest TCN concentrations would occur, effectively reducing the apparent abandonment age of the terrace (e.g. Hancock et al., 1999).

The applicable shielding scaling factor of the overlying soil horizon was described in Chapter 3. This equation is revisited here as Equation 7.2 for shielding by burial, where z is the thickness of the overburden, ρ is the density of the overburden and Λ the attenuation length for spallogenic reactions (Dunne et al.,1999; Chapter 3).

$$f_{cover} = e^{\frac{-z\rho}{\Lambda}} \qquad 7.2$$

Substituting 60 cm for z, 1.52 g·cm^{-3} for ρ, and 160 g·cm^{-2} for Λ, yields a shielding scaling factor of 0.57. The presence of the overlying soil horizon would therefore cause a 43% reduction in production rate in the underlying terrace material. The effect of erosion would depend on the rate of erosion, for which there is no available estimation.

In the case of a terrace continuously eroding at a steady pace, the TCN content of the terrace material can be calculated as a function of time, depth and erosion rate with the use of analytical formulae (Muzikar, 2009; Chapter 3). When the erosion rate is not known, a Chi-squared inverse modelling technique (Siame et al., 2004; Braucher et al., 2009; Chapter 3) can be used to solve for the denudation rate and exposure age that best describe the TCN concentrations of the samples and model for inheritance (e.g. Carretier et al., 2006; Chapter 3). As discussed in Braucher et al. (2009) a minimum of 6 samples is required to accurately constrain the exponential decrease in TCN concentrations with depth; with fewer samples one might not be able to discern outliers from the norm. For terrace S2, three data points (S2.1-S2.3) are known. Too few data points exist to satisfactorily solve for the large number of unknowns by means of Chi-squared inverse modelling.

In the absence of a suitable method to account for these uncertainties with so few data points, paleodenudation rate and abandonment age were calculated under the assumption that erosion has not affected terrace S2 and that the soil cover has been in place since the formation of the terrace. The two-sample method of Anderson et al. (1996) and Repka et al. (1997) was applied to yield a minimum terrace exposure age which can be viewed as the minimum abandonment age of the terrace. The assumption of no erosion is not necessarily a gross misrepresentation of the true field conditions as the presence of the soil horizon also indicates that, *at present*, the terrace is not eroding.

The validity of the above calculation is, however, questioned by the poor fit of the original AMS data to an exponential curve. Given that terrace S1 is likely to have been reworked, there is reason to suspect that terrace S2 may have been similarly reworked. As only three data points exist, it cannot be stated whether the decrease in sample TCN concentration with depth in terrace S2 is, in fact, the result of decreasing production rate with depth in an undisturbed deposit, or whether it is simply a random occurrence amongst reworked material. Further sampling is required to resolve this issue. Nevertheless, terrace S2 yields a paleodenudation rate of ~7.2 ± 1.1 m·Myr^{-1} and an abandonment age of ~0.13 ± 0.02 Ma, based on the above assumptions of the two-sample method. An estimation of denudation rates within the Bokkeveld Group shales to the south of the Langeberg Range can be estimated using the exposure age of terrace S2 (0.13 Ma) and its elevation above the present-day Tradouw River (~13 m) which results in a denudation rate of 100 m·Myr^{-1}.

Providing that terrace S2 has not been reworked, in which case the calculations of abandonment age and paleodenudation rate are reliable, it becomes evident that terrace S2 records an event during which the denudation rate, as measured in pebbles sourced from the quartzites of the mountains, was approximately twice as high as that recorded by sand sourced from these self-same mountains. In addition, the abandonment age of the terrace lies within the time period over which catchment-averaged denudation rates for the south-western Cape Mountains are averaged.

The averaging timescale of a catchment-averaged denudation rate is equivalent to the amount of time that the analysed target minerals spend within a depth of one absorption path length from the rock surface (Lal, 1991; Dunai, 2001; von Blanckenburg, 2005; Chapter 3). Disregarding production by muons, this corresponds to the amount of time spent within the upper 0.6 cm in a horizontal, unshielded silicate rock. Naturally, this averaging timescale is inversely proportional to the rate at which these minerals are excavated. Low denudation rates, such as those reported here for the coastal Cape Mountains, average over a long time period and have the potential to average over short-lived fluctuations in denudation rate (Bierman and Steig, 1996; Schaller et al., 2002; von Blanckenburg, 2005; Chapter 3). The term 'short-lived' implies that the elevated denudation

rates do not prevail for long enough to uncover material which lies more than one absorption length below the surface of the rock.

If terrace S2 represented one such short-lived event, the TCN content of its pebbles would be similarly high to that of sediment found in the rivers of the coastal Cape Mountains. Erosion would have been both rapid and brief, removing the upper few centimetres of rock without uncovering material lying below one absorption length, thus not removing material with a notably lower TCN content to that found at the surface of the rock. In such a scenario the TCN content of river sediment sourced from the same rock would remain relatively undisturbed; however, gravel deposits would report denudation rates similar to that determined from river sediment and not a denudation rate which is approximately twice as high as that determined from river sediment. The disparity between the low denudation rates determined from river sediment and the elevated denudation rate reported from the terrace pebbles is therefore not considered to be the work of a short-lived fluctuation in overall catchment-averaged denudation rates occurring approximately 0.3 Myr in the past.

The difference in denudation rates reported from terrace pebbles and river sediment is interpreted to reflect different processes occurring in the catchment in much the same way that bedrock samples S15, S17 and S18 are considered to reflect different denudational processes to S5.1 and S5.2. The pebbles of terrace S2 may represent material lost from bedrock surfaces in shallow rock falls or rock slides, or the regolith that one sees atop the mountain spurs that has been removed from the heavily jointed bedrock as rock spalls of centimetre-scale thickness, and that has subsequently been reduced to its current size through down-hill comminution and in-stream abrasion. Niemi et al. (2005) note that a landslide with a 10 m radius can erode to a depth of approximately 100 cm, with larger landslides eroding deeper. Processes of mass wasting therefore erode to a great depth far quicker than granular disintegration, thus supplying clasts with lowered TCN concentrations to the rivers.

The implication of the above is that terrace remnants do not represent periods of increased denudation rates characterised by a change in the denudational processes operating in the catchments. The ‘paleodenudation rate’ reported from

terrace S2 might very well be reported from similar sized pebbles collected within the present-day channel and be representative of processes currently active within the catchments. While the reworking of terrace S1 prevents the calculation of the paleodenudation rate and abandonment age of the terrace, as well as the calculation of denudation rates reported by individual terrace samples, these samples might still be of value to the argument presented here. As a rough evaluation, the ^{10}Be content of S1.2, S1.3 and S1.4 can be compared to that of S2.1, S2.2 and S2.3. Doing so shows the TCN content of S1.2, S1.3 and S1.4 to be very similar to that of S2.1, S2.2 and S2.3, with all terrace S1 samples falling within the range defined by terrace S2 samples. This might reflect continuity in the rates of denudational processes through time, indicating that the elevated paleodenudation rate reported by terrace S2 may not necessarily be a 'paleo' phenomenon at all.

Terrace S2 does, however, evidence increased discharge in the streams, as the gravel which lies motionless on the present-day river beds had to have been mobilised, transported and deposited to create the terrace. No doubt such an increase in discharge brings with it an increase in channel abrasion due to the mobilisation of this course sediment which would otherwise shield the underlying bedrock channel (Chapter 2). In doing so, the protective gravel is effectively converted into tools for channel abrasion. The inference that catchment-averaged denudation rates increased to 7.2 ± 1.1 m · Myr^{-1} during these episodic flood events is, however, not necessarily supported by the data.

7.2.3 Radiocarbon analysis

Radiocarbon analysis of three organic-rich samples collected at varying depths within the ~4 m mud deposit overlying terrace S1 returned unique ages for each sample. This horizon, accrued over the past ~3.5 ka, may represent the successive deposition of over-bank deposits related to episodic flooding or, alternatively, the slow, incremental growth of muddy channel deposits of a more sluggish Tradouw River (or Grootvaderbos River) than is seen today. It is interesting to note that the present-day Tradouw River has since incised through this ~4 m mud deposit and uncovered the pebbly deposit of terrace S1 below it.

Tradouw River is not the only river to have incised meters into its deposits. Similar incision was recorded at the sampling site of S7, on Tierkloof farm, where the unnamed river had worn its way through 3-4 m of overlying mud to reach its present day position. There is thus evidence for local river incision in the flood plains, while denudation rates recorded in the quartzite of the mountains do not reflect this. Two factors are likely responsible for this apparent disparity.

1. Both that portion of the river which drains the quartzites and that portion which flows out into the adjacent lowlands may have experienced increased incision rates during short-lived episodes of river stream-power rejuvenation under some external forcing, be it climatic or tectonic. Such episodes of incision would necessarily be shorter than the timescale over which the cosmogenic nuclide data averages, and therefore not resolved by cosmogenic nuclide analysis which tends to average over short-lived fluctuations in denudation rate. Denudation rates as low as those in the coastal Cape Mountains would average out moderate fluctuations in denudation rate over time periods equivalent to that of glacial-interglacial periods (~20-120 ka) and thus not reflect short-lived periods of increased denudation rate (von Blanckenburg, 2005; Schaller et al., 2002; Bierman and Steig, 1996; Chapter 3).
2. Small-scale stream rejuvenation is likely to be dampened once the signal, propagating up the river channels, reaches the resistant quartzites and metasandstones of the mountains. Strong-rock landforms have been reported to act as near-permanent knickpoints in the landscape where signals for river incision are dramatically dampened or lost all together (e.g. Bishop and Goldrick, 2000; Goldrick and Bishop, 2007; Jansen et al., 2010). This phenomenon is often associated with postorogenic or nonorogenic regions where long-term denudation has removed the young incompetent rocks and sediments of the Cenozoic and exposed the more resistant, crystalline basement rock (Jansen et al., 2010). Incision is therefore at a minimum in the resistant quartzites but at a maximum in the incompetent muds and underlying shales of the flood plains. The vastly different competency and erosional potentials of shales as compared

to quartzite has been shown by Sklar and Dietrich (2001), Selby, (1980) and Montgomery and Schmidt (1995) as discussed in Chapter 2.

While the data do not allow for commentary on most episodes of incision and deposition recorded in the landscape, the timing of the most recent incision event, in which rivers to the south of the Langeberg have incised ~4-5 m into their flood plains, is constrained by the radiocarbon data to the last ~4-3.5 ka. Climatic fluctuations, local epeirogenic uplift, sea level fluctuations which could potentially lower river baselevel, and the natural occurrence of low-frequency, high-magnitude weather phenomenon could be called upon to explain this observation.

Eustatic curves are provided by Haq et al. (1987), Fleming et al. (1998), Waelbroeck et al. (2002), Bintanja et al. (2005) and Rohling et al. (2009). Data on sea level fluctuations around the southern African coastlines are provided by Siesser and Dingle (1981), Ramsay and Cooper (2002), Compton (2001), Carr et al. (2010) and Compton and Wiltshire (2009).

The eustatic curve of Haq et al. (1987) shows a constant increase in global sea level since the late-Pleistocene. This is supported by the more detailed work of Fleming et al. (1998) which likewise shows a constant rise in global sea levels at a rate of 10 $m \cdot ka^{-1}$ that begins to plateau at 7 ka. This same plateau appears in the sea level curve of Waelbroeck et al. (2002), Bintanja et al. (2005), and Rohling et al. (2009); although the sea level curve of Rohling et al. (2009) shows numerous minor fluctuations within the plateau region.

Sea level curves for southern Africa are very similar to eustatic curves. The work of Siesser and Dingle (1981) shows the same constant rise in sea level since the start of the Quaternary. Mention is made of Pleistocene sea level fluctuations; however their magnitude and timing is not described. Compton and Wiltshire (2009) report a similar pattern to that already outlined; however, their work comments only on the timing of sea level fluctuations and not on the magnitudes. The work of Carr et al. (2010) focuses on sea level fluctuations between 90-150 ka and is thus not applicable to the timeframe in question here. Ramsay and Cooper (2002), similar to previous authors, report a steep rise in sea level from ~18 ka - ~7 ka, at which point sea level remains constant. The detailed study of Compton (2001) on the Langebaan Lagoon, Western Cape, reports the same plateau in sea

level as seen in the work of the above mentioned authors; however, a number of ~ 1 m amplitude fluctuations are reported from 5 ka to present day.

If sea level were the driving force behind river incision seen south of the Langeberg Range, a relative drop in sea level of at least 4-5 m would be expected along the southern coast of South Africa. However, no relative drop in sea level of sufficient magnitude, and at the appropriate timing, is reported in the above-mentioned studies. There is thus little reason to suggest that the latest episode of incision is the result of sea-level fluctuations.

Data on climatic fluctuations across southern Africa since the late-Pleistocene are provided by Partridge (1993) and Partridge et al. (1990), with graphs showing the trends of temperature and wetness variations but not the magnitude of variations, available from Partridge et al. (1990). Whilst the southern and south-western coast of Africa – the location of the coastal Cape Mountains – have experienced both warmer and wetter conditions in the past (17-9 ka), conditions were drier between 8-5 ka. Since ~ 5 ka, climate has remained fairly constant with only minor fluctuations in temperature (± 2°) and similarly small fluctuations in wetness. One of these minor increases in wetness occurs between 3-2 ka, and thus overlaps with the time constraints placed on river incision. The increase in relative moisture noted between 3 ka and 2 ka could be associated with the most recent incision event seen in the landscape south of the Langeberg range, provided incision did not take place after 2 ka. However, it is doubtful whether such a small increase in precipitation could be the driving force behind 5 m of river incision.

Local epeirogenic flexure has also been proposed for the region by Taljaard (1949), who suggested an uplift axis to lie south of the Langeberg Range between Swellendam and Riversdale; and more recently by Lenz (1953) who inferred two uplift axes synonymous with two uplift events in the region. According to Lenz, the more recent of the two uplifts took place in the Mio-Pliocene along the same axis proposed by Taljaard, and succeeded in tilting the drainage network of the regions to the north. However, the timing of these proposed uplift events already excludes them from consideration as a trigger for the recent incision seen within rivers to the south of the Langeberg.

In the field it is seen that the course of the rivers, through the region of incision, are littered with cobbles and boulders up to 2 m in diameter. The larger of this coarse grained bedload (boulders meters in diameter) lies only in the present day channel and is not seen exposed in the flood plain muds or pebble terrace material through which these rivers have cut. As this material is not locally derived, a very large amount of discharge would have been required to transport such large quartzite boulders downstream from the mountains or to uncover and transport them from their original positions on higher (~300 masl or less) abandoned terraces that abut against the mountains, to their present position in the flood plains of these small, under fit rivers which drain the Langeberg Range. When one considers the strength of the flow which is required to move these boulders and that the rivers have incised through unconsolidated muds and sands to reach their present-day position, it is not unrealistic to propose that such deep incision may represent the effects of one flash flood event. Furthermore, the denudation rate approximated for the flood plains (100 $m \cdot Myr^{-1}$) based on the age of terrace S2 (130 ka) and the difference in elevation between terrace S2 and the present-day Tradouw River (13 m), might be the result of a series of such flash flood events cutting down through the incompetent shales and muds of the main river valley. The short-lived nature of these events and the notable resistance of quartzites prevents the cosmogenic nuclide data from reflecting such events while the high erodibility of main basin shales allows for incision through the valley floor with successive flood events.

7.2.4 Basin morphometrics

Catchment-averaged denudation rates show a positive correlation with catchment-averaged slope (Figure 7.2), well described by a linear function ($R^2 = 0.6$). Sample S4 (Tradouw River) plots some way from the general linear trend of the data due to an anomalously low catchment-averaged slope value of $12.4^{\mathbf{0}}$. Tradouw River catchment, however, is the largest in the dataset measuring ~329 km^2 and is one of only two that traverse the mountains. The majority of the Tradouw River catchment lies to the north of the Langeberg Range within the flat, low-lying shales of the Little Karoo basin. Selectively sampling sediment in the 250-500 µm grain size fraction would have had the effect of excluding any material derived

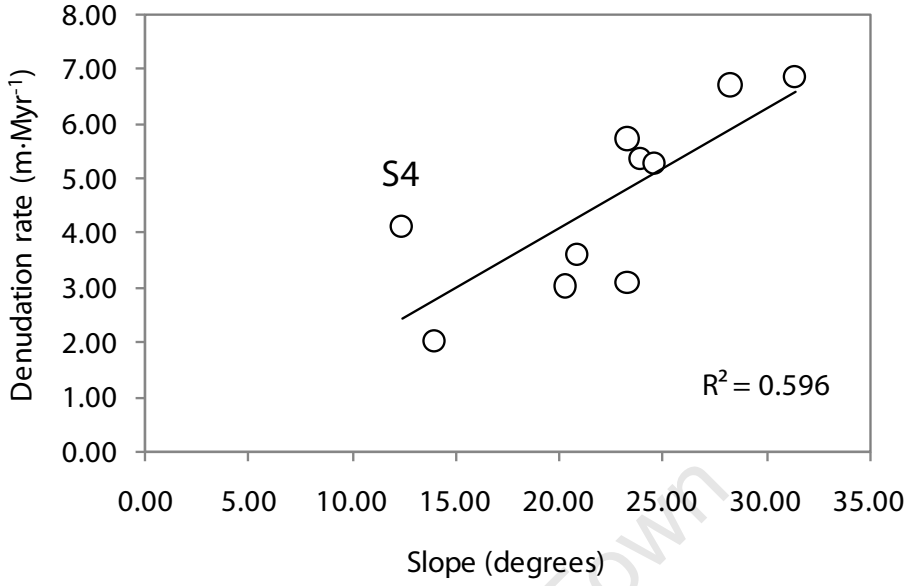

Figure 7.2: Catchment-averaged denudation rate versus catchment-averaged slope for the coastal Cape Mountains data set.

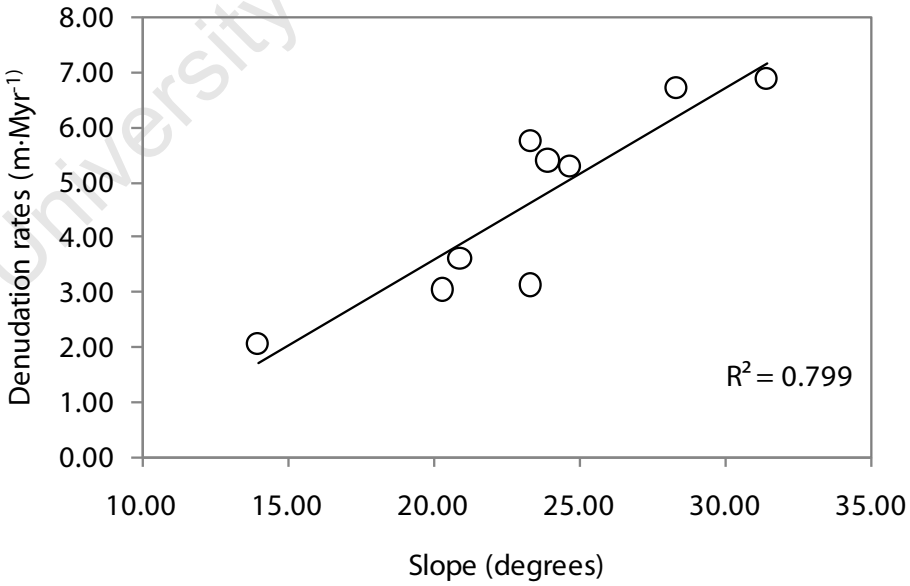

Figure 7.3: Catchment-averaged denudation rate versus catchment-averaged slope for the coastal Cape Mountains data set, S4 removed.

from the shales, from the sampled material. Sediment removed from Tradouw River is largely representative of the quartzites and metasandstones comprising the Langeberg Range, and not the low lying shales to the north thereof. It should be noted that while sandstone horizons do occur in the low-lying extensions of Tradouw River catchment to the north of the Langeberg Range they do not constitute the majority of this area and are not likely to contribute noticeably to overall catchment sediment due to the low slope of the region. Consequently, erosion rates largely reflect processes occurring in the canyon of Tradouw River while the catchment-averaged slope values reflect, to a large extent, the low-lying basin to its north. It should be noted that Seven Weeks River (S6), which also traverses the mountains, does not appear as an anomaly on the denudation rate-slope curve. This is likely due to the fact that the catchment upstream of the sampling point within Seven Weeks River lies largely within the mountains and not in the intermountain regions (cf. Figure 6.1, Chapter 6). Removing S4 yields a strong linear correlation between mean catchment slope and catchment-averaged denudation rates ($R^2 = 0.8$) as seen in Figure 7.3.

A similar positive, linear relationship exists between the catchment-averaged denudation rates and total catchment relief (Figure 7.4); however, this correlation is strongly off-set by the anomalously high relief of S6. S6 was collected from Seven Weeks River which flows through Seven Weeks Pass, host to the highest peaks of the Cape Mountains (~2325 masl). Removing point S6 from the data set yields a strong linear correlation with an R^2 value of 0.67 (Figure 7.5).

A further positive linear correlation is noted between catchment-averaged denudation rate and mean catchment steepness index (Figure 7.6). Once again, S4 is offset from the general trend due to the location of the majority of its catchment in the low-lying, highly erodible shales to the north of the Langeberg Range which results in a lower catchment-averaged value for channel steepness index. Removing S4 from the data set produces a strong linear correlation with an R^2 value of 0.7 (Figure 7.7).

The positive linear correlations between catchment-averaged denudation rate, catchment mean slope and catchment mean normalised channel steepness index,

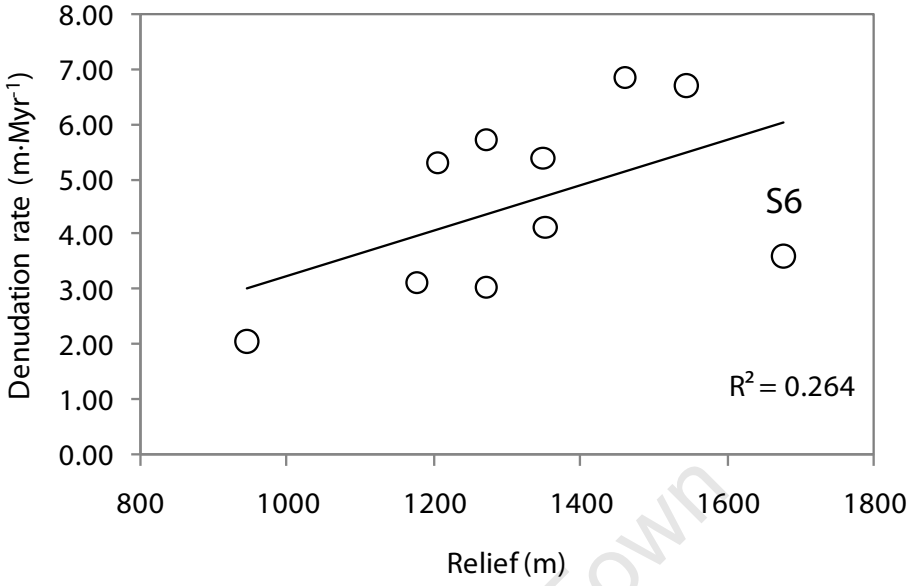

Figure 7.4: Catchment-averaged denudation rate versus total catchment relief for the coastal Cape Mountains data set.

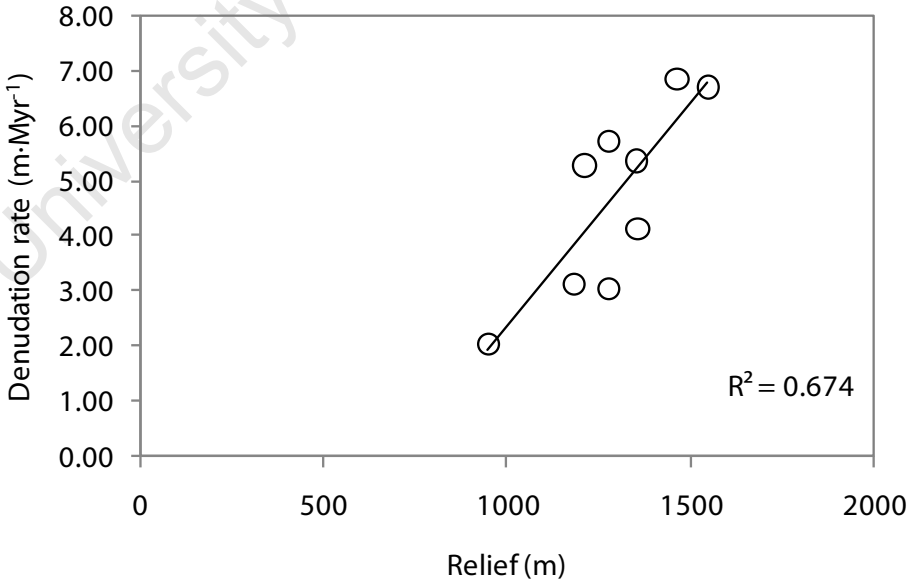

Figure 7.5: Catchment-averaged denudation rate versus catchment relief for the coastal Cape Mountains data set, S7 removed.

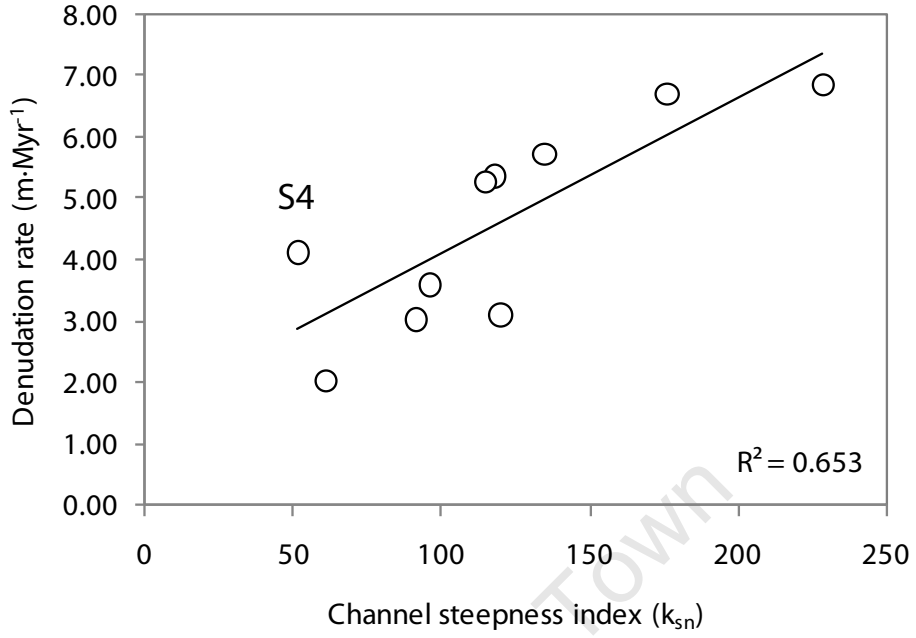

Figure 7.6: Catchment-averaged denudation rate versus catchment-averaged normalised channel steepness index for the coastal Cape Mountains data set.

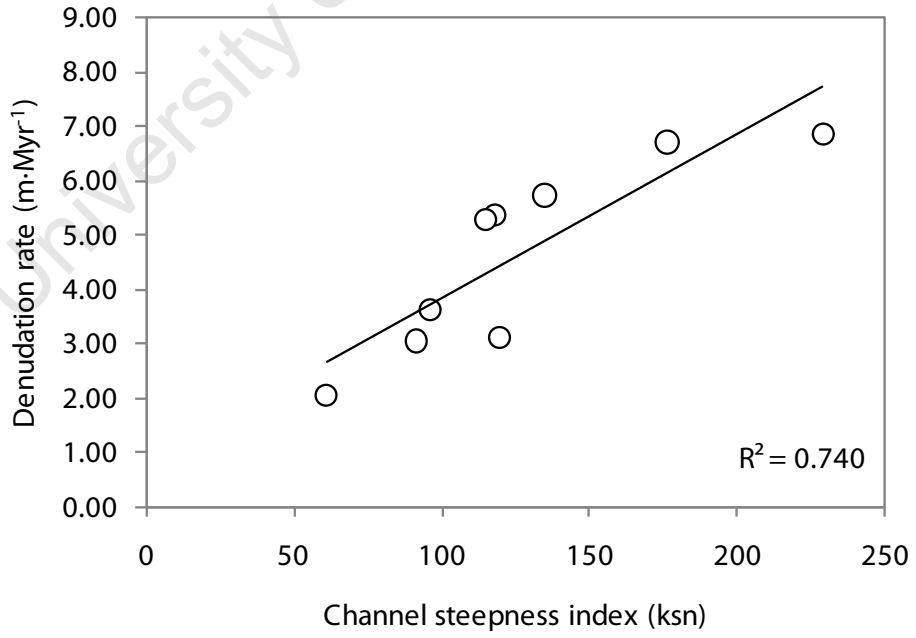

Figure 7.7: Catchment-averaged denudation rate versus normalised catchment-averaged channel steepness index for the coastal Cape Mountains data set, S4 removed.

indicate a coupling between hillslope and channel processes. Denudation on hillslopes keeps pace with that in river channels, which proceeds at fairly low rates of 2.1 $m \cdot Myr^{-1}$ to 6.9 $m \cdot Myr^{-1}$. Neither the exponential, positive relationship commonly reported for hillslope angles over 25° and attributed to debris flows, nor the decoupling of denudation rates and hillslope angles reported at slope angles of approximately 30° or more and attributed to landsliding, is seen in the data for the coastal Cape Mountains. This implies that these forms of uncontrolled mass wasting are not the dominant erosional processes operating in the area. The notably low catchment-averaged denudation rates indicate that, if these processes do occur, they must do so very infrequently. This is in agreement with deductions made in Section 7.2.1, based on comparisons of denudation rates obtained from river sediment, bedrock from the interfluves and bedrock in the present-day river channel.

7.2.5 Commentary on conditions prevailing in the coastal Cape Mountains

The persistently low denudation rates throughout the study area in the coastal Cape Mountains, coupled with low variability amongst these rates, indicates a large degree of stability in the landscape. Given the close agreement between bedrock denudation rates reported from the interfluves with that reported from river sediment, it appears that rates of soil production on hillslopes are in near equilibrium with rates of sediment flux in the catchment. Denudation rates on hillslopes are therefore limited by the rate of bedrock spalling and granular disintegration i.e. the slopes of Tradouw Canyon are a detachment-limited environment (e.g. Reneau and Dietrich, 1991).

One could also argue that the catchment is approaching topographic steady state under its present climatic conditions. Given that bedrock denudation rates on high elevation interfluves closely resemble the average denudation rate for the catchment – with the exception of possible infrequent mass wasting – there is reason to believe the valley floor is eroding at a pace very similar to that of its interfluves. Samples S5.1 and S5.2 complicate this interpretation in that they give evidence of the rapid loss of massive rock spalls that are likely made susceptible to erosion through bedding plane-joint plane intersections. However, these events

appear to be highly infrequent and furthermore, may in fact contribute to the long-term reduction of channel-bed abrasion by supplying large blocks of rock to the rivers which will effectively shield its channel bed. The relative importance of these two effects of mass wasting, namely the erosional and shielding effects, cannot be ascertained from the limited data presented here. However, as the rate of channel bed lowering sets the pace, in a general sense, for erosion rates throughout a catchment (Chapter 2), this question is central to understanding the nature of erosional dynamics and thus long-term geomorphological development of these catchments. Systematic sampling of bedrock at the base of the valleys could help ascertain whether S5.1 and S5.2 are indeed anomalous and representative of as rare a phenomenon as is suggested here. A compliment to such a study, would be to determine the pace at which the coarse bedload is transported out of the mountain catchments.

An exact case of equilibrium cannot be argued for, however, because if erosion rates were spatially uniform across all points within the catchments, no correlation would be found between denudation rates and topographic parameters such a relief, hilllslope angle, and normalised channel steepness index (von Blanckenburg, 2005). In contrast to this the region is characterised by strong linear correlations in all cases. It is therefore suggested that the slowly denuding ranges of the coastal Cape Mountains, in which hillslope and channel processes are strongly coupled, are part of a landscape approaching topographic steady state, having suffered very little disturbance of the sediment production-sediment flux balance that exists upon its slopes. Furthermore, the high degree of stability evidenced in the landscape suggests that both conditions of approximate topographic steady state and equilibrium between soil production and loss on hillslopes, are likely to prevail throughout most of the south-western coastal Cape Mountains.

Cosmogenic nuclide analysis of sediment sourced from catchments of the Cape Mountains suggests that relative landscape stability and inactivity has prevailed since the late-Pleistocene. Due to sampling bias, however, these conditions are only applicable to the highlands of the Cape Mountains and not the surrounding lowlands dominated by shales. In contrast, the Little Karoo intermontane basin nestled between the Langeberg and Swartberg Ranges, as well as the coastal plain immediately south of the Langeberg Range, preserve a far more energetic history

for the same time period. Alternating episodes of river aggradation and incision are evidenced by the many remnants of fluvial deposits occurring at various altitudes throughout the study area, while varying stream power can be inferred from the nature of these deposits which varies between boulders meters in diameter (as are seen in the river channels), pebbles and gravel (such as are found at terraces S1 and S2) and fine-grained deposits of silt and mud (as is seen to overlie terrace S1). The disparity between denudation rates in the lowlands and adjacent highlands was noted in Section 6.2, where variations in rock strength, and short-lived periods of increased stream power in comparison to the averaging timescale of the catchment-averaged denudation rates, were proposed to explain this observation.

While approximate topographic steady-state is suggested by the cosmogenic nuclide analysis, the presence of terraces and incision events suggest that the region may be subject to low-frequency, high-amplitude storm events to which most of the erosion within the river channels is likely due. In order to test this hypothesis, one could use available rainfall data to model the 'storminess' of the region and its effects on river channel abrasion rates, using the Channel-Hillslope Integrated Landscape Development (CHILD) model (e.g. Tucker and Bras, 1999). However, a hindrance to such an investigation is that local rainfall data are only available for the past decade, and consequently may not accurately record the variability in local climatic conditions.

7.3 Implications for the geomorphic evolution of the Cape Mountains

7.3.1 Controls on denudation rates within the coastal Cape Mountains

The topography of the coastal Cape Mountains is comparable to that of present-day active orogens such as the Himalayas, Andes and Alps yet its catchment-averaged denudation rates are amongst the lowest recorded globally (Figure 7.8). In effect, the coastal Cape Mountains display an alpine topography whose denudation rates are of the same order of magnitude as those reported from low-relief, cratonic regions (c.f. Figure 3.6, Chapter 3) and whose absolute denudation

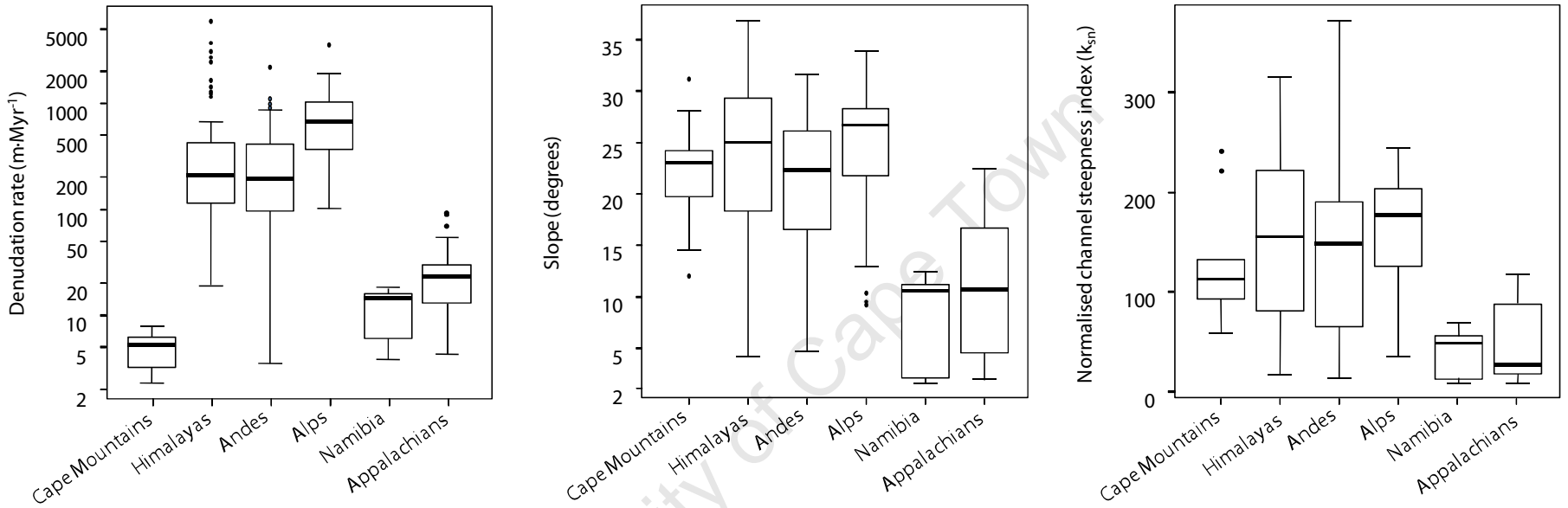

Figure 7.8: Comparison of the denudation rates and morphometric parameters found in the coastal Cape Mountains, with those found in present-day tectonically active orogens, post-orogenic regions, and tectonically inactive regions. Chosen examples for tectonically active regions are the Himalayas (Finnegan et al., 2008; Ouimet et al., 2009; Palumbo et al., 2010; Palumbo et al., 2011), Andes (Abbühl et al., 2010; Safran et al., 2005; Vanacker et al., 2007; Insel et al., 2010) and Alps (Wittmann et al., 2007; Norton et al., 2008; Delunel et al., 2010; Norton et al., 2010; Norton et al., 2011). The chosen example for a post-orogenic region is the Appalachians (Matmon et al., 2003; Reuter, 2005) and that for a non-orogenic, tectonically quiescent setting is the Namib Desert (Bierman and Caffee, 2001; Codilean et al., 2008). Catchment-averaged denudation rates for catchments up to 500 km^2 in area were used. All data points have been renormalized to the KNSTD2007 standard of Nishiizumi et al. (2007). Slope statistics were calculated from the SRTM 90 m resolution digital elevation model. Normalised channel steepness indices were calculated as outlined in Chapter 6. Boxes show the 25th, 50th and 75th percentiles of the data; whiskers show the maximum and minimum values of the data set; circles indicate the outliers of the data set. The coastal Cape Mountains appear anomalous in that their catchments are morphometrically similar to catchments from actively uplifting mountain ranges, yet exhibit denudation rates that are lower than most tectonically quiescent regions.

rates are lower than most reported catchment-averaged denudation rates world-wide (Portenga and Bierman, 2011). This phenomenon has not yet been reported elsewhere in the world.

This anomalous behaviour, in seeming contradiction to the present-day understanding of hillslope processes (Chapter 2), begs the question as to what is responsible for the unexpectedly low denudation rates within the coastal Cape Mountains. Elsewhere in the world, studies have linked denudation rates to tectonic setting, basin morphometrics, climate, lithology and structure, and anthropogenic influences (Chapter 2). Let us consider, in turn, each of these controls and their potential to influence denudation rates within the Cape Mountains.

From the outset, significant anthropogenic influence can be ruled out as denudation rates reported for the region are only applicable to the largely uncultivated and relatively uninhabited highlands of the fold belt where only forestry is present, and not the adjacent low-lying farmlands. This is largely the result of sampling bias which ensured that only course-grained sand was collected from the river beds, at the river's exit from the mountains. Those sample sites whose upstream catchment area lay in the intermontane basins and coastal plain, such as S4 (Tradouw River), S6 (Seven Weeks River) and S7 (unnamed river in Tierkloof), report denudation rates that are both indistinguishable from rates determined for catchments confined to the slopes of the mountains, and amongst the lowest values reported for the region. This could indicate that the proportion of 250-500 µm quartz grains sourced from sandstone horizons in the lowlands is insignificant in comparison to that sourced from the mountains; alternatively, it could indicate that the averaging timescale of these denudation rates has dampened the signal of anthropogenically enhanced erosion rates in the farmlands. In both cases, the catchment-averaged denudation rates do not report the influence of humans on rates of mechanical erosion but instead reflect natural, background rates of denudation (Chapter 3). The unexpectedly low denudation rates must therefore be due to moderation by some long-standing, natural phenomenon.

Evidence of mild tectonic activity along the west coast of southern Africa is presented by Viola et al. (2012) and Viola et al. (2005); however, low denudation rates recorded from the sampled mountain catchments indicate the absence of a strong active tectonic forcing in the region. Tectonic stability alone, however, does not explain the behaviour of coastal Cape Mountains' landscape which returns denudation rates that are amongst the lowest reported for all post-orogenic mountains and cratonic regions – save the hyperarid Atacama Desert – despite having a terrain far more rugged than these regions.

Second to tectonic setting, is the influence of basin morphometrics: stream power and thus erosive potential has been shown to increase with an increase in hillslope angle, channel steepness and relief. All else held constant, a region of rugged topography will denude faster than a region of subdued topography (Chapter 2). We note that these empirical laws are obeyed within the Cape Mountains as steeper slopes and channel gradients are associated with higher catchment-averaged denudation rates (Figure 7.2-Figure 7.7). It is thus expected that in the tectonically quiescent landscape of southern Africa, the rugged Cape Mountains would return higher catchment-averaged denudation rates than the coastal plains and interior plateau; however, this is not the case (Chapter 1). Other than the coastal Cape Mountains, catchment-averaged denudation rates have been determined for the low-relief coastal plain and interior plateau, and high-relief escarpment of the Namib Desert (e.g. Codilean et al., 2008; Bierman and Caffee, 2001) and South African eastern Drakensburg (e.g. Fleming et al., 1999); all three of which very often return denudation rates that are higher than those of the coastal Cape Mountains. Clearly topography does not exert a dominant control on denudation rates.

The effects of climate within the coastal Cape Mountains are not easily discussed as sample sites related to this study were situated in climatically-comparable regions. Ideally, a thorough investigation into the effects of climate on denudation rates in the coastal Cape Mountains would compare catchment-averaged, as well as bedrock, denudation rates from various climatic zones along the mountain ranges. In the case of the coastal Cape Mountains, however, the merit of such an investigation must be questioned as denudation rates of the order of $10^{1} m \cdot Myr^{-1}$ are sufficient to average over glacial-interglacial periods, a cycle of

approximately 30 ka; (von Blanckenburg, 2005; Schaller et al., 2002; Chapter 3). Denudation rates from the coastal Cape Mountains, which do not exceed 7 $m \cdot Myr^{-1}$ and have an averaging timescale of 0.1-0.3 Ma, are clearly low enough to average over these climatic cycles and report an average denudation rate since the late-Pleistocene.

Southern Africa has experienced notable climatic fluctuations since the Pliocene (Partridge, 1993; Partridge et al., 1990). The late-Pleistocene to Holocene was a period of particularly frequent fluctuations in both temperature and wetness which resulted in significant changes in climate throughout this period. A comparison of present-day climate to denudation rates which average over the fluctuating climatic conditions since the late-Pliocene, may therefore be of questionable value.

Further complications are presented by Peizhen et al. (2001) whose discussion of the effects of Quaternary climate instability on landscapes concludes that the continued alternation of warm, wet interglacial periods with cool, dry glacial periods has the effect of destabilizing a landscape and increasing rates of denudation, thus preventing the establishment of erosional steady-state. In support of this theory, Peizhen et al. (2001) point towards the global phenomenon of increased denudation rates since ~ 3-4 Ma. The argument presented by Peizhen et al. (2001) suggests that denudation rates from the coastal Cape Mountains are likely to be elevated denudation rates relative to the preceding Miocene, during which climate is thought to have been somewhat more stable (Partridge, 1993). If this is so, climate has had the effect of increasing, not repressing, denudation rates in the coastal Cape Mountains. It must be noted, however, that Willenbring and von Blanckenburg (2010) have countered this argument with an analysis of the ocean dissolved $^{10}Be/^{9}Be$ ratio, which can be used as a proxy for global chemical weathering flux, and have found it to be constant over the past 10 Myr. These authors have attributed the apparent global phenomenon of increased denudation rates since 5 Ma to sampling bias. The work of Willenbring and von Blanckenburg (2010) casts doubt on the argument of Peizhen et al. (2001) by questioning the validity of the apparent increase in sedimentation rates noted for the past 5 Ma.

In the absence of cosmogenic nuclide data from various climatic regimes across the coastal Cape Mountains, the effects of climate will be analysed by comparing topographic parameters across the mountains with variations in precipitation and temperature and noting any correlations which may arise. This is done with an understanding that topography is a function of the spatial and temporal variation in denudation rate thus, if denudation rate is primarily a function of climate, topographic parameters can be expected to scale with changes in climatic parameters.

The different climatic zones found within the coastal Cape Mountains were briefly reviewed in Chapters 1 and 4. Due to orographic effects, rainfall is moderate to high on the seaward-facing slopes with an annual mean of 400-500 mm, falling to half that value in the rain-shadow of the mountains, particularly north of the Swartberg. All catchments sampled in this study receive between 330 mm and 550 mm rainfall per annum. Regions of notably high annual rainfall where the annual mean lies between 900 mm and over 1000 mm, occur to the south-west between Cape Town and Hermanus and to the south-east between Harolds Bay and Humansdorp (Figure 6.9 B).

Increased precipitation leads to increased stream power and a steepening of rivers in their headwaters (Tucker and Bras, 1999; Chapter 3). If rainfall is the factor limiting denudation rates within the Langeberg and Swartberg Ranges, we would expect denudation rates and therefore channel steepness and slope steepness to covary with mean annual precipitation. Given the argument that seasonality leads to increased erosion (Anhert, 1970), one might expect to find steeper slopes along the western limb of the coastal Cape Mountains where precipitation is highly seasonal (Chapter 1). Alternatively, given the argument that 'storminess' might lead to increased erosion rates (Molner and England, 1990; Tucker and Bras, 1999; Chapter 2) one might expect to find steeper slopes and river channels along the southern limb of the coastal Cape Mountains were precipitation is of greater intensity than in the west. No such patterns are observed; instead, channel steepness indices and slope steepness are uniformly distributed throughout the Cape Mountains and correlate only with outcrops of the Table Mountain and Witteberg Group rocks (Figure 7.9). It is also noted that relief, here interpreted to represent depth of incision (maximum catchment elevation minus minimum

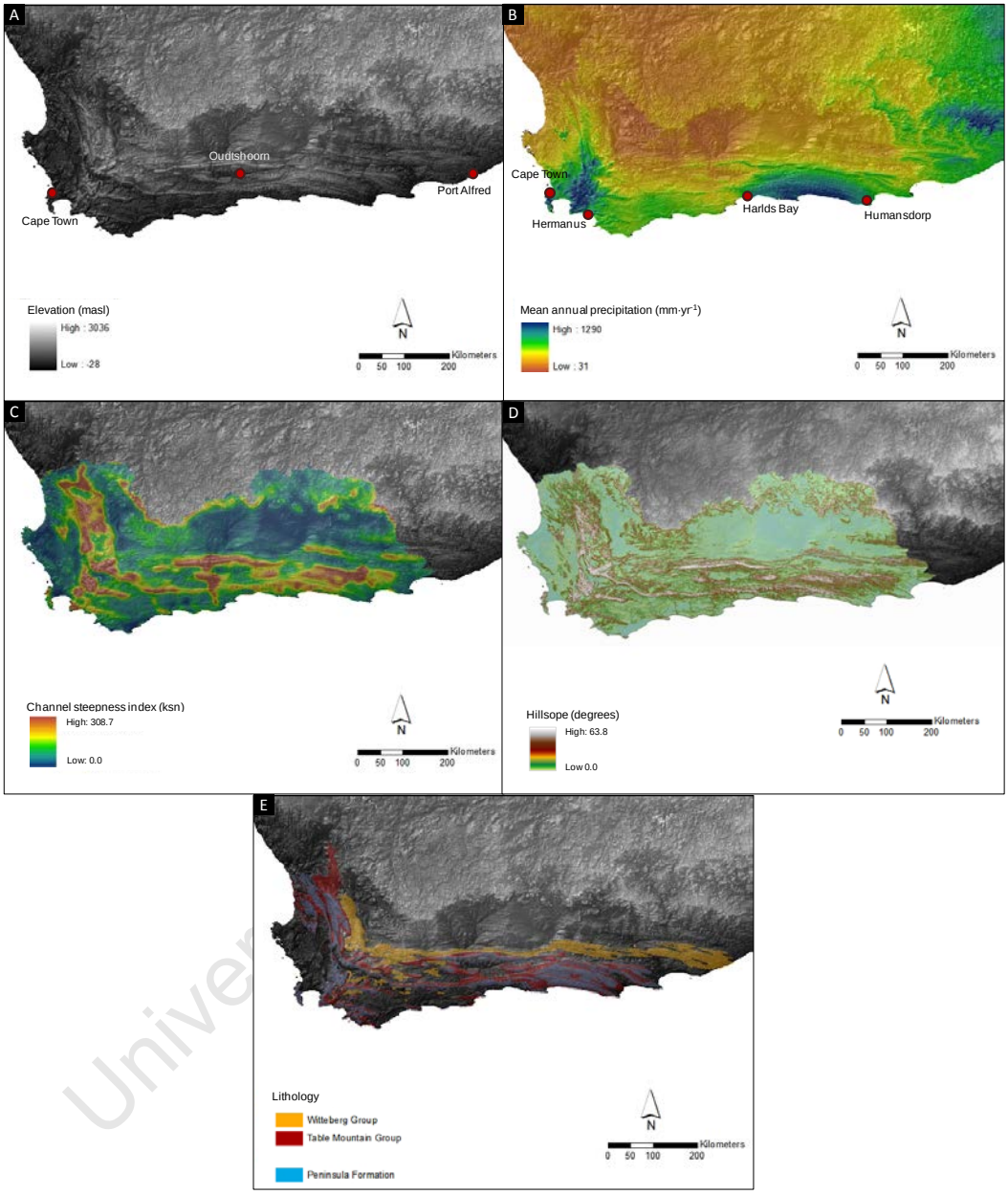

Figure 7.9: A) Distribution of elevation across the coastal Cape Mountains. B) Distribution of mean annual precipitation across the coastal Cape Mountains. C) Variation of channel steepness indices across the coastal Cape Mountains D) Variation of normalised slope steepness across the coastal Cape Mountains. E) Outcrops of the Table Mountain Group and Witteberg Group rocks coincide with the high elevation anticlinal ranges of the coastal Cape Mountains and regions of high channel steepness. This figure was constructed using the SRTM 90 m digital elevation model sourced from the AEON database.

catchment elevation), covaries with elevation alone. Areas of maximum relief thus correspond with areas of maximum elevation, with areas of highest elevation found where outcrops of the Penninsula Formation quartzite cap the anticlinal ranges (Figure 7.9).

Climate might have an effect on erosion rates through its influence on vegetation. It was mentioned that the mean annual precipitation within the sampled catchments lies in the range of 300-500 $mm \cdot yr^{-1}$. At a mean annual precipitation of approximately 360 mm, sufficient vegetation occurs to protect the underlying rock and soil from mechanical erosion (Summerfield and Hulton, 1994; Chapter 2). Vegetation may help to minimise mechanical erosion within the slopes of the catchments of the coastal Cape Mountains; however, precipitation does not seem to be the dominant factor governing the rate of topographic development in this tectonically quiescent landscape.

As mentioned, normalised channel steepness index, hillslope, and relief are uniformly distributed throughout the coastal Cape Mountains, their location pinned to the outcrop of Table Mountain and Witteberg Group rocks. Relief is associated with elevation, with greatest elevation occurring on those anticlinal ranges capped by quartzites of the Peninsula Formation. It appears, therefore, that lithology is directly related to topography, and thus very likely to subareal denudation rates within the coastal Cape Mountains.

The suggestion that lithology is responsible for regional topography is neither new nor unique to the coastal Cape Mountains but has been alluded to in the local literature (e.g. King, 1962), with similar phenomena reported from Scotland (Jansen et al., 2010; Chapter 2) and the British Isles (Clayton and Shamoon, 1998; Chapter 2). Both Jansen et al. (2010) and Clayton and Shamoon (1998) made particular mention of the resistance of quartzites in which higher relief, steeper slopes and steeper, narrower river channels occurred. Furthermore, the rock-strength classification system developed by Selby (1980) (Chapter 2) has identified quartzite as one of the hardest rock types and, once again, linked to steeper slopes than most other lithologies. The rugged terrain of the coastal Cape Mountains appears to be a natural response to the overall lithological strength of the quartzites from which these ranges are built.

Lithological strength on the mountain scale is dependent on intergranular cohesion, chemical composition and structural fabric of the rock (Korup, 2008; Chapter 2). Intergranular cohesion is responsible for the tensile strength of the rock and therefore its ability to resist abrasion and rockfalls. The above-average intergranular strengths of quartzite is demonstrated by the work of Sklar and Dietrich (2001) and Selby (1980). The inherent internal cohesion of the rocks of the Table Mountain and Witteberg Group rocks should therefore result in a low abrasion capacity as shown by the very low denudation rates reported for the area, the low sediment content of the rivers, and the notably narrow bedrock channels that lie in these mountains. The infrequency of rockfalls has already been discussed in Section 7.2. These findings mirror those of Jansen et al. (2010), where the tensile strength of quartzites in catchments of western Scotland was responsible for dampening of denudation rates and an increase in the relief decay time of the landscape.

The relative inactivity and low solubility of quartz is well known (Flint, 1963; White and Blum, 1995; Chapter 2). Chemical weathering of quartzites is low, which has the secondary effect of retarding mechanical erosion which is often aided by the process of chemical weathering. The catchments targeted in this study were those carved into the high-lying peaks of the coastal Cape Mountains, and thus into the mature quartz arenites of the Peninsula Formation, which contain little else other than quartz grains and are thus particularly resistant to chemical alteration and dissolution. Rates of chemical weathering are thus likely at a minimum in rocks of this nature.

In Section 7.2, the denudational processes active in the catchments of the coastal Cape Mountains were discussed. It was mentioned that granular disintegration was likely one of the greatest contributors to the sediment yield of the catchments, based on the close agreement between the mean of the catchment-averaged denudation rates for the region and the mean of bedrock denudation rates. As rates of granular disintegration are limited by the rate of chemical weathering (Sparks, 1960) and quartzite of the Peninsula Formation is particularly resistant to chemical weathering, it might be that the unexpectedly low bedrock denudation rates are largely aided by the chemical resistance of these rocks.

Inherent structural weaknesses such as bedding planes, joints and fractures affect overall lithological strength through the density in which they occur. While joint and fracture spacing were not looked at in this study, the thick-bedded nature of the Peninsula Quartzite was noted (>1 m in places). The work of Moon (1986), who applied the rock-strength classification system of Selby (1980) to rocks of the coastal Cape Mountains, has shown that strength-equilibrium slopes - bedrock slopes whose gradients are determined by the strength of the rock on the hillslope scale - are common in the coastal Cape Mountains. The denudation rate data set determined through cosmogenic nuclide analysis compliments the work of Moon (1986) through its suggestion that the slopes of the Cape Mountains represent detachment-limited settings in near topographic steady state. Furthermore, Moon noted that slope gradient varies as joint spacing and therefore whole-rock strength, varies. This supports the above suggestion that lithology (i.e. composition of rock and structural fabric defined by joint, fracture, fault and bedding planes) is likely the main control on denudation rates within the Cape Mountains.

Internal cohesion (i.e. how well consolidated the rock is) and structural fabric of rock (density and orientation of bedding, joint and fracture planes) affects the nature of bedload supplied to the channels which in turn affects mechanical erosion within the channels as bedload provides the tools for channel abrasion to occur. In the upper, cliff-bounded reaches of the rivers, little to no sediment is found. The low bedrock denudation rates determined on the interfluves suggest that very little sediment is supplied to these rivers and that they are deprived of tools for abrasion. Field observations confirmed that, in regions of bedrock channels, the rivers were sediment starved. Channels are, however, lined with gravel, pebbles and boulders, particularly in the foothills of the mountains. These are likely derived from the spallation of bedrock on mountain spurs and within bedrock channels, and occurrences of slope failure.

Clasts that are over 3.5 mm tend to settle to the channel floor, effectively armouring the channel floors from abrasion (Sklar and Dietrich, 2001). Given that the rivers in the coastal Cape Mountains appear underfit for their gorges and unable to transport their bedload, it is unlikely that these gravels, pebbles and boulders are abraded much between flood events, and thus are unlikely to supply much sediment to the rivers. The landscape model produced by Tucker and Bras

(1999) suggests that it is not just mean annual precipitation that affects denudation rate but also rainfall intensity. High intensity precipitation leads to high run-off and therefore high river discharge. It is hypothesised that these channels in the coastal Cape Mountains are abraded during occasional flood events during which the streams have enough strength to mobilise their channel lag, such as that evidenced by the 5 m incision of rivers in their flood plains during which river discharge had the power to relocate boulders up to 2 m in diameter (Section 7.2). The infrequency of these events is likely to contribute to the exceptionally low denudation rates reported from the sampled catchments.

The effects of climate on denudation rate, however, are largely speculative. Modelling the effects of local climate on bedrock channel abrasion rates, and comparing model erosion rates with analytically determined denudation rates for the area, may help to identify the relative contribution of overall lithological strength on the hillslope scale, and climate, to the maintenance of low denudation rates in the region. Model erosion rates which over-predict analytically measured denudation rates could be taken to indicate that the overall lithological strength of these rocks on the mountain scale is particularly high. Alternatively, model erosion rates which agree well with, or under-predict, measured denudation rates, may favour the interpretation that climate (mean annual precipitation and intensity of rainfall) is the limiting factor on denudation rates within these mountains. The Channel-Hillslope Integrated Landscape Development (CHILD) model may be suitable for such an investigation.

Alternatively, careful sampling for cosmogenic nuclide analysis within notably different climatic regions of the Cape Mountains (e.g. high rainfall Cape syntaxis and semi-arid north-facing slopes of the Swartberg Range) would allow one to assess the effects of climate on denudation rates. Investigations into climatic forcing on denudational processes within the Cape Mountains may prove particularly successful in comparison to studies conducted elsewhere in the world, as two important denudational controls can be accounted for, namely the effects of active tectonics and lithology. The low denudation rates reported from the south western coastal Cape Mountains indicate the absence of a strong, active tectonic forcing in the region; the presence of which would have the potential to obscure the effects of milder environmental forcings on denudation rates (Chapter 2).

Lithologies repeat throughout the coastal Cape Mountains, making it possible to sample a similar lithology, if not the same stratigraphic unit, within more than one of the anticlinal ranges of the coastal Cape Mountains. One should, however, be aware that lateral variations in lithological properties may occur within the same stratigraphic unit over large distances, e.g. variance in the degree of tectonism and metamorphism which has affected these rocks, is likely to occur. However, if one is aware that such variance can occur, care can be taken to select sampling sites that minimise their effects.

Repressed denudation rates and the conservation of rugged terrain in the coastal Cape Mountains are here interpreted to be the result of a remarkable lithological competence of the quartzites which form these mountains. Climate may assist by providing enough moisture to support vegetation on the south-facing slopes which shields the underlying rock from mechanical erosion but not enough to support frequent high-intensity precipitation events which can produce enough run-off and river discharge to move the coarse bedload in the rivers of these mountains.

7.3.2 Timing of canyon formation

Past attempts to explain the formation of gorges – locally known as 'poorts' – in the coastal Cape Mountains, have led to contradictory theories in the literature, with certain authors (e.g. Rogers, King, Du Toit, Van Zyl) advocating an origin through superimposition in one form or another, whilst others (e.g. Davis, Taljaard, Lenz, Maske) campaign for headward extension of streams along structural and lithological weaknesses in the rock (Chapter 1). There is also disagreement on the timing of poort formation, with proposed ages ranging from as young as Pleistocene (e.g. Prins Poort, as dated by Taljaard and Lenz) to as old as Cretaceous (e.g. Prins Poort as dated by Van Zyl). Despite being subject to over a century of investigative science, the geomorphic evolution of the coastal Cape Mountains, and indeed the Cape Mountains as a whole, remains poorly resolved. Denudation rates and exposure ages for the Cape Mountains determined through the use of *in-situ* produced cosmogenic ^{10}Be, as presented in this study, provide some of the first high-resolution, quantitative data on the region. Here, the

implications of these new results with respect to timing of gorge ('poort') formation in the coastal Cape Mountains, is considered.

Catchment-averaged denudation rates for the south western coastal Cape Mountains, as determined in the research area, apply to the late-Pleistocene. Given the high degree of stability indicated by these low denudation rates and the low variability amongst denudation rates, one can infer that denudation rates within the study area were likely similarly low throughout the early and mid-Pleistocene so as to allow the present, wide-spread stability to have been established since the late-Pleistocene. Further evidence for the long-term prevalence of low denudation rates within the Cape Mountains is the agreement between the catchment averaged denudation rates which average over the mid-term, and the long-term estimates provided by AFTA of Tinker (2005), Tinker et al. (2008a, 2008b) and Tinker and de Wit (2004) for denudation rates over the southern Cape which averages over the Cenozoic (10-15 $m \cdot Myr^{-1}$). It is noted that the estimate provided by AFTA is higher than the denudation rates determined by cosmogenic nuclide analysis, but given that the AFTA estimates are averaging over a far longer time period (65 Myr as opposed to 0.1-0.3 Myr), a far larger region, and a wide variety of lithologies, most of which will exhibit higher erosional potentials than the resistant quartzites of the coastal Cape Mountains, this is not surprising. It is thus tentatively suggested that the catchment-averaged denudation rates may have persisted for longer than can be detected by cosmogenic nuclide analysis, and possibly into the Pliocene. It is acknowledged, however, that such a hypothesis requires testing by a chronometry technique with a temporal resolution that is larger than that of cosmogenic nuclide analysis, and with a greater sensitivity to exhumation than apatite fission track analysis. (U-Th)/He analysis is one such technique that might be suitable for the task (Farley, 2002). Basement-rock inliers which outcrop in the mountain belt and shales of the intermontane basins may yield samples suitable for such an analysis.

To assess the chronology proposed by Lenz, it is assumed that prior to the breeching of the mountains, the respective rivers had not yet worn down through the quartzites to the level of the Lower Surface, but instead stood at an elevation just above it. Through the course of the Pleistocene, these rivers have incised from their starting elevation that is slightly higher than the Lower Surface, to the

level of current local baselevel. Lenz does not consistently report, for each of these gorges, how far the respective river has succeeded in incising below the regional Lower Surface; furthermore, the Lower Surface is usually absent in the vicinity of those gorges which he deems to be Pleistocene in age. Lenz does, however, report a few incision depths which are distributed throughout the region of the Little Karoo. The incision depths given are 153.6 m, 120 m, 180 m, 105 m and 90 m. It appears, then, that for any mountain to have been breeched in the Pleistocene, the respective river needs to have incised many tens of meters in the past 2.6 Ma. At a regional average of 4.59 $m \cdot Myr^{-1}$, this is unlikely. Given the exceptionally low denudation rates within the coastal Cape Mountains, it is unlikely that any of these ranges were breeched during the Pliocene or Pleistocene. Instead, the work of Van Zyl, which suggests that the most of the drainage in the region is Mesozoic or early Cenozoic in age, appears more reasonable.

As discussed in Chapter 1, Macfarlane (1949) investigated the gravel deposits south of the Langeberg Range that Lenz termed the Higher Surface and assigned Eo-Oligocene age to, and concluded that these gravels are late-Pleistocene in age based on stone implements found in the gravel deposits. Based on the depth of local river incision below these gravel deposits, Macfarlane infers that the rivers have incised ~150 m through the Table Mountain quartzites since, at earliest, the late-Pleistocene. Not only does this contradict the work of Lenz, but it is also incompatible with the catchment-averaged denudation rates for the region, as determined in this study.

From these two examples, it is clear that geomorphic evolution of the coastal Cape Mountains' canyons is poorly explained. Relative age constraints place on their development appear unreliable and contradictory. This highlights the necessity of quantitative data on denudational processes and surface ages in an investigation of landscape evolution, and the dangers of 'relative-age dating' based on correlating supposed erosion surfaces over broad regions (or even single mountain ranges) based on similarities in surface height or morphology (cf. Chapter 1).

7.4 Implications for southern African geomorphology

7.4.1 Long-term preservation of erosion surfaces

Classical models for landscape evolution as laid out by King (1951, 1953, 1957, 1962) and Partridge and Maud (1987, 2000) maintain that remnant erosion surfaces, originally part of regional planation surfaces which developed through successive events of uplift and scarp retreat, can be identified and correlated based on their elevation and 'characteristic' physical identifying features. Furthermore, a number of epeirogenic flexure-uplift events, the most recent of which are thought to have occurred between 3-5 Ma (Partridge and Maud, 2000) and are said to have warped the surface of southern Africa and played an important role in defining its present-day topography. The identification of these flexure-uplift events have, in part, been based on the regional correlation of these erosion surfaces which shows them to have been warped since their formation. The Cape Mountains are not exempt from these models. The *African Surface* has been identified within the coastal Cape Mountains at heights of 600-900 m, while uplift of the *Post-Africa I* and *Post-Africa II* events are said to have affected the southern and western coastal hinterlands, causing incision of coastal rivers (Chapter 1). For both events, uplift along the south coast is said to have been at a maximum of approximately 200 m in the region of Oudtshoorn, while overall uplift across the subcontinent was at a maximum along the east coast (Partridge et al., 2006).

The practice of correlating erosion surfaces is based on two assumptions which have been widely criticised:

1. Erosion surfaces of similar elevation are remnants of the same general surface or conversely, remnants of a similar surface will be lowered by comparable amounts through time regardless of underlying lithology or variations in climatic conditions across the subcontinent.
2. The 'identifying' physical characteristics of these surfaces have remained intact, despite any lowering which might have occurred.

Flemming et al. (1999), van der Wateren and Dunai (2001) and Decker (2010) have presented strong arguments against the preservation of erosion surfaces based

on bedrock denudation rates determined from cosmogenic nuclide analyses of dolerite outcrops across southern Africa (Decker, 2010) and of quartz veins in terrace and pediment remnants in the Namib Desert (van der Wateren and Dunai, 2001). Decker's findings that the exposure age of dolerite outcrop surfaces said to lie on the *African* and *Post-Africa I* Surfaces are two orders of magnitude less than the proposed ages for these regional planation surfaces, and that in each case several hundred meters of surface denudation has taken place despite the lithological strength of the dolerites in comparison to surrounding country rock, casts serious doubt on whether such surfaces can be correlated across eastern and southern South Africa. The work of van der Wateren and Dunai (2001) has shown that, even in the hyper arid Namib Desert where denudation rates are expected to approach a regional minimum, land surfaces are undergoing erosion and their preservation over the time periods suggested by King and Partridge and Maud is not likely. Denudation rates obtained for the coastal Cape Mountains stand in support of both Decker (2010) and van der Wateren and Dunai (2001).

There is ample evidence to suggest that denudation rates across southern Africa were significantly higher in the Cretaceous and have declined throughout the Cenozoic to their present day values (Chapter 1), implying that the catchment-averaged denudation rates reported here for the coastal Cape Mountains are likely at or near the minimum for the Cenozoic. Both King and Partridge and Maud have mapped the *African Surface* as preserved between the quartzite ranges of these mountains. According to King, the erosional cycle of the *African Surface* continued until the Oligocene, thus making this planation surface 33.9 Ma in age. Partridge and Maud, however, considered the *African Surface* to be late-Cretaceous in age (65 Ma). If the average of these catchment-averaged denudation rates (4.6 $m \cdot Myr^{-1}$) were to be extrapolated back some 33.9 Myr and 65 Myr, the result would be the removal of 155.6 m and 298.4 m of resistant quartzitic rock, respectively. As these catchment averaged denudation rates are a minimum for the Cenozoic, and far below rates at the end-Mesozoic, it is likely that these approximations underestimate the amount of rock material denudated since 33.9 Ma and 65 Ma. Similar estimations using the average of bedrock denudation rates determined from S15, S17 and S18 (3 $m \cdot Myr^{-1}$) indicates the removal of 101.7 m of rock since the Oligocene and 195 m of rock since the close of

the Cenozoic. It is clear that even in the exceptionally resistant quartzites of the Cape Mountains the preservation of recognisable land surfaces over the time period and distances suggested by King and Partridge and Maud is questionable.

These results, together with those of Fleming et al. (1999), van der Wateren and Dunai (2001) and Decker (2010) give reason to question whether the proposed regional erosion surfaces may indeed be preserved unlowered, as suggested by King, or with their identifying features intact, as suggested by Partridge and Maud, across the spectrum of lithologies, climates and terrains analysed in these studies. Their use as datum surfaces in studies of the geomorphic evolution of the subcontinent should therefore be treated with caution.

7.4.2 Landscape stability of southern Africa

AFTA and offshore sedimentary data for southern Africa consistently report a notable decline in onshore denudation rates throughout the Cenozoic. It has been argued, however, that successive uplift events in the Miocene and Pleistocene have significantly altered the landscape of southern Africa (Chapter 1). Such a proposal is hard to evaluate as AFTA is not capable of resolving local or short-lived exhumational events, and average denudation rates across southern Africa, determined through cosmogenic nuclide analyses, consistently average over timescales of 10^3-10^6 years and thus fall short of the timescale required to assess denudation rates related to events in the Miocene and Pleistocene. Assessment of available offshore sedimentation data, cosmogenic nuclide analysis data and AFTA across southern Africa does, however, provide some first order clues.

In line with cosmogenic nuclide analysis across southern Africa, data from the coastal Cape Mountains reports particularly low denudation rates, indicative of a stable environment devoid of large-scale active tectonic input since at least the late-Pleistocene. Similarly, AFTA reports relatively low onshore denudation rates for the southern Cape (Tinker et al., 2008b) throughout the late-Cenozoic, with a maximum denudation rate of 15 $m \cdot Myr^{-1}$ to conform with the removal of <1 km of surface material. These relative low denudation rates for the Cenozoic are supported by numerous AFTA studies throughout southern Africa where denudation rates are consistently estimated to be lower than 20 $m \cdot Myr^{-1}$ (Chapter

1). In addition, offshore sedimentary basins around southern Africa report a declining offshore sedimentation rate which reaches a minimum in the late-Cenozoic, thus supporting the findings of AFTA and cosmogenic nuclide analysis across southern Africa (Chapter 1). The general agreement between AFTA analysis, offshore sedimentation data, and cosmogenic nuclide analyses (Chapter 1) suggests that, following the rifting of Gondwana, southern Africa has not experienced any major tectonic disturbance.

It must be noted, however, that the denudation rates gathered in this study apply to the quartzites of the coastal Cape Mountains which appear to be particularly robust. This raises the question as to whether a mild to moderate tectonic disturbance (e.g. ~150-200 m uplift in the Pliocene, as suggested by Partridge and Maud, 1987 and 2000) would be clearly expressed in the denudation rates of these quartzites. Establishing the rate at which the intermontane basins denude, may help answer this question.

Analysis of normalised channel steepness indices (k_{sn}) has been successfully used to identify differential uplift in numerous studies (Chapter 2), and was here applied to the coastal Cape Mountains. Classical hypotheses of landscape evolution suggest that discrete uplift events incited the *Post African I* (~ 20 Ma) and *Post-African II* (~3-5 Ma) erosion cycles. In both these cases, uplift was not uniform across southern Africa but was most intense along the eastern margin of southern Africa, with intensity declining to the west. Within the coastal Cape Mountains, k_{sn} values are comparable to those in actively uplifting orogens; however, they are constant throughout the mountain belt, showing no spatial differentiation. This suggests that the forces responsible for the cutting of steep canyons across southern Africa operated uniformly over western, southern and south-eastern coastal sectors of southern Africa. This does not support a theory which proposes that the eastern margin has suffered recent (~3-5 Ma) uplift (~900 m) in comparison to uplift within the southern (~200 m) and western (~100 m) coastal hinterland of southern Africa, a phenomenon attributed to the presence of the 'African Superswell' below eastern southern Africa (Chapter 2). This is in agreement with Doucoure and de Wit (2003) who suggest that the elevated topography of eastern Africa is long-lived and inherited from the early-Cretaceous, and not due to recent uplift in the late-Cenozoic.

Cosmogenic nuclide analyses carried out in southern Africa have consistently yielded low denudation rates from both bedrock and river sediment samples. Data are summarised in Tables 1.3A and 1.3B, Chapter 1. It is noted that, regardless of lithology, climate, terrain (slope and relief), denudation rates remain below 20 $m \cdot Myr^{-1}$ except in the case of vertical rock faces where greater denudation rates are considered to reflect the work of episodic rock falls (e.g. Flemming et al., 1999; Cockburn et al., 2000). It may be that the landscape of southern Africa has experienced long term stability on the regional scale, thus reporting similar denudation rates for most geomorphic features analysed.

Whilst the existing data do not disprove competing models of uplift, they do give good reason to challenge them. As of yet, no quantitative, unambiguous evidence is forthcoming in support of episodic uplift events in the mid- and late-Cenozoic; however, long-term landscape stability is suggested. A combination of data from cosmogenic nuclide analysis, AFTA and offshore sedimentary deposits suggest that the present-day southern Africa may display a relict landscape and not one that owes its origin to recent differential warping of the subcontinent.

The question of the validity of the proposed uplift events may be further investigated through apatite (U-Th)/He analysis, given its greater sensitivity to shallow crustal exhumation, as compared to that of apatite fission track analysis (Farley, 2002). Furthermore, dated molecular phylogenies can be used to place age constraints on landscape evolution as formative geomorphic events have the potential to influence biodiversity evolution (Cotterill and de Wit, 2011; Goodier et al., 2011). Cowling et al. (2008) have used dated molecular phylogenies of clades of the Cape Floristic Region (which coincides with the location of the coastal Cape Mountains) to place age constraints on the radiation of these clades. These authors infer that the timing of radiations are linked to the proposed epeirogenic uplift events of Partridge and Maud (1987), suggesting that these tectonic pulses altered the topography of the coastal Cape Mountains and exposed previously buried shale topographies, thus inciting diversification of the Cape flora. However, Cowling et al. (2008) failed to test their hypothesis by investigating substrate occupation of the species investigated. Currently, work is underway to date the shifts from sandstone to shale substrates by species within the Cape Floristic Region (Hoffman, 2011), the results of which would provide a valuable

test of the hypothesis proposed by Cowling et al. (2008) and possibly the uplift hypothesis of Partridge and Maud (1987).

7.5 Implications for global geomorphology

The coastal Cape Mountains are comparable in relief, slope steepness and normalised channel steepness index to present-day active orogens such as the Himalayas, Andes and Alps; and show a strong dissimilarity to the subdued relief and gentler slopes characteristic of cratonic and post-orogenic regions, world-wide. A comparison of the catchment-averaged denudation rates reported for all three regions (those that are tectonically active, those that are tectonically relatively quiescent, and the coastal Cape Mountains) shows that catchment-averaged denudation rates within the coastal Cape Mountains are out of character for both their morphology and tectonic setting, being two to three orders of magnitude lower than those reported for active orogens and lower still than those found in most tectonically passive regions world-wide. This anomalous behaviour was illustrated in Figure 7.8.

Catchment-averaged denudation rates within the coastal Cape Mountains are, in fact, some of the lowest of their kind in the world. The significance of these results stems from the present-day understanding of denudation rates and their controls, as discussed in Chapter 2. Denudation rates are consistently reported to scale primarily with slope angle, a correlation described by a positive linear relationship at low slope angles (<25°) and a positive power function at higher slope angles (>25°), usually associated with an active tectonic forcing. Analysis of the catchment-averaged denudation rates and slope angles for all catchments reported in published literature shows that this slope-denudation rate relationship is closely adhered to, globally. The Cape Mountains, however, with their contradiction of steep hillslopes, steep river channels, high relief and surprisingly low denudation rates, appear to be the exception to the rule (Figure 7.10).

While appearing at first to contradict these empirical laws, closer analysis shows that catchment-averaged denudation rates of the coastal Cape Mountains do, in fact, scale with hillslope; however, the relationship is not the power law usually reported for slopes of this steepness but rather the linear relationship

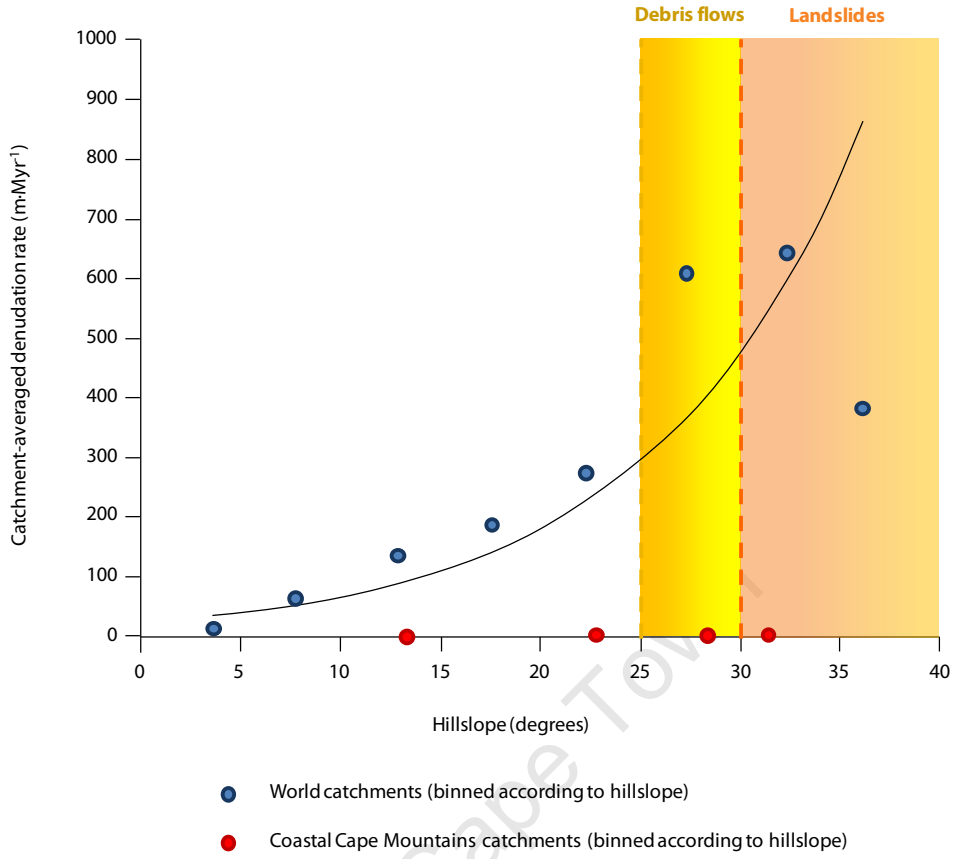

Figure 7.10 Plot of published catchment-averaged denudation rates from around the world (Portenga and Bierman, 2011), versus catchment-averaged denudation rates from the coastal Cape Mountains. Globally, the exponential hillslope-denudation rate relationship is obeyed. The Cape Mountains appear anomalous in that the hillslope-denudation rate relationship is described by a positive linear function at all slope angles.

characteristic of low-slope angles. Furthermore, the commonly reported positive correlations between denudation rate and normalised channel steepness index, and denudation rate and relief are also found to be true for the coastal Cape Mountains (Section 7.2).

Data from the coastal Cape Mountains highlights the fact that these empirical relationships appear to have their basis on a sampling bias. High-slope regions consistently report non-linear correlations with denudation rates as these studies have consistently been based in actively uplifting mountain belts where rapid river incision, seismicity and high rainfall conditions cause slope instability, associated landslides and rockfalls; and a resultant decoupling of slope and denudation rates. Tectonically quiescent regions are not subject to such tectonic and climatic

forcings and denudation rates reported from these regions are considerably lower. Furthermore, the topography in these cratonic and post-orogenic tectonic settings are generally mature and peneplained, thus associating low denudation rates with gentle topography. The coastal Cape Mountains differ from previous cosmogenic nuclide studies in tectonically quiescent environments in that its topography has not relaxed due to suitable lithological and possibly climatic conditions. These mountains give evidence of long-term landscape preservation, namely, a landscape which has not degraded since its last episode of large-scale rejuvenation but which is clearly no longer subject to the forcings which incited this rejuvenation. Note that in the case of the Cape Mountains, this last 'rejuvenation' of the landscape is likely to be the excavation of a buried, rugged terrain at the end of the Mesozoic (Tinker and de Wit, 2004). This is in contrast to a typical active orogen (e.g. Himalaya) whose rugged topography is the result of tectonic uplift that increases the erosive power of streams, allowing these streams to dissect the landscape.

The coastal Cape Mountains are therefore host to the seemingly contradictory combination of rugged terrain and low denudation rates. Following the discussion in Sections 7.2 and 7.3, this anomalous behaviour of the coastal Cape Mountains appears to be largely the result of an overwhelmingly strong lithological control which has repressed denudation rates and preserved the landscape of these mountains through time, supported by a climate dry enough to inhibit erosive high-intensity precipitation events yet moist enough to support protective vegetative cover.

Three conclusions can be drawn from this:

1. The power-law function often used to describe denudation rates in rugged terrains predicts an exponential increase in denudation rates once hillslopes steepen beyond ~25° and a decoupling of hillslopes and denudation rates near a commonly reported threshold angle of ~30°. This has been attributed to the occurrence of debris flows at ~25° and landsliding at ~30°. Despite a spectrum of catchment-averaged slope angles ranging from 12° to 30°, no such exponential increase in erosion rates is seen in the coastal Cape Mountains data. Instead, erosion rates increase linearly with slope angle. It appears that while denudation rates do scale with slope

steepness, steep slope angles alone are not sufficient to incite high denudation rates. Frequent excitation by an external trigger, such as seismics or high rainfall that are common in actively uplifting orogens, is required to destabilise material on hillslope faces and bring about an exponential increase in denudation rate with increase in slope angle. In the absence of such triggers slope failure is a rare phenomenon. High denudation rates are therefore not only dependent on steep slopes but also the presence of external forcings. Similar hypotheses were suggested by both Summerfield and Hulton (1994) and von Blanckenburg et al.(2004), and are here further supported by data from the coastal Cape Mountains. In addition, this general trend of an exponential increase in denudation rates with slope has overlooked the case of a strong lithological control as is apparent in the coastal Cape Mountains.

It would therefore be incorrect to infer high denudation rates by a priori from steep hillslopes and steep river channels. While this may often be the case the coastal Cape Mountains are evidence that, given the appropriate specific conditions of lithology and climate, steep topography may be preserved over long periods of time and thus be unrelated to the current surface processes operating in the landscape, i.e. such rugged topography can also be associated with severely repressed denudation rates.

2. Topography does not always reflect the rates of surface processes. The coastal Cape Mountains are an example where steep topography has become 'decoupled' from high erosion rates. The long-term preservation of a landscape has resulted in an ancient rugged terrain within a present-day tectonically quiescent setting, where anomalously low denudation rates prevail. This unusual combination of an 'alpine' topography and 'cratonic' denudation rates is likely the result of suitable lithologic and climatic conditions. It should be noted that this is not the first study to report a decoupling of topography and denudation rates, as Gabet et al. (2011) report that high mean annual rainfall in areas of the Himalayas has resulted in a notable reduction of hillslope in comparison to drier regions of the Himalayas, with no accompanying reduction in denudation rates.

3. The empirical relationships defining slope-denudation functions deserve some revision. Data from the coastal Cape Mountains give good reason to believe that the linear slope-denudation rate relationship considered descriptive of low-relief regions would be more correctly understood as descriptive of tectonically quiescent environments, regardless of the topography. With this comes an understanding that a rugged topography can still yield exceptionally low denudation rates under the correct circumstances.

7.6 Summary and conclusions

7.6.1 Denudational controls within the coastal Cape Mountains

The coastal Cape Mountains exhibit unusually low denudation rates in a very rugged terrain. This phenomenon makes the coastal Cape Mountains an anomaly in the global hillslope-denudation rate trend (Figure 7.10).

These unusual results may be attributed to a strong lithological control on denudation rates in the absence of an active tectonic forcing, supported by appropriate climatic conditions. The relief of these coastal ranges appears to be maintained by the robust quartzites of which they are principally comprised, particularly the Peninsula Formation quartzite of the Table Mountain Group, Cape Supergroup. These quartzites are resistant to chemical weathering and physical abrasion and, in the absence of an external destabilising force such as seismic activity or high precipitation rates, can maintain high hillslope angles. Furthermore, they contribute particularly coarse bedload to the mountain rivers that serves to shield the underlying bedrock channels from abrasion. Accumulatively, these aspects of lithology can act to suppress denudation rates within the mountains.

Climate may contribute to low denudation rates by supporting vegetation growth on the mountain slopes which shields the underlying bedrock, and through the infrequency of flood events that have the power to mobilise the coarse bedload that overlies and shields the bedrock channels.

The implication of these results that indicate a rugged terrain coupled with low denudation rates, is a cautionary note: although denudation rates may scale primarily with hillslope angle, this relationship is qualitative and not quantitative. Steep hillslopes do not necessarily reflect rapid denudation rates. The coastal Cape Mountains reflect one such environment where steep topography has become decoupled from rapid denudation rates. Furthermore, the linear hillslope-denudation rate relationship considered descriptive of gentle terrains in tectonically quiescent environments appears equally applicable to rugged terrains in tectonically quiescent environments.

7.6.2 Landscape evolution

Denudation rates and exposure ages determined for the study area are some of the first quantitative, analytical data for the area. As such, they offer valuable insight into the denudational dynamics that govern the geomorphic evolution of catchments in the coastal Cape Mountains and thus the geomorphic evolution of the ranges in which they occur. Furthermore, these data provide a means of assessing previous landscape evolution models that have been applied in the region.

The results of this study indicate that the landscape of the coastal Cape Mountains has been relatively undisturbed since at least the late-Pleistocene and is further interpreted to be approaching geomorphic steady-state. Denudation rates estimated by apatite fission track analysis for the southern Cape over the period of the Cenozoic, are in close agreement with the low denudation rates reported here for the mountain slopes of the coastal Cape Mountains, through the analysis of *in situ*-produced cosmogenic ^{10}Be, since the late-Pleistocene. The low denudation rates and their spatial invariance does not support the work of previous authors who suggest that rapid river incision within the quartzites of the coastal Cape Mountains since the Mio-Pliocene or late-Pleistocene, has contributed in a significant manner to the formation of the steep canyons which dissect it. This, coupled with the suggestion that the landscape may have experienced stability for periods of time longer than the late-Pleistocene to present, gives reason to question the landscape evolution hypotheses which suggest that epeirogenic uplift as recent as ~3-5 Ma have rejuvenated rivers within the coastal Cape Mountains of southern Africa.

7.6.3 Concluding remarks

This study of the denudation rates prevailing in the coastal Cape Mountains, and their implications for the recent geomorphic evolution of the region, highlights the importance of placing 'dates' and 'rates' on geomorphic forms and processes. Without quantitative analytical data, interpretations of a landscape may be inaccurate and unreliable. Such information is lacking in the Cape Mountains and indeed throughout much of southern Africa. The need for further chronometric studies in the region is clear.

References

Abbühl, L.M., Norton, K.P., Schlunegger, F., Kracht, O., Aldahan, A. and Possnert, G., 2010, El Niño forcing on ^{10}Be-based surface denudation rates in the north-western Peruvian Andes. Geomorphology, v. 123, no. 3-4, p. 257-268.

Anderson, R.S., Repka, J.L. and Dick, G.S., 1996, Explicit treatment of inheritance in dating depositional surfaces using *in situ* ^{10}Be and ^{26}Al. Geology, v. 24, no. 1, p. 47-51.

Anhert, F., 1970, Functional relationships between denudation, relief, and uplift in large mid-latitude drainage basins. American Journal of Science, v. 268, p. 243-263.

Balco, G., Stone, J.O., Lifton, N.A. and Dunai, T.J., 2008, A complete and easily accessible means of calculating surface exposure ages or erosion rates from ^{10}Be and ^{26}Al measurements. Quaternary Geochronology, v. 3, no. 3, p. 174-195.

Baldwin, J., Whipple, K.X. and Tucker, G.E., 2003, Implications of the shear stress river incision model for the timescale of post-orogenic decay of topography. Journal of Geophysical Research, v. 108.

Bierman, P.R. and Caffee, M., 2001, Slow rates of rock surface erosion and sediment production across the Namib Desert and escarpment, southern Africa. American Journal of Science, v. 301, no. 4-5, p. 326-358.

Bierman, P.R. and Caffee, M., 2002, Cosmogenic exposure and erosion history of Australian bedrock landforms. Geological Society of America, no. 7, p. 787-803.

Bierman, P.R., Caffee, M.W., Davis, P.T., Marsella, K., Pavich, M., Colgan, P., Mickelson, D. and Larsen, J., 2002, Rates and timing of earth surface processes from *in situ*-produced cosmogenic ^{10}Be. Reviews in Mineralogy and Geochemistry, v. 50, no. 1, p. 147-205.

Bierman, P. and Steig, E.J., 1996, Estimating rates of denudation using cosmogenic isotope abundances in sediment. Earth Surface Processes and Landforms, v. 21, p. 125-139.

Binnie, S. A., Phillips, W.M., Summerfield, M. A. and Fifield, L.K., 2007, Tectonic uplift, threshold hillslopes, and denudation rates in a developing mountain range. Geology, v. 35, no. 8, p. 743.

Binnie, S.A., Phillips, W.M., Summerfield, M.A., Fifield, L.K. and Spotila, J.A., 2008, Patterns of denudation through time in the San Bernardino Mountains, California: Implications for early-stage orogenesis. Earth and Planetary Science Letters, v. 276, no. 1-2, p. 62-72.

Bintanja, R., van de Wal, R.S.W. and Oerlemans, J., 2005, Modelled atmospheric temperatures and global sea levels over the past million years. Nature, v. 437, no. 7055, p. 125-128.

Bishop, P., 2007, Long-term landscape evolution : linking tectonics and surface processes. Earth Surface Processes and Landforms, v. 32, no. 3, p. 329-365.

Bishop, P. and Goldrick, G., 2000, Geomorphological evolution of the East Australian continental margin. *In* Summerfield, M.A. (ed.), Geomorphology and Global Tectonics, Wiley, Chichester, p. 227-255.

Braucher, R., Brown, E.T., Bourlès, D.L. and Colin, F., 2003, *In situ*-produced ^{10}Be measurements at great depths: implications for production rates by fast muons. Earth and Planetary Science Letters, v. 211, no. 3-4, p. 251-258.

Braucher, R., Del Castillo, P., Siame, L., Hidy, A. J. and Bourlés, D.L., 2009, Determination of both exposure time and denudation rate from an *in situ*-produced ^{10}Be depth profile: A mathematical proof of uniqueness. Model sensitivity and applications to natural cases. Quaternary Geochronology, v. 4, no. 1, p. 56-67, doi.

Brock, F., Higham, T., Ditchfield, P. and Ramsey, C.B., 2010, Current pre-treatment methods for AMS radiocarbon dating at the Oxford radiocarbon accelerator unit (ORAU): Radiocarbon, v. 52, no. 1. p. 103-112.

Bronk Ramsey, C., 1995, Radiocarbon calibration and analysis of stratigraphy : The OxCal Program. Radiocarbon, v. 37, no. 2, p. 425-430.

Bronk Ramsey, C., Dee, M., Lee, S., Nakagawa, T. and Staff, R.A., 2010, Developments in the calibration and modelling of radiocarbon dates. Radiocarbon, v. 52, no. 2-3, p. 953-961.

Brown, R.W., Gallagher, K., Gleadow, A.J.W. and Summerfield, M.A., 2000, Morpho-tectonic evolution of the South Atlantic margins of Africa and South Africa. *In* Summerfield, M.A. (ed.): Geomorphology and Global Tectonics, John Wiley and Sons Ltd., p. 255-284.

Brown, R., Johnson, C. and Gallagher, K., 1998, Fission track analysis and its applications to geological problems. Annual Review of Earth and Planetary Science, no. 26, p. 519-572.

Brown, R.W., Rust, D.J., Summerfield, M.A., Gleadow, A.J.W. and de Wit, M.C.J., 1990, An early Cretaceous phase of accelerated erosion on the south-western margin of Africa: evidence from apatite fission track analysis and the offshore sedimentary record. Nuclear Tracks and Radiation Measurements, v. 17, no. 3, p. 339-350.

Brown, E.T., Stallard, R.F., Larsen, M.C., Raisbeck, G.M. and Yiou, F., 1995, Denudation rates determined from the accumulation of *in situ*-produced ^{10}Be in the Luquillo experimental forest, Puerto Rico. Earth and Planetary Science Letters, v. 129, no. 1-4, p. 193-202.

Brown, R.W., Summerfield, M.A. and Gleadow, A.J.W., 2002, Denudational history along a transect across the Drakensberg Escarpment of southern Africa derived from apatite fission track thermo-chronology. Journal of Geophysical Research, v. 107, no. B12, p. 1-17.

Burbank, D.W., Leland, J., Fielding, E., Anderson, R.S., Brozovic, N., Reid, M.R. and Duncan, C., 1996, Bedrock incision, rock uplift and threshold hillslopes in the north-western Himalayas. Nature, v. 379, no. 8, p. 505-510.

Carr, A.S., Bateman, M.D., Roberts, D.L., Murray-Wallace, C.V., Jacobs, Z. and Holmes, P.J., 2010, The last interglacial sea-level high stand on the southern Cape coastline of South Africa. Quaternary Research, v. 73, no. 2, p. 351-363.

Carretier, S., Ritz, J.F., Vassallo, R., Brown, E.T. and Bourles, D.L., 2006, Using *in situ*-produced ^{10}Be to quantify active tectonics in the Gurvan Bogd mountain range (Gobi-Altay, Mongolia). Geological Society of America, v. 2415, no. 06, p. 87-110.

Chmeleff, J., von Blanckenburg, F., Kossert, K. and Jakob, D., 2010, Determination of the ^{10}Be half-life by multi-collector ICP-MS and liquid scintillation counting. Nuclear Instruments and Methods in Physics Research, B, v. 268, p. 192-199.

Clayton, K. and Shamoon, N., 1998, A new approach to the relief of Great Britain II. A classification of rocks based on relative resistance to denudation. Geomorphology, v. 25, p. 155-171.

Cockburn, H.A.P., Brown, R.W., Summerfield, M.A. and Seidl, M.A., 2000, Quantifying passive margin denudation and landscape development using a combined fission-track thermo-chronology and cosmogenic isotope analysis approach. Earth and Planetary Science Letters, v. 179, p. 429-435.

Cockburn, H.A.P., Seidl, M.A. and Summerfield, M.A., 1999, Quantifying denudation rates on inselbergs in the central Namib Desert using *in situ*-produced cosmogenic ^{10}Be and ^{26}Al. Geology, v. 27, no. 5, p. 399-402.

Codilean, A.T., 2006, Calculation of the cosmogenic nuclide production topographic shielding scaling factor for large areas using DEMs. Earth Surface Processes and Landforms, v. 31, p. 785-794.

Codilean, A.T., 2008, Single grain detrital cosmogenic ^{21}Ne analysis : A new tool to study long-term landscape evolution: University of Glasgow. (PhD thesis)

Codilean, A.T., Bishop, P., Stuart, F.M., Hoey, T.B., Fabel, D. and Freeman, S.P.H.T., 2008, Single-grain cosmogenic ^{21}Ne concentrations in fluvial sediments reveal spatially variable erosion rates. Geology, v. 36, no. 2, p. 159.

Compton, J.S., 2001, Holocene sea-level fluctuations inferred from the evolution of depositional environments of the southern Langebaan lagoon salt marsh, South Africa. The Holocene, v. 11, no. 4, p. 395-405.

Compton, J.S. and Wiltshire, J.G., 2009, Terrigenous sediment export from the western margin of South Africa on glacial/interglacial cycles. Marine Geology, v. 266, p. 212-222.

Cotterill, F.P.D. and de Wit, M.J., 2011, Geo-ecodynamics and the Kalahari epeirogeny: linking its genomic record, tree of life and palimpsest into a unified narrative of landscape evolution. South African Journal of Geology, v. 114, no. 3-4, p. 489-514.

Cowling, R.M., Procheş, S. and Partridge, T.C., 2009, Explaining the uniqueness of the Cape flora: incorporating geomorphic evolution as a factor for explaining its diversification. Molecular Phylogenetics and Evolution, v. 51, no. 1, p. 64-74.

Dale, V., King, A., Mann, L., Washington-Allen, R. and McCord, R., 1998, Assessing land-use impacts on natural resources. Environmental Management, v. 22, no. 2, p. 203-211.

Davies, T.A., Hay, W.W., Southam, J.R. and Worsley, T.R., 1977, Estimates of Cenozoic oceanic sedimentation rates. Science, v. 197, p. 53-55.

Davis, W.M., 1906a, Observations in South Africa. Geological Society of America, v. 17. p. 378-450.

Davis, W.M., 1906b, The Mountains of southernmost Africa. Bulletin of the Geological Society of America, v. 38, no. 10, p. 593-623.

Decker, J.E., 2010, Landscape evolution and equilibrium in Southern Africa : insights from cosmogenic noble gases in Karoo dolerites and geospatial analysis: University of Cape Town. (PhD thesis)

Decker, J.E., Niedermann, S. and de Wit, M.J., 2012, Soil erosion rates in South Africa compared with cosmogenic ^{3}He-based rates of soil production. South African Journal of Geology, v. 114, no. 3-4, p. 475-488.

Delunel, R., van der Beek, P. A., Carcaillet, J., Bourlès, D.L. and Valla, P.G., 2010, Frost-cracking control on catchment denudation rates: Insights from *in situ*-produced ^{10}Be concentrations in stream sediments (Ecrins–Pelvoux massif, French Western Alps). Earth and Planetary Science Letters, v. 293, no. 1-2, p. 72-83.

Desilets, D. and Zreda, M., 2003, Spatial and temporal distribution of secondary cosmic-ray nucleon intensities and applications to *in situ* cosmogenic dating. Earth and Planetary Science Letters, v. 206, p. 21-42.

Desilets, D., Zreda, M. and Lifton, N.A., 2001, Comment on 'Scaling factors for production rates of *in situ*-produced cosmogenic nuclides : a critical re-evaluation by T. J. Dunai. Earth and Planetary Science Letters, v. 188, p. 283-287.

Desilets, D., Zreda, M. and Prabu, T., 2006, Extended scaling factors for *in situ* cosmogenic nuclides : New measurements at low latitude. Earth and Planetary Science Letters, v. 246, p. 265-276.

De Wit, M., 2007, The Kalahari epeirogeny and climate change: differentiating cause and effect from core to space. South African Journal of Geology, v. 110, p. 367-392.

DiBiase, R.A., Whipple, K.X., Heimsath, A.M. and Ouimet, W.B., 2010, Landscape form and millennial erosion rates in the San Gabriel Mountains, CA. Earth and Planetary Science Letters, v. 289, p. 134-144.

Dingle, R.V., 1982, Continental margin subsidence: a comparison between the east and west coasts of Africa. *In* Dynamics of Passive Margins, R.A. Scrutton (ed.): American Geophysical Union, Geodynamics Series, v. 6, p. 59-71.

Dorman, L.I., Valdes-Galicia, J.F. and Dorman, I.V., 1999, Numerical simulation and analytical description of solar neutron transport in the Earth's atmosphere. Journal of Geophysical Research, v. 104, p. 22417 - 22426.

Doucouré, C.M. and de Wit, M.J., 2003, Old inherited origin for the present near-bimodal topography of Africa. Journal of African Earth Sciences, v. 36, p. 371-388.

Dunai, T.J., 2000, Scaling factors for production rates of *in situ*-produced cosmogenic nuclides : a critical re-evaluation. Earth and Planetary Science Letters, v. 176, p. 157-169

Dunai, T.J., 2001, Reply to comment on: Scaling factors for production rates of *in situ*-produced cosmogenic nuclides : a critical re-evaluation by Darin Desilets, Marek Zreda and Nathaniel Lifton. Earth and Planetary Science Letters, v. 188, p. 289-298.

Dunai, T.J., 2001, Influence of secular variation of the geomagnetic field on production rates of *in situ*-produced cosmogenic nuclides. Earth and Planetary Science Letters, v. 193, p. 197-212.

Dunai, T.J., 2010, Cosmogenic Nuclides: Principles, concepts and applications in the earth surface sciences. Cambridge University Press, Cambridge, 198 pp.

Dunne, J., Elmore, D. and Muzikar, P., 1999, Scaling factors for the rates of production of cosmogenic nuclides for geometric shielding and attenuation at depth on sloped surfaces. Geomorphology, v. 27, p. 3-11.

Du Toit, A.L., 1933, Crustal movement as a factor in the geographical evolution of South Africa. South African Geographical Journal, no. 16, p. 3-20.

Du Toit, A.L., 1937: Our wandering continents: Oliver and Boyd Ltd., Edinburgh, 366 pp.

Farley, K. A., 2002, (U-Th)/He Dating: techniques, calibrations, and applications. Reviews in Mineralogy and Geochemistry, v. 47, no. 1, p. 819-844.

Farnsworth, K.L. and Milliman, J.D., 2003, Effects of climatic and anthropogenic change on small mountainous rivers: The Salinas River. Global and Planetary Change, v. 39, p. 53-64.

Fey, M., Hughes, J. and Lamprecht, J., 2010, Soils of South Africa. Cambridge University Press, Cape Town, 288 pp.

Finnegan, N.J., Hallet, B., Montgomery, D.R., Zeitler, P.K., Stone, J., Anders, A. and Liu, Y., 2008, Coupling of rock uplift and river incision in the Namche Barwa-Gyala Peri massif, Tibet. Geological Society of America Bulletin, v. 120, no. 1-2, p.142-155.

Fleming, K., Johnston, P., Zwartz, D., Yokoyama, Y., Lambeck, K. and Chappell, J., 1998, Refining the eustatic sea-level curve since the last glacial maximum using far- and intermediate-field sites. Earth and Planetary Science Letters, v. 163, p. 327-342.

Fleming, A., Summerfield, M.A., Stone, J.O., Fifield, L.K. and Cresswell, R.G., 1999, Denudation rates for the southern Drakensberg escarpment, SE Africa, derived from *in-situ*-produced cosmogenic ^{36}Cl: initial results. Journal of the Geological Society, London, v. 156, p. 209-212.

Flint, R.F., 1963, Altitude and lithology and the fall zone in Connecticut. Journal of Geology, v. 71, p. 683-697.

Flint, J.J., 1974, Stream gradient as a function of order, magnitude, and discharge. Water Resources Research, v. 10, p. 969-973.

Flowers, R.M. and Schoene, B., 2010, (U-Th)/He thermo-chronometry constraints on unroofing of the eastern Kaapvaal craton and significance for uplift of the southern African Plateau. Geology, v. 38, no. 9, p. 827-830.

Gabet, E.J., Pratt-Sitaula, B.E. and Burbank, D.W., 2011, Climatic controls on hillslope angle and relief in the Himalayas. Geological Society of America, v. 32, no. 7, p. 629-632.

Gilbert, G.K., 1877, Report on the geology of the Henry Mountains: Geographical and geological survey of the Rocky Mountain region: Washington, D.C. Government Printing Office, p. 69.

Gilbert, G.K., 1909, The convexity of hilltops. Geology, v. 17, no. 4, p. 344-350.

Gilchrist, A.R., Kooi, H. and Beaumont, C., 1994, Post-Gondwana geomorphic evolution of south-western Africa: Implications for the controls on landscape development from observations and numerical experiments. Journal of Geophysical Research, v. 99, p. 12211–12228.

Goldrick, G. and Bishop, P., 2007, Regional analysis of bedrock stream long profiles : evaluation of Hack's SL form, and formulation and assessment of an

alternative (the DS form). Earth Surface Processes and Landforms, v. 32, p. 649-671.

Gosse, J.C. and Phillips, F.M., 2001, Terrestrial *in situ* cosmogenic nuclides : theory and application. Quaternary Science Reviews, v. 20, p. 1475-1560.

Goodier, S.A.M., Cotterill, F.P.D., O'Ryan, C., Skelton, P.H. and de Wit, M.J., 2011, Cryptic diversity of African tigerfish (Genus *Hydrocynus)* reveals palaeogeographic signatures of linked Neogene geotectonic events (N. J. Gemmell, ed.). PLos ONE, v. 6, no. 12, p. e28775.

Granger, D.E., Kirchner, J.W. and Finke, R., 1996, Spatially averaged long-term erosion rates measured from *in situ*-produced cosmogenic nuclides in alluvial sediment. The Journal of Geology, v. 104, p. 249-257.

Granger, D.E. and Riebe, C.S., 2007, Cosmogenic nuclides in weathering and erosion. *In* Treatise in Geochemistry, Elsevier, Amsterdam, p. 11-43.

Greenwood, N.N. and Earnshaw, A., 1997, Chemistry of the elements. Butterworth Heinemann, Oxford, 340 pp.

Gupta, D., Carolina, X. and Strelow, F.W.E., 1960, An ion-exchange selectivity scale of cations based on equilibrium distribution coefficients. Analytical Chemistry, v. 32, no. 9, p. 1185-1188.

Hancock, G.S., Anderson, R.S., Chadwick, O.A. and Finkel, R.C., 1999, Dating fluvial terraces with ^{10}Be and ^{26}Al profiles : application to the Wind River, Wyoming. Geomorphology, v. 27, p. 41-60.

Haq, B.U., Hardenboi, J. and Vail, P.R., 1987, Chronology of fluctuating sea level since the Triassic. Science, v. 235, p. 1156-1167.

Harrison, C.G.A., 2000, What factors control mechanical erosion rates? International Journal of Earth Sciences, v. 88, no. 4, p. 752-763.

Hedges, R.E.M., Wand, J.O. and White, N.R., 1980, The Production of C-beams for radiocarbon dating with accelerators. Nuclear Instruments and Methods, v. 173, p. 409-421.

Heisinger, B., Lal, D., Jull, A.J.T., Kubik, P., Ivy-Ochs, S., Knie, K. and Nolte, E., 2002a, Production of selected cosmogenic radionuclides by muons: 1. Fast muons. Earth and Planetary Science Letters, v.200, p. 345-355.

Heisinger, B., Lal, D., Jull, A.J.T., Kubik, P., Ivy-Ochs, S., Knie, K. and Nolte, E., 2002b, Production of selected cosmogenic radionuclides by muons: 2. Capture of negative muons. Earth and Planetary Science Letters, v. 200, p. 357-369.

Hermanns, R.L., Niedermann, S., Ivy-Ochs, S. and Kubik, P. W., 2004, Rock avalanching into a landslide-dammed lake causing multiple dam failure in Las Conchas valley (NW Argentina) – evidence from surface exposure dating and stratigraphic analyses: Landslides, v. 2, no. 1, p. 113-122.

Hewawasam., 2003, Increase of human over natural erosion rates in tropical highlands constrained by cosmogenic nuclides: Geological Society of America, no. 7, p. 597-600.

Hoffmann, V., 2011, Linking landscape evolution and past climatic changes to the evolution and diversity of plant ecology specialists in the Cape Fold Belt. Geosynthesis: 8th Annual Inkaba Workshop, Cape Town, 2011.

Hooke, R.L., 2000, On the history of humans as geomorphic agents. Geology, no. 9, p. 843-846.

Howard, A.D., 1994, A detachment-limited model of drainage basin evolution. Water Resources Research, v. 30, no. 7, p. 2261.

Insel, N., Ehlers, T. A., Schaller, M., Barnes, J.B., Tawackoli, S. and Poulsen, C.J., 2010, Spatial and temporal variability in denudation across the Bolivian Andes from multiple geochronometers. Geomorphology, v. 122, no. 1-2, p. 65-77.

Jakica, S., Quigley, M.C., Sandiford, M., Clark, D., Fifield, L.K. and Alimanovic, A., 2011, Geomorphic and cosmogenic nuclide constraints on escarpment evolution in an intra-plate setting, Darling Escarpment, Western Australia. Earth Surface Processes and Landforms, v. 36, no. 4, p. 449-459.

Jansen, J.D., Codilean, A.T., Bishop, P. and Hoey, T.B., 2010, Scale dependence of lithological control on topography: bedrock channel geometry and catchment morphometry in Western Scotland. The Journal of Geology, v. 118, no. 3, p. 223-246.

Kent, L.E., 1980, Cape Supergroup. *In* de Grys, A. (ed.): Stratigraphy of South Africa, Handbook 8, Government Printer, Pretoria, p. 690.

King, L.C., 1951, South African Scenery: Oliver and Boyd Ltd., London, 308 pp.

King, L.C., 1953, Canons of landscape evolution. Geological Society of America Bulletin, no. 7, p. 721-752.

King, L.C., 1957, The uniformitarian nature of hillslopes. Transactions of the Edinburgh Geological Society, no. 17, p. 81-102.

King, L.C., 1962, The morphology of the earth. Oliver and Boyd Ltd., London, 699 pp.

Kirby, E. and Ouimet, W., 2011, Tectonic geomorphology along the eastern margin of Tibet: insights into the pattern and processes of active deformation adjacent to the Sichuan Basin. *In* Gloaguen, R. and Ratschbacher, L. (eds.): Growth and collapse of the Tibetan Plateau, Geological Society, London, Special Publications, London, p. 165-188.

Kirby, E. and Whipple, K.X., 2003, Distribution of active rock uplift along the eastern margin of the Tibetan Plateau: Inferences from bedrock channel longitudinal profiles. Journal of Geophysical Research, v. 108, no. B4, p. 16-22.

Kirby, E., Johnson, C., Furlong, K. and Heimsath, A., 2007, Transient channel incision along Bolinas Ridge, California: Evidence for differential rock uplift adjacent to the San Andreas Fault. Journal of Geophysical Research, v. 112, p. 1-17.

Kirchner, J.W., Finkel, R.C., Riebe, C.S., Granger, D.E., Clayton, J.L., King, J.G. and Megahan, W.F., 2001, Mountain erosion over 10 yr, 10 k.y., and 10 m.y. time scales. Geology, v. 29, no. 7, p. 591.

Kohl, C.P., and Nishiizumi, K., 1992, Chemical isolation of quartz for measurement of *in situ*-produced cosmogenic nuclides. Geochimica et Cosmochimica Acta, v. 56, p. 3583-3587.

Koppes, M.N. and Montgomery, D.R., 2009, The relative efficacy of fluvial and glacial erosion over modern to orogenic timescales. Nature Geoscience, v. 2, no. 9, p. 644-647.

Korschinek, G., Bergmaier, A., Faestermann, T., Gerstmann, U.C., Knie, K., Rugel, G., Wallner, A., Dillmann, I., Dollinger, G., Lierse von Gostomski, C., Kossert, K., Maiti, M., Poutivtsev, M. and Remmert, A., 2009, A new value for the half-life of ^{10}Be by heavy-ion elastic recoil detection and liquid scintillation counting. Nuclear Instruments and Methods in Physics Research B, v. 268, p. 187-191.

Korup, O., 2008, Rock type leaves topographic signature in landslide-dominated mountain ranges. Geophysical Research Letters, v. 35, no. 11, p. 1-5.

Kounov, A., Niedermann, S., de Wit, M.J. and Viola, G., 2007, Present denudation rates at selected sections of the South African escarpment and the elevated continental interior based on cosmogenic ^{3}He and ^{21}Ne. South African Journal of Geology, v. 110, p. 235-248.

Kounov, A., Viola, G., de Wit, M. and Andreoli, M.A.G., 2009, Denudation along the Atlantic passive margin: new insights from apatite fission-track analysis on the western coast of South Africa. Geological Society, London, Special Publications, v. 324, no. 1, p. 287-306.

Kubik, P.W. and Christl, M., 2010, ^{10}B and ^{26}Al measurements at the Zurich 6 MV Tandem AMS facility. Nuclear Instruments and Methods in Physics Research, B, v. 268, no. 7-8, p. 880-883

Kubik, P.W., Christl, M. and Alfimov, V., 2009, New Primary ^{10}Be Standard and $T_{1/2}$ for AMS at ETH: Recalibration of the in-house ^{10}Be standards. Ion Beam Physics, ETH Zurich, Annual report, p. 12.

Lal, D., 1988, *In situ*-produced cosmogenic isotopes in terrestrial rocks. Annual Review of Earth and Planetary Science, v. 16, p. 355-388.

Lal, D., 1991, Cosmic ray labelling of erosion surfaces : *in situ* nuclide production rates and erosion models. Earth and Planetary Science Letters, v. 104, p. 424-439.

Lal, D., and Chen, J., 2005, Cosmic ray labelling of erosion surfaces II: Special cases of exposure histories of boulders, soils and beach terraces. Earth and Planetary Science Letters, v. 236, p. 797-813.

Lal, D. and Peters, B., 1967, Cosmic ray produced radioactivity on the earth. *In* Handbook of Physics, Springer, Berlin, p. 551-612.

Lenz, C.J., 1957, The river evolution and the remnants of the Tertiary surfaces in the western Little Karoo. *In* Annals of the University of Stellenbosch: Series A, v.33, no. 5, p.193-234

Lifton, N.A., Bieber, J.W., Clem, J.M., Duldig, M.L., Evenson, P., Humble, J.E. and Pyle, R., 2005, Addressing solar modulation and long-term uncertainties in scaling secondary cosmic rays for *in situ* cosmogenic nuclide applications. Earth and Planetary Science Letters, v. 239, no. 1-2, p. 140-161.

Macfarlane, D.R., 1949, A preliminary report on the age of the high-level gravels between Napier and Riversdale. South African Archaeological Bulletin, v. 4, p. 95-97.

Masarik, J. and Beer, J., 1999, Simulation of particle fluxes and cosmogenic nuclide production in the earth's atmosphere. Journal of Geophysical Research, v. 104, no. 10, p. 1-15.

Masarik, J. and Reedy, R.C., 1995, Terrestrial cosmogenic-nuclide production systematics calculated from numerical simulations. Earth and Planetary Science Letters, v. 136, p. 381-395.

Masarik, J., Frank, M., Schäfer, J.M. and Wieler, R., 2001, Correction of *in situ* cosmogenic nuclide production rates for geomagnetic field intensity variations during the past 800,000 years. Geochimica et Cosmochimica Acta, v. 65, p. 2995-3003.

Maske, S., 1957, A critical review of superimposed and antecedent rivers in southern Africa. *In* Annals of the University of Stellenbosch: Series A, v. 33, no.1, p.1-22.

Matmon, A., Bierman, P.R., Larsen, J., Southworth, S., Pavich, M., Finkel, R. and Caffee, M., 2003, Erosion of an ancient mountain range, the Great Smokey Mountains, North Carolina and Tennessee. American Journal of Science, v. 303, p. 817-866.

Macfarlane, D.R., 1949, A preliminary report on the age of the High-Level gravels between Napier and Riversdale. South African Archeological Society, v. 9, p.95-97.

McAlister, D.R. and Horwitz, E., 2005, A method for the separation of beryllium from spectral interfering elements in ICP-AES analysis. Talanta, v. 67, p. 873-879.

McKean, J.A., Dietrich, W.E., Finkle, R.C., Southon, J.R. and Caffee, M.W., 1993, Quantification of soil production and down-slope creep rates from cosmogenic ^{10}Be accumulations of a hillslope profile. Geology, v. 21, p. 343-346.

McMillan, I.K., 2003, Foraminiferally defined biostratigraphic episodes and sedimentation pattern of the Cretaceous drift succession (Early Barremian to Late Maastrichtian) in seven basins on the South African and southern Namibian continental margin. South African Journal of Science, v. 99, p. 537-576.

Merrill, R.T., McElhinny, M.W. and McFadden, P.L., 1998, The magnetic field of the earth. Academic Press, San Diego, 531 pp.

Milani, E.J. and de Wit, M.J., 2008, Correlations between the classic Parana and Cape-Karoo sequences of South American and southern Africa and their basin infills flanking the Gondwanides: du Toit revisited, *in* Pankhurst, R.J., Trouw, R.A.J., Brito Neves, B.B., and de Wit, M.J. (Eds.): West Gondwana: Pre-Cenozoic correlations across the South Atlantic region. Geological Society, London, Special Publications, 294, p. 319-342.

Milliman, J.D. and Syvitski, J.P.M., 1992, Geomorphic/tectonic control of sediment discharge to the ocean : The importance of small mountainous rivers. Journal of Geology, v. 100, no. 5, p. 525-544.

Milliman, J.D., Yun-shan, Q., Mei-e, R. and Saito, Y., 1987, Man's influence on the erosion and transport of sediment by Asian rivers : The Yellow River (Huanghe) Example. Journal of Geology, v. 95, no. 6, p. 751-762.

Molnar, P., Anderson, R.S. and Anderson, S.P., 2007, Tectonics, fracturing of rock, and erosion. Journal of Geophysical Research, v. 112, p. 1-12.

Molnar, P. and England, P., 1990, Late Cenozoic uplift of mountain ranges and global climate change: chicken or egg?. Nature, v. 346, p. 29-34.

Montgomery, D.R., 2003, Predicting landscape-scale erosion rates using elevation models. Comptes Rendus Geosciences, v. 335, no. 16, p. 1121-1130.

Montgomery, D.R. and Brandon, M.T., 2002, Topographic controls on erosion rates in tectonically active mountain ranges. Earth and Planetary Science Letters, v. 201, no. 3-4, p. 481-489.

Montgomery, D.R. and Foufoula-Georgiou, E., 1993, Channel network representation using digital elevation models. Water Resources Research, v. 29, p. 1178 - 1191.

Montgomery, D.R. and Schmidt, K.M., 1995, Limits to relief. Science, v. 270, no. October, p. 617-620.

Montgomery, D.R., Balco, G. and Willett, S.D., 2001, Climate, tectonics, and the morphology of the Andes. Geology, v. 29, no. 7, p. 579.

Moon, B.P., 1984, The forms of rock slopes in the Cape Fold Mountains. The South African Geographical Journal, v. 66, no. 1, p.16-31.

Moore, A.E., 1999, A reappraisal of epeirogenic flexure axes in southern Africa. South African Journal of Geology, v. 4, no. 102, p. 363- 376.

Moore, A. and Blenkinsop, T., 2006, Scarp retreat versus pinned drainage divide in the formation of the Drakensberg escarpment, southern Africa. South African Journal of Geology, v. 100, p. 599-610.

Moulton, K.L. and Berner, R.A., 1998, Quantification of the effect of plants on weathering : Studies in Iceland. Geology, v. 26, no. 10, p. 895-898

Muzikar, P., 2009, General models for episodic surface denudation and its measurement by cosmogenic nuclides. Quaternary Geochronology, v. 4, no. 1, p. 50-55.

Newton, A.R., Shone, R.W. and Booth, P.K., 2006, The Cape Fold Belt, *in* Johnson, M.R., Anhaeusser, C., and Thomas, R. (Eds.): The Geology of South Africa. Geological Society of South Africa, Johannesburg/Council for Geoscience, Pretoria, p. 691.

Niedermann, S., 2002, Cosmic-ray-produced noble gases in terrestrial rocks: dating tools for surface processes. Reviews in Mineralogy and Geochemistry, v. 47, p. 731-784.

Niemi, N.A., Oskin, M., Burbank, D.W., Heimsath, A.M. and Gabet, E.J., 2005, Effects of bedrock landslides on cosmogenically determined erosion rates. Earth and Planetary Science Letters, v. 237, no. 3-4, p. 480-498.

Nishiizumi, K., Imamura, M., Caffee, M., Southon, J., Finkel, R. and McAninch, J., 2007, Absolute calibration of ^{10}Be AMS standards. Nuclear instruments and methods in Physics Research Section B: Beam Interactions with Materials and Atoms, v. 258, no. 2, p. 403-413.

Norton, K.P., von Blanckenburg, F., Schlunegger, F., Schwab, M. and Kubik, P.W., 2008, Cosmogenic nuclide-based investigation of spatial erosion and hillslope channel coupling in the transient foreland of the Swiss Alps: Geomorphology, v. 95, no. 3-4, p. 474-486.

Norton, K.P., von Blanckenburg, F. and Kubik, P.W., 2010, Cosmogenic nuclide-derived rates of diffusive and episodic erosion in the glacially sculpted upper Rhone Valley, Swiss Alps. Earth Surface Processes and Landforms, v. 35, p. 651-662.

Norton, K.P., von Blanckenburg, F., DiBiase, R., Schlunegger, F. and Kubik, P.W., 2011, Cosmogenic ^{10}Be-derived denudation rates of the Eastern and Southern European Alps. International Journal of Earth Sciences, v. 100, no. 5, p. 1163-1179.

Nyblade, A.A. and Robinson, S.W., 1994, The African superswell. Geophysical Research Letters, v. 21, p. 765-768.

Ouimet, W.B., Whipple, K.X. and Granger, D.E., 2009, Beyond threshold hillslopes: Channel adjustment to base-level fall in tectonically active mountain ranges. Geology, v. 37, no. 7, p. 579-582.

Palumbo, L., Hetzel, R., Tao, M., and Li, X., 2010, Topographic and lithologic control on catchment-wide denudation rates derived from cosmogenic ^{10}Be in two mountain ranges at the margin of NE Tibet. Geomorphology, v. 117, no. 1-2, p. 130-142.

Partridge, T.C., 1993, Warming phases in Southern Africa during the last 150 000 years: an overview. Palaeogeography, Paleoclimatology, Paleoecology, v. 101, p. 237-244.

Partridge, T.C., 1998: Of diamonds, dinosaurs and diastrophism: 150 million years of landscape evolution in southern Africa. South African Geographical Journal, v. 101, no. 3, p. 167-184.

Partridge, T.C. and Maud, R.R., 1987, Geomorphic evolution of southern Africa since the Mesozoic. South African Journal of Geology, v. 90, no. 2, p. 179-208.

Partridge, T.C., Avery, D.M., Botha, G.A., Brink, J.S., Deacon, J., Herbert, R.S., Maud, R.R., Scholtz, A., Scott, A., Scott, L., Talma, A.S. and Vogel, J.S., 1990, Late Pleistocene and Holocene climatic change in southern Africa. South African Journal of Science, v. 86, p. 302-306.

Partridge, T.C. and Maud, R.R., 2000, Macro-scale geomorphic evolution of southern Africa. *In* Partridge, T.C. and Maud, R.R. (eds.): The Cenozoic of Southern Africa, Oxford University Press, New York, p. 3-18.

Partridge, T.C., Botha, G.A. and Haddon, I.G., 2006, Cenozoic deposits of the interior. *In* Johnson, M.R., Anhaeusser, C.R. and Thomas, R.J. (eds.): Geology of South Africa, Geological Society of South Africa, Johannesburg/Council for Geoscience, Pretoria, p. 585-604.

Peizhen, Z., Molnar, P. and Downs, W.R., 2001, Increased sedimentation rates and grain sizes 2-4 Myr ago due to the influence of climate change on erosion rates. Nature, v. 410, no. 6831, p. 891- 897.

Penk, W., 1924, Die morphologische Analyse: Stuttgart, 42 pp.

Pettifer, G.S. and Fookes, P.G., 1994, A revision of the graphical method for assessing the excavatability of rock. Quarterly Journal of Engineering Geology and Hydrogeology, v. 27, no. 2, p. 145-164.

Phillips, F.M., Stone, W.D. and Fabryka-Martin, J.T., 2001, An improved approach to calculating low-energy cosmic ray neutron fluxes near the land/atmosphere interface. Chemical Geology, v. 175, p. 689-701.

Pinet, P. and Souriau, M., 1988, Continental erosion and large-scale relief. Tectonics, v. 7, no. 3, p. 563-582.

Portenga, E.W. and Bierman, P.R., 2011, Understanding Earth's eroding surface with ^{10}Be. GSA Today, v. 21, no. 8, p. 4-10.

Potts, P.J., 1987a, Classical and rapid methods of analysis. *In* A Handbook of Silicate Rock Analysis: Blackie and Son Ltd, Glasgow, p. 47-76.

Potts, P.J., 1987b, Ion exchange pre-concentration procedures. *In* A Handbook of Silicate Rock Analysis: Blackie and Son Ltd, Glasgow, p. 472-485.

Quigley, M., Sandiford, M., Fifield, K. and Alimanovic, A., 2007a, Bedrock erosion and relief production in the northern Flinders Ranges, Australia. Earth Surface Processes and Landforms, v. 944, p. 929-944.

Quigley, M., Sandiford, M., Fifield, L.K. and Alimanovic, A., 2007b, Landscape responses to intraplate tectonism: quantitative constraints from ^{10}Be nuclide abundances. Earth and Planetary Science Letters, v. 261, no. 1-2, p. 120-1330.

Ramsay, P.J. and Cooper, J.A., 2002, Late quaternary sea-level change in South Africa. Quaternary Research, v. 57, no. 1, p. 82-90.

Raymo, M.E. and Ruddiman, W.F., 1992, Tectonic forcing of late Cenozoic climate. Nature, v. 359, p. 117-122.

Reneau, S.L. and Dietrich, W.E., 1991, Erosion rates in the southern Oregon Coast Range: evidence for an equilibrium between hillslope erosion and sediment yield. Earth Surface Processes and Landforms, v. 16, p. 307-322.

Repka, J.L., Anderson, R.S. and Finkel, R.C., 1997, Cosmogenic dating of fluvial terraces, Fremont River, Utah. Earth and Planetary Science Letters, v. 152, p. 59-73.

Rethemeyer, J., Dewalk, A., Fülöp, R., Hajdas, I., Höfle, S., Patt, U., Stapper, B. and Wacker, L., 2011, Sample preparation facilities for ^{14}C analysis at the new Cologne AMS center. The Twelfth International Conference on

Accelerator Mass Spectrometry Program an Abstracts Handbook, March, p. 116.

Reuter, J.M., 2005, Erosion rates and patterns inferred from cosmogenic ^{10}Be in the Susquehanna River basin. The University of Vermont. (MSc thesis)

Riebe, C.S., Kirchner, J.W., Granger, D.E. and Finkel, R.C., 2001a, Minimal climatic control on erosion rates in the Sierra Nevada, California. Geology, v. 29, no. 5, p. 447.

Riebe, C.S., Kirchner, J.W., Granger, D.E. and Finkel, R.C., 2001b, Strong tectonic and weak climatic control of long-term chemical weathering rates. Geology, v. 29, no. 6, p. 511.

Riebe, C.S., Kirchner, J.W. and Finkel, R.C., 2004, Erosional and climatic effects on long-term chemical weathering rates in granitic landscapes spanning diverse climate regimes. Earth and Planetary Science Letters, v. 224, no. 3-4, p. 547-562.

Riemer, P.J., Bailie, M.G.L., Bayliss, A., Beck, J.W., Blackwell, P.G., Bronk Ramsay, C., Buck, C.E., Burr, G.S., Edwards, R.L., Friedrich, M., Grootes, P.M., Guilderson, T.P., Hajdas, I., Heaton, T.J. et al., 2009, IntCal09 and Marine09 radiocarbon age calibration curves, 0-50.000 years calBP. Radiocarbon, v. 51, no. 4, p. 1111-1150.

Roering, J.J., Kirchner, J.W. and Dietrich, W.E., 2001, Hillslope evolution by nonlinear, slope-dependent transport: Steady state morphology and equilibrium adjustment timescales. Journal of Geophysical Research, v. 106, no. B8, p. 16499-16513.

Roering, J.J., Perron, J.T. and Kirchner, J.W., 2007, Functional relationships between denudation and hillslope form and relief. Earth and Planetary Science Letters, v. 264, no. 1-2, p. 245-258.

Rogers, A.W., 1903, The geological history of the Gouritz River system. Transactions of the South African Philosophical Society, v. 2, p. 375-385.

Rohling, E.J., Grant, K., Bolshaw, M., Roberts, A.P., Siddall, M., Hemleben, C. and Kucera, M., 2009, Antarctic temperature and global sea level closely coupled over the past five glacial cycles. Nature Geoscience, v. 2, no. 7, p. 500-504,.

Rust, D.J. and Summerfield, M.A., 1990, Isopach and borehole data as indicators of rifted margin evolution in south-western Africa. Marine and Petroleum Geology, v. 7, no. 3, p. 277-287.

Safran, E.B., Bierman, P.R., Aalto, R., Dunne, T., Whipple, K.X. and Caffee, M., 2005, Erosion rates driven by channel network incision in the Bolivian Andes. Earth Surface Processes and Landforms, v. 30, no. 8, p. 1007-1024.

Schaller, M., von Blanckenburg, F., Veldkamp, A., Tebbens, L.A., Hovius, N. and Kubik, P.W., 2002, A 30 000 yr record of erosion rates from cosmogenic ^{10}Be in middle European river terraces. Earth and Planetary Science Letters, v. 204, p. 307-320.

Schulze, B.R., 1994: Climate regions in South Africa and a general summary of their characteristics. *In* Climate of South Africa: Part 8 General Survey, Department of Environmental Affairs: Weather Bureau, Pretoria, p. 313-322

Schulze, R.E., 2007, South African Atlas of Climatology and Agrohydrology. Water Research Commission, Pretoria.

Schumm, S.A., 1956, Evolution of drainage systems and slopes in Badlands at Perth Amboy, New Jersey. Bulletin of the Geological Society of America, v. 67, no. 43, p. 697-646.

Schwabedissen, H. and Freundlich, J., 1966, Köln radiocarbon measurements 1. Radiocarbon, v. 8, p. 239-247.

Selby, M.J., 1980, A rock mass strength classification. Annals of Geomorphology, v. 24, no. 1, p. 31-51.

Siame, L., Bellier, O., Braucher, R., Sébrier, M., Cushing, M., Bourlès, D., Hamelin, B., Baroux, E., de Voogd, B., Raisbeck, G. and Yiou, F., 2004, Local erosion rates versus active tectonics: cosmic ray exposure modelling in Provence (south-east France). Earth and Planetary Science Letters, v. 220, no. 3-4, p. 345-364.

Siesser, W.G. and Dingle, R.V., 1981, Tertiary sea-level movements around southern Africa. The Journal of Geology, v. 89, no. 4, p. 523-536.

Simpson, J.A. and Fagot, W.C., 1953, Properties of the low energy nucleonic component at large atmospheric depths. Physical Review, v. 90, p. 934-950.

Sklar, L.S. and Dietrich, W.E., 2001, Sediment and rock strength controls on river incision into bedrock. Geological Society of America, v. 29, no. 12, p. 1087-1090.

Small, E.E., Anderson, R.S., Repka, J.L. and Finkel, R., 1997, Erosion rates of alpine bedrock summit surfaces deduced from *in situ* ^{10}Be and ^{26}Al. Earth and Planetary Science Letters, v. 150, no. 3-4, p. 413-425.

Small, E.E., Anderson, R.S. and Hancock, G.S., 1999, Estimates of the rate of regolith production using ^{10}Be and ^{26}Al from an alpine hillslope. Geomorphology, v. 27, no. 1999, p. 131-150.

Snyder, N.P., Whipple, K.X., Tucker, G.E., Merritts, D.J. and College, M., 2000, Landscape response to tectonic forcing: Digital elevation model analysis of stream profiles in the Mendocino triple junction region, northern California. Geological Society of America, v. 112, no. 8, p. 1250-1263.

Southon, J.R., Vogel, J.S., Nowikow, I., Nelson, D.E., Korteling, R.G., Ku, T., Kusakabe, M. and Huh, C.-A., 1983, The measurement of ^{10}Be concentrations with a tandem accelerator. Nuclear Instruments and Methods, v. 205, p. 251-257.

Sparks, B.W., 1960, Geomorphology: Longman, London, 371 pp.

Stankiewicz, J. and de Wit, M.J., 2005, River networks of southern Africa: Scaling laws governing their geometry and deviations from scaling. Geochemistry Geophysics Geosystems, v. 6, no. 9, p. 1-19.

Stankiewicz, J. and de Wit, M.J., 2008, Fractal river networks of southern Africa. South African Journal of Geology, v. 108, p. 333-344.

Stone, J.O., 2000, Air pressure and cosmogenic isotope production. Journal of Geophysical Research, v. 105, no. B10, p. 23753-23759.

Stone, J., Fifield, K., Beer, J., Vonmoos, M., Obrist, C., Grajcar, M., Kubik, P., Muscheler, R., Finkel, R. and Caffee, M., 2004, Co-precipitated silver-metal oxide aggregates for accelerator mass spectrometry of ^{10}Be and ^{26}Al. Nuclear Instruments and Methods in Physics Research, v. 224, p. 272-277.

Strelow, F.W.E., Rethemeyer, R. and Bothma, C.J., 1965, Ion exchange selectivity scales for cations in nitric acid and sulfuric acid media with a sulfonated polystyrene resin. Analytical Chemistry, v. 37, no. 1, p. 106-111.

Strelow, F.W.E., Weinert, C.H.S.W. and Eloff, C., 1972, Distribution Coefficients and Anion Exchange Behavior of Elements in Oxalic Acid-Hydrochloric Acid Mixtures. Analytical Chemistry, v. 44, no. 14, p. 1-5.

Stuiver, M. and Polach, H., 1977, Discussion: Reporting of ^{14}C data. Radiocarbon, v. 19, no. 3, p. 355-363.

Summerfield, M.A., 1985, Plate tectonics and landscape development on the African continent: Tectonic Geomorphology.Pproceedings of the 15th Annual Binghampton Geomorphology Symposium, v. 15, no. 15, p. 27-51.

Summerfield, M.A., 1996, Tectonics, geology, and long-term landscape development. *In* Adams, W.M., Goudie, A.S. and Orne, A.R. (eds.): The Physical Geography of Africa, Oxford University Press, New York, p. 1-17.

Summerfield, M.A. and Hulton, N.J., 1994, Natural controls of fluvial denudation rates in major world drainage basins. Journal of Geophysical Research, v. 99, no. B7, p. 13 871 - 13 883.

Synal, H.A., Bonani, G., Ender, R.M., Gartenmann, P., Kubik, P. W., Schnabel, C. and M, S., 1997, Status report of the PSI/ETH AMS facility. Nuclear Instruments and Methods in Physics Research B, no. 123, p. 62-68.

Taljaard, J.J., 1994, Part 1: Controls of the weather and climate of South Africa. *In* Atmospheric circulation systems, synoptic climatology and weather phenomena in South Africa, Department of Environmental Affairs and Tourism – Weather Bureau, Pretoria, 45 pp.

Taljaard, J.J., 1996a, Part 5: Temperature phenomena in South Africa. *In* Atmospheric circulation systems, synoptic climatology and weather phenomena of South Africa, Department of Environmental Affairs and Tourism – Weather Bureau, p. 53.

Taljaard, J.J., 1996b, Part 6: Rainfall in South Africa. *In* Atmospheric circulation systems, synoptic climatology and weather phenomena of South Africa, Department of Environmental Affairs and Tourism – Weather Bureau, 105pp

Taljaard, M.S., 1948, On some concepts in geomorphology. The South African Geographer, v. 50, p. 5-16.

Taljaard, M.S., 1949, A glimpse of South Africa. The University Publishers and Booksellers (Pty) Ltd., Grahamstown, 226 pp.

Tera, F., Brown, L., Morris, J., Sacks, I.S., Middleton, R.O.Y. and Klein, J., 1986, Sediment incorporation in island-arc magmas: Inferences from ^{10}Be. Geochimica et Cosmochimica Acta, v. 50, p. 535-550.

Thamm, A.G. and Johnson, M.R., 2006, The Cape Supergoup. *In* Johnson, M.R., Annhaeusser, C.R., and Thomas, R.J. (eds.): Geology of South Africa, Geological Society of South Africa, Johannesburg/Council for Geoscience, Pretoria, p. 691.

Tinker, J., 2005, Quantifying South African uplift, using apatite fission track thermo-chronology and offshore sediment volumes to test the balance between denudation (onshore) and deposition (offshore) since Gondwana break-up. University of Cape Town, 484 pp.

Tinker, J. and de Wit, M.J., 2004, Balancing erosion and deposition on and around southern Africa since Gondwana break-up. Geoscience Africa 2004, Abstract Volume, p. 634-635.

Tinker, J., de Wit, M. and Brown, R., 2008, Linking source and sink : Evaluating the balance between onshore erosion and offshore sediment accumulation since Gondwana break-up, South Africa. Tectonophysics, v. 455, p. 94 - 103.

Tinker, J., de Wit, M. and Brown, R., 2008, Mesozoic exhumation of the southern Cape, South Africa, quantified using apatite fission track thermochronology. Tectonophysics, v. 455, p. 77- 93.

Tucker, G.E. and Bras, R.L., 1999, A stochastic approach to modelling drainage basin evolution. Technical report, Part A-D, p. 0-14.

Tucker, G.E. and Whipple, K.X., 1999, Dynamics of the stream-power river incision model: Implications for height limits of mountain ranges, landscape response timescales, and research needs. Journal of Geophysical Research, v. 104, no. B8, p. 17 661-17 674.

Tucker, G.E., Gasparini, N.M., Bras, R.L. and Lancaster, S.T., 1999, Overview of the CHILD Model Version 2. Technical report, Part 1-B, p. 0-17.

Turowski, J.M., Lague, D. and Hovius, N., 2007, Cover effect in bedrock abrasion: A new derivation and its implications for the modelling of bedrock channel morphology. Journal of Geophysical Research, v. 112, p. 1-16.

Twidale, C.R. and van Zyl, J.A., 1981, Some comments on the poorts and pediments of the western Little Karoo. South African Geographer, v. 9, no. 1, p. 11-24.

Vanacker, V., von Blanckenburg, F., Govers, G., Molina, A., Poesen, J., Deckers, J. and Kubik, P., 2007, Restoring dense vegetation can slow mountain erosion to near natural benchmark levels. Geology, v. 35, no. 4, p. 303.

Van der Beek, P., Summerfield, M.A., Braun, J., Brown, R.W. and Fleming, A., 2002, Modelling post-break-up landscape development and denudational history across the southeast African (Drakensberg Escarpment) margin. Journal of Geophysical Research, v. 107.

Van der Wateren, F.M. and Dunai, T.J., 2001, Late Neogene passive margin denudation history - cosmogenic isotope measurements from the central Namib desert. Global and Planetary Change, v. 30, p. 271-307.

Van Zyl, J.A., 1982, The Age and origin of Prins Poort in the Little Karoo. The South African Geographer, no. 2, v. 10, p, 135- 143

Vermeesch, P., Fenton, C.R., Kober, F., Wiggs, G.F.S., Bristow, C.S. and Xu, S., 2010, Sand residence times of one million years in the Namib Sand Sea from cosmogenic nuclides. Nature Geoscience, v. 3, p. 862-865.

Viola, G., Andreoli, M., Ben-Avraham, Z., Stengel, I. and Reshef, M., 2005, Offshore mud volcanoes and onland faulting in south-western Africa: neotectonic implications and constraints on the regional stress field. Earth and Planetary Science Letters, v. 231, p. 147-160.

Viola, G., Kounov, A., Andreoli, M. and Mattila, J., 2012, Brittle tectonic evolution along the western margin of South Africa: More than 500 Myr of continued reactivation. Tectonophysics, v. 514-517, p. 93-114.

Von Blanckenburg, F., Belshaw, N.S. and Nions, R.K.O., 1996, Separation of ^{9}Be and cosmogenic ^{10}Be from environmental materials and SIMS isotope dilution analysis. Chemical Geology, v. 129, p. 93-99.

Von Blanckenburg, F., Kubik, P.W. and Hewawasam, T., 2004, Cosmogenic nuclide evidence for low weathering and denudation in the wet, tropical highlands of Sri Lanka. Jounral of Geophysical Research, v. 109, F03008.

Von Blanckenburg, F., 2005, The control mechanisms of erosion and weathering at basin scale from cosmogenic nuclides in river sediment. Earth and Planetary Science Letters, v. 237, no. 3-4, p. 462-479.

Waelbroeck, C., Labeyrie, L., Michel, E., Duplessy, J.C., McManus, J.F., Lambeck, K., Balbon, E. and Labracherie, M., 2002, Sea-level and deep water temperature changes derived from benthic foraminifera isotopic records. Quaternary Science Reviews, v. 21, p. 295-305.

Whipple, K.X., Wobus, C., Crosby, B., Kirby, E. and Sheehan, D., 2007, New tools for quantitative geomorphology: extraction and interpretation of stream profiles from digital topographic data. *In* GSA Annual Meeting, p. 26.

White, A.F. and Blum, A.E., 1995, Effects of climate on chemical, weathering in watersheds. Cosmochemica et Cosmochemica Acta, v. 59, no. 9, p. 1729-1747.

Wilkinson, B.H. and McElroy, B.J., 2007, The impact of humans on continental erosion and sedimentation. Geological Society of America Bulletin, v. 119, no. 1-2, p. 140-156.

Wilkinson, M.J., 1988, Arid Landscapes. *In* Moon, B.P. and Dardis, G.F., (eds): The Geomorphology of Southern Africa, Southern Book Publishers (Pty) Ltd. p. 78-102

Willenbring, J.K. and von Blanckenburg, F., 2010, Long-term stability of global erosion rates and weathering during late-Cenozoic cooling. Nature, v. 465, no. 7295, p. 211-214.

Wittmann, H., von Blanckenburg, F., Kruesmann, T., Norton, K.P. and Kubik, P.W., 2007, Relation between rock uplift and denudation from cosmogenic nuclides in river sediment in the Central Alps of Switzerland. Journal of Geophysical Research, v. 112, no. F04, p 1-20.

Wood, A., 1942, The development of hillside slopes. Geological Society of America, v. 53, p. 128-138.

Appendix

AMS analysis

Introduction

Appendix A is divided into four sections, namely A.1: River sediment analysis; A.2: Bedrock analysis; A.3: Alluvial terrace analysis; and A.4: Radiocarbon analysis. Abbreviations and instrumental uncertainties applicable to the data throughout the appendix include:

Latitude (Lat.) Longitude (Long) Elevation (Elev.)	Latitudes and longitudes were measured with a Garmin 60CSx hand-held GPS and are referenced to WGS 84. Each measurement has a recorded accuracy of ±4 m. Elevation was similarly measured with a Garmin 60CSx hand-held GPS which has a maximum resolution of 33 cm. However, as waypoints were not logged an altitudinal error of 6-10 m is expected in these measurements.
Sample density	Sample densities are estimated to that of quartz, given the purity of the quartz-rich sediments, quartzites and quartz pebbles sampled.
$^{10}Be/^{9}Be$ ratios	The tabulated $^{10}Be/^{9}Be$ ratios have been corrected with a procedural blank. The relevant blank is provided alongside the respective sample and information on the ^{10}Be content of each blank is provided. Samples were analysed in two batches thus two procedural blanks are present, namely BLK-TS1-01.11 for Batch 1 samples and BLK-TS2-01.11 for batch 2 samples,
Radiocarbon ages	Both conventional radiocarbon ages (CRA) and calibrated radiocarbon ages (calBP) are provided.

A.1 River sediment analysis

Table A.1: Physical parameters of samples.

Sample ID	Lat. (deg.)	Long. (deg.)	Elev (masl)	Mass (g)	Density ($g \cdot cm^{-3}$)
S03	-33.99541	20.66277	119	29.517	2.65
S04	-33.99296	20.70459	129	28.275	2.65
S06	-33.43325	21.40669	619	28.705	2.65
S07	-34.02089	21.35044	194	28. 665	2.65
S08	-33.98339	20.84508	247	30.050	2.65
S09	-33.98122	20.37606	211	29.865	2.65
S10	-33.98514	20.42211	230	29.893	2.65
S11	-33.46236	21.215	529	29.455	2.65
S12	-33.39631	22.357	747	28.160	2.65
S13	-33.35956	22.179	737	30.340	2.65

Table A.2: Original AMS results. Uncertainties are reported to one sigma level.

Sample ID	$^{10}Be/^{9}Be \times 10^{-13}$	Blank
S03	23.12 ± 0.69	BLK-TS2-01.11
S04	23.89 ± 0.72	BLK-TS1-01.11
S06	44.28 ± 1.33	BLK-TS1-01.11
S07	38.58 ± 1.16	BLK-TS1-01.11
S08	36.97 ± 1.11	BLK-TS1-01.11
S09	23.11 ± 0.69	BLK-TS1-01.11
S10	20.76 ± 0.62	BLK-TS1-01.11
S11	26.97 ± 0.81	BLK-TS1-01.11
S12	56.49 ± 1.69	BLK-TS1-01.11
S13	35.22 ± 1.06	BLK-TS1-01.11
BLK-TS1-01.11	1.10 ± 0.85	-
BLK-TS2-01.11	0.80 ± 0.59	-

Table A.3: Mass of ^{9}Be carrier solution and ^{9}Be spike added to each sample. The carrier solution has a ^{9}Be concentration of 372.5 ± 3.5 ppm. Uncertainties are reported to one sigma level.

Sample ID	Carrier mass (g)	^{9}Be spike (µg)
S03	0.4393	163.7 ± 1.6
S04	0.4381	163.2 ± 1.6
S06	0.4379	163.1 ± 1.5
S07	0.4390	163.5± 1.6
S08	0.4358	162.3 ± 1.5
S09	0.4376	163.0 ± 1.5
S10	0.4388	163.4 ± 1.6
S11	0.4381	163.2 ± 1.5
S12	0.4377	163.0 ± 1.5
S13	0.4402	164.0 ± 1.5
BLK-TS1-01.11	0.4350	162.1 ± 1.5
BLK-TS2-01.11	0.4378	163.1 ± 1.6

A.2 Bedrock analysis

Table A.4: Physical parameters of samples. Uncertainties are reported to one sigma level.

Sample ID	Lat. (deg.)	Long. (deg.)	Elev. (masl)	Mass (g)	Density (g·cm^{3})	Thickness (cm)	Dip (deg.)
S5.1	-33.95593	20.70795	232	28.110	2.65	5	5.0 ± 1.0
S5.2	-33.95593	20.70809	216	27.060	2.65	5	4.3 ± 1.0
S15	-33.96211	20.70775	489	28.470	2.65	5	17.1 ± 3.3
S17	-33.95719	20.71817	811	58.900	2.65	5	10.8 ± 1.6
S18	-33.95706	20.71817	815	29.035	2.65	5	10.5 ± 3.3

Table A.5: Original AMS data. Uncertainties are reported to one sigma level.

ID	$^{10}Be/^{9}Be \times 10^{-13}$	Blank
S5.1	7.93 ± 0.26	BLK-TS1-01.11
S5.2	1.23 ± 0.06	BLK-TS1-01.11
S15	42.54 ± 1.28	BLK-TS1-01.11
S17	27.73 ± 0.83	BLK-TS2-01.11
S18	36.65 ± 1.10	BLK-TS1-01.11
BLK-TS1-01.11	1.10 ± 0.85	-
BLK-TS2-01.11	0.80 ± 0.59	-

Table A.6: Mass of ^{9}Be carrier solution and ^{9}Be spike added to each sample. The carrier solution has a concentration of 372.5 ± 3.5 µg·g^{-1}. Uncertainties are reported to one sigma level.

ID	Carrier mass (g)	^{9}Be spike (µg)
S5.1	0.4379	163.1 ± 1.5
S5.2	0.4360	162.4 ± 1.5
S15	0.4381	163.2 ± 1.54
S17	0.4387	326.6 ± 3.1
S18	0.4387	163.4 ± 1.5
BLK-TS1-01.11	0.4350	162.1 ± 1.5
BLK-TS2-01.11	0.4378	163.1 ± 1.6

A.3 Alluvial terrace analysis

Table A.7: Physical parameters of samples.

Sample ID	Lat. (deg.)	Long. (deg.)	Elev. (masl)	Depth† (m)	Mass (g)	Density ($g \cdot cm^{-3}$)
S1.2	-34.00639	20.70333	122	0.0 - 0.1	27.86	2.65
S1.3	-34.00639	20.70333	122	0.2 - 0.3	16.67	2.65
S1.4	-34.00639	20.70333	122	0.5 - 0.6	24.36	2.65
S1.5	-34.00639	20.70333	122	1.0 – 1.2	30.07	2.65
S2.1	-34.00458	20.70661	135	3.6 - 3.8	27.12	2.65
S2.2	-34.00458	20.70661	135	2.9 - 3.0	31.93	2.65
S2.3	-34.00458	20.70661	135	0.6 - 0.8	29.01	2.65
BLK-TS1-01.11	-	-	-	-	$1.62 \cdot 10^{-4}$	-
BLK-TS2-01.11	-	-	-	-	$1.63 \cdot 10^{-4}$	-

†Depth was measured from the upper limit of the pebbly depositional terrace. In addition to the depth presented in Table A.7, terrace S1 lay beneath 3.8 m of silty mud and terrace S2 lay beneath 0.6 m of sandy soil, the density of which was approximated to be $1.52 g \cdot cm^{-3}$.

Table A.8: Raw AMS data. Uncertainties are to one sigma level.

Sample ID	$^{10}Be/^{9}Be \times 10^{-13}$	Blank
S1.2	9.86 ± 0.51	BLK-TS2-01.11
S1.3	21.9 ±1.14	BLK-TS2-01.11
S1.4	9.09 ± 0.30	BLK-TS2-01.11
S1.5	-	BLK-TS2-01.11
S2.1	4.98 ± 0.29	BLK-TS2-01.11
S2.2	9.58 ± 0.32	BLK-TS2-01.11
S2.3	13.45 ± 0.79	BLK-TS2-01.11
BLK-TS1-01.11	1.10 ± 0.85	-
BLK-TS2-01.11	0.80 ± 0.59	-

Table A.9: Mass of ^{9}Be carrier solution added to each sample. The carrier solution has a concentration of 372.5 ± 3.5 µg·g^{-1}. Uncertainties are reported to one sigma level.

ID	^{9}Be carrier mass (µg)
S1.2	162 ± 1.53
S1.3	163 ± 1.53
S1.4	164 ± 1.54
S1.5	163 ± 1.56
S2.1	163 ± 1.56
S2.2	163 ± 1.57
S2.3	164 ± 1.55
BLK-TS1-01.11	162 ± 1.53
BLK-TS2-01.11	163 ± 1.55

A.4 Radiocarbon analysis

Table A.10: Physical parameters of samples and pre-treatment method.

Sample ID	Lat (deg.)	Long. (deg.)	Burial depth (m)	Mass (mg)	Pre-treatment
R1.1	-34.00639	20.70333	3.82	0..67	acid-alkali-acid
R1.2	-34.00639	20.70333	3.02	1.00	acid-alkali-acid
R1.3	-34.00639	20.70333	1.72	1.00	acid-alkali-acid

Table A.11: Radiocarbon data for charcoal samples removed from a 4 m thick mud horizon overlying terrace S1. Uncertainties are reported to one sigma level

Sample ID	^{14}C (pmC)	CRA (yrs BP)	CalBP (yrs BP)	
			95.4% probability	68.2% probability
R1.1	64.15	3567 ± 31	3980-3820 (84.5%) 3800-3760 (6.6 %) 3750-3720 (4.3 %)	3920-3830 (68.2 %)
R1.2	67.00	3217 ± 30	3560-3540 (1.6 %) 3490-3370 (93.8%)	3460-3390 (68.2 %)
R1.3	68.56	3032 ± 30	3350-3150 (95.4%)	3330 - 3280 (25.2%) 3270-3210 (43.0 %)